

國立交通大學
土木工程學系碩士班
碩士論文

受限背填土對主動土壓力之影響

Effects of Constrained Backfill on Active Earth Pressure

研究生：陳威廷

指導教授：方永壽 博士

中華民國九十九年七月

受限背填土對主動土壓力之影響

**Effects of Constrained Backfill on Active Earth
Pressure**

研究生：陳威廷

Student : Wei-Ting Chen

指導教授：方永壽 博士

Advisor : Dr. Yung-Show Fang

國立交通大學土木工程學系碩士班

碩士論文

A Thesis

Submitted to the Department of Civil Engineering

College of Engineering

National Chiao Tung University

in Partial Fulfillment of the Requirements

for the Degree of

Master of Engineering

in Civil Engineering

July, 2010

Hsinchu, Taiwan, Republic of China

中華民國九十九年七月

受限背填土對主動土壓力之影響

研究生：陳威廷 指導教授：方永壽 博士

國立交通大學土木工程學系碩士班

摘要

本研究探討受限背填土對主動土壓力之影響。本研究利用國立交通大學模型擋土牆設備來探討受限背填土作用在擋土牆上的主動土壓力。本研究以氣乾渥太華砂作為回填土，相對密度 $D_r = 36\%$ ，回填土高 0.5 公尺。為了模擬束制背填土的岩層介面，本研究設計並建造一片鋼製傾斜界面板及其支撐系統。本研究兩個重要參數為界面板與擋土牆底之水平間距 b 及界面板傾角 β 。試驗結果顯示，以空中實降法填入土槽之背填土密度均勻，且背填土之相對密度不受界面板位置與傾角影響。當界面板遠離擋土牆 ($b/H = 4.0$)，量測到的水平主動土壓力與 Coulomb 解符合良好。當 $b/H = 1.0$ ，量測到的主動土壓力接近於 Coulomb 解，於此狀況界面板對主動土壓力沒有明顯的影響。當界面板逐漸接近擋土牆時 (b/H 減小)，界面板逐漸侵入主動土楔，造成主動土楔無法完全發展，且牆後填土量逐漸減少，隨著逐漸減小的水平距離 b ，和逐漸增大的界面板傾斜角度 β ，主動土壓力逐漸下降。於 $\beta = 90^\circ$ (牆面垂直) 且 $b/H < 1.0$ 狀況，量測到的主動土壓力小於 Coulomb 解，靠近牆面之垂直界面板對於主動土壓力的影響相當明顯。於 $b/H = 0.3$ 、 0.5 、 0.7 及 1.0 ，主動土壓力合力作用點的位置大約都在距牆底 $H/3$ 處。當傾斜岩石介面逐漸接近擋土牆，依據 Coulomb 理論所求之擋土牆抗滑動之安全係數及抗傾覆之安全係數增大。

關鍵字：主動土壓力、受限背填土、土壓力、模型試驗、擋土牆、砂

Effects of Constrained Backfill on Active Earth Pressure

Student : Wei-Ting Chen

Advisor : Dr. Yung-Show Fang

Department of Civil Engineering

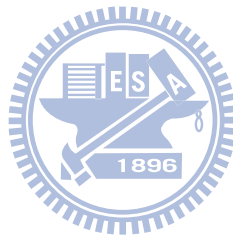
National Chiao Tung University

Abstract

This thesis investigates the effects of constrained backfill on active earth pressure. The instrumented model retaining wall facilities at National Chiao Tung University was used to study the active earth pressure on retaining wall with constrained backfill. Loose Ottawa sand with the relative density $D_r = 36\%$ was used as backfill material. The height of backfill H was 0.5 m. To simulate an inclined rock face, a steel interface plate and its supporting system were designed and constructed. Two main parameters considered were rock face inclination angle β and the horizontal spacing b between the rock face and the wall base. The backfill in the soil bin was prepared by air-pluviated method. Test results show the distribution relative density in the soil bin is uniform and independent of the interface plate inclination and location. With a faraway interface plate ($b/H = 4.0$), the measured active pressure distribution was in good agreement with Coulomb's solution. When the vertical boundary was relatively far from the wall face, the measured stress was not strongly affected by the existence of the vertical plate. With the approaching of the interface plate (b/H ratio decreasing), the plate intruded the active soil wedge, so that the active soil wedge behind the wall can not develop fully. The active earth pressure coefficient $K_{a,h}$ decreased with decreasing wall-plate spacing b . Coefficient $K_{a,h}$ decreased with decreasing plate inclination angle β . For $\beta = 90^\circ$ (vertical plate) and $b/H < 1.0$, the measured active pressure was less than Coulomb's solution. Coulomb's solution is the upper bound for all experimental $K_{a,h}$ values based on different b/H ratios and β angles. The constrained backfill would result in a greater

factor of safety against sliding for the retaining wall. Under the aspect ratio $b/H = 0.3, 0.5, 0.7,$ and $1.0,$ the point of application of the active soil thrust was located at about $H/3$ above the wall base. The evaluation of the factors of safety against sliding and overturning with Coulomb's solution would be on safe side.

Keywords: Active pressure; Constrained backfill; Earth pressure; Model test; Retaining wall; Sand



Acknowledgements

The author wishes to give his sincere appreciation to his advisor, Dr. Yung-Show Fang for his enthusiastic advice and continuous encouragement in the past two years. If there is not the guidance from him, the thesis can not be accomplished.

Very special thanks are extended to Dr. Yi-Wen Pan, Dr. Jhih-Jhong Liao, Dr. An-Bin Huang, Dr. Shen-Yu Shan and Dr. Chih-Ping Lin for their teaching and valuable suggestions. In addition, the author also felt a great gratitude to the members of his supervisory committee, Dr. Mei-Ling Lin and Dr. Tao-Wei Feng for their suggestions and discussions.

The author must extend his gratitude to Dr. Tsang-Jiang Chen, Mr. Kuo-Hua Li, Mr. Hao-Chen Chang, Mr. Po-Shou Chen, Mr. Sheng-Feng Huang and Miss Yi-Jhen Jiang for their support and encouragement. Appreciation is extended to all my friends and classmates, especially for Mr. Cho-Min Lin, Miss Yu-Fen Hsu, Mr. Kuan-Yu Chen, Mr. Ting-Yuen Huang and Mr. Min-Yi Huang for their encouragement and assistance.

Finally, the author would dedicate this thesis to his grandmother, parents and brother for their continuing encouragement and moral support.

Table of Contents

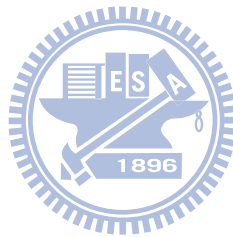
| | |
|---|----------|
| Abstract (in Chinese) | I |
| Abstract..... | II |
| Acknowledgements | IV |
| Table of Contents..... | V |
| List of Tables | VIII |
| List of Figures..... | IX |
| List of Symbols..... | XVIII |
| Chapter 1 Introduction | 1 |
| 1.1 Objectives of Study..... | 1 |
| 1.2 Research Outline..... | 2 |
| 1.3 Organization of Thesis..... | 3 |
| Chapter 2 Literature Review..... | 4 |
| 2.1 Active Earth Pressure Theories..... | 4 |
| 2.1.1 Coulomb Earth Pressure Theory..... | 4 |
| 2.1.2 Rankine Earth Pressure Theory | 6 |
| 2.1.3 Terzaghi General Wedge Theory | 7 |
| 2.1.4 Spangler and Handy's Theory | 9 |
| 2.2 Laboratory Model Retaining Wall Tests | 10 |
| 2.2.1 Model Study by Mackey and Kirk..... | 10 |
| 2.2.2 Model Study by Fang and Ishibashi | 10 |
| 2.2.3 Model Retaining Wall Study by Huang..... | 11 |
| 2.2.4 Centrifuge Model Study by Frydman and Keissar | 12 |
| 2.3 Numerical Studies..... | 14 |
| 2.3.1 Numerical Study by Leshchinsky, et al. | 14 |

| | |
|--|-----------|
| 2.3.2 Numerical Study by Lawson and Yee..... | 15 |
| 2.3.3 Numerical Study by Yang and Liu..... | 16 |
| 2.3.4 Numerical Study by Fan and Fang | 17 |
| 2.4 Plane Strain State-of-Stress | 18 |
| Chapter 3 Experimental Apparatus..... | 20 |
| 3.1 Model Retaining Wall..... | 20 |
| 3.2 Soil Bin..... | 21 |
| 3.3 Driving System | 22 |
| 3.4 Data Acquisition | 22 |
| Chapter 4 Interface Plate and Supporting System..... | 24 |
| 4.1 Interface Plate | 24 |
| 4.1.1 Steel Plate | 24 |
| 4.1.2 Reinforcement with Steel Beams..... | 24 |
| 4.2 Supporting System..... | 25 |
| 4.2.1 Top Supporting Beam..... | 25 |
| 4.2.2 Base Supporting Block | 25 |
| 4.2.3 Base Boards | 26 |
| Chapter 5 Backfill and Interface Characteristics..... | 27 |
| 5.1 Backfill Properties | 27 |
| 5.2 Model Wall Friction..... | 28 |
| 5.3 Side Wall Friction | 29 |
| 5.4 Interface Plate Friction | 30 |
| 5.5 Control of Soil Density..... | 31 |
| 5.5.1 Air-Pluviation of Backfill | 31 |
| 5.5.2 Distribution of Soil Density..... | 31 |
| Chapter 6 Test Results..... | 33 |

| | |
|---|-----|
| 6.1 Horizontal Earth Pressure with Faraway Plate | 33 |
| 6.2 Horizontal Earth Pressure for $b = 150$ mm..... | 35 |
| 6.3 Horizontal Earth Pressure for $b = 250$ mm..... | 37 |
| 6.4 Horizontal Earth Pressure for $b = 350$ mm..... | 38 |
| 6.5 Horizontal Earth Pressure for $b = 500$ mm..... | 39 |
| 6.6 Active Soil Thrust..... | 39 |
| 6.6.1 Magnitude of Active Soil Thrust | 41 |
| 6.6.2 Point of Application of Active Soil Thrust | 42 |
| 6.7 Lateral Pressure in Silo..... | 42 |
| 6.8 Displacement Vector in Backfill..... | 43 |
| 6.9 Design Considerations..... | 45 |
| 6.9.1 Factor of Safety against Sliding..... | 45 |
| 6.9.2 Factor of Safety against Overturning..... | 46 |
| Chapter 7 Conclusions | 47 |
| References | 49 |
| Appendix A: Calibration of Soil Pressure Transducers..... | 204 |

List of Tables

| | |
|--|----|
| Table 2.1. Comparison of experimental and theoretical values..... | 54 |
| Table 2.2. Wall displacements required to reach an active state..... | 55 |
| Table 6.1 Test Program..... | 56 |



List of Figures

| | |
|---|----|
| Fig. 1.1. Fig. 1.1. Retaining walls with constrained backfill | 57 |
| Fig. 1.2. Cylindrical silo filled with granular material | 58 |
| Fig. 1.3. Model test for $b = 150$ mm | 59 |
| Fig. 1.4. Model test for $b = 250$ mm | 60 |
| Fig. 1.5. Model test for $b = 350$ mm | 61 |
| Fig. 1.6. Model test for $b = 500$ mm | 62 |
| Fig. 1.7. Model test for $b = 2,000$ mm | 63 |
| Fig. 2.1. Coulomb's theory of active earth pressure | 64 |
| Fig. 2.2. Coulomb's active pressure determination | 65 |
| Fig. 2.3. Rankine's theory of active earth pressure | 65 |
| Fig. 2.4. Failure surface in soil by Terzaghi's log-spiral method | 66 |
| Fig. 2.5. Evaluation of active earth pressure by trial wedge method | 67 |
| Fig. 2.6 Stability of soil mass abd_1f_1 | 68 |
| Fig. 2.7 Active earth pressure determination with Terzaghi's log-spiral failure surfaces | 69 |
| Fig. 2.8. Fascia retaining wall of backfill width B and wall friction F | 70 |
| Fig. 2.9. Horizontal element of backfill material | 71 |
| Fig. 2.10. Distribution of soil pressure against fascia walls due to partial support from wall friction F | 72 |
| Fig. 2.11. University of Manchester model retaining wall | 73 |
| Fig. 2.12. Earth pressure with wall movement | 74 |
| Fig. 2.13. Failure surfaces | 75 |
| Fig. 2.14. Distributions of horizontal earth pressure at different wall displacement | 76 |
| Fig. 2.15. Change of normalized lateral pressure with translation wall displacement | 77 |
| Fig. 2.16. Coefficient of horizontal active thrust as a function of soil density | 78 |
| Fig. 2.17. Different interface inclinations for $b = 0$ | 79 |

| | |
|--|----|
| Fig. 2.18. Different interface inclinations for $b = 50$ mm | 80 |
| Fig. 2.19. Different interface inclinations for $b = 100$ mm | 81 |
| Fig. 2.20. Distribution of active earth pressure at different β angles for $b = 0$ | 82 |
| Fig. 2.21. Distribution of active earth pressure at different β angles for $b = 50$ mm | 82 |
| Fig. 2.22. Distribution of active earth pressure at different β angles for $b = 100$ mm | 83 |
| Fig. 2.23. Active earth pressure coefficient $K_{a,h}$ versus interface inclination angle β | 84 |
| Fig. 2.24. Point of application of active soil thrust versus interface inclination angle β | 85 |
| Fig. 2.25 Schematic representation of retaining wall near rock face | 86 |
| Fig. 2.26. Model retaining wall | 87 |
| Fig. 2.27. Distribution of K'_a with z/b from silo pressure equation | 88 |
| Fig. 2.28. Typical geometry: (a) analyzed (b) notation | 89 |
| Fig. 2.29. Predictions by ReSSA versus centrifugal test results for $\phi = 36^\circ$ and $m = \infty$ | 90 |
| Fig. 2.30. Analysis results | 90 |
| Fig. 2.31. Forces acting on wall face, wedge angles, and horizontal force coefficients for fill $\phi' = 30^\circ$ | 91 |
| Fig. 2.32. Illustration of the simulated case | 92 |
| Fig. 2.33. Finite element (a) meshes for at-rest case and (b) model for active case | 93 |
| Fig. 2.34. Normalized earth pressure coefficient profiles along the wall face for (a) at-rest and (b) active case | 94 |
| Fig. 2.35. Normalized equivalent earth pressure coefficients for (a)at-rest and (b) active case | 95 |
| Fig. 2.36. Typical geometry of backfill zone behind a retaining wall used in this study | 96 |
| Fig. 2.37. The finite element mesh for a retaining wall with limited backfill space ($\beta=70^\circ$ and $b=0.5m$) | 96 |

| | |
|---|-----|
| Fig. 2.38. Distribution of earth pressures with the depth at various wall displacements for walls in translation (T mode) | 97 |
| Fig. 2.39. Variation of the coefficient of active earth pressures ($K_{a(\text{Computed})}/K_{a(\text{Coulomb})}$) with the inclination of rock faces at various fill widths (b) for walls undergoing translation | 98 |
| Fig. 2.40. Variation of the location of resultant (h/H) of active earth pressures with the inclination of rock faces at various fill widths (b) for walls undergoing translation (T mode) | 99 |
| Fig. 2.41. Definition of plane strain state-of-stress | 100 |
| Fig. 3.1. NCTU Model Retaining-Wall Facility | 101 |
| Fig. 3.2. NCTU model retaining wall | 102 |
| Fig. 3.3. Displacement transducer (Kyowa DT-20D) | 102 |
| Fig. 3.4. Locations of pressure transducers on NCTU model wall | 103 |
| Fig. 3.5. Locations of pressure transducers on model wall | 104 |
| Fig. 3.6. Soil pressure transducer (Kyowa PGM-0.2KG) | 104 |
| Fig. 3.7. Plastic-sheet on each sidewall | 105 |
| Fig. 3.8. Picture of Data acquisition system | 106 |
| Fig. 4.1. NCTU model retaining wall with inclined interface plate | 107 |
| Fig. 4.2. Steel interface plate | 108 |
| Fig. 4.3. Steel interface plate (picture) | 109 |
| Fig. 4.4 Top-view of model wall | 110 |
| Fig. 4.5. NCTU model retaining wall with interface plate supports | 111 |
| Fig. 4.6. Top supporting beam | 112 |
| Fig. 4.7. Steel interface plate and top supporting beam | 113 |
| Fig. 4.8. Base supporting block | 114 |
| Fig. 4.9. Base supporting boards | 116 |
| Fig. 5.1. Grain size distribution of Ottawa sand | 117 |
| Fig. 5.2. Shear box of direct shear test device | 118 |
| Fig. 5.3. Relationship between unit weight γ and internal friction angle ϕ | 119 |

| | |
|--|-----|
| Fig. 5.4. Direct shear test to determinate wall friction | 120 |
| Fig. 5.5. Relationship between unit weight γ and wall friction angle δ_w | 121 |
| Fig. 5.6. Plastic-sheet lubrication layers on side walls | 122 |
| Fig. 5.7. Schematic diagram of sliding block test | 123 |
| Fig. 5.8 Sliding block test apparatus | 124 |
| Fig. 5.9 Variation of side-wall friction angle with normal stress | 125 |
| Fig. 5.10. Direct shear test to determine interface friction angle | 126 |
| Fig. 5.11. Relationship between unit weight γ and interface plate friction angle δ_i | 127 |
| Fig. 5.12. Relationship friction angle δ and soil unit weight γ | 128 |
| Fig. 5.13. Soil hopper | 129 |
| Fig. 5.14. Pluviation of Ottawa sand into soil bin | 130 |
| Fig. 5.15. Relationship between relation density and drop height | 131 |
| Fig. 5.16. Soil-density control cup | 132 |
| Fig. 5.17. Soil-density cup | 133 |
| Fig. 5.18. Locations of density cups for $b = 150$ mm and $\beta = 90^\circ$ | 134 |
| Fig. 5.19. Locations of density cups for $b = 250$ mm and $\beta = 90^\circ$ | 135 |
| Fig. 5.20. Locations of density cups for $b = 350$ mm and $\beta = 90^\circ$ | 136 |
| Fig. 5.21. Locations of density cups for $b = 500$ mm and $\beta = 90^\circ$ | 137 |
| Fig. 5.22. Locations of density cups for $b = 150$ mm and $\beta = 80^\circ$ | 138 |
| Fig. 5.23. Locations of density cups for $b = 150$ mm and $\beta = 70^\circ$ | 139 |
| Fig. 5.24. Locations of density cups for $b = 150$ mm and $\beta = 60^\circ$ | 140 |
| Fig. 5.25 Distribution of relative density | 141 |
| Fig. 6.1. Model wall test with faraway interface plate ($b = 2,000$ mm and $\beta = 90^\circ$) | 142 |
| Fig. 6.2. Distribution of horizontal earth pressure for $b = 2,000$ mm and $\beta = 90^\circ$ (Test 0119-1) | 144 |
| Fig. 6.3. Distribution of horizontal earth pressure for $b = 2,000$ mm and $\beta = 90^\circ$ (Test 0427-2) | 144 |

| | |
|---|-----|
| Fig. 6.4 Earth pressure coefficient K_h versus wall movement for $b = 2,000$ mm and $\beta = 90^\circ$ | 145 |
| Fig. 6.5. Location of total thrust application for $b = 2,000$ mm and $\beta = 90^\circ$ | 145 |
| Fig. 6.6. Model wall test with interface spacing $b = 150$ mm and $\beta = 90^\circ$ | 146 |
| Fig. 6.7. Distribution of horizontal earth pressure for $b = 150$ mm and $\beta = 90^\circ$ (Test 0305-1) | 148 |
| Fig. 6.8. Distribution of horizontal earth pressure for $b = 150$ mm and $\beta = 90^\circ$ (Test 0503-4) | 148 |
| Fig. 6.9. Model wall test with interface spacing $b = 150$ mm and $\beta = 80^\circ$ | 149 |
| Fig. 6.10 Distribution of horizontal earth pressure for $b = 150$ mm and $\beta = 80^\circ$ (Test 0315-3) | 151 |
| Fig. 6.11 Distribution of horizontal earth pressure for $b = 150$ mm and $\beta = 80^\circ$ (Test 0316-2) | 151 |
| Fig. 6.12. Model wall test with interface spacing $b = 150$ mm and $\beta = 70^\circ$ | 152 |
| Fig. 6.13. Distribution of horizontal earth pressure for $b = 150$ mm and $\beta = 70^\circ$ (Test 0413-1) | 154 |
| Fig. 6.14. Distribution of horizontal earth pressure for $b = 150$ mm and $\beta = 70^\circ$ (Test 0413-2) | 154 |
| Fig. 6.15. Model wall test with interface spacing $b = 150$ mm and $\beta = 60^\circ$ | 155 |
| Fig. 6.16. Distribution of horizontal earth pressure for $b = 150$ mm and $\beta = 60^\circ$ (Test 0420-3) | 157 |
| Fig. 6.17. Distribution of horizontal earth pressure for $b = 150$ mm and $\beta = 60^\circ$ (Test 0512-3) | 157 |
| Fig. 6.18. Earth pressure coefficient K_h versus wall movement for $b = 150$ mm and $\beta = 90^\circ$ | 158 |
| Fig. 6.19. Earth pressure coefficient K_h versus wall movement for $b = 150$ mm and $\beta = 80^\circ$ | 158 |
| Fig. 6.20. Earth pressure coefficient K_h versus wall movement for $b = 150$ mm and $\beta = 70^\circ$ | 159 |

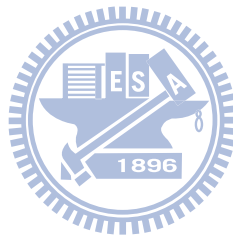
| | |
|---|-----|
| Fig. 6.21. Earth pressure coefficient K_h versus wall movement for $b = 150$ mm and $\beta = 60^\circ$ | 159 |
| Fig. 6.22. Location of total soil thrust for $b = 150$ mm and $\beta = 90^\circ$ | 160 |
| Fig. 6.23. Location of total soil thrust for $b = 150$ mm and $\beta = 80^\circ$ | 160 |
| Fig. 6.24. Location of total soil thrust for $b = 150$ mm and $\beta = 70^\circ$ | 161 |
| Fig. 6.25. Location of total soil thrust for $b = 150$ mm and $\beta = 60^\circ$ | 161 |
| Fig. 6.26. Model wall test with interface spacing $b = 250$ mm and $\beta = 90^\circ$ | 162 |
| Fig. 6.27. Distribution of horizontal earth pressure for $b = 250$ mm and $\beta = 90^\circ$ (Test 0322-3) | 164 |
| Fig. 6.28. Distribution of horizontal earth pressure for $b = 250$ mm and $\beta = 90^\circ$ (Test 0323-3) | 164 |
| Fig. 6.29. Model wall test with interface spacing $b = 250$ mm and $\beta = 80^\circ$ | 165 |
| Fig. 6.30. Distribution of horizontal earth pressure for $b = 250$ mm and $\beta = 80^\circ$ (Test 0518-3) | 167 |
| Fig. 6.31. Distribution of horizontal earth pressure for $b = 250$ mm and $\beta = 80^\circ$ (Test 0518-4) | 167 |
| Fig. 6.32. Model wall test with interface spacing $b = 250$ mm and $\beta = 70^\circ$ | 168 |
| Fig. 6.33. Distribution of horizontal earth pressure for $b = 250$ mm and $\beta = 70^\circ$ (Test 0524-1) | 170 |
| Fig. 6.34. Distribution of horizontal earth pressure for $b = 250$ mm and $\beta = 70^\circ$ (Test 0524-3) | 170 |
| Fig. 6.35. Earth pressure coefficient K_h versus wall movement for $b = 250$ mm and $\beta = 90^\circ$ | 171 |
| Fig. 6.36. Earth pressure coefficient K_h versus wall movement for $b = 250$ mm and $\beta = 80^\circ$ | 171 |
| Fig. 6.37. Earth pressure coefficient K_h versus wall movement for $b = 250$ mm and $\beta = 70^\circ$ | 172 |
| Fig. 6.38. Location of total soil thrust for $b = 250$ mm and $\beta = 90^\circ$ | 173 |
| Fig. 6.39. Location of total soil thrust for $b = 250$ mm and $\beta = 80^\circ$ | 173 |



| | |
|---|-----|
| Fig. 6.40. Location of total soil thrust for $b = 250$ mm and $\beta = 70^\circ$ | 174 |
| Fig. 6.41. Model wall test with interface spacing $b = 350$ mm and $\beta = 90^\circ$ | 175 |
| Fig. 6.42. Distribution of horizontal earth pressure for $b = 350$ mm and $\beta = 90^\circ$ (Test 0330-2) | 177 |
| Fig. 6.43. Distribution of horizontal earth pressure for $b = 350$ mm and $\beta = 90^\circ$ (Test 0330-3) | 177 |
| Fig. 6.44. Model wall test with interface spacing $b = 350$ mm and $\beta = 80^\circ$ | 178 |
| Fig. 6.45. Distribution of horizontal earth pressure for $b = 350$ mm and $\beta = 80^\circ$ (Test 0525-1) | 180 |
| Fig. 6.46. Distribution of horizontal earth pressure for $b = 350$ mm and $\beta = 80^\circ$ (Test 0525-2) | 180 |
| Fig. 6.47. Earth pressure coefficient K_h versus wall movement for $b = 350$ mm and $\beta = 90^\circ$ | 181 |
| Fig. 6.48. Earth pressure coefficient K_h versus wall movement for $b = 350$ mm and $\beta = 80^\circ$ | 181 |
| Fig. 6.49. Location of total thrust application for $b = 350$ mm and $\beta = 90^\circ$ | 182 |
| Fig. 6.50. Location of total thrust application for $b = 350$ mm and $\beta = 80^\circ$ | 182 |
| Fig. 6.51. Model wall test with interface spacing $b = 500$ mm and $\beta = 90^\circ$ | 183 |
| Fig. 6.52. Distribution of horizontal earth pressure for $b = 500$ mm and $\beta = 90^\circ$ (Test 0412-2) | 185 |
| Fig. 6.53. Distribution of horizontal earth pressure for $b = 500$ mm and $\beta = 90^\circ$ (Test 0412-3) | 185 |
| Fig. 6.54. Earth pressure coefficient K_h versus wall movement for $b = 500$ mm and $\beta = 90^\circ$ | 186 |
| Fig. 6.55. Location of total thrust application for $b = 500$ mm and $\beta = 90^\circ$ | 186 |
| Fig. 6.56. Distribution of active earth pressure at different interface inclination angle β for $b = 150$ mm | 187 |
| Fig. 6.57 Distribution of active earth pressure at different interface inclination angle β for $b = 250$ mm | 187 |

| | |
|--|-----|
| Fig. 6.58. Distribution of active earth pressure at different interface inclination angle β for $b = 350$ mm | 188 |
| Fig. 6.59. Distribution of active earth pressure for $b = 500$ mm | 188 |
| Fig. 6.60. Variation of earth pressure coefficient K_h with wall movement for $b = 150$ mm | 189 |
| Fig. 6.61. Variation of earth pressure coefficient K_h with wall movement for $b = 250$ mm | 189 |
| Fig. 6.62. Variation of earth pressure coefficient K_h with wall movement for $b = 350$ mm | 190 |
| Fig. 6.63. Variation of earth pressure coefficient K_h with wall movement for $b = 500$ mm | 190 |
| Fig. 6.64. Variation of total thrust location with wall movement for $b = 150$ mm | 191 |
| Fig. 6.65. Variation of total thrust location with wall movement for $b = 250$ mm | 191 |
| Fig. 6.66. Variation of total thrust location with wall movement for $b = 350$ mm | 192 |
| Fig. 6.67. Variation of total thrust location with wall movement for $b = 500$ mm | 192 |
| Fig. 6.68. Active earth pressure coefficient $K_{a,h}$ versus constrained backfill aspect ratio b/H | 193 |
| Fig. 6.69. Normalized active earth pressure coefficient with aspect ratio b/H | 194 |
| Fig. 6.70. Point of application of active soil thrust versus aspect ratio b/H | 195 |
| Fig. 6.71. Cylindrical silo filled with granular material | 196 |
| Fig. 6.72. Distribution of active earth pressure at different backfill aspect ratio b/H for $\beta = 90^\circ$ | 196 |
| Fig. 6.73. Variation of earth pressure coefficient K_h with wall movement for $\beta = 90^\circ$ | 197 |
| Fig. 6.74. Variation of soil thrust location with wall movement for $\beta = 90^\circ$ | 197 |
| Fig. 6.75. Comparison of the distribution of active earth pressures | 198 |
| Fig. 6.76. Observed backfill displacement for $b = 500$ mm and $\beta = 90^\circ$ for (a) $S = 0$ (b) $S/H = 0.04$ | 199 |

| | |
|--|-----|
| Fig. 6.77 Accumulated displacement for $b = 500$ mm and $\beta = 90^\circ$ for $S = 20$ mm ($S/H = 0.04$) | 200 |
| Fig. 6.78 Observed backfill displacement for $b = 150$ mm and $\beta = 90^\circ$ for (a) $S = 0$ and (b) $S = 20$ mm ($S/H = 0.04$) | 201 |
| Fig. 6.79 Accumulated displacement for $b = 150$ mm and $\beta = 90^\circ$ for $S = 20$ mm ($S/H = 0.04$) | 202 |
| Fig. 6.80. Normalized driving moment versus backfill aspect ratio b/H | 203 |



List of Symbols

| | |
|------------|--|
| C_u | = Uniformity Coefficient |
| b | = Distance between Interface Plate and Model Wall |
| D_r | = Relative Density |
| D_{10} | = Diameter of Ottawa Sand whose Percent finer is 10% |
| D_{60} | = Diameter of Ottawa Sand whose Percent finer is 60% |
| e_{max} | = Maximum Void Ratio of Soil |
| e_{min} | = Minimum Void Ratio of Soil |
| F | = Force |
| G_s | = Specific Gravity of Soil |
| h | = Location of Total Thrust |
| $(h/H)_a$ | = Point of Application of Active Soil Thrust |
| H | = Effective Wall Height |
| i | = Slop of Ground Surface behind Wall |
| K_o | = Coefficient of Earth Pressure At-Rest |
| K_a | = Coefficient of Active Earth Pressure |
| K_h | = Coefficient of Horizontal Earth Pressure |
| $K_{a,h}$ | = Coefficient of Horizontal Active Earth Pressure |
| P_a | = Total Active Force |
| β | = Angle of Inclination Rock Face |
| S | = Wall Displacement |
| T | = Translation |
| z | = Depth from Surface |
| σ_h | = Horizontal Earth Pressure |
| σ_N | = Normal Stress |

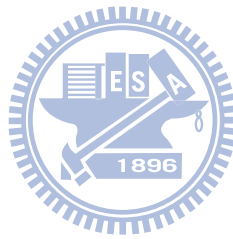
γ = Unit Weight of Soil

ϕ = Angle of Internal Friction of Soil

δ_i = Angle of Interface Friction

δ_{sw} = Angle of Side-Wall Friction

δ_w = Angle of Wall Friction



Chapter 1

Introduction

This thesis studies the effects of a constrained soil backfill on the active earth pressure against a retaining wall as shown in Fig. 1.1. In the figure, an inclined rock face is near the retaining wall. The backfill is constrained and the active soil failure wedge behind the wall can not develop fully. Under such a condition, the active earth pressure may be different from Coulomb's and Rankine's theories. In this study, experiments were conducted to investigate the distribution of active earth pressure as a function of the inclination angle β and the horizontal spacing b of the inclined rock face.

1.1 Objectives of Study

The calculation of forces exerted by soil against structures was one of the oldest problems in soil mechanics. The most widely accepted theories to estimate earth pressure are those of Coulomb and Rankine. For the gravity wall shown in Fig. 1.1, the Rankine active soil wedge is bounded by the wall and the failure plane with the inclination angle of $45^\circ + \phi/2$ with the horizontal.

If the retaining wall is constructed adjacent to an existence stable face such as a stiff rock face near the retaining wall shown in Fig. 1.1, the stiff rock face might intrude the active soil wedge as the wall moves away from the backfill. In this case, can the Coulomb and Rankine theories be used to estimate the active earth pressure on the wall with constrained backfill? Would the distribution of active earth pressure still be linear with depth? To correctly calculate the factor of safety against sliding and overturning of the wall, it is necessary for the designer to understand how would the nearby rock face influence the active earth pressure. In Fig. 1.1, the horizontal spacing between the inclined rock face and the base of the wall is defined as b and

the inclination angle of the rock face with the horizontal is expressed as β .

Valuable studies associated with earth pressure on retaining walls with constrained backfill had been conducted. Based on the arching theory, Spangler and Handy (1984) developed a theoretical equation for calculating the lateral earth pressure acting on the wall of a silo. The granular particles in the silo were constrained by the vertical silo walls. Based on the limit equilibrium method and the computer program ReSSA 2.0, Leshchinsky et al. (2004) numerically investigated the lateral earth pressure on a Mechanically-Stabilized-Earth wall with constrained fill. Lawson and Yee (2005) used the limit equilibrium method to numerically investigate the lateral earth pressure acting on retaining walls with constrained reinforced fill. Yang and Liu (2007) conducted finite element analysis to study the earth pressure for narrow retaining. Fan and Fang (2009) used the non-linear finite element program PLAXIS (PLAXIS, BV, 2002) to investigate the earth pressure against a rigid wall close to an inclined rock face. Huang (2009) used the model retaining wall facilities at National Chiao Tung University to investigate the active earth pressure on retaining walls near an inclined rock face.

Fig. 1.2 shows a cylindrical storage silo filled with granular material. It is important for designer to know how much lateral pressure is acting on the inside of silo walls. The silo wall deforms under the lateral pressure due to the granular. Due to symmetry, the center axis of the silo remains at-rest, which is similar to the vertical rock-face nearby. The granular material behind the deformable silo wall was restrained by the central axis of the silo. In this study, the lateral pressure in silo is discussed.

1.2 Research Outline

The National Chiao Tung University (NCTU) model retaining wall facility was modified to investigate the effects of a constrained backfill on the active earth

pressure. As shown in Fig. 1.1, two main parameters considered were the horizontal spacing b and the inclination angle β of the rock face. Fig. 1.3 to Fig. 1.7 shows all constrained condition for backfill for $b = 150$ mm, 250 mm, 350 mm, 500 mm and 2000 mm. For all tests, the height of the backfill H was 0.5 m, and air-dry Ottawa sand was used as the backfill material. The soil was placed between the wall and the interface plate with the air-pluviation method. The variation of lateral earth pressure σ_h was measured with the soil pressure transducers (SPT) on the surface of the model wall. Based on experimental results, the distribution of active earth pressure was obtained. Based on the test results, the magnitude of active soil thrust and the location of the active thrust were calculated and compared with the Coulomb and Rankine solutions. The displacement of backfill under a large wall movement was observed.

1.3 Organization of Thesis

This paper is divided into the following parts:

Chapter 1: Introduction of the subject

Chapter 2: Review of past investigations regarding the active earth pressures theories, numerical studies and laboratory test results

Chapter 3: Description of experimental apparatus

Chapter 4: Description of the Interface plate and supporting system

Chapter 5: Characteristics of the backfill and the interfaces

Chapter 6: Test results regarding horizontal earth pressure, active soil thrust, and movement of the backfill

Chapter 7: Conclusions and design recommendations

Chapter 2

Literature Review

Geotechnical engineers frequently use the Coulomb and Rankine's earth pressure theories to calculate the active earth pressure behind retaining structures. These theories are discussed in the following sections. Mackey and Kirk (1967), Fang and Ishibashi (1986), Frydman and Keissar (1987), and Huang (2009) made experimental investigations regarding active earth pressure. Frydman and Keissar (1987) used the centrifuge technique to test a small model wall. Numerical investigation was studied by Leshchinsky, et al. (2004), Lawson and Yee (2005) Yang and Liu (2007) and Fan and Fang (2009). Their major findings are introduced in this chapter.



2.1 Active Earth Pressure Theories

2.1.1 Coulomb Earth Pressure Theory

Coulomb (1776) proposed a method of analysis that determines the resultant horizontal force on a retaining system for any slope of wall, wall friction, and slope of backfill. The Coulomb theory is based on the assumption that soil shear resistance develops along the wall and the failure plane. Detailed assumptions are made as the followings:

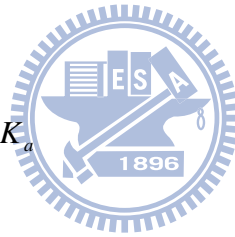
1. The backfill is isotropic and homogeneous.
2. The rupture surface is plane, as plane BC in [Fig. 2.1\(a\)](#). The backfill surface AC is a plane surface as well.
3. The frictional resistance is distributed uniformly along the rupture surface BC.

4. Failure wedge is a rigid body.
5. There is a friction force between soil and wall when the failure wedge moves toward the wall.
6. Failure is a plane strain condition.

In order to develop an active state, the wall is designed moved away from the soil mass. If the wedge ABC in Fig. 2.1(a) moves down relative to the wall, the wall friction angle δ will develop at the interface between the soil and wall. Let the weight of wedge ABC be W and the force on BC be F. With the given value θ and the summation of vertical forces and horizontal forces, the resultant soil thrust P can be calculated as shown in Fig. 2.1(b).

Similarly, the active forces of other trial wedges, such as ABC₂, ABC₃ (See Fig 2.2) can be determined. The maximum value of P_a thus determined is the Coulomb's active force.

$$P_a = \frac{1}{2} \gamma H^2 K_a \quad (2.1)$$



where

P_a = total active force per unit length of wall

K_a = coefficient of active earth pressure

γ = unit weight of soil

H = height of wall

And

$$K_a = \frac{\sin^2(\phi + \beta)}{\sin^2 \beta \sin(\beta - \delta) \left\{ 1 + \sqrt{\frac{\sin(\phi + \delta) \sin(\phi - i)}{\sin(\beta - \delta) \sin(\beta + i)}} \right\}^2} \quad (2.2)$$

where

ϕ = internal friction angle of soil

δ = wall friction angle

β = slope of back of the wall to horizontal

i = slope of ground surface behind wall

2.1.2 Rankine Earth Pressure Theory

Rankine (1875) considered the soil in a state of plastic equilibrium and used essentially the same assumptions as Coulomb. The Rankine theory further assumes that there is no wall friction and failure surfaces are straight planes, and that the resultant force acts parallel to the backfill slope. Detailed assumptions are made as the followings:

1. The backfill is isotropic and homogeneous.
2. The retaining wall is a rigid body. The wall surface is vertical and the friction force between the wall and the soil is neglected.

Rankine assumed no friction between wall surface and backfill, and the backfill is cohesionless. The earth pressure on plane AB of Fig. 2.3(a) is the same as that on plane AB inside a semi-infinite soil mass in Fig. 2.3(b). For active condition, the active earth pressure σ_a at a given depth z can be expressed as:

$$\sigma_a = \gamma z K_a \quad (2.3)$$

The total active force P_a per unit length of the wall is equal to

$$P_a = \frac{1}{2} \gamma H^2 K_a \quad (2.4)$$


The direction of resultant force P_a is parallel to the ground surface as Fig. 2.3(b), where

$$K_a = \cos i \frac{\cos i - \sqrt{(\cos^2 i - \cos^2 \phi)}}{\cos i + \sqrt{(\cos^2 i - \cos^2 \phi)}} \quad (2.5)$$

2.1.3 Terzaghi General Wedge Theory

The assumption of plane failure surface made by Coulomb and Rankine, however, does not apply in practice. Terzaghi (1941) suggested that the failure surface in the backfill under an active condition was a log spiral curve, like the curve bd in Fig. 2.4, but the failure surface dc is still assumed a plane.

Fig. 2.5 illustrates the procedure to elevate the active resistance by trial wedge method (Terzaghi and Peck, 1967). The line d_1c_1 makes an angle of $45^\circ + \phi/2$ with the surface of the backfill. The arc bd_1 of trial wedge abd_1c_1 is a logarithmic spiral formulated as the following equation

$$r_1 = r_0 e^{\theta \tan \phi} \quad (2.6)$$


O_1 is the center of the log spiral curve in Fig. 2.5, where $O_1b = r_1$, $O_1d_1 = r_0$, and $\angle bO_1d_1 = \theta$. For the equilibrium and the stability of the soil mass abd_1f_1 in Fig. 2.6, the following forces per unit width of the wall are considered.

1. Soil weight per unit width in abd_1f_1 : $W_1 = \gamma \times (\text{area of } abd_1f_1)$
2. The vertical face d_1f_1 is in the zone of Rankine's active state; hence, the force

P_{d1} acting on the face is

$$P_{d1} = \frac{1}{2} \gamma (H_{d1})^2 \tan^2(45^\circ - \frac{\phi}{2}) \quad (2.7)$$

where

$$H_{d1} = d_1f_1$$

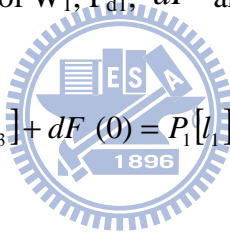
P_{d1} acts horizontally at a distance of $H_{d1}/3$ measured vertically

upward from d_1 .

γ is the unit weight of soil

3. The resultant force of the shear and normal forces dF , acting along the surface of sliding bd_1 . At any point of the curve, according to the property of the logarithmic spiral, a radial line makes an angle ϕ with the normal. Since the resultant dF makes an angle ϕ with the normal to the spiral at its point of application, its line of application will coincide with a radial line and will pass through the point O_1 .
4. The active force per unit width of the wall P_1 acts at a distance of $H/3$ measured vertically from the bottom of the wall. The direction of the force P_1 is inclined at an angle δ with the normal drawn to the back face of the wall.
5. Moment equilibrium of W_1, P_{d1}, dF and P_1 about the point O_1 :

$$W_1[l_2] + P_{d1}[l_3] + dF(0) = P_1[l_1] \quad (2.8)$$



or

$$P_1 = \frac{1}{l_1} [W_1 l_2 + P_{d1} l_3] \quad (2.9)$$

where l_2 , l_3 , and l_1 are the moment arms for forces W_1, P_{d1} , and P_1 , respectively.

The trial active forces per unit width in various trial wedges are shown in [Fig. 2.7](#). Let P_1, P_2, P_3, \dots , and P_n be the forces that respectively correspond to the trial wedges 1, 2, 3, \dots , and n . The forces are plotted to the same scale as shown in the upper part of the figure. A smooth curve is plotted through the points 1, 2, 3, \dots , n . The maximum P_1 of the smooth curve defines the active force P_a per unit width of the wall.

2.1.4 Spangler and Handy's Theory

Spangler and Handy (1984) have applied Janssen's (1895) theory to design problem of fascia retaining walls. Fig. 2.8 defines the soils with a width B bounded by two unyielding frictional boundaries (the rock face and wall face). The vertical force equilibrium of the thin horizontal soil element in Fig. 2.9 requires

$$(V + dV) + 2K\mu \frac{V}{B} dh = V + \gamma B dh \quad (2.10)$$

This is a linear differential equation, the solution for which is

$$V = \gamma B^2 \frac{1 - e^{-2K\mu(h/B)}}{2K\mu} \quad (2.11)$$

where

$\mu = \tan \delta$, the coefficient of friction between the soil and the wall

γ = unit weight of the soil

B = backfill width

h = backfill depth (i.e. z)

K = the coefficient of lateral earth pressure

V = the vertical force

From the solution of eq.(2.11), an equation for lateral earth pressure σ_h can be calculated

$$\sigma_h = \frac{\gamma B}{2\mu} \left[1 - e^{-2K\mu(h/B)} \right] \quad (2.12)$$

Some solutions for different values of B are shown in Fig. 2.10. The soil pressure, instead of continuing to increase with increasing values of h , levels off at a maximum value $\sigma_{h,\max}$ defined as follows.

$$\sigma_{h_{\max}} = \frac{\gamma B}{2\mu} = \frac{\gamma B}{2 \tan \delta} \quad (2.13)$$

2.2 Laboratory Model Retaining Wall Tests

2.2.1 Model Study by Mackey and Kirk

Mackey and Kirk (1967) experimented on lateral earth pressure by using a steel model wall. This soil tank was made of steel with internal dimensions of 36 in. × 16 in. × 15 in. (914 mm × 406 mm × 381 mm) as shown in [Fig. 2.11](#). In this investigation, when the wall moves away from the soil, the earth pressure decreases (see [Fig. 2.12](#)) and then increases slightly until it reaches a constant value. Mackey and Kirk reported that if the backfill is loose, the active earth pressure obtained experimentally are within 14 percent off those obtained theoretically from almost any of the methods list in [Table 2.1](#).

Mackey and Kirk utilized a powerful beam of light to observe the failure surface in the backfill. It could trace the position of the shadow, formed by changes of the sand surface in different level. It was found that the failure surface in the backfill due to the translational wall movement was approximated a curve in the backfill ([Fig. 2.13](#)), rather than a plane assumed by Coulomb.

2.2.2 Model Study by Fang and Ishibashi

Fang and Ishibashi (1986) conducted laboratory model experiments to investigate the distribution of the active stresses due to three different wall movement modes: (1) rotation about top, (2) rotation about base, and (3) translation. The experiments were conducted at the University of Washington.

[Fig. 2.14](#) shows the horizontal earth pressure distributions at different translational wall movements. The measured active stress is slightly higher than

Coulomb's solution at the upper one-third of wall height H is 3.33 ft (1.01 m), approximately in agreement with Coulomb's prediction in the middle one-third, and lower than Coulomb' at the lower one-third of wall surface. However, the magnitude of the active total thrust P_a at $S = 20 \times 10^{-3}$ in. (0.5 mm) is nearly the same as that calculated from Coulomb's theory.

Fig. 2.15 shows lateral earth pressures measured at various depths decreased rapidly with the translational active wall displacement. Most measurements reach the minimum value at approximately 10×10^{-3} in (0.25 mm, or 0.00025H) wall displacement and stay steady thereafter. Table 2.2 shows the range of wall displacement reported by previous researchers for the translational wall to achieve an active state.

Fig. 2.16 shows the K_a as a function of soil density and internal friction angle. In this figure, the K_a value decreases with increasing ϕ angle. The Coulomb's solution might underestimate the coefficient K_a for rotational wall movements.

2.2.3 Model Retaining Wall Study by Huang

Huang (2009) used the model retaining wall facilities at National Chiao Tung University to investigate the active earth pressure on retaining walls near an inclined rock face. The backfill height H is 0.5 m. The parameters considered for that study were the rock face inclination angles $\beta = 0^\circ, 50^\circ, 60^\circ, 70^\circ, 80^\circ, 90^\circ$, the horizontal spacing $b = 0, 50$ mm, 100 mm as illustrated in Fig. 2.17 to Fig. 2.19.

Fig. 2.20 to Fig. 2.22 shows the distribution of active earth pressure at different interface inclination angle for $b = 0, 50$ mm, 100 mm. Fig. 2.23 shows the active earth pressure coefficient $K_{a,h}$ versus interface inclination angle β . The point of application of active soil thrust versus interface inclination angle β is shown in Fig. 2.24. Based on the test result, the following conclusions are drawn:

1. With the approaching of the interface plate, the soil mass behind the wall decreased. The active earth pressure coefficient $K_{a,h}$ decreased with increasing interface inclination angle β or decreasing spacing b .

2. As the interface angle β increased or spacing b decreased (the rock face approached the wall face), the inclined rock face intruded the active soil wedge, the active pressure decreased near the base of the wall. This change of earth pressure distribution caused the active thrust to rise to a slightly higher location.
3. For all $b = 0$, $b = 0.1H$, and $b = 0.2H$, the horizontal component of active soil thrust $P_{a,h}$ would decrease with increasing β angle. The intrusion of the inclined rock face would actually increase the FS against sliding of the wall. The evaluation of FS against sliding with Coulomb's theory would be on the safe side.

2.2.4 Centrifuge Model Study by Frydman and Keissar

Frydman and Keissar (1987) used the centrifuge modeling technique to test a small model wall near a vertical rock face as shown in Fig. 2.25, and changes in pressure from the at-rest to the active condition was observed. The centrifuge system has a mean radius of 1.5 m, and can develop a maximum acceleration of 100 g, where g is the acceleration due to gravity. The models are built in an aluminum box of inside dimensions $327 \times 210 \times 100$ mm. Each model includes a retaining wall made from aluminum (195 mm high \times 100 mm wide \times 20 mm thick) as shown in Fig. 2.26. The rock face is modeled by a wooden block, which can, through a screw arrangement, be positioned at varying distances b from the wall. Face of the block is coated with the sand used as fill, so that the friction between the rock and the fill is equal to the angle of internal friction of the fill. The granular fill between the wall and the rock face was modeled by uniform fine sand, the uniformity coefficient, $C_u = 1.5$. The model tests were carried out with the sand placed at a relative density of 70%. Simple shear tests performed on the sand at this relative density gave the angle of internal friction $\phi = 36^\circ$. Direct shear tests between the sand and aluminum yielded a friction angle $20^\circ \sim 25^\circ$.

Frydman and Keissar (1987) found that Spangler and Handy (1984) developed equation, (2.12) base on Janssen's (1895) arching theory, for calculating the lateral pressure acting on the wall of a silo. In the silo, the lateral pressure σ_x at any given depth, z , is given as:

$$\sigma_x = \frac{\gamma b}{2 \tan \delta} \left[1 - \exp\left(-2K \frac{z}{b} \tan \delta\right) \right] \quad (2.14)$$

where

σ_x = lateral pressure acting on the wall (i.e. σ_h)

b = distance between silo walls

z = depth from top at which σ_x is required

K = coefficient of lateral earth pressure

γ = unit weight of the backfill

δ = angle of friction between the wall and the backfill

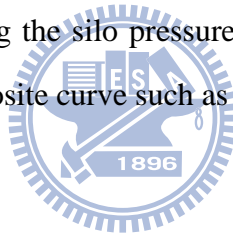
The coefficient K value depends on the lateral movement of the silo wall. For walls without any lateral movement, the Jaky's equation was suggested for estimating the K value. In the active condition, Frydman and Keissar derived the K value by taking into account the friction between the wall and the fill, and assuming that the soil near the wall reached a state of failure. The K value is given by

$$K = \frac{(\sin^2 \phi + 1) - \sqrt{(\sin^2 \phi + 1)^2 - (1 - \sin^2 \phi)(4 \tan^2 \delta - \sin^2 \phi + 1)}}{(4 \tan^2 \delta - \sin^2 \phi + 1)} \quad (2.15)$$

Where ϕ = the angle of internal friction of the fill. The coefficient of lateral earth pressure in the active condition at given depth z can be determined as the ratio of σ_x over $\sigma_v (= \gamma z)$, and is expressed as

$$K_a = \frac{1}{2 \tan \delta} \frac{b}{z} \left[1 - \exp \left(-2K \frac{z}{b} \tan \delta \right) \right] \quad (2.16)$$

The coefficient of active earth pressures at given depth z for a retaining wall near a vertical rock face can be theoretically estimated by substituting Eq. 2.15 into Eq. 2.16. The distribution of K_a with the depth in Eq. 2.16 was verified using the experimental data obtained from the centrifuge model test, in which the wall rotated about its base (RB model). The K_a value obtained decreased considerably with depth. Additionally, the measured K_a value was significantly less than the Rankine's or Coulomb's coefficient of active earth pressure. Fig. 2.27 shows the distribution of K_a ' as a function of z/b . It is seen that for z/b less than about 1, the horizontal stress estimated using the silo pressure equation is greater than that corresponding to Rankine distribution. Obviously this is unacceptable. A more reasonable distribution may be obtained by assuming the silo pressure curve to be limited by the Rankine pressure, resulting in a composite curve such as ABC in Fig. 2.27.



2.3 Numerical Studies

2.3.1 Numerical Study by Leshchinsky, et al.

Leshchinsky, et al. (2004) used the limit equilibrium method with computer program ReSSA 2.0 (ADAMA, 2003) to numerically investigate the lateral earth pressure acting on a Mechanically-Stabilized-Earth wall. A baseline 5m-high wall was specified, the geometrical modeling was shown in Fig. 2.28(a). A single layer of reinforcement at 1/3 of the height of the wall was simulated in the analysis. In Fig. 2.28 the foundation was considered as competent bedrock to eliminate external effects on its stability. Various types of reinforced cohesionless fill were used in the analysis, all having a unit weight of $\gamma = 20 \text{ kN/m}^3$ and the internal angle of friction ϕ of the fill varying from 20° to 45° . Fig. 2.28(b) shows the base width of the fill was B , and the slope of the rear section of the fill was m .

Fig. 2.29 shows the results predicted by ReSSA versus values reported by Frydman and Keissar (1987). The bedrock constraining the sand in all tests was vertical (i.e., $m = \infty$). Frydman and Keissar (1987) reported an internal angle of friction of 36° and interface friction between the aluminum and sand $\delta = 20^\circ \sim 25^\circ$. Note that rather than using K_a' , the ratio K_a'/K_a is used, $K_a = \tan^2(45^\circ - \phi/2)$ is Rankine's active lateral earth pressure coefficient. Fig. 2.29 implies that as the retained soil space narrows (i.e., H/B increases) both ReSSA and the experimental data show the K_a'/K_a ratio decreases.

Fig. 2.30 presents the variation of active earth pressure coefficient K_a' as a function of the rock face slope m . K_a' was determined with the numerical analysis, and K_a was calculated with the Rankine theory $K_a = \tan^2(45^\circ - \phi/2)$. The normalization of K_a' with K_a produces charts that are independent of ϕ . For $B = 0$, the coefficient K_a' rapidly decreased with increasing slope m . The amount of fill between the wall and bedrock was very small. For $B = 0.1H$ and $0.2H$, K_a' also decreases with increasing slope m , however the space between the wall and the bedrock slope was becoming wider.

2.3.2 Numerical Study by Lawson and Yee

Lawson and Yee (2005) used the limit equilibrium method to numerically investigate the lateral earth pressure acting on retaining walls with constrained reinforced fill. The forces acting on the reinforced fill zone are shown in Fig. 2.31(a). The height of wall is H , and L_t is the width of fill at top. L_t/H represents the normalized width of fill. The destabilizing force is due to the weight of the fill, W , within the potential failure surface. For simplicity, it is assumed that the stabilizing force P_h acting on the rear of the wall face is horizontal and the wall face is vertical.

Fig. 2.31(b) shows values of earth pressure coefficient K for various wall L_t/H ratio for a fill with an internal friction angle $\phi' = 30^\circ$. For L_t/H ratios greater than 0.5,

the active wedge can develop fully within the granular fill zone, hence the value of $K = K_a = \tan^2(45^\circ - \phi/2) = 0.333$. For L_t/H ratio less than 0.5, the active wedge cannot develop fully, hence the magnitude of K decreases for decreasing L_t/H .

2.3.3 Numerical Study by Yang and Liu

Yang and Liu (2007) used the finite element program Plaxis version 8 (Plaxis, 2005) to investigate the earth pressures for narrow retaining walls. Fig. 2.32 illustrates the narrow retaining walls in front of a stable rock face. L is the width of backfill and H is the height of wall. Fig. 2.33(a) shows the finite element mesh for at-rest condition, and Fig. 2.33(b) is the finite element model for active condition. The wall height H was fixed to 10 m while wall width L corresponding to desired wall aspect ratio $L/H = 0.1, 0.3, 0.5, 0.7$. Predicted earth pressure coefficients were normalized by Rankine K_a .

Normalized earth pressure coefficient profiles for at-rest condition are shown in Fig. 2.34(a), the earth pressure coefficient K_0 decreases with decreasing aspect ratio L/H . Normalized earth pressure coefficient profiles for active condition are addressed in Fig. 2.34(b), the data are scattered around K_a and do not show a clear tendency. Even so, it can be observed that the earth pressure coefficient profiles decrease with decreasing aspect ratio. The effects of boundary constraint still can be recognized.

Fig. 2.35(a) shows the equivalent earth pressure coefficients K_w' (along the wall face), K_c' (along the center of the backfill) and the equivalent earth pressure coefficients computed from arching equation for at-rest condition. All the pressure coefficients are normalized by Rankine K_a . The data from finite element analyses show the normalized equivalent earth pressure coefficients are less than K_0/K_a by 10% to 60%, when the aspect ratio changed from 0.7 to 0.1.

Fig. 2.35(b) is the analytical results for active case. All pressure coefficients are normalized by Rankine K_a . The decreasing tendency of equivalent earth pressure from finite element analyses is not obvious until $L/H < 0.3$. This implies that the

boundary constraint starts to play a role when the shape of backfill become very slender. The difference between the earth pressures along the wall face and the earth pressures along the center of the backfill is apparent. This is most likely because all the stress points along the wall face are inside the failure wedge, but not all of stress points at the center of the backfill are at in the active wedge. Data from limit equilibrium analyses by Lawson and Yee (2005) and Leshchinsky et al. (2003) are compared with data calculated from finite element simulation. The results generally show a similar trend.

2.3.4 Numerical Study by Fan and Fang

Fan and Fang (2009) used the non-linear finite element program PLAXIS (PLAXIS BV, 2002) to investigate the earth pressure against a rigid wall close to an inclined rock face (Fig. 2.36). The wall used for analysis is 5 m high, the back of the wall is vertical, and the surface of the backfill is horizontal. Typical geometry of the backfill zone used in the study is shown in Fig. 2.36. To investigate the influence of the adjacent rock face on the behavior of earth pressure, the inclination angle β of the rock face and the spacing b between the wall and the foot of the rock face were the parameters for numerical analysis. The wall was prevented from any movement during the placing of the fill. After the filling process, active wall movement was allowed until the earth pressure behind the wall reached the active condition. The finite element mesh, for a retaining wall with restrained backfill space ($\beta = 70^\circ$ and $b = 0.5\text{m}$) is shown in Fig. 2.37. The finite element mesh consists of 1,512 elements, 3,580 nodes, and 4,536 stress points.

Base on the numerical analysis, distributions of horizontal earth pressures with the depth (z/H) at various wall displacements for $b = 0.5\text{ m}$ and $\beta = 80^\circ$ are shown in Fig. 2.38. In the figure, the distribution of active earth pressure with depth is non-linear. Due to the nearby rock face, the calculated active pressure is considerably less than that computed using the Coulomb's theory.

Fig. 2.39 shows the variation of the active earth pressure coefficient ($K_{a(\text{Computed})} / K_{a(\text{Coulomb})}$) as a function of the inclination angle β of the rock face and the wall-rock spacing b , for walls under translation movement. For $\beta > 60^\circ$, the analytical active K values are less than those calculated with Coulomb's solution. The analytical K value decreased with increasing β angle.

Fig. 2.40 shows the variation of the location of active soil thrust with the β angle and wall-rock spacing b . For $\beta > 60^\circ$, the active soil thrust rises with increasing β angles, and the active h/H value increased with decreasing fill width b .

2.4 Plane Strain State-of-Stress

In many soil mechanics problems, a type of state-of-stress that is often encountered is the plane strain condition. Referring to Fig. 2.41, for the retaining wall, the normal strain in the y direction at any point P in the soil mass is equal to zero ($\epsilon_y = 0$). To reduce the side wall deflection, due to lateral earth pressure the NCTU model retaining wall (Fig. 1.7) used U-shaped steel beams and steel columns to confine the side walls deformation. The soil bin is nearly rigid that lateral deformation of side wall becomes negligible.

The normal stresses σ_y at all sections in the xz plane (intermediate principal plane) are the same, and the shear stresses on these xz planes are zero ($\tau_{yx} = \tau_{yz} = 0$). To minimize the side wall friction on xz plane, the NCTU model retaining wall used lubrication layers to reduce the interface friction between the sidewall and the backfill.

Under a plane-strain state of stress, the normal and shear stresses on the yz plane are equal to σ_x and τ_{xz} . Similarly, the normal and shear stress on the xy plane are σ_z and τ_{zx} ($\tau_{zx} = \tau_{xz}$). The relationship between the normal stresses can be expressed as

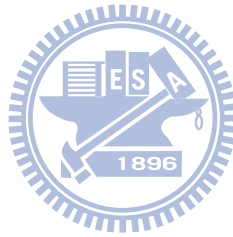
$$\varepsilon_y = \frac{\sigma_y}{E} - \nu\left(\frac{\sigma_x}{E}\right) - \nu\left(\frac{\sigma_z}{E}\right) \quad (2.17)$$

where ν is Poisson's ratio.

for a plane strain condition, $\varepsilon_y = 0$

$$0 = \sigma_y - \nu\sigma_x - \nu\sigma_z$$

$$\sigma_y = \nu(\sigma_x + \sigma_z) \quad (2.18)$$



Chapter 3

Experimental Apparatus

In order to study the earth pressure behind retaining structures, the National Chiao Tung University (NCTU) has built a model retaining wall system which can simulate different kinds of wall movements. All of the investigations described in the thesis were conducted in this model wall, which will be carefully discussed in this chapter. The entire facility consists of four components namely, model retaining wall, soil bin, driving system, and data acquisition system. The arrangement of the NCTU model retaining wall system is shown in [Fig. 3.1](#).

3.1 Model Retaining Wall



The movable model retaining wall and its driving systems are shown in [Fig. 3.1](#). The model wall is a 1000-mm-wide, 550-mm-high, and 120-mm-thick solid plate, and is made of steel. Note that in [Fig. 3.1](#) the effective wall height H is only 500 mm. The retaining wall is vertically supported by two unidirectional rollers, and is laterally supported by four driving rods. Two sets of wall-driving mechanisms, one for the upper rods and the other for the lower rods, provide various kinds of movements for the wall. A picture of the NCTU model wall facility is shown in [Fig. 3.2](#).

Each wall driving system is powered by variable-speed motor. The motors turn the worm driving rods which cause the driving rods to move the wall back and forth. [Fig. 3.3](#) shows two displacement transducers (Kyowa DT-20D) are installed at the back of retaining wall and their sensors are attached to the movable wall. Such an arrangement of displacement transducers would be effective in describing the wall

translation.

To investigate the distribution of earth pressure, nine earth pressure transducers were attached to the model wall. The arrangement of the earth pressure cells should be able to closely monitor the variation of the earth pressure of the wall with depth. Base on this reason, the earth pressure transducers SPT1 through SPT9 have been arranged at two vertical columns as shown in [Fig. 3.4](#).

A total of nine earth pressure transducers have been arranged within a narrow central zone to avoid the friction that might exist near the side walls of the soil bin as shown in [Fig. 3.5](#). The Kyowa model PGM-02KG (19.62 kN/m² capacity) transducer shown in [Fig. 3.6](#) was used for these experiments. To reduce the soil-arching effect, earth pressure transducers with a stiff sensing face are installed flush with the face of the wall. They provide closely spaced data points for determining the earth pressure distribution with depth.

3.2 Soil Bin



The soil bin is fabricated of steel members with inside dimensions of 2,000 mm × 1,000 mm × 1,000 mm (see [Fig. 3.1](#)). Both sidewalls of the soil bin are made of 30-mm-thick transparent acrylic plates through which the behavior of backfill can be observed. Outside the acrylic plates, steel beams and columns are used to confine the side walls to ensure a plane strain condition.

The end wall that sits opposite to the model retaining wall is made of 100 mm thick steel plates. All corners, edges and screw-holes in the soil bin have been carefully sealed to prevent soil leakage. The bottom of the soil bin is covered with a layer of SAFETY-WALK to provide adequate friction between the soil and the base of the soil bin.

In order to constitute a plane strain condition, the soil bin is built very rigid so that the lateral deformations of the side walls will be negligible. The friction between the backfill and the side walls is to be minimized to nearly frictionless, so

that shear stress induced on the side walls will be negligible. To eliminate the friction between backfill and sidewall, a lubrication layer with 3 layers of plastic sheets was furnished for all model wall experiments. The “thick” plastic sheet was 0.152 mm thick, and it is commonly used for construction, landscaping, and concrete curing. The “thin” plastic sheet was 0.009 mm thick. It is widely used for protection during painting, and therefore it is sometimes called painter’s plastic. Both plastic sheets are readily available and neither is very expensive. The lubrication layer consists of one thick and two thin plastic sheets were hung vertically on each sidewall of the soil bin before the backfill was deposited (see Fig. 3.7). The thick sheet was placed next to the soil particles. It is expected that the thick sheet would help to smooth out the rough interface as a result of plastic-sheet penetration under normal stress. Two thin sheets were placed next to the steel sidewall to provide possible sliding planes. For more information regarding the reduction of boundary friction with the plastic-sheet method, the reader is referred to Fang et al. (2004).



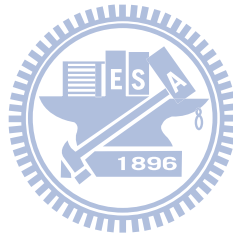
3.3 Driving System

Fig. 3.1 shows the variable speed motors M1 and M2 (Electro, M4621AB) are employed to compel the upper and lower driving rods, respectively. The shaft rotation compels the worm gear linear actuators, while the actuator would push the model wall. To investigate the variation of earth pressure and the failure wedge caused by the translational wall movement, the motor speeds at M1 and M2 were kept the same speed of 0.015 mm/s for all experiments in this study.

3.4 Data Acquisition System

A data acquisition system was used to collect and store the considerable amount of data generated during the tests. The data acquisition system was composed of the

following four parts: (1) dynamic strain amplifiers (Kyowa: DPM601A and DPM711B); (2) NI adaptor card (NIBNC-2090); (3) AD/DA card; and (4) personal computers shown in Fig. 3.8. An analog-to-digital converter digitized the analog signals from the sensors. The digital data were then stored and processed by a personal computer. For more details regarding the NCTU retaining-wall facility, the reader is referred to Wu (1992) and Fang et al. (1994).



Chapter 4

Interface Plate and Supporting System

A steel interface plate is designed and constructed in the soil bin to simulate the constrained backfill shown in Fig. 1.1. In Fig. 4.1, the plate and its supporting system are developed to fit in the NCTU model retaining-wall facility. The interface plate consists of two parts: (1) steel plate; and (2) reinforcing steel beams. The supporting system consists of the following three parts: (1) top supporting beam; (2) base supporting block; and (3) base boards. Details of the interface plate and its supporting system are introduced in the following sections.

4.1 Interface Plate

4.1.1 Steel Plate



The steel plate shown in Fig. 4.2 is 1.370 m-long, 0.998 m-wide, and 5 mm-thick. The unit weight of the steel plate is 76.52 kN/m^3 and its total mass is 83 kg (814 N). A layer of anti-slip material (SAFETY-WALK, 3M) is attached on the steel plate to simulate the friction that acts between the backfill and rock face as illustrated in Fig. 4.2 and Fig. 4.3. For the wall height $H = 0.5 \text{ m}$ and the inclination angle $\beta = 50^\circ$, the length of the interface plate should be at least 1.370 m. On the other hand, the inside width of the soil bin is 1.0 m. In order to put the interface plate into the soil bin, the width of the steel plate has to be less than 1.0 m. As a result, the steel plate was designed to be 1.370 m-long and 0.998 m-wide.

4.1.2 Reinforcement with Steel Beams

To simulate the rock face shown in Fig. 1.1, the steel interface plate should be nearly rigid. To increase the rigidity of the 5 mm-thick steel plate, Fig. 4.2 (b) and Fig. 4.3 (b) shows 5 longitudinal and 5 transverse steel L-beams were welded to the back

of steel plate. Section of the steel L-beam (30 mm × 30 mm × 3 mm) was chosen as the reinforced material for the thin steel plate. On top of the interface plate, a 65 mm × 65 mm × 8 mm steel L-beam was welded to reinforce the connection between the plate and the hoist ring shown in Fig. 4.3 (b).

4.2 Supporting System

To keep the steel interface plate in the soil bin stable during testing, a new supporting system for the interface plate was designed and constructed. A top-view of the base supporting frame is illustrated in Fig. 4.4. The supporting system composed of the following three parts: (1) top supporting beam; (2) base supporting block and (3) base boards. These parts are discussed in following sections.

4.2.1 Top Supporting Beam

In Fig. 4.5, the top supporting steel beam is placed at the back of the interface plate and fixed at the bolt slot on the side wall of the soil bin. Details of top supporting beam are illustrated in Fig. 4.6. The section of supporting steel beam is 65 mm × 65 mm × 8 mm and its length is 1700 mm. Fig. 4.4 shows bolt slots were drilled on each side of the steel beam on the side wall of the soil bin. The locations of bolt slots were calculated for the interface plate at difference horizontal spacing b and inclined angle β . Fig. 4.7 shows the top supporting beam was fixed at the slots with bolts.

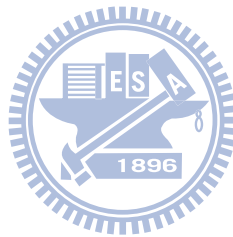
4.2.2 Base Supporting Block

The base supporting block used to support the steel interface plate is shown in Fig. 4.8. The base supporting block is 1.0 m-long, 0.6 m-wide, and 0.113 m-thick. Fig.4.8 shows seven trapezoidal grooves were carved to the face of the base supporting block. Fig. 1.2 to Fig.1.5 shows the foot of the interface plate could be

inserted into the groove at different distance from base of the model wall. In Fig.4.8, different horizontal spacing b adopted for testing includes: (1) $b = 0$; (2) $b = 50$ mm; (3) $b = 100$ mm; (4) $b = 150$ mm; (5) $b = 250$ mm; (6) $b = 350$ mm; and (7) $b = 500$ mm.

4.2.3 Base Boards

Fig. 4.5 shows 6 pieces of base boards are stacked between the base supporting block and the end wall, to keep the base block stable. The base boards show in Fig. 4.9 is 1400 mm-long, 1000 mm-wide and 113 mm-thick. To provide adequate friction between the backfill and the base board, the surface of the top base board was cover with a layer of anti-slip material SAFETY-WALK.



Chapter 5

Backfill and Interface Characteristics

This chapter introduces the properties of the backfill, and the interface characteristics between the backfill and the wall. Laboratory experiments have been conducted to investigate the following subjects: (1) backfill properties; (2) model wall friction; (3) side wall friction; (4) interface plate friction; and (5) distribution of soil density in the soil bin.

5.1 Backfill Properties

Air-dry Ottawa sand (ASTM C-778) was used throughout this investigation. Physical properties of the soil include $G_s = 2.65$, $e_{\max} = 0.76$, $e_{\min} = 0.50$, $D_{60} = 0.40$ mm, and $D_{10} = 0.22$ mm. Grain-size distribution of the backfill is shown in [Fig. 5.1](#). Major factors considered in choosing Ottawa sand as the backfill material are summarized as follows.

1. Its round shape, which avoids effect of angularity of soil grains.
2. Its uniform distribution of grain size (coefficient of uniformity $C_u = 1.82$), which avoids the effects due to soil gradation.
3. High rigidity of solid grains, which reduces possible disintegration of soil particles under loading.
4. Its high permeability, which allows fast drainage of pore water and therefore reduces water pressure behind the wall.

To establish the relationship between the unit weight γ of backfill and its internal friction angle ϕ , direct shear tests have been conducted. The shear box used has a square (60 mm×60 mm) cross-section, and its arrangement is shown in [Fig.](#)

5.2.

Chang (2000) established the relationship between the internal friction angle ϕ and unit weight γ of the Ottawa sand as shown in Fig. 5.3. It is obvious from the figure that soil strength increases with increasing soil density. For the air-pluviated backfill, the empirical relationship between soil unit weight γ and ϕ angle can be formulated as follows

$$\phi = 6.43\gamma - 68.99 \quad (5.1)$$

where

ϕ = angle of internal friction of soil (degree)

γ = unit weight of backfill (kN/m³)

Eqn. (5.1) is applicable for $\gamma = 15.45 \sim 17.4$ kN/m³ only.



5.2 Model Wall Friction

To evaluate the wall friction angle δ_w between the backfill and model wall, special direct shear tests have been conducted. A 88 mm × 88 mm × 25 mm smooth steel plate, made of the same material as the model wall, was used to replace the lower shear box. Ottawa sand was placed into the upper shear box and vertical load was applied on the soil specimen. The arrangement of this test is shown in Fig. 5.4.

To estimate the wall friction angles δ_w developed between the steel plate and sand, soil specimens with different unit weight were tested. Air-pluviation methods was used to achieve different soil density, and the test results are shown in Fig. 5.5. For air-pluviated Ottawa sand, Lee (1998) suggested the following relationship:

$$\delta_w = 2.33\gamma - 17.8 \quad (5.2)$$

where

δ_w = wall friction of angle (degree)

γ = unit weight of backfill (kN/m^3)

Eqn. (5.2) is applicable for $\gamma = 15.5\sim 17.5 \text{ kN/m}^3$ only. The ϕ angle and δ_w angle obtained in section 5.1 and 5.2 are used for calculation of active earth pressure based on Coulomb, and Rankine's theories.

5.3 Side Wall Friction

To constitute a plane strain condition for model wall experiments, the shear stress between the backfill and sidewall should be eliminated. Lubrication layers fabricated with plastic sheets were equipped for all experiments to reduce the interface friction between the sidewall and the backfill. The lubrication layer consists of one thick and two thin plastic sheets as suggested by Fang et al. (2004). Plastic sheets were vertically hung next to the side-wall as shown in Fig. 5.6.

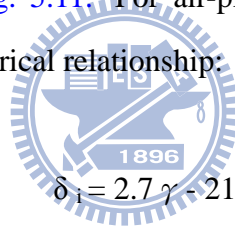
The friction angle between the plastic sheets and the sidewall was determined by the sliding block tests. The schematic diagram and the photograph of the sliding block test suggested by Fang et al. (2004) are illustrated in Fig. 5.7 and Fig. 5.8, respectively. The sidewall friction angle δ_{sw} is determined based on basic physics principles. In Fig. 5.8, the handle was turned to tilt the sliding plate, which the soil box on the plate starts to slide. Then measure the inclination δ_{sw} that the plate makes with the horizontal.

Fig. 5.9 shows the variation of interface friction angle δ_{sw} with normal stress σ based on the sliding block tests. The friction angle measured was 7.5° . With the plastic – sheet lubrication method, the interface friction angle is almost independent of the applied normal stress. The shear stress between the acrylic side-wall and backfill has been effectively reduced with the plastic-sheet lubrication layer.

5.4 Interface Plate Friction

To evaluate the interface friction between the interface plate and the backfill, special direct shear tests were conducted as shown in Fig. 5.10. In Fig. 5.10(b), a 80 mm × 80 mm × 15 mm steel plate was covered with a layer of anti-slip material “SAFETY-WALK” to simulate the surface of the interface plate. The interface-plate was used to simulate the rock face near the wall shown in Fig. 1.1. Dry Ottawa sand was placed into the upper shear box and vertical stress was applied on the soil specimen as shown in Fig. 5.10(a).

To establish the relationship between the unit weight γ of the backfill and the interface-plate friction angle δ_i , soil specimens with different unit weight were tested. Air-pluviation methods was used to achieve different soil densities, and the test results are shown in Fig. 5.11. For air-pluviated Ottawa sand, Wang (2005) suggested the following empirical relationship:


$$\delta_i = 2.7 \gamma - 21.39$$

(5.3)

where

δ_i = interface-plate friction angle (degree)

γ = unit weight of backfill (kN/m^3)

Eqn. (5.3) is applicable for $\gamma = 15.1 \sim 16.36 \text{ kN/m}^3$ only.

The relationships between soil unit weight γ and friction angle for different interface materials are summarized in Fig. 5.12. The internal friction angle of Ottawa sand ϕ , model wall-soil friction angle δ_w , interface-plate friction angle δ_i , and lubricated sidewall friction angle δ_{sw} as a function of soil unit weight γ are compared in the figure. It is clear in Fig. 5.12 that, with the same unit weight, the order of the four different friction angles involved for the model wall experiment is $\phi > \delta_i > \delta_w > \delta_{sw}$.

5.5 Control of Soil Density

5.5.1 Air-Pluviation of Backfill

To achieve a uniform soil density in the backfill, air-dry Ottawa sand was deposited by air-pluviation method into the soil bin. The air-pluviation method had been widely used for a long period of time to reconstitute laboratory sand specimens. Rad and Tumay (1987) reported that pluviation is a method that provides reasonably homogeneous specimens with desired relative density. Lo Presti et al. (1992) reported that the pluviation method could be performed for greater specimens in less time. As indicated in Fig. 5.13, the soil hopper that lets the sand pass through a calibrated slot opening at the lower end was used for the spreading of sand. A picture showing air-pluviation of the Ottawa sand into soil bin is indicated in Fig. 5.14. Air-dry Ottawa sand was shoveled from the soil storage bin to the sand hopper, weighted on the electric scale, then pluviated into the soil bin. As indicated in Fig. 5.15, four types of slot openings (5 mm, 7 mm, 10 mm and 15 mm) were adopted by Ho (1999), and the drop height of soil varied from 0.25 m to 2.5 m.

Das (2010) suggested that the granular soil with a relative density of 15% ~ 50% is defined as loose. In this study, the drop height of 1.0 m and the slot opening of 15 mm were selected to achieve the loose backfill with a relative density of approximately 36%.

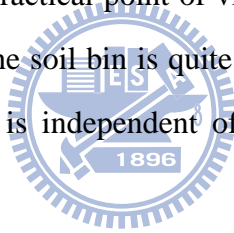
5.5.2 Distribution of Soil Density

To investigate the distribution of soil density in the soil bin, soil density measurements were made. The soil density control cup made of acrylic is illustrated in Fig. 5.16 and Fig. 5.17. For the air-pluviated backfill, the density cups were used to measure the soil density at different elevations and locations.

In Fig. 5.18 to Fig. 5.21, interface plate was placed with the inclination angle

$\beta = 90^\circ$ and the horizontal spacing $b = 150$ mm, 250 mm, 350 mm, and 500 mm. In [Fig. 5.22](#) to [Fig. 5.24](#), interface plate was placed with the inclination angle $\beta = 80^\circ$, 70° , 60° , and $b = 150$ mm. A layer of 100 mm-thick Ottawa sand was placed in the soil bin as a soil blanket. The bottom density cup was then put on the surface of soil blanket. Locations of the density cups buried in the fill are illustrated in [Fig.5.18](#) to [Fig.5.24](#). Ottawa sand was placed layer by layer into the soil bin up to 0.5 m thick.

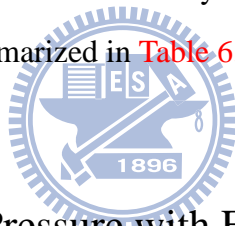
After the soil has been placed in the soil bin to the top, soil cups were dug out of the backfill carefully. Soil density is determined by dividing the mass of soil in the cup by the inside volume of the cup. The distributions of relative density of loose sand measured at different elevations with the plate inclination angle $\beta = 90^\circ$ are shown in [Fig. 5.25](#). Test result for $b = 150$ mm are also shown in [Fig. 5.25](#). In the figure, the mean relative density is 35.6%, with a standard deviation of relative density was 1.39%. From a practical point of view, it may be concluded from these data that the soil density in the soil bin is quite uniform. The relative density of the Ottawa sand in the soil bin is independent of the interface plate inclination and location.



Chapter 6

Test Results

This chapter reports the experimental results of the lateral earth pressure on a retaining wall with a constrained cohesionless backfill. Test conditions for the interface plate located at the horizontal spacing $b = 150$ mm, 250 mm, 350 mm, 500 mm and 2000 mm are illustrated in Fig. 1.3 to Fig. 1.7, respectively. The height of backfill H is 0.5 m and the air-pluviation method was used to prepare the loose backfill. The loose Ottawa sand has a relative density $D_r = 35.6$ % and a unit weight $\gamma = 15.6$ kN/m. Based on direct shear tests by Ho, (1999) the corresponding internal friction angle ϕ for the loose backfill would be 31.3° . The γ and ϕ values are used to calculate earth pressures based on the Jaky and Coulomb theories. The testing program for this study is summarized in Table 6.1.



6.1 Horizontal Earth Pressure with Faraway Plate

The variation of horizontal earth pressure against the wall as function of active wall movement was investigated. After the loose backfill was placed into the soil bin as shown in Fig. 6.1 (a) and (b). The model wall slowly moved away from the soil mass in a translation mode at the constant speed of 0.015 mm/s. No compaction was applied to the loose backfill.

Distributions of horizontal earth pressure σ_h measured at different stages of wall displacements S/H (S : horizontal wall displacement, H : backfill height) for Test 0119-1 and Test 0427-2 are illustrated in Fig. 6.2 and Fig. 6.3. As the wall started to move, the earth pressure decrease, and eventually a limiting active pressure was reached. The pressure distributions are essentially linear at each stage of wall movement. Active earth pressures calculated with Rankine and Coulomb theories

are also indicated in the figure. The ultimate experiment active pressure distribution at $S/H = 0.004$ is in fairly good agreement with that estimated with Coulomb and Rankine theories.

The variation of horizontal earth-pressure coefficient K_h as a function of wall displacement is shown in Fig. 6.4. The coefficient K_h is defined as the ratio of the horizontal component of total soil thrust P_h to $\gamma H^2/2$. The horizontal soil thrust P_h was calculated by summing the pressure diagram shown in Fig. 6.2 and Fig. 6.3. In Fig. 6.4 the coefficient K_h decreased with increasing wall movement S/H until a minimum value was reached then remained approximately a constant. The ultimate value of K_h is defined as the horizontal active earth-pressure coefficient $K_{a,h}$. In Fig. 6.4, the active condition was reached at approximately $S/H = 0.004$.

In Fig. 6.4, it may not be an easy task to define the point of active wall movement S_a . For a wall that moved away from a loose sandy backfill in a translational mode, Mackey and Kirk (1967) concluded the wall displacement required to reach an active state is $S_a = 0.004 H$. The S_a values recommended by Mackey and Kirk (1967), Bros. (1972), Fang and Ishibashi (1986) Fang et al. (1997) illustrated in Fig. 6.4. In this study the active wall movement is assumed to be $S_a = 0.004 H$.

Das (2004) stated that, in the actual design of retaining walls, the wall friction angle δ is generally assumed to be between $\phi/2$ and $2\phi/3$. Potyondy (1961) investigated the skin friction between various soils and construction materials. It was concluded that, among several other factors, the interface friction was influenced by the roughness of the wall material. For this study, the model-wall surface was made of smooth steel, as a result the wall friction angle was assumed to be $\delta = \phi/2 = 15.65^\circ$. The wall friction angle mentioned above was assumed for calculation of earth pressure for the Coulomb theory in the following sections. It may be observed in Fig. 6.4 that the Coulomb theory ($\delta = \phi/2$) provide a good estimate of the active soil thrust. The wall friction calculated with Equation 5.2 is $\delta = 18.5^\circ$. For comparison purposes, the $K_{a,h}$ determined with $\delta = 18.5^\circ$ is also illustrated in Fig.

6.4.

In Fig 6.2 and Fig. 6.3, the distribution of earth pressure with depth at different wall movements is nearly linear. As a result, the point of application of the total soil thrust should act at about $H/3$ above the wall base ($h/H = 0.333$). The vertical distance between the point of application of the total soil thrust and wall base is designed as h . Test results in Fig. 6.5 shows that the points of application of soil thrust are located at about $0.33 H \sim 0.36 H$ above the wall base.

6.2 Horizontal Earth Pressure for $b = 150$ mm

Fig. 6.6 (a) and (b) show the steel interface plate was placed in the soil bin for $b = 150$ mm and $\beta = 90^\circ$. It is clear in the figures that only a thin layer of soil was sand which between the wall and the interface plate. The distributions of earth pressure at different stages of wall movement are illustrated in Fig. 6.7 and Fig. 6.8. The measured σ_h was significantly lower than Jaky's solution at $S/H = 0$. At the wall movement $S/H = 0.004$, the active earth pressure is significantly less than that of Coulomb's solution. In Fig. 6.6(a), the interface plate constrained the backfill so the active soil wedge cannot develop fully. It is reasonable to expect the measured σ_h to be less than Coulomb's prediction.

Fig. 6.9 (a) and (b) show the steel interface plate was placed in the soil bin for $b = 150$ mm and $\beta = 80^\circ$. The distributions of earth pressure at different stages of wall movement are illustrated in Fig. 6.10 and Fig. 6.11. The measured σ_h was slightly lower than Jaky's solution at $S/H = 0$. At $S/H = 0.004$, the measured σ_h was lower than Coulomb's solution. It may be observed in Fig. 6.9, with the β angle decreasing from $\beta = 90^\circ$ to $\beta = 80^\circ$, the horizontal distance between the model wall and interface plate was increased. The amount of soil mass between the wall and the inclined plate increased.

Fig. 6.12 (a) and (b) show the inclined plate was standing in the soil bin with $b =$

150 mm and $\beta = 70^\circ$. The distributions of earth pressure at different stages of wall movement are shown in Fig. 6.13 and Fig. 6.14. The stress measured at $S/H = 0$ was lower than Jaky's solution near the bottom of the wall. However, the active earth pressure in Fig. 6.13 and Fig. 6.14 was close to Coulomb's solution. It was clear in Fig. 6.12 (a) with β angle decreased from 80° to 70° , the interface plate did not intrude the active soil wedge. It is possible for the active soil wedge to develop fully in the backfill. As a result, the measured active earth pressure was close to Coulomb's solution.

The steel interface plate with $b = 150$ mm and $\beta = 60^\circ$ is shown in Fig. 6.15 (a) and (b). The distributions of earth pressure at different stages of wall movement are shown in Fig. 6.16 and Fig. 6.17. The measured σ_h at $S/H = 0$ was close to Jaky's solution, and the active pressure distribution was close to Coulomb's solution. Fig. 6.15 (a) shows the interface plate was relatively far from the wall face, thus the measured lateral stress was not be strongly affected by the existence of the steel interface plate.

Fig. 6.18 to Fig. 6.21 presents the variation of horizontal earth pressure coefficient K_h as a function of wall movement for $\beta = 90^\circ, 80^\circ, 70^\circ$ and 60° . As the wall started to move, the lateral soil thrust decreased with increasing wall movement until a stable value was reached, then remained approximately a constant. The ultimate value of K_h was defined as the horizontal active earth pressure coefficient $K_{a,h}$. For $b = 150$ mm, the active condition was observed at approximately $S/H = 0.004$.

The Fig. 6.22 to Fig. 6.25 demonstrate the variation of the point of application of the soil thrust as a function of active wall movement for $\beta = 90^\circ, 80^\circ, 70^\circ$ and 60° . At the active wall movement of $0.004 H$, for $\beta = 90^\circ, 80^\circ, 70^\circ$ and 60° , the $(h/H)_a$ values were 0.332, 0.345, 0.340 and 0.332. The point of application of the active soil thrust was located at $1/3 H$ above the base of the wall.

6.3 Horizontal Earth Pressure for $b = 250$ mm

Fig. 6.26 (a) and (b) illustrate the steel interface plate was placed in the soil bin for $b = 250$ mm and $\beta = 90^\circ$. In Fig. 6.26 (a), the vertical interface plate intruded the active soil wedge. In Fig. 6.27 and Fig. 6.28, the distributions of earth pressure at different stages of wall movement are presented. At $S/H = 0$, the stress measured was less than Jaky's solution. The active earth pressure at $S/H = 0.004$ was lower than Coulomb's solution.

Fig. 6.29 (a) and (b) show the steel interface plate was placed in the soil bin for $b = 250$ mm and $\beta = 80^\circ$. The distributions of earth pressure at different stages of wall movement are shown in Fig. 6.30 and Fig. 6.31. At $S/H = 0$, the stress measured was slightly less than Jaky's solution. The active earth pressure at $S/H = 0.004$ was close to Coulomb's solution.

Fig. 6.32 (a) and (b) show the steel interface plate was placed in the soil bin for $b = 250$ mm and $\beta = 70^\circ$. The distributions of earth pressure at different stages of wall movement are shown in Fig. 6.33 and Fig. 6.34. For $\beta = 70^\circ$, the stress measured at $S/H = 0$ was close to Jaky's solution, and the active earth pressure was near Coulomb's solution. Fig. 6.32 (a) shows the inclined interface plate did not intrude the active soil wedge and the interface plate was far from the wall. The active soil wedge can develop fully, therefore, the measured active earth pressure was close to Coulomb's solution.

Fig. 6.35 to Fig. 6.37 show the variation of lateral soil thrust as a function of wall movement for $\beta = 90^\circ$, 80° and 70° . As the wall started to move, the lateral soil thrust decreased with increasing wall movement until a stable value was reached, then remained approximately a constant. For $b = 250$ mm, the active condition was reached at the wall movement of approximately 0.004.

Fig. 6.38 to Fig. 6.40 show the point of application of the soil thrust as a function of wall movement. At the active wall movement of 0.004 H, the $(h/H)_a$

values were 0.330, 0.324 and 0.330 for $\beta = 90^\circ$, 80° , and 70° , respectively. It is clear that the active soil thrusts act at about $H/3$ above the wall base.

6.4 Horizontal Earth Pressure for $b = 350$ mm

Fig. 6.41 (a) and (b) illustrate the steel interface plate was placed in the soil bin for $b = 350$ mm and $\beta = 90^\circ$. In Fig. 6.41 (a), the steel interface plate does not invade the active soil wedge. The distributions of earth pressure at different stages of wall movement are shown in Fig. 6.42 and Fig. 6.43. At $S/H = 0$, the measured σ_h was slightly lower than Jaky's solution at the lower part of the wall. At active wall movement $S/H = 0.004$, the σ_h measured at the lower part of the wall was lower than Coulomb's solution.

The steel interface plate with $b = 350$ mm and $\beta = 80^\circ$ is shown in Fig. 6.44 (a) and (b). Fig. 6.45 and Fig. 6.46 present the distributions of earth pressure at different stages of wall movement. In Fig. 6.44 (a), the interface plate was relatively far from the wall face. Therefore, the measured σ_h at $S/H = 0$ was close to Jaky's solution, and the active earth pressure measured at $S/H = 0.004$ was close to Coulomb's solution.

Fig. 6.47 and Fig. 6.48 show the variation of lateral soil thrust as a function of wall movement for $\beta = 90^\circ$ and 80° . As the wall started to move, the lateral soil thrust decreased with increasing wall movement until a stable value was reached, then remained approximately a constant. For $b = 350$ mm, the active condition was observed at approximately $S/H = 0.004$.

The Fig. 6.49 and Fig. 6.50 show the point of application of the soil thrust as a function of wall movement. At the active wall movement of $0.004 H$ the $(h/H)_a$ values reached 0.342 and 0.332 for $\beta = 90^\circ$ and 80° . It may be concluded that the point of application of the total thrust was located at $H/3$ above the base of the wall.

6.5 Horizontal Earth Pressure for $b = 500$ mm

Fig. 6.51 (a) and (b) show the steel interface plate was placed in the soil bin for $b = 500$ mm and $\beta = 90^\circ$. Fig. 6.52 and Fig. 6.53 show the distributions of earth pressure at different stages of wall movement. The lateral stress measured at $S/H = 0$ was close to Jaky's solution, and the measured active earth pressure was close to Coulomb's solution. In Fig. 6.51 (a), the interface plate was relatively far from the wall and the active soil wedge. As a result, the measured stress was good agreement with Jaky's and Coulomb's predictions.

Fig. 6.54 present the variation of lateral soil thrust as a function of active wall movement. As the wall started to move, the lateral soil thrust decreased with increasing wall movement until a stable value was reached, then remained approximately a constant. For 500 mm, Fig. 6.54 shows the active condition was reached at the wall movement of $S/H = 0.004$.

Fig. 6.55 shows the point of application of the soil thrust as a function of wall. At the active wall movement of $0.004 H$, the $(h/H)_a$ value was 0.336. It means that the active thrust was located at $H/3$ above the base of the wall.

6.6 Active Soil Thrust

The distributions of active earth pressure for interface plates with horizontal spacing $b = 150$ mm, 250 mm, 350 mm and 500 mm with the difference interface inclination angle β were shown in Fig. 6.56 to Fig. 6.59. In Fig. 6.56, for $b = 150$ mm, the active earth pressure increased with decreasing β angle. In Fig 6.6(a) and Fig 6.15(a), the plate inclination angle decreased from $\beta = 90^\circ$ to $\beta = 60^\circ$. In these figures, the amount of soil mass behind the wall increased with decreasing β angle. In Fig 6.15(a), the active soil wedge can fully develop in the backfill. The interface was relatively far from the retaining wall. It would be reasonable to expect that the

active earth pressure on the wall would reach Coulomb's solution. Fig. 6.57 shows the active earth pressure distributions for $b = 250$ mm. For $\beta = 90^\circ$, the measured active earth pressure was slightly less than Coulomb's solution. In Fig 6.26(a), the interface plate intruded the active soil wedge so the active earth pressure was less than Coulomb's solution. For $\beta = 80^\circ$ and 70° , the interface plate did not intrude the active soil wedge are shown in Fig 6.29(a) and Fig 6.32(a). As a result, the measured active earth pressure was close to Coulomb's solution. In Fig. 6.58, a similar trend that the active earth pressure increased with decreasing β angle can be observed. In Fig. 6.59, the measured active earth pressure was in fairly good agreement with Coulomb's solution, because the interface plate was relatively far ($b = 500$ mm) from the wall.

The variation of horizontal earth pressure coefficient K_h as a function of wall movement S/H for $b = 150$ mm, 250 mm, 350 mm and 500 mm are shown in Fig. 6.60 to Fig. 6.63. In these figures, the active condition can be observed at the wall movement of $S/H = 0.004$. In Fig. 6.60, the active earth pressure coefficient $K_{a,h}$ for $\beta = 90^\circ, 80^\circ, 70^\circ$ and 60° is 0.199, 0.261, 0.282 and 0.288, respectively. With $\delta = \phi/2$, the Coulomb's solution for $K_{a,h}$ was 0.286. It was clear in Fig. 6.60 that the active earth pressure coefficient $K_{a,h}$ increased with decreasing β angle. In Fig. 6.61, for $\beta = 90^\circ$, the active earth pressure coefficient $K_{a,h}$ was 0.214, which was less than Coulomb's solution. For $\beta = 80^\circ$ and 70° , the $K_{a,h}$ values was 0.281 and 0.287, which were close to Coulomb's solution. In Fig. 6.61, the active earth pressure coefficient $K_{a,h}$ increased with decreasing β angle. In Fig. 6.62, the $K_{a,h}$ value for $\beta = 90^\circ$ and 80° was 0.258 and 0.280, respectively. In Fig. 6.63, the active earth pressure coefficient $K_{a,h}$ is 0.287, which was in very good agreement with Coulomb's solution $K_{a,h} = 0.286$. In Fig. 6.51, the interface was quite far from the active soil wedge and retaining wall. Therefore, the active wedge can fully develop. The influence of the interface plate on the active earth pressure becomes negligible.

Fig. 6.64 to Fig. 6.67 present the point of application of the soil thrust as a function of wall movement for $b = 150$ mm, 250 mm, 350 mm and 500 mm. In these

figures, with increasing wall movement, the point of application of the earth pressure resultant remained at about $H/3$ above the wall base. In Fig. 6.56, from $\beta = 90^\circ$ to $\beta = 60^\circ$, the distributions of active earth pressure were approximately linear with depth. As a result, the point of application of active soil thrust was located at about $H/3$ above the wall base. A similar trend can be observed in Fig. 6.65 to Fig. 6.67.

6.6.1 Magnitude of Active Soil Thrust

The active earth pressure coefficient $K_{a,h}$ as a function of the aspect ratio b/H of the constrained backfill for $\beta = 90^\circ$, 80° , 70° and 60° were shown in Fig. 6.68. In the figure, with the same β angle, the active earth pressure coefficient $K_{a,h}$ increased with increasing aspect ratio b/H . For the aspect ratio $b/H > 1.0$, the interface plate was faraway from the retaining wall, the influence of the plate on σ_a vanish. The $K_{a,h}$ value converged to Coulomb's solution, because the active failure wedge could develop fully.

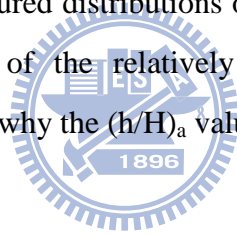
For comparison purposes, the numerical solutions reported by Leshchinsky, et al. (2004), Yang and Liu (2007) and experimental results based on centrifuge tests by Frydman and Keissar (1987) were plotted in Fig. 6.69. In the figure, All active pressure coefficients were for $\beta = 90^\circ$ and normalized by Rankine K_a . The experimental coefficient $K_{a,h}/K_a$ values in this study were lower than numerical $K_{a,h}/K_a$ values. However, the research findings show a similar trend that, for $b/H < 1.0$ the normalized active pressure coefficient $K_{a,h}/K_a$ increased with increasing aspect ratio b/H . As b/H ratio approached 1.0 the test data in this study and the numerical solution by Yang and Liu (2007) converged to Coulomb's solution. The $K_{a,h}$ coefficient obtained by Leschinsky et al. (2004) converged to Rankine's solution.

6.6.2 Point of Application of Active Soil Thrust

Fig. 6.70 shows the point of application of active soil thrust with increasing backfill aspect ratio b/H for $\beta = 90^\circ, 80^\circ, 70^\circ$ and 60° . For $b/H = 0$, the point of application of active soil thrust $(h/H)_a$ for $\beta = 80^\circ, 70^\circ, 60^\circ$ is 0.463, 0.417, 0.380, respectively. For $b/H = 0$, the interface plate was near the wall resulted in a thin layer of backfill. The active earth pressure measured at lower part of wall was significantly less than Coulomb's prediction. This is the reason why the active soil thrust moved to a higher location. For $b/H < 0.3$, the point of application of active soil thrust $(h/H)_a$ increased with decreasing backfill aspect ratio.

For the aspect ratio b/H between 0.3 to 1.0, even though the active earth pressure was influenced by the interface plate, the distributions of active earth pressure were approximately linear with depth, so that the $(h/H)_a$ values were near $1/3$.

For $b/H > 1.0$, the measured distributions of active pressure were nearly linear with depth. The influence of the relatively faraway interface plate becomes negligible. This is the reason why the $(h/H)_a$ values were approximately $1/3$.



6.7 Lateral Pressure in Silo

Fig. 6.71 shows a cylindrical storage silo filled with granular material. It is important for designer to know how much lateral pressure is acting on the inside of the silo wall. The granular material in the silo is generally constrained by the parallel vertical walls. At an active condition, the movable model wall simulates the vertical silo wall which yields laterally under the internal pressure. At $\beta = 90^\circ$, the steel interface plate simulates the vertical central axis of the silo that remains unyielding due to symmetry.

Fig. 6.72 illustrates the distributions of active earth pressure at different aspect ratio b/H for $\beta = 90^\circ$. For $b/H < 1.0$, the active earth pressure was less than Coulomb's solution. This implies that the interface plate constraint starts to play a

role when the shape of fill becomes slender. For $b/H \geq 1.0$, the measured active earth pressure was close to Coulomb's solution. It implies the boundary constraint was relatively far from the wall face, the measured stress was not strongly affected by the existence of the steel interface plate.

The variation of horizontal earth pressure coefficient K_h as a function of wall movement S/H for $\beta = 90^\circ$ is shown in Fig. 6.73. With a faraway interface plate ($b/H \geq 1.0$), the active earth pressure coefficient $K_{a,h}$ was in fairly good agreement with Coulomb's equation ($\delta = \phi/2$). However, with the approaching of the interface plate b decreasing, the soil mass behind the wall became narrow. In Fig. 6.73 at the active wall movement $S/H = 0.004$, the active earth pressure coefficient $K_{a,h}$ decreased with decreasing backfill aspect ratio b/H .

Fig. 6.74 shows the point of application of the soil thrust as a function of wall movement for $\beta = 90^\circ$. Huang (2009) reported the point of application of the soil thrust for $b/H = 0.1$ and 0.2 was higher than $H/3$ above the wall base. Based on the test result in this study, for $b/H = 0.3, 0.5, 0.7, 1.0$ and 4.0 , the point of application of the active earth pressure resultant was located at about $H/3$ above the wall base.

Fig. 6.75 shows the distribution of normalized horizontal active pressure ($\sigma_{a,h}/\gamma z$) based on the theoretical solution by Spangler and Handy (1982), experimental results based on centrifuge tests by Frydman and Keissar (1987), and the 1-g physical model tests of this study. In Fig. 6.75, with a constrained backfill, the normalized active pressure $\sigma_{a,h}/\gamma z$ was not a constant with depth as assumed by Coulomb and Rankine, it decreased with depth. It can be concluded that, with a constrained backfill, both Coulomb and Rankine theories would overestimate the active earth pressure against the vertical silo wall.

6.8 Displacement Vector in Backfill

Fig. 6.76 (a) and (b) show the observed backfill displacement for $b = 500$ mm

and $\beta = 90^\circ$ Vertical and horizontal black lines were drawn on the acrylic side walls with the spacing of 50 mm. The movement of backfill was traced with black plastic balls ($\phi = 3$ mm) placed next to the acrylic side wall. The active soil wedge based on Rankine theory is also marked on the side wall. At the wall movement of $S = 20$ mm ($S/H = 0.04$), the accumulated displacement of the black plastic ball is shown in Fig. 6.77. The observed displacement occurred at the upper part of the fill, the soils tend to move downward with the active wedge. The largest surface settlement measured was 24.8 mm. It is obvious that the magnitude of displacement reduced progressively with increasing distance to the wall. A surface crack was observed at 246 mm from the wall, which happens to be fairly close to Coulomb's prediction of 264 mm.

Fig. 6.78 (a) and (b) show the observed displacement vector of backfill with $b = 150$ mm and $\beta = 90^\circ$. At the wall movement of $S = 20$ mm ($S/H = 0.04$), the accumulated displacement vectors is shown in Fig. 6.79. It can be seen from this figure that large soil displacements were observed at the upper part of the wall. In Fig. 6.78 (b), the surface of backfill settled significantly. The largest fill settlement measured was 38.2 mm. The magnitude of displacement reduced progressively with increasing depth of the backfill. In Fig. 6.79, the active soil wedge was constrained by the vertical interface plate. At the upper part of the backfill, a sliding surface developed along the interface plate

At the horizontal wall movement of $S = 20$ mm ($S/H = 0.04$), the active wedge slide into the extra volume created by the large wall movement. In Fig. 6.77, the interface plate was faraway from the retaining wall, the active soil wedge can develop fully. In Fig. 6.79, the interface plate intruded the active soil wedge, the active soil wedge cannot develop fully. At the wall movement of 20 mm, an extra space was created behind the wall. The backfill behind the wall moved to fill extra space. In Fig. 6.78 (b), the amount of backfill was limited. This is the reason why the displacement vectors in the backfill for $b = 150$ mm are larger than the displacement vectors in backfill for $b = 500$ mm..

It should be noted that, to observe the movement of the backfill clearly, no plastic-sheet lubrication layer was provided between the backfill and the side-wall. As a result, friction existed between the backfill and the side-wall. Fig. 6.76 and 6.78, the pictures showed the backfill movement with boundary effects. It does not simulate a plane strain condition. However, the trend of backfill deformation can be observed in there pictures.

6.9 Design Considerations

In the design of a rigid retaining structure, it is often necessary to check its adequacy. It is important to evaluate how the constrained backfill influence the Factor of Safety (F.S.) against sliding and overturning of the retaining wall.

6.9.1 Factor of Safety against Sliding

The factor of safety against sliding of the retaining structure is defined as:

$$FS_{\text{sliding}} = \frac{\sum F_R}{\sum F_D} \quad (6.1)$$

Where $\sum F_R$ = the sum of horizontal resisting forces and $\sum F_D$ = the sum of horizontal driving forces. For the retaining wall shown in Fig. 1.1, the horizontal driving force on the wall was the horizontal component of the active soil thrust. The horizontal active thrusts $K_{a,h}$ as a function of backfill aspect ratio b/H for $\beta = 90^\circ$, 80° , 70° and 60° were shown in Fig. 6.68. In the figure, the magnitude of active thrust increased with increasing backfill aspect ratio b/H . The Coulomb's solution is the upper bound for all experimental $K_{a,h}$ values based on different b/H ratios and β angles.

In Eq. (6.1), if the driving force on the wall was reduced due to the constrained backfill, and the resisting force remained the same, the factor of safety against

sliding would increase. From a practical point of view, the constrained backfill would result in a greater FS against sliding. In other words, the evaluation of F.S. against sliding with Coulomb's theory would be on the safe side.

6.9.2 Factor of Safety against Overturning

The Factor of safety against overturning of the retaining wall is defined as:

$$FS_{\text{overturning}} = \frac{\sum M_R}{\sum M_o} \quad (6.2)$$

where $\sum M_R$ = the sum of resisting moments and $\sum M_o$ = the sum of overturning moments about toe. The overturning moment in Eq. (6.2) is the product of the horizontal active thrust $P_{a,h}$ and the moment arm h . Fig. 6.80 shows the normalized driving moment $K_{a,h} \times (h/H)$ as a function of the backfill aspect ratio b/H . It is clear in the figure that the driving moment calculated based on Coulomb's solution is the upper bound value. For $b/H < 1.0$, the overturning moment due to active soil thrust decreased with decreasing backfill aspect ratio b/H .

In Eq. (6.2), if the overturning moment was reduced while the resisting moment remained the same, the factor of safety against overturning would increase. The constrained backfill would result in a greater FS against overturning. In other words, the evaluation of F.S. against overturning with Coulomb's theory would be on the safe side.

Chapter 7

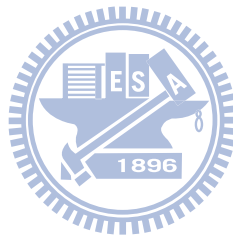
Conclusions

In this study, the effects of a constrained backfill on active earth pressure were investigated. Based on the experimental data, the following conclusions are drawn.

1. The backfill in the soil bin prepared by air-pluviated is quite uniform. The distribution relative density of Ottawa sand in the soil bin is independent of the interface plate inclination and location.
2. With a faraway interface plate ($b = 2,000$ mm), the earth pressure decreased with increasing wall movement, and eventually a limiting active pressure was reached. For the wall with loose backfill, the ultimate pressure was measured at the active wall movement of $0.004 H$. The measured active pressure distribution was in good agreement with Coulomb's solution.
3. With the approaching of the interface plate, the plate intruded the active soil wedge, so that the active soil wedge cannot develop fully behind the wall. The active earth pressure coefficient $K_{a,h}$ decreased with decreasing wall-plate spacing b and increasing plate inclination angle β .
4. For $\beta = 90^\circ$ and $b/H < 1.0$, the measured active earth pressure was less than Coulomb's solution. This implies that the vertical constraint play a role when the shape of fill becomes slender. For $b/H \geq 1.0$, the measured active earth pressure converged to Coulomb's solution. When the vertical boundary was relatively far from the wall, the measured stress was not affected by the existence of the vertical plate.
5. Under the aspect ratio $b/H = 0.3, 0.5, 0.7,$ and 1.0 , the point of application of active soil thrust was located at about $H/3$ above the wall base.
6. For $b/H < 1.0$, the magnitude of active thrust increased with increasing backfill aspect ratio b/H . Coulomb's solution is the upper bound for all experimental $K_{a,h}$ values based on different b/H ratios and β angles. The constrained backfill

would result in a greater factor of safety against sliding for the retaining wall. The evaluation of factor of safety against sliding with Coulomb's theory would be on the safe side.

7. For $b/H < 1.0$, the overturning moment due to active soil thrust decreased with decreasing backfill aspect ratio b/H . The driving moment about the toe calculated with Coulomb's solution is the upper bound value. The constrained backfill would result in a greater factor of safety against overturning for the wall. The evaluation of factor of safety against overturning with Coulomb's theory would be on the safe side.



References

1. Ang, A. H., and Tang, W. H., (1975) "Probability Concepts in Engineering Planning and Design Volume I - Basic Principles," John Wiley and Sons, Inc, New York, N.Y., pp. 286-294.
2. Brinch Hansen, J., (1953), "Earth Pressure Calculation," Danish Technical Press, Copenhagen.
3. Bros, B., (1972), "The Influence of Model Retaining Wall Displacements on Active and Passive Earth Pressure in Sand," Proceedings, 5th European Conference on Soil Mechanics, Vol.1, Madrid, Spain, pp. 241-249.
4. Chang, S. Y., (2000), "Effect of Backfill Density on Active Earth Pressure," Master of Engineering Thesis, Dept. of Civil Engineering, National Chiao Tung University, Hsinchu, Taiwan.
5. Chen, C. Y., (1995), "Active Earth Pressure with Inclined Backfill," Master of Engineering Thesis, National Chiao Tung University, Hsinchu, Taiwan.
6. Chen, H. R., (1997), "Earth Pressure At-Rest with Different Soil Densities and Backfill Inclinations," Master of Engineering Thesis, National Chiao Tung University, Hsinchu, Taiwan.
7. Chen, T. J., (2003). "Earth Pressures Due to Vibratory Compaction." Ph.D. dissertation, National Chiao Tung University, Hsinchu, Taiwan.
8. Chien, Y. L., (2007). "Variation of Soil Density and Earth Pressure due to a Strip Compaction" Master of Engineering Thesis, National Chiao Tung University, Hsinchu, Taiwan.
9. Clough, G. W., and Duncan, J. M., (1971), "Finite Element Analysis of Retaining Wall Behavior," Journal of Geotechnical Engineering, ASCE, Vol. 87, No. SM12, pp. 1657-1673.
10. Das, B. M. (2004), "Principles of Foundation Engineering", 5th Ed., Brooks/Cole.
11. Das, B. M., (2010), "Principles of Geotechnical Engineering," 7th Edition,

Cengage Learning , Stamford, CT, USA.

12. Fan, C. C., and Chen K. H, (2006), “Earth Pressure of Retaining Walls near Faces” Master of Engineering Thesis, Department of Construction Engineering, National Kaohsiung First University of Science and Technology, Kaohsiung, Taiwan.
13. Fan, C. C., and Fang, Y. S., (2009), “Active Earth Pressure on Rigid Retaining Walls Built at Constrained Fill Space.” Soils and Foundations, Japanese Geotechnical Society. (submitted for possible publication)
14. Fang, Y. S., and Ishibashi, I., (1986), “Static Earth Pressures with Various Wall Movements,“ Journal of Geotechnical Engineering, ASCE, Vol. 112, No. 3, Mar., pp. 317-333.
15. Fang, Y. S., Cheng F. P., Cheng, R. T., and Fan, C. C., (1993), “Earth Pressure under General Wall Movements,“ Geotechnical Engineering, SEAGS, Vol. 24, No. 2, December., pp. 113-131.
16. Fang, Y. S., Chen, J. M., and Chen, C. Y., (1997), “Earth Pressures with Sloping Backfill” Journal of Geotechnical and Geoenvironmental Engineering, ASCE, 123(3), March, 250-259.
17. Fang, Y. S., Chen, T. J., and Wu, B. F., (1994), “Passive Earth Pressure with Various Wall Movements,“ Journal of Geotechnical Engineering, ASCE, Vol. 120, No. 8, Aug., pp. 1307-1323.
18. Fang, Y. S., Chen, J. J., Holtz, R. D., and Lee, W. F. (2004), “Reduction of Boundary Friction in Model Tests,“ Geotechnical Testing Journal, ASTM, 27(1), 1-10.
19. Frydman. S., and Keissar, I. (1987). “Earth Pressure on Retaining Walls near Rock Faces.” Journal of Geotechnical Engineering, ASCE, 113(6), 586-599.
20. Ho, Y. C., (1999), “Effects of Backfill Compaction on Passive Earth Pressure,“ Master of Engineering Thesis, National Chaio Tung University, Hsinchu, Taiwan.
21. Huang, S. F., (2009) “Active Earth Pressure on Retaining Walls near Rock

- Faces” Master of Engineering Thesis, National Chiao Tung University, Hsinchu, Taiwan.
22. Ishibashi, I., and Fang, Y. S., (1987), “Dynamic Earth Pressures with Different Wall Movements Modes,” *Soils and Foundations, JSSMFE*, Vol. 27, No. 4, Dec., pp. 11-22.
 23. Janbu, N., (1957), “Earth Pressure and Bearing Capacity Calculation by General Procedure of Slices,” *Proceedings, 4th Int. Conf. Soil Mechs. Found. Eng.*, 2, pp. 207-212.
 24. Janssen, H. A., (1895), “Versuche uber Getreidedruck in Silozellen,” *Aeitschrift, Verein Deutscher Ingenieure*, 39: 1045-1049. (Partial English Translation in *Proceedings of Institute of Civil Engineers, London, England, 1896*)
 25. Lawson, C. R., and Yee, T.W. (2005) “Reinforced soil retaining walls with constrained reinforced fill zones” *Proceedings, Geo-Frontiers 2005, ASCE, Geo-Institute Conference*, 2721-2734.
 26. Lee, C. C., (1998), “Passive Earth Pressure with Various Backfill Densities,” *Master of Engineering Thesis, National Chiao Tung University, Hsinchu, Taiwan.*
 27. Leshchinsky, D., Hu, Y., and Han, J. (2004). “Limited Reinforced Space in Segmental Retaining Walls.” *Geotextiles and Geomembranes*, 22(6),543-553.
 28. Lo Presti, D. C. F., Pedroni, S., and Crippa, V. (1992). “Maximum dry density of cohesionless soils by pluviation and by ASTM D 4253-83 : A comparative study.” *Geotechnical Testing Journal, ASTM*, 15(2),180-189.
 29. Mackey, R. D., and Kirk, D. P., (1967), “At Rest, Active and Passive Earth Pressures,” *Proceedings, South East Asian Conference on Soil Mechanics and Foundation Engineering, Bangkok*, pp. 187-199.
 30. Nakai, (1985), “Finite Element Computations for Active and Passive Earth Pressure Problems of Retaining Wall,” *Soils and Foundations, JSSMFE*, Vol. 25, No. 3, pp. 98-112.

31. Naval Facilities Engineering Command. (1982). Foundations and earth structures design manual 7.2, NAVFAC DM-7.2, Dept. of the Navy, Naval Facilities Engineering Command, Virginia.NAVFAC DM-7.2.
32. PLAXIS BV. (2002): User's manual of PLAXIS, A.A. Balkema Publishers.
33. PLAXIS (2005). Plaxis Finite Element Code for Soil and Rock Analyses, Version 8.2, Delft, Netherlands.
34. Potts, D. M., and Fourie, A. B., (1986), "A Numerical Study of the Effects of Wall Deformation on Earth Pressures," International Journal for Numerical and Analytical Methods in Geomechanics, Vol. 10, pp. 383-405.
35. Potyondy, J. G.,(1961). "Skin Friction between Various Soils and Construction Materials." Geotechnique, 11, 329-353.
36. Rad, N.S., and Tumay, M. T. (1987). "Factors affecting sand specimen preparation by raining." Geotechnical Testing Journal, ASTM, 10(1), 31-37.
37. Rowe, P. W., and Barden, L. (1964). "Importance of Free Ends in Triaxial Testing." Journal of the Soil Mechanics and Foundations Division, ASCE, 90(SM1), 1-77.
38. Sherif, M. A., Fang, Y. S., and Sherif, R. I., (1984), "Ka and Ko behind Rotating and Non-Yielding Walls," Journal of Geotechnical Engineering, ASCE, Vol. 110, No. 1, Jan., pp. 41-56.
39. Sowers, G. F. (1979), "Introductory Soil Mechanics and Foundations" 4th Ed., Macmillan Publishing Co., New York.
40. Spangler, M.G and Handy, R.L. (1984):Soil Engineering, Harper and Row, New York.
41. Take, W. A. and Valsangker, A. J. (2001)."Earth pressures on unyielding retaining walls of narrow backfill width." Canadian Geotechnical Journal, 38, 1220-1230.
42. Tatsuoka, F., and Haibara, O., (1985), "Shear Resistance between Sand and Smooth or Lubricated Surface," Soils and Foundations, JSSMFE, Vol. 25, No. 1,

- Mar., pp. 89-98.
43. Tatsuoka, F., Molenkamp, F., Torii, T., and Hino, T. (1984). "Behavior of Lubrication Layers of Platens in Element Tests." *Soils and Foundations*, JSSMFE, 24(1), 113-128.
44. Tejchman, J., and Wu, W., (1995) "Experimental and Numerical Study of Sand-Steel Interfaces", *International Journal for Numerical and Analytical Methods in Geotechnics*, Vol. 19, No. 8, pp.513-536.
45. Terzaghi, K., (1932), "Record Earth Pressure Testing Mechine," *Engineering News-Record*, Vol. 109, Sept., 29, pp. 365-369.
46. Terzaghi, K., (1941), "General Wedge Theory of Earth Pressure," *ASCE Transaction*, Vol. 106, pp. 68-80.
47. Terzaghi, K., and Peck, R. B.,(1967), *Soil Mechanics in Engineering Practice*,Wiley, New York.
48. Wang, F. J., (2005), "Effects of Ajacent Rock Face Inclination on Earth Pressure At-Rest," *Master of Engineering Thesis*, National Chiao Tung University, Hsinchu, Taiwan.
49. Wu, B. F., (1992), "Design and Construction of National Chiao Tung University Model Retaining Wall," *Master of Engineering Thesis*, National Chiao Tung University, Hsinchu, Taiwan.
50. Yang, K. H., and Liu, C. N., (2007) "Finite Element Analysis of Earth Pressures for Narrow Retaining Walls." *Journal of GeoEngineering*, TGS, Vol. 2, No. 2, Aug., pp. 43-52.
51. Zheng, Y. C., (2008) "Active Earth Pressure on Retaining Walls with Intrusion of a Stiff Interface into Backfill," *Master of Engineering Thesis*, National Chiao Tung University, Hsinchu, Taiwan.

Table 2.1. Comparison of experimental and theoretical values (after Mackey and Kirk, 1967)

| Theories | Active Pressure Coefficient | | | | | |
|----------------------|-----------------------------|-------------|-------------|-------------|-------------|-------------|
| | Sand 1 | | Sand 2 | | Sand 3 | |
| | Loose | Dense | Loose | Dense | Loose | Dense |
| Coulomb | 0.25 | 0.13 | 0.22 | 0.14 | 0.19 | 0.13 |
| Rankine | 0.26 | 0.13 | 0.24 | 0.14 | 0.19 | 0.13 |
| Krey(ϕ circle) | 0.26 | 0.21 | 0.25 | 0.21 | 0.21 | 0.19 |
| Ohde | 0.26 | 0.21 | 0.25 | 0.21 | 0.21 | 0.19 |
| Caquot and Kerisel | 0.25 | 0.13 | 0.23 | 0.14 | 0.19 | 0.13 |
| Janbu | 0.27 | 0.12 | 0.22 | 0.13 | 0.18 | 0.13 |
| Rowe | 0.21 | 0.16 | 0.21 | 0.16 | 0.21 | 0.16 |
| Experimental | 0.22 | 0.32 | 0.19 | 0.29 | 0.17 | 0.27 |

Table 2.2. Wall displacements required to reach an active state

| Investigator | Soil Type | Type of Wall Movement | Max. Wall Displacement Required |
|---------------------------|------------|-----------------------|---------------------------------|
| Mackey and Kirk (1967) | Loose Sand | T mode | 0.00400 H |
| Bros (1972) | Sand | T mode | 0.00060 H |
| Fang and Ishibashi (1986) | Loose Sand | T mode | 0.00050 H |
| Fang et al. (1997) | Loose Sand | T mode | 0.00150 H |

Note: T = Translation; and H = Wall height

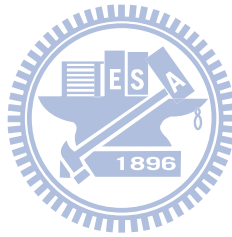


Table 6.1 Test Program

| Horizontal Spacing b, (mm) | Interface Inclination Angle, β (degree) | Test No. |
|-------------------------------|--|----------|
| 150 | 90 | 0305-1 |
| | | 0503-4 |
| | 80 | 0315-3 |
| | | 0316-2 |
| | 70 | 0413-1 |
| | | 0413-2 |
| | 60 | 0420-3 |
| | | 0512-3 |
| 250 | 90 | 0322-3 |
| | | 0323-3 |
| | 80 | 0518-3 |
| | | 0518-4 |
| | 70 | 0524-1 |
| | | 0524-3 |
| 350 | 90 | 0330-2 |
| | | 0330-3 |
| | 80 | 0525-1 |
| | | 0525-2 |
| 500 | 90 | 0412-2 |
| | 90 | 0412-3 |
| 2,000 | 90 | 0119-1 |
| | 90 | 0427-2 |

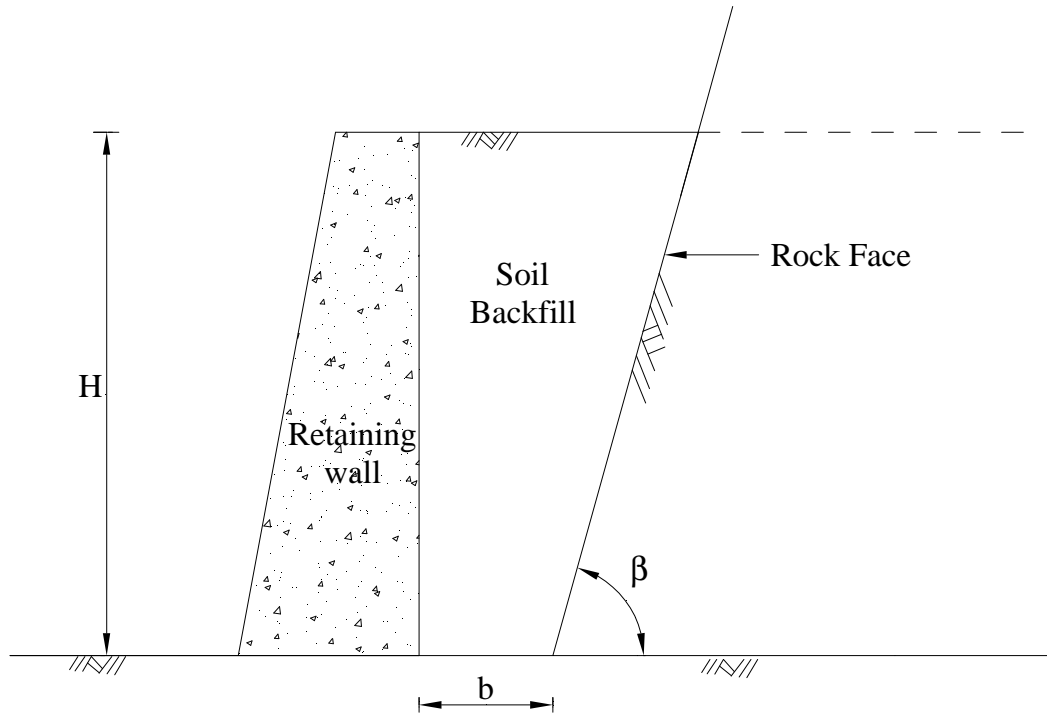


Fig. 1.1. Retaining walls with constrained backfill





Fig. 1.2. Cylindrical silo filled with granular material



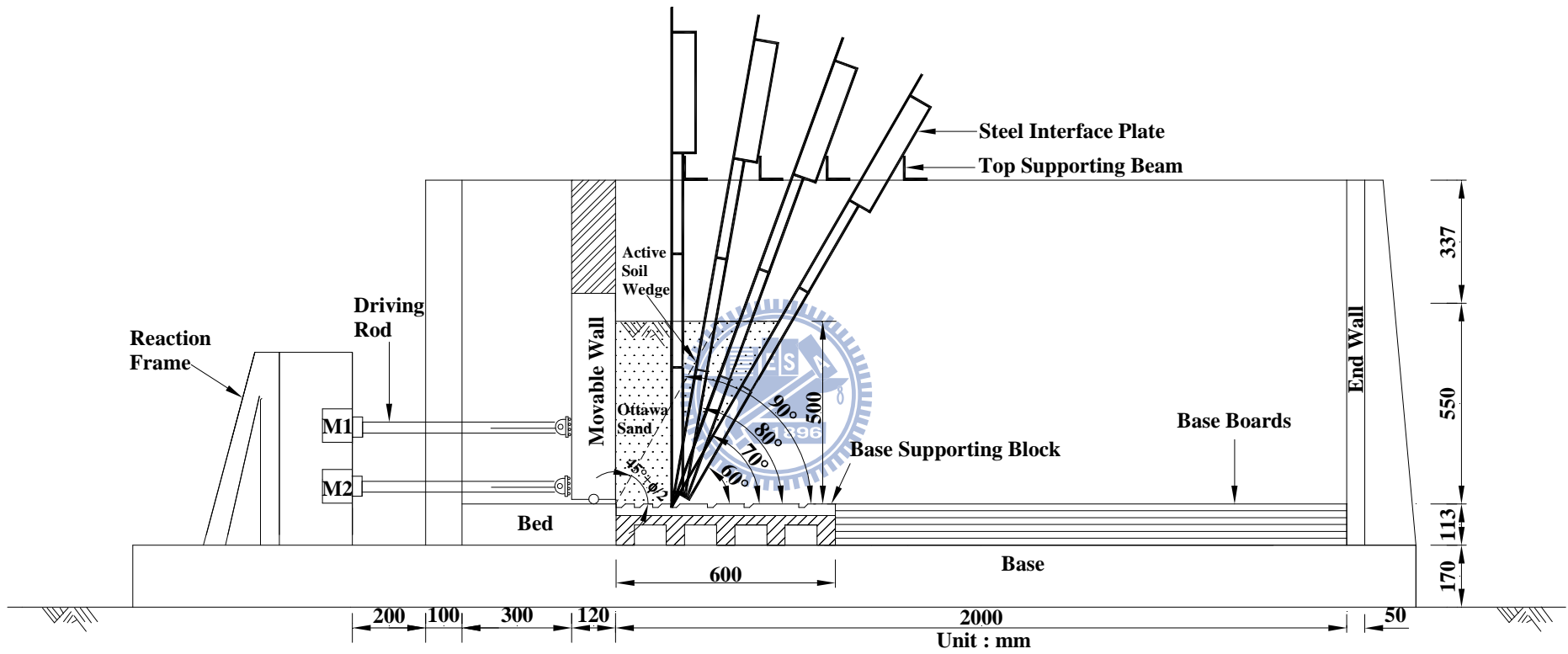


Fig. 1.3. Model test for $b = 150$ mm

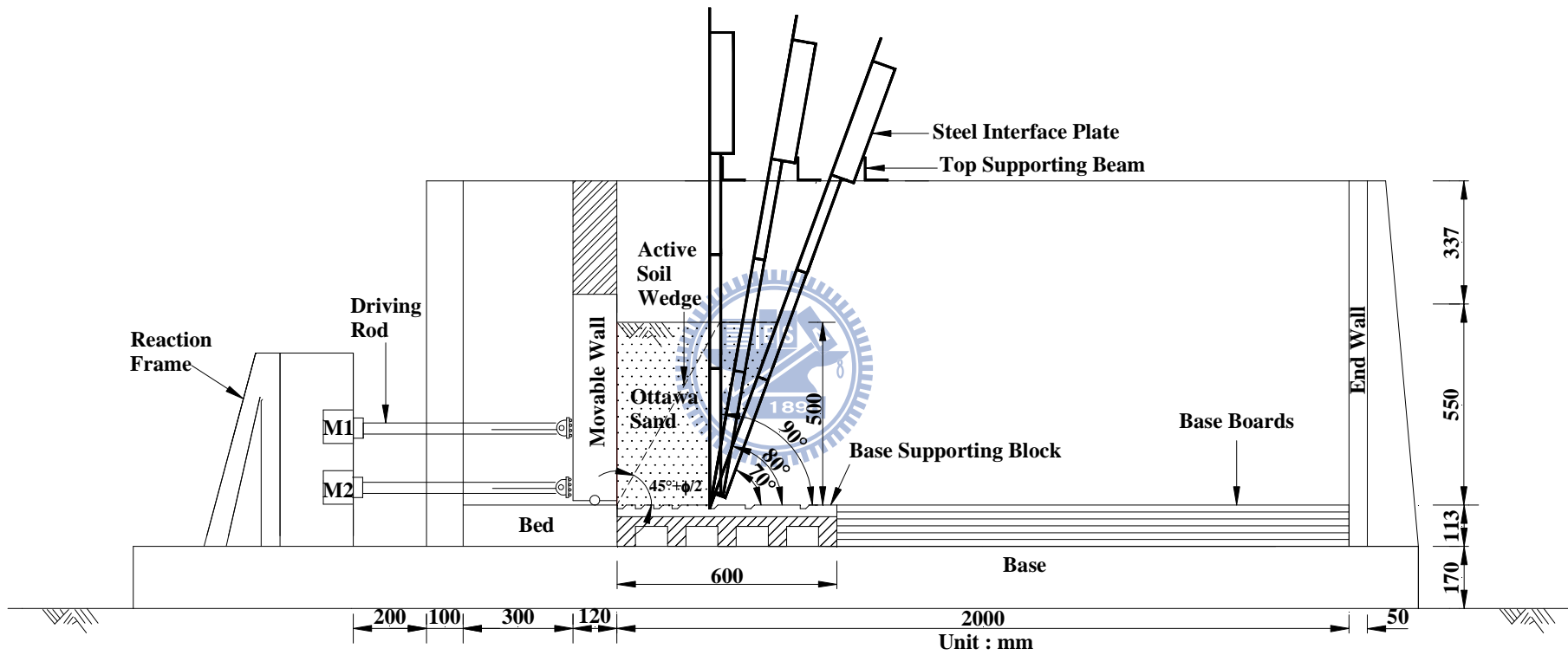


Fig. 1.4. Model test for $b = 250$ mm

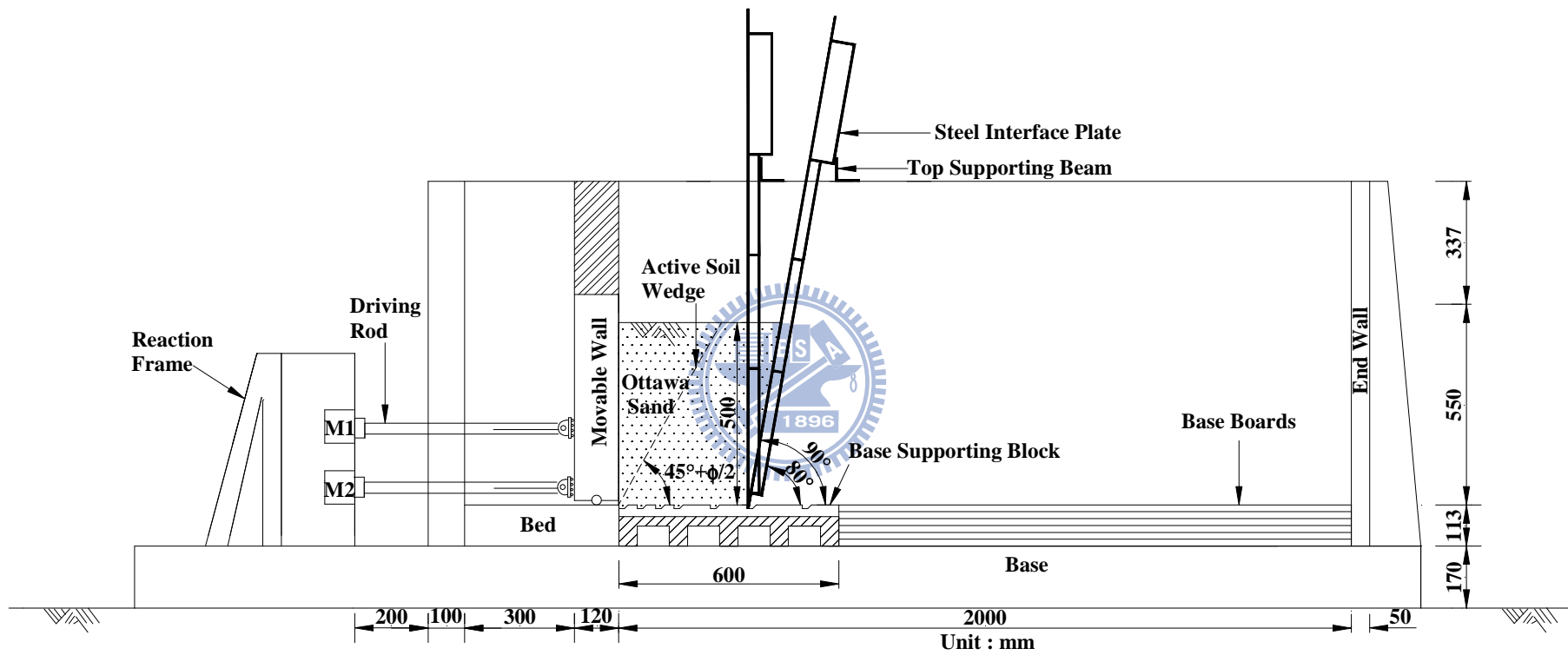


Fig. 1.5. Model test for $b = 350$ mm

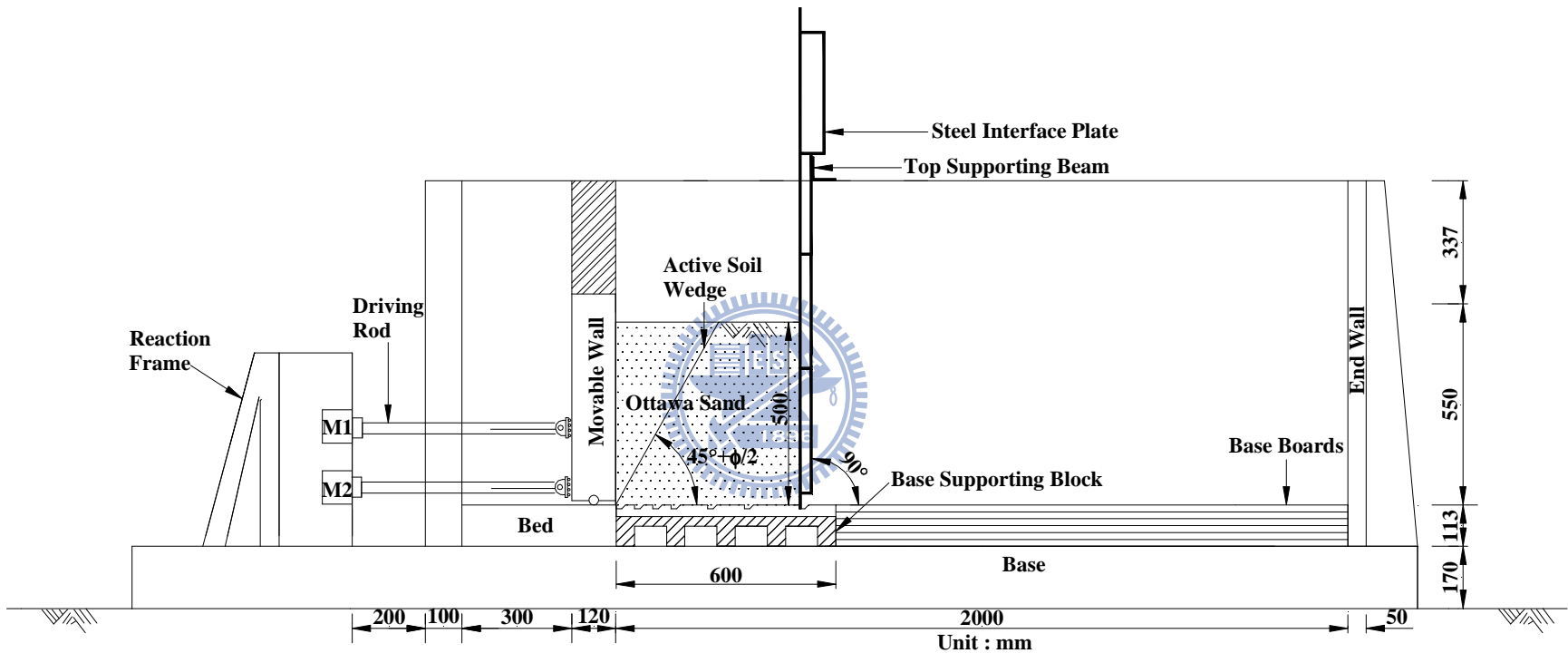


Fig. 1.6. Model test for $b = 500$ mm

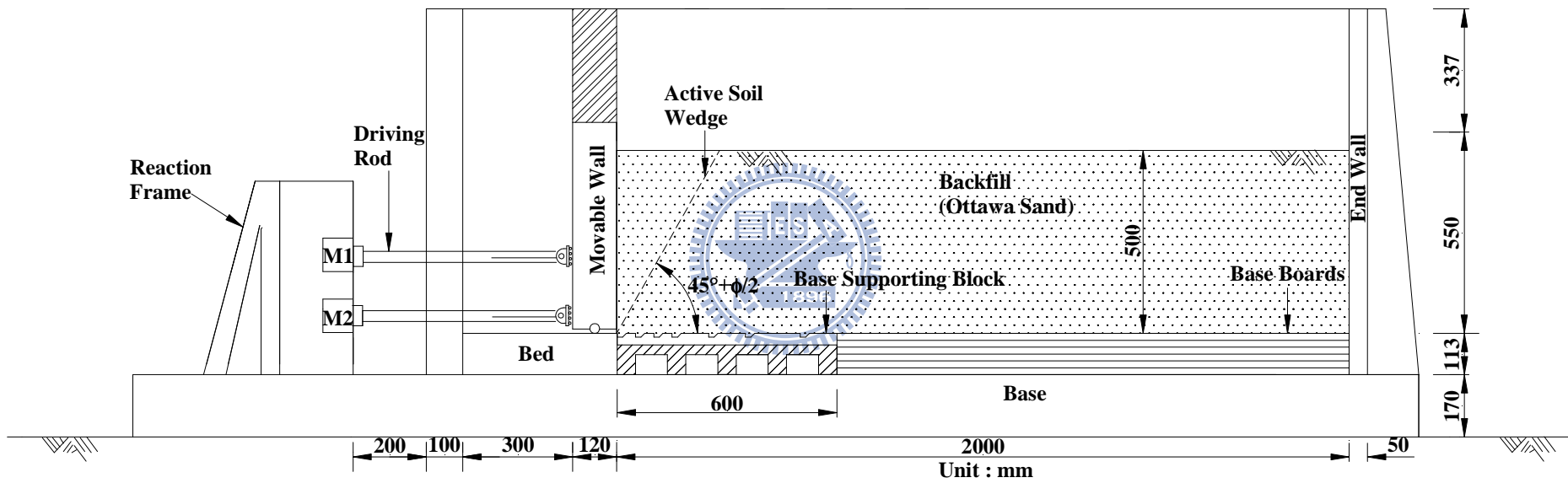
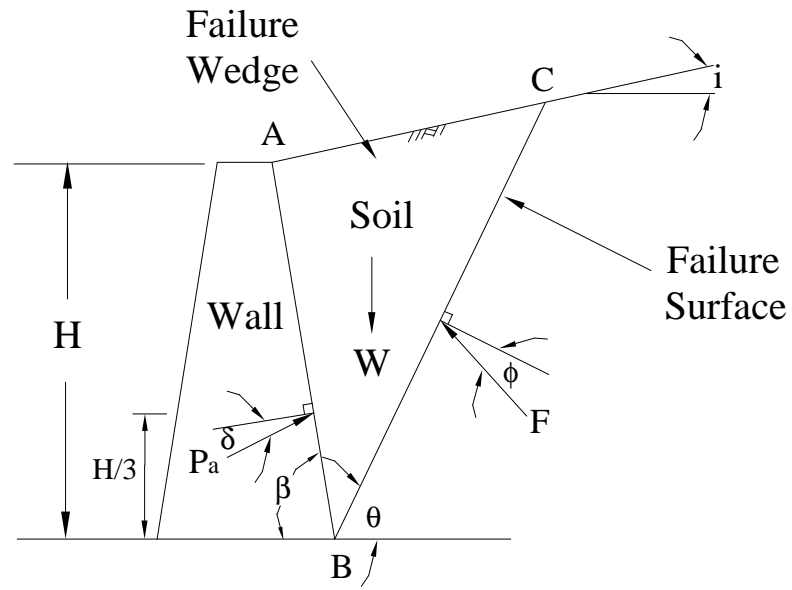
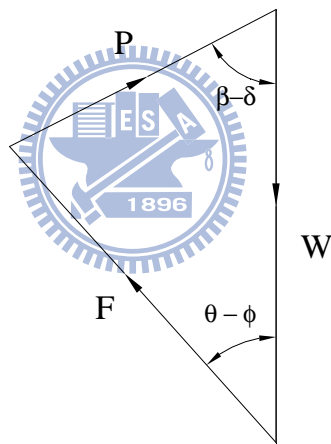


Fig. 1.7. Model wall test with $b = 2,000$ mm



(a)



(b)

Fig. 2.1. Coulomb's theory of active earth pressure

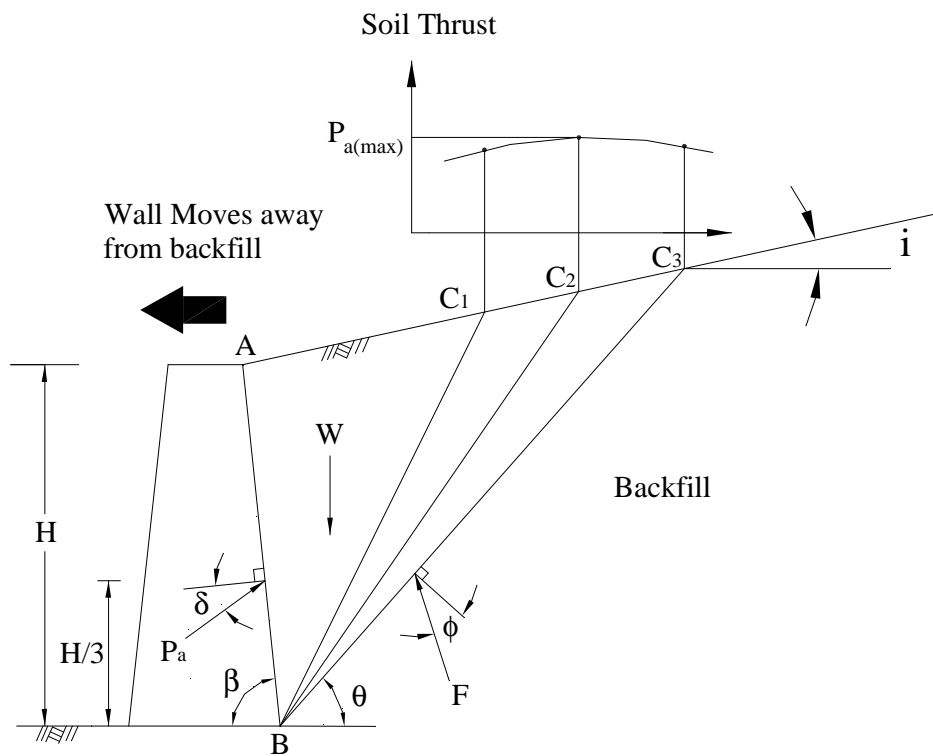


Fig. 2.2. Coulomb's active pressure determination

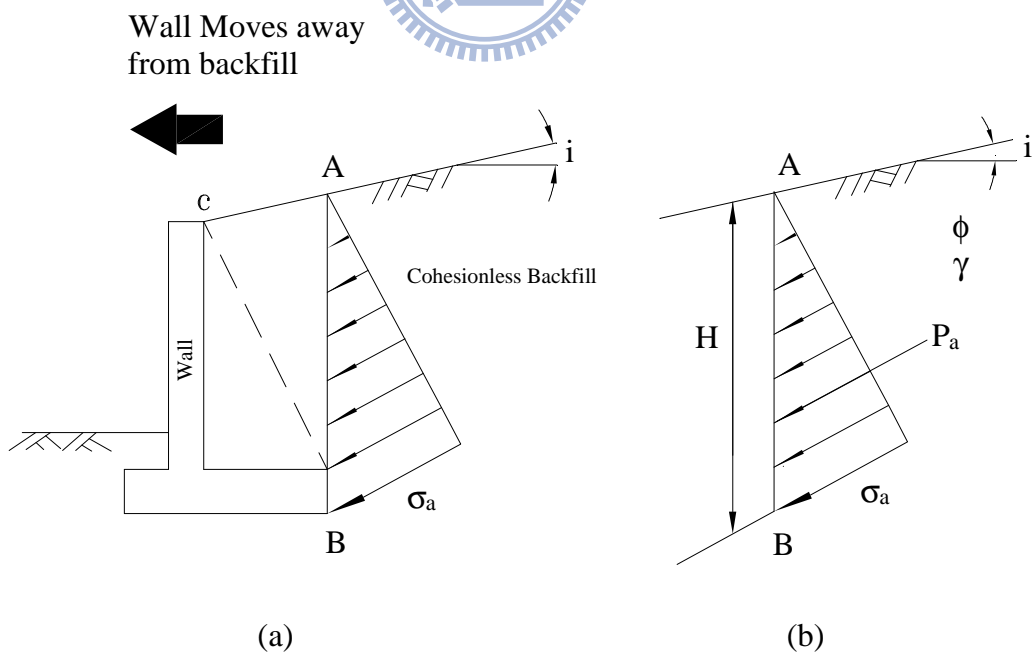


Fig. 2.3. Rankine's theory of active earth pressure

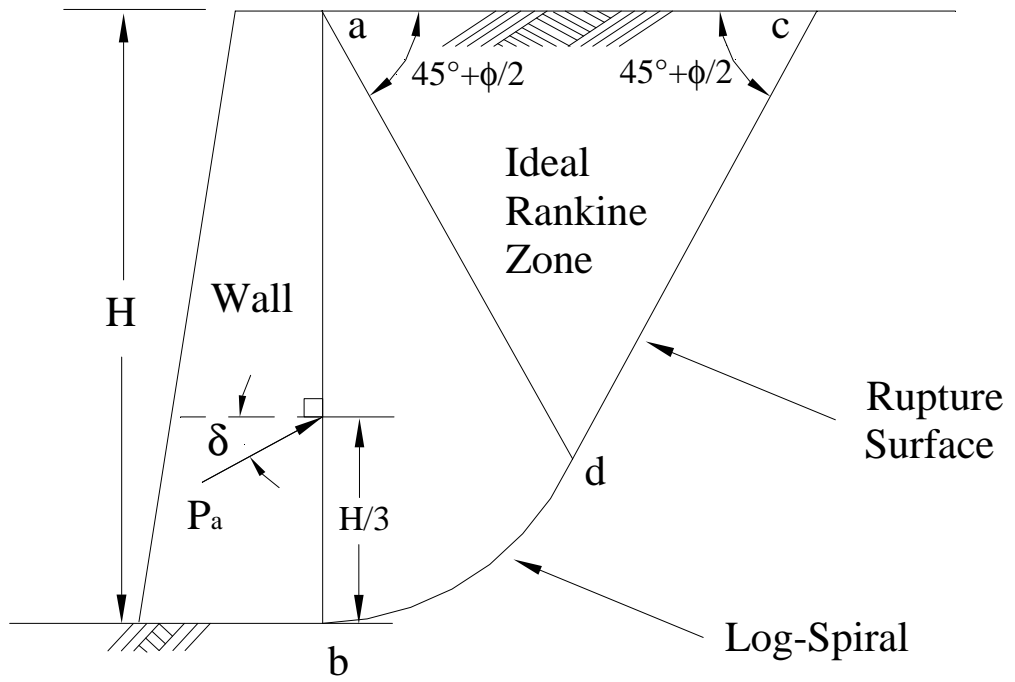
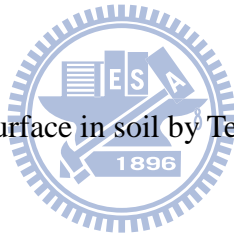


Fig. 2.4. Failure surface in soil by Terzaghi's log-spiral method



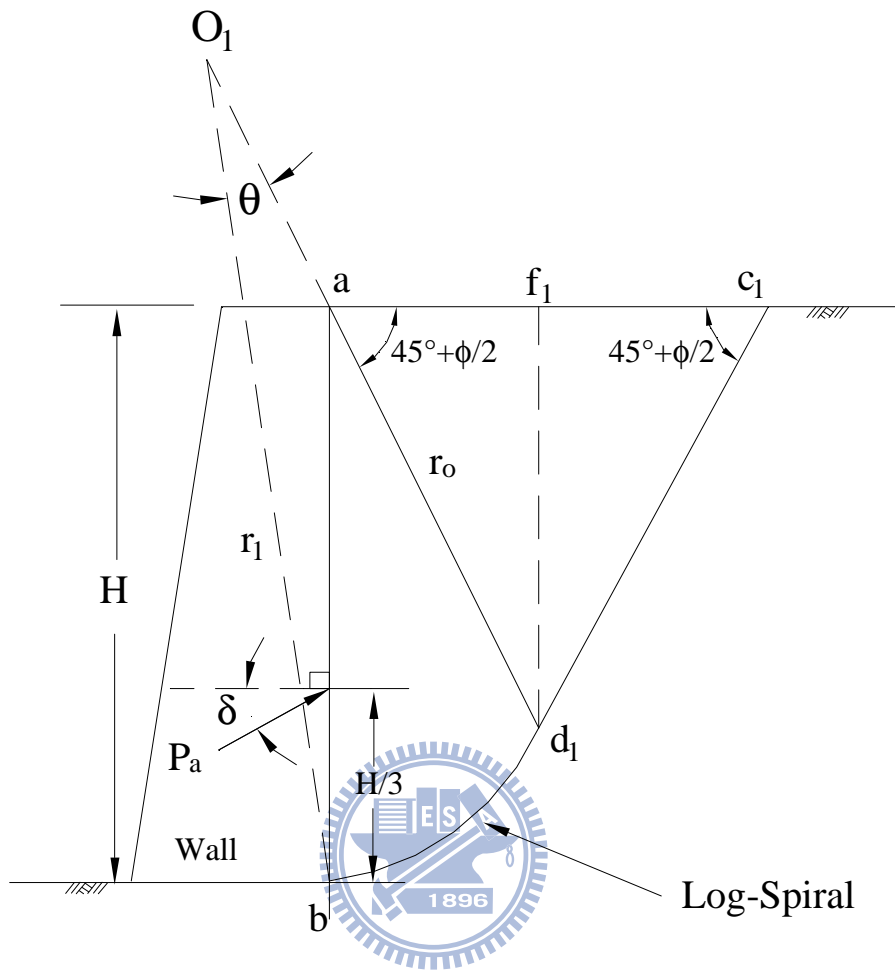


Fig. 2.5. Evaluation of active earth pressure by trial wedge method

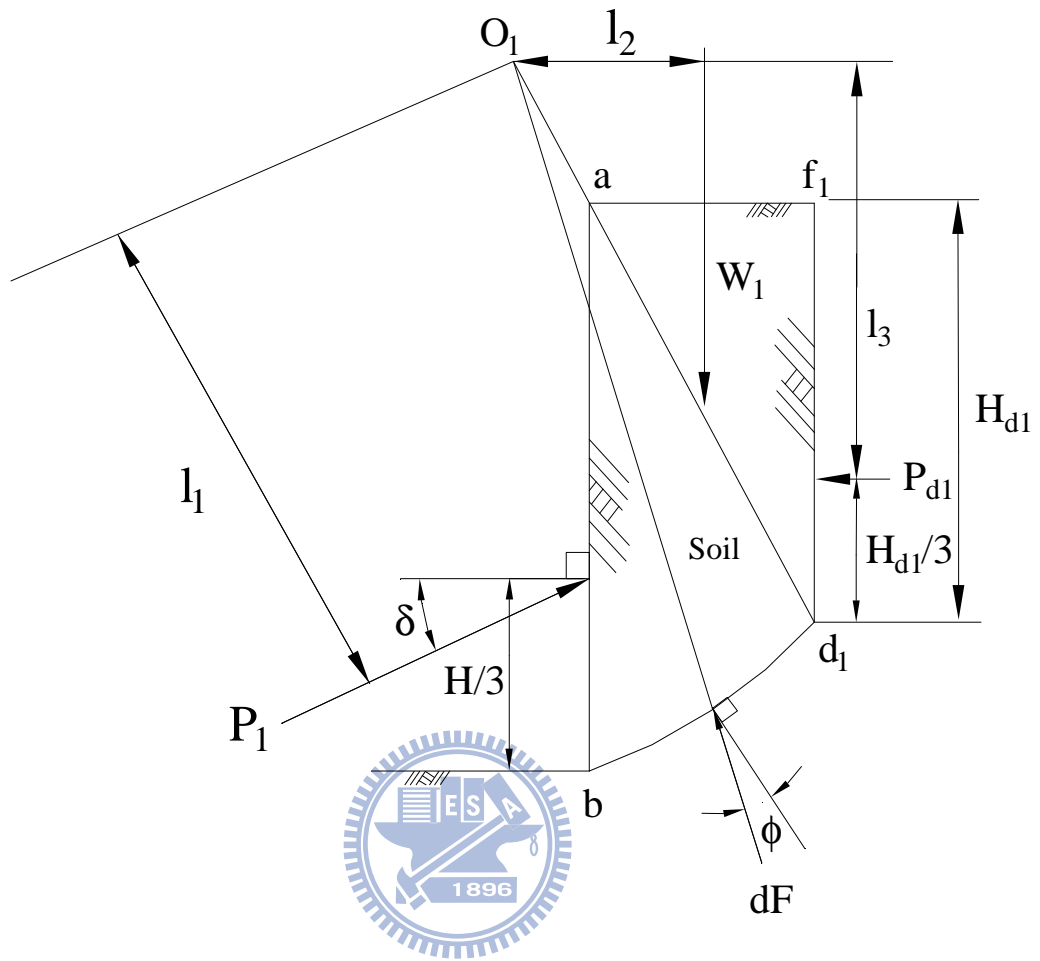


Fig. 2.6 Stability of soil mass abd_1f_1

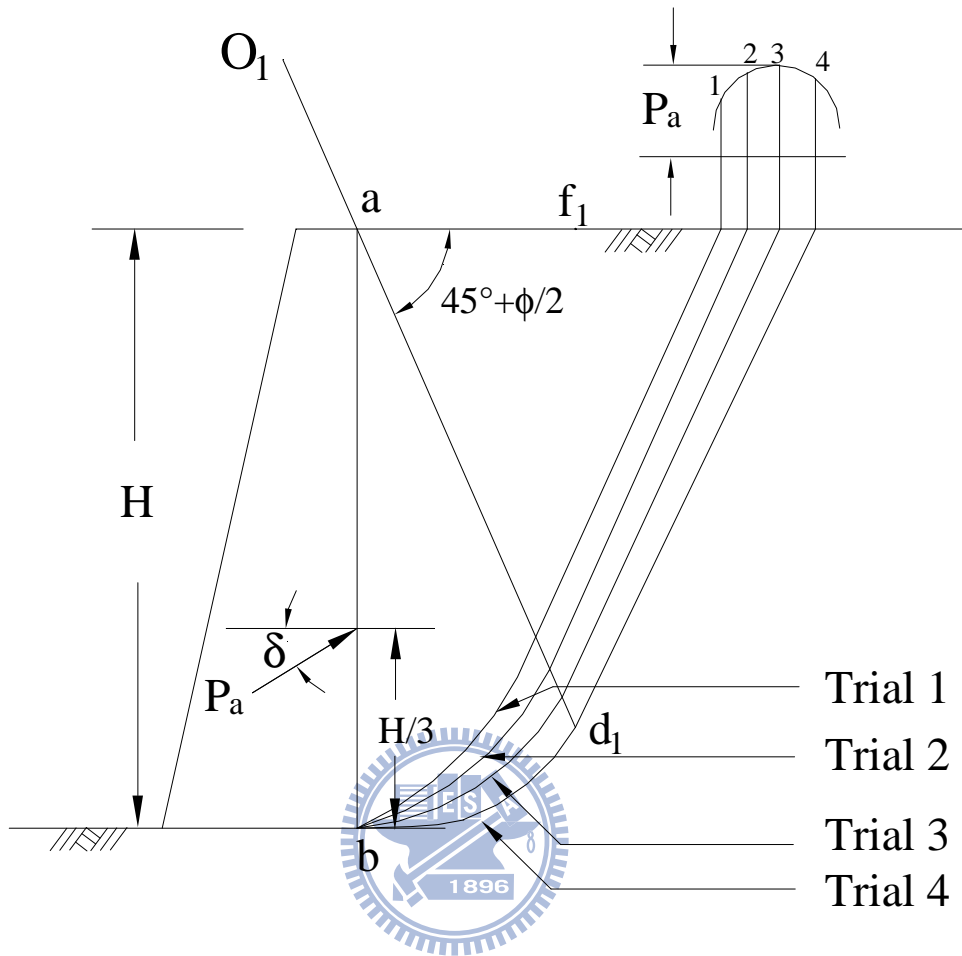


Fig. 2.7. Active earth pressure determination with Terzaghi's log-spiral failure surfaces

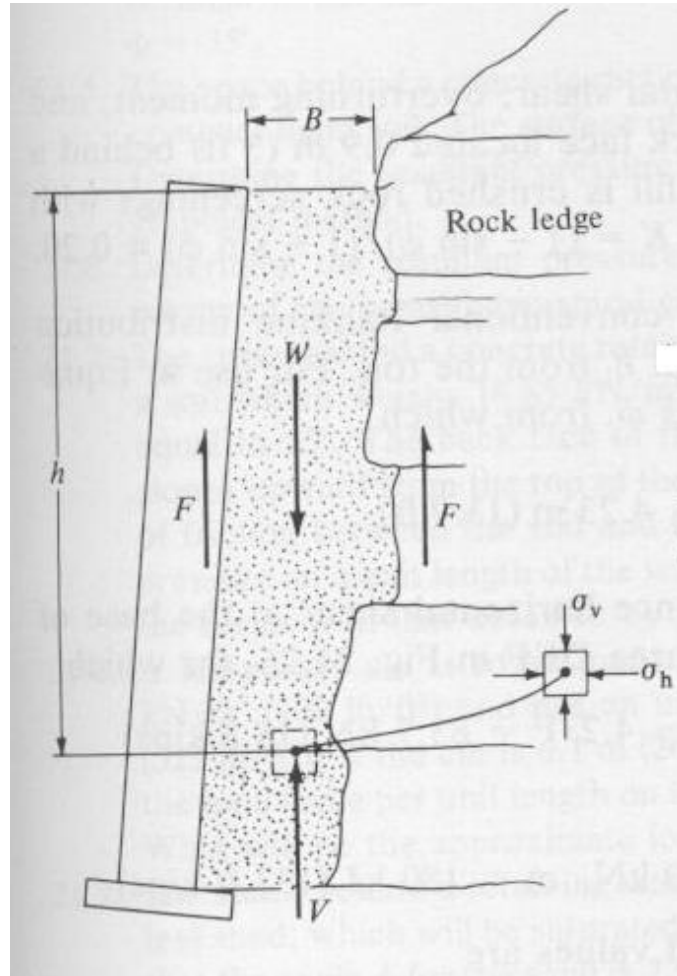


Fig. 2.8. Fascia retaining wall of backfill width B and wall friction F
(after Spangler and Handy, 1984)

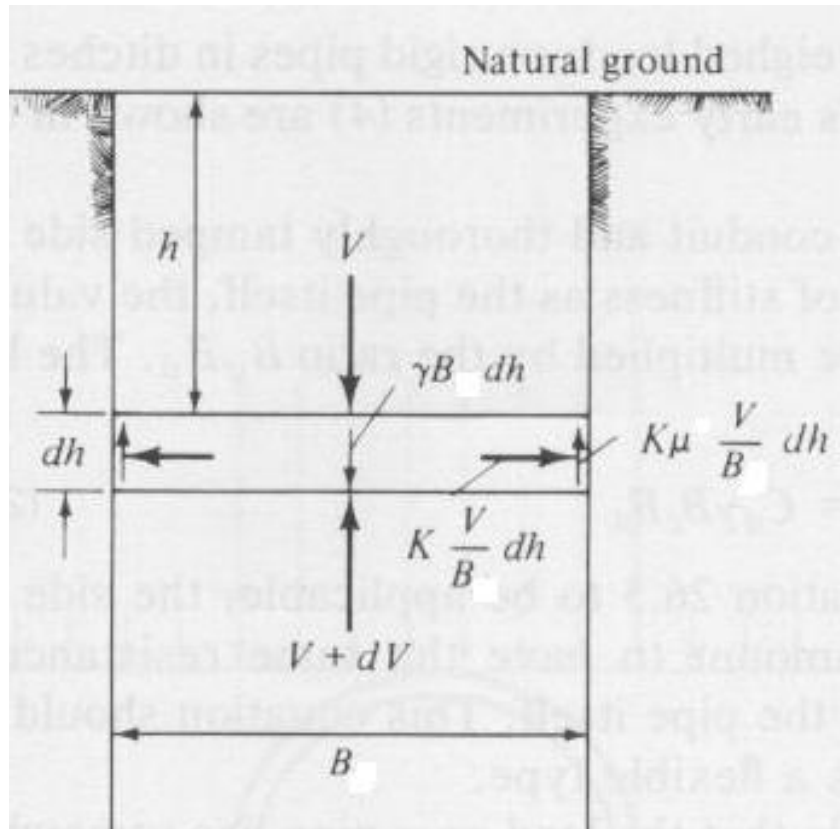


Fig. 2.9. Horizontal element of backfill material
(after Spangler and Handy, 1984)

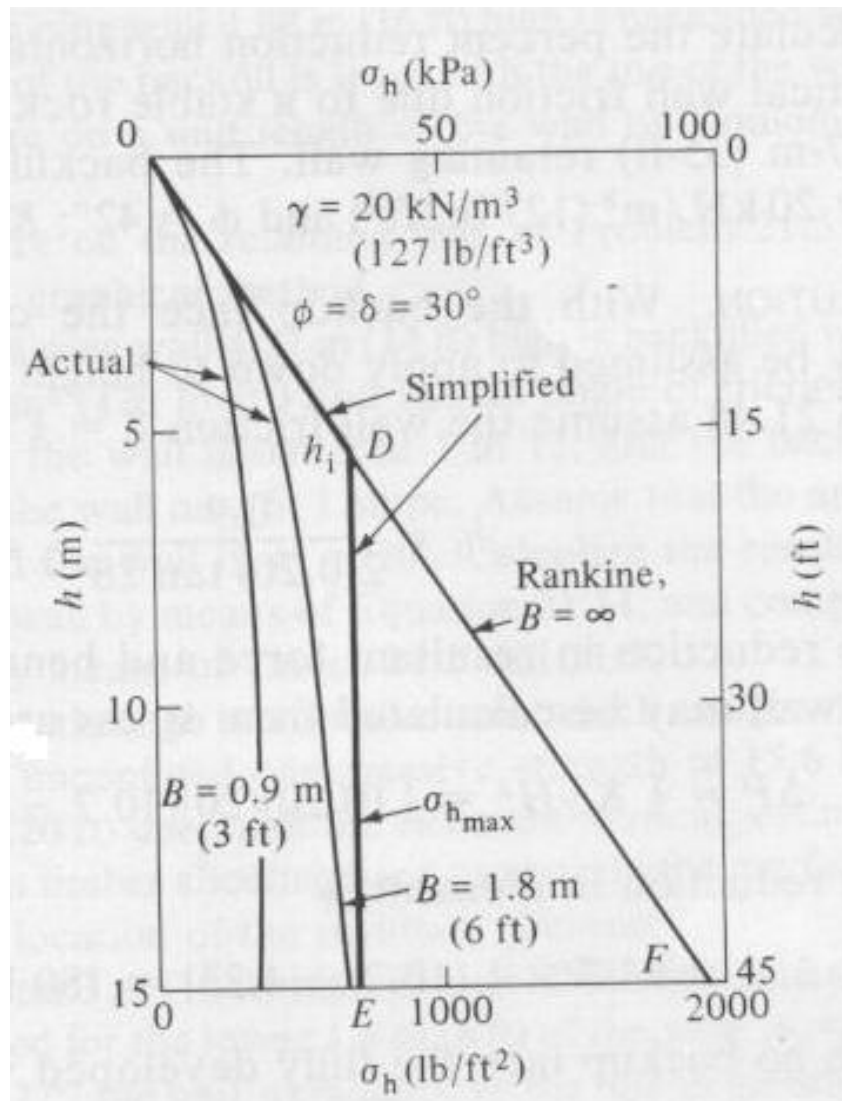


Fig. 2.10. Distribution of soil pressure against fascia walls due to partial support from wall friction F (after Spangler and Handy, 1984)

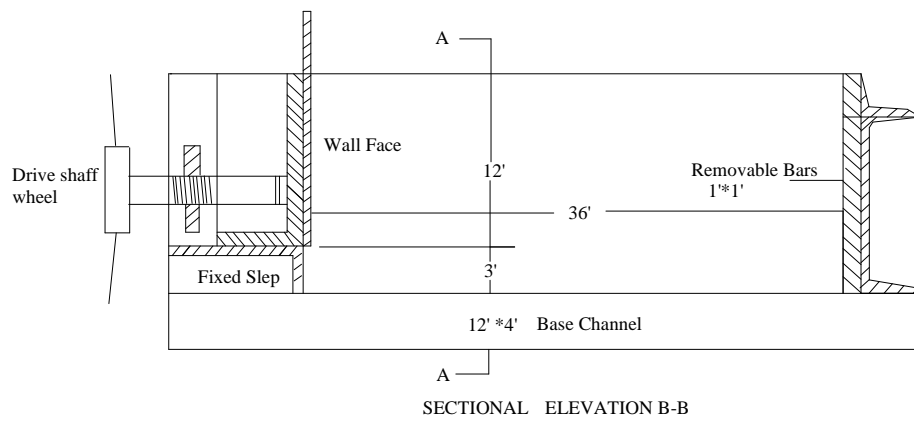
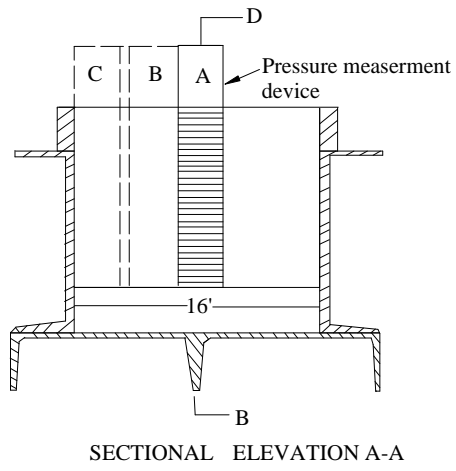


Fig. 2.11. University of Manchester model retaining wall
(after Mackey and Kirk, 1967)

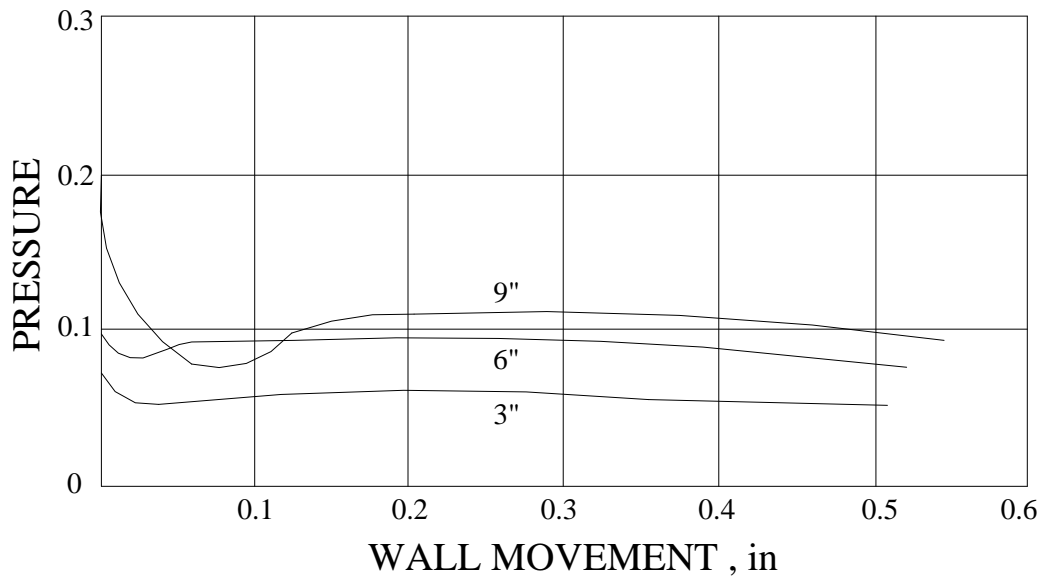
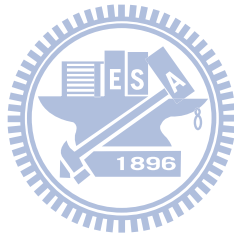
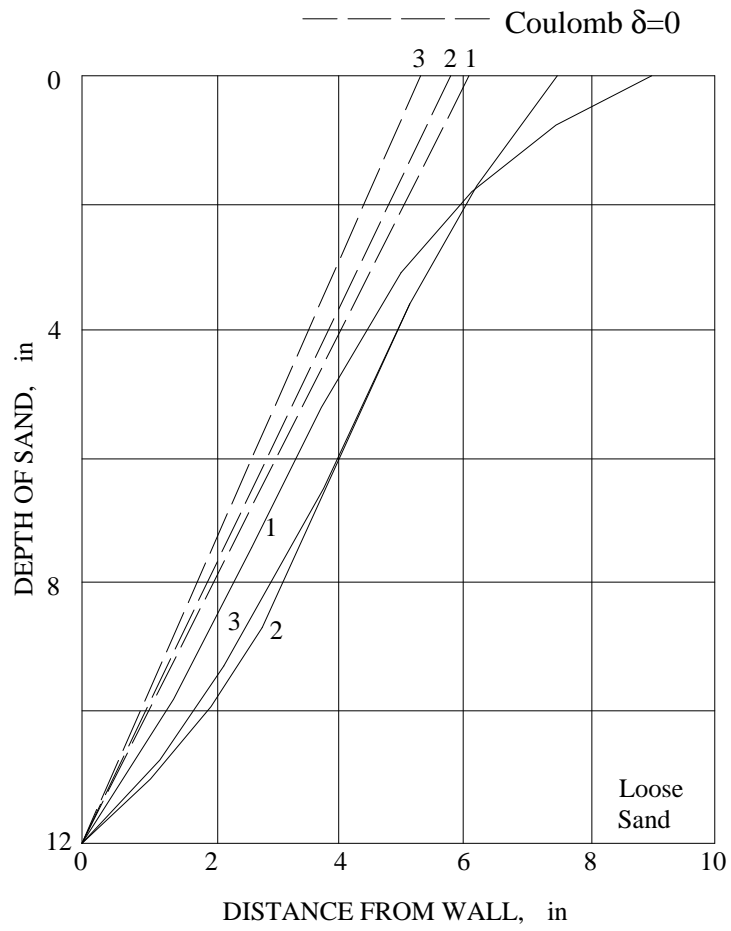


Fig. 2.12. Earth pressure with wall movement (after Mackey and Kirk, 1967)





- Sand 1: A uniformly graded fine sand
- Sand 2: A medium graded sand
- Sand 3: A uniformly graded coarse sand

Fig. 2.13. Failure surfaces (after Mackey and Kirk, 1967)

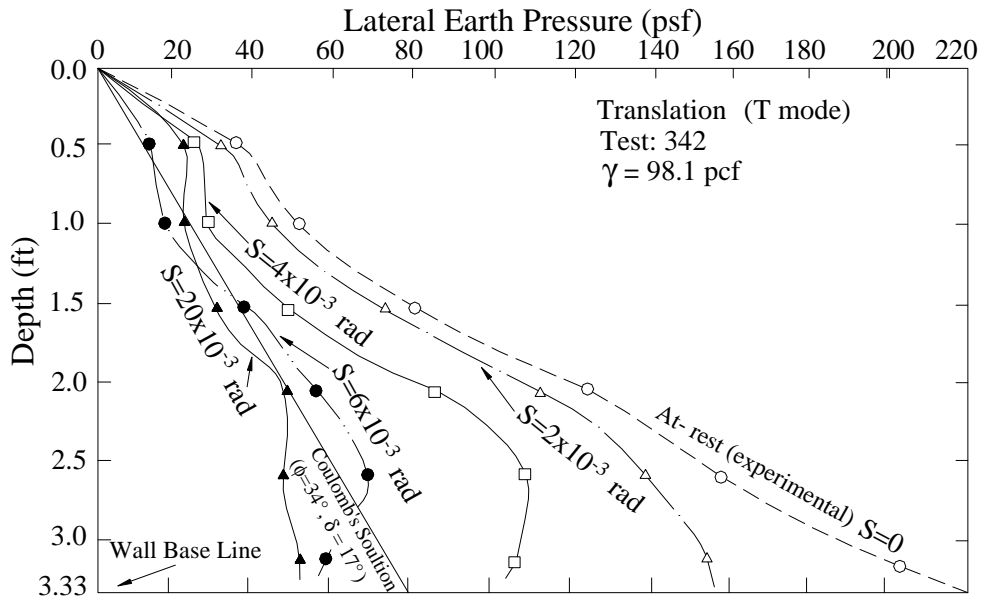
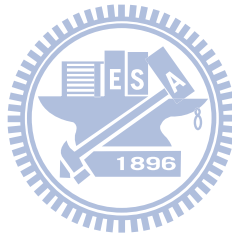


Fig. 2.14. Distributions of horizontal earth pressure at different wall displacement (after Fang and Ishibashi, 1986)



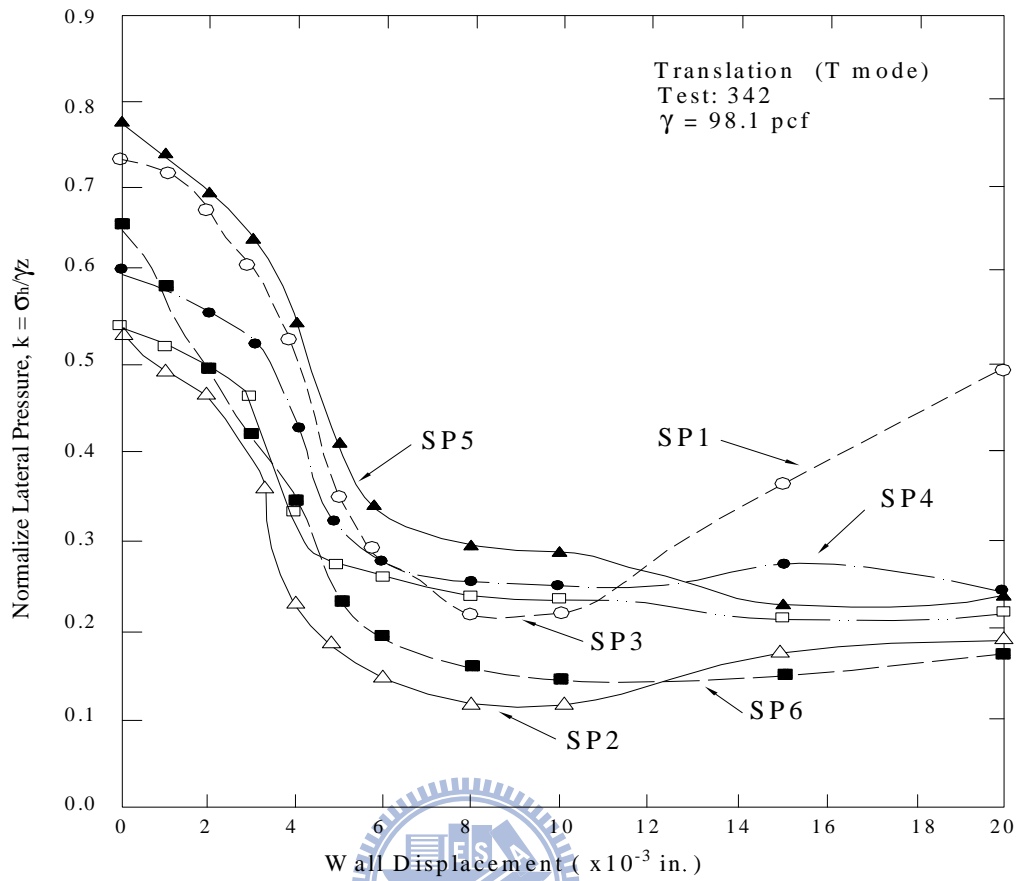


Fig. 2.15. Change of normalized lateral pressure with translation wall displacement (after Fang and Ishibashi, 1986)

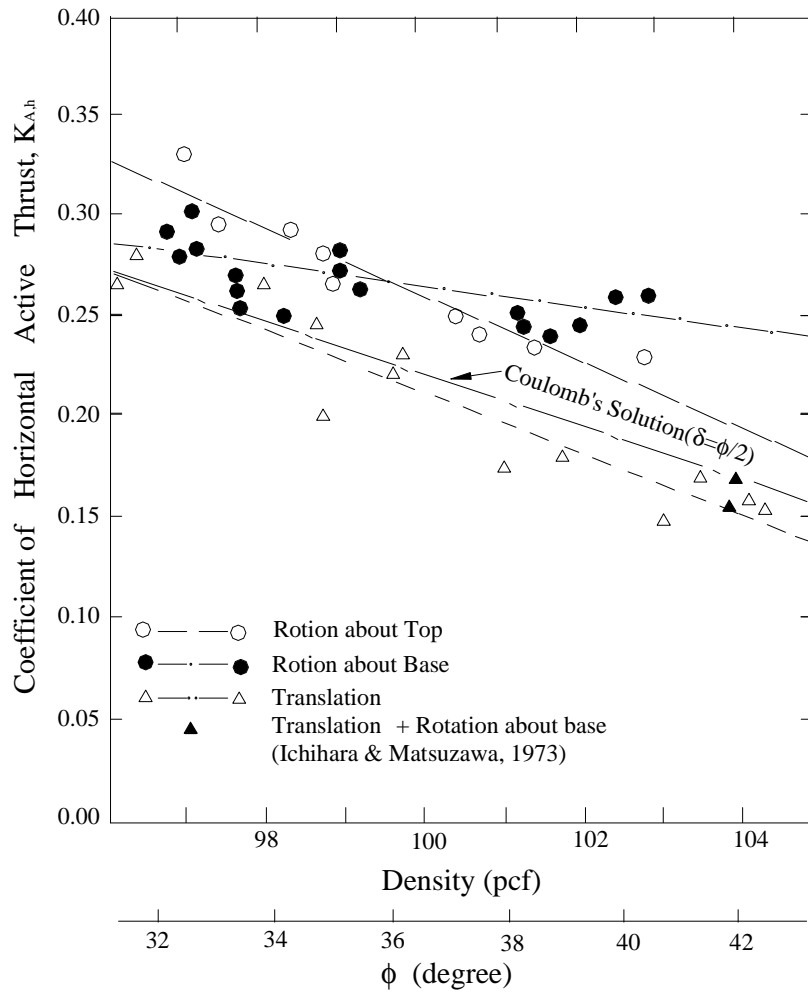


Fig. 2.16. Coefficient of horizontal active thrust as a function of soil density (after Fang and Ishibashi, 1986)

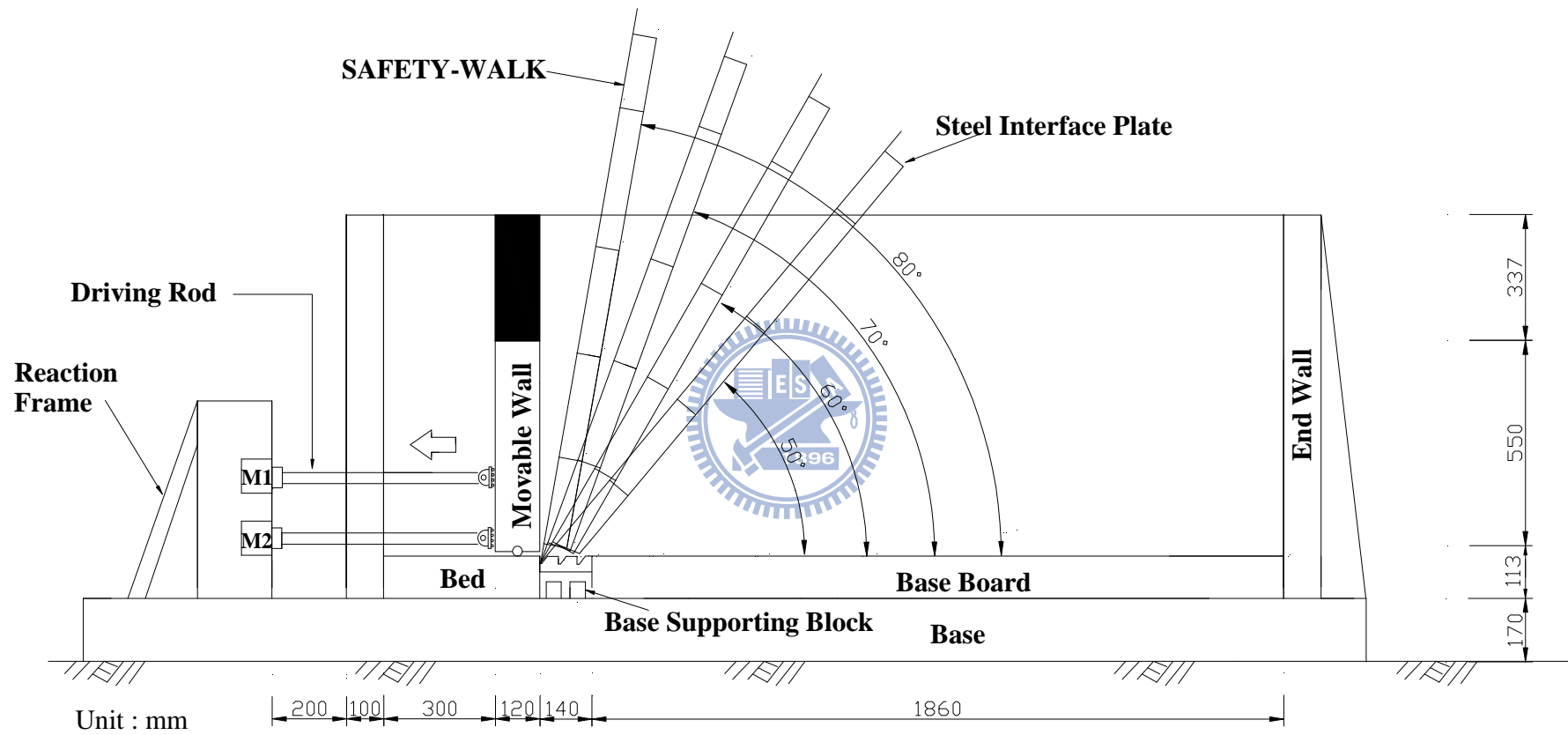


Fig. 2.17. Different interface inclinations for $b = 0$ (after Huang, 2009)

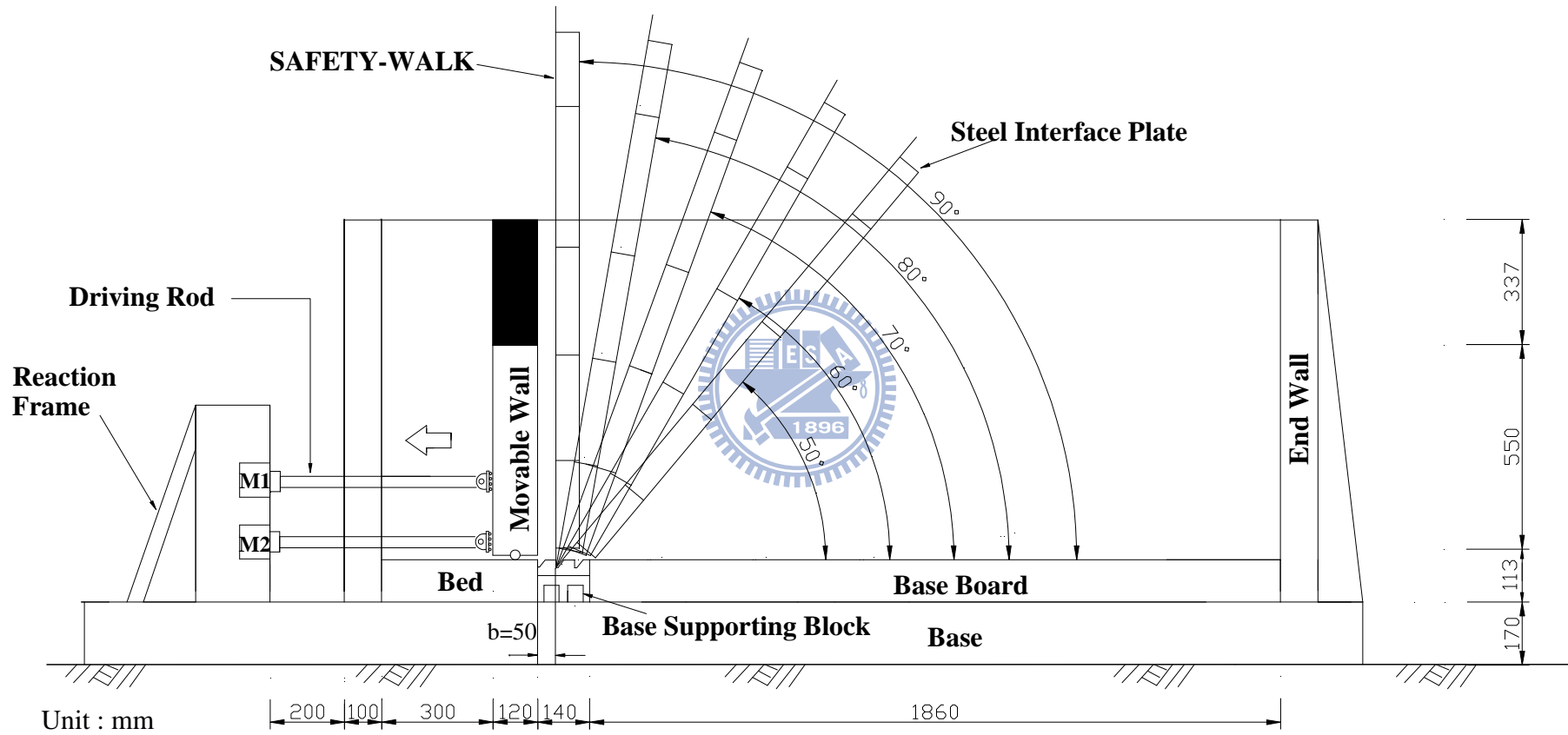


Fig. 2.18. Different interface inclinations for $b = 50$ mm (after Huang, 2009)

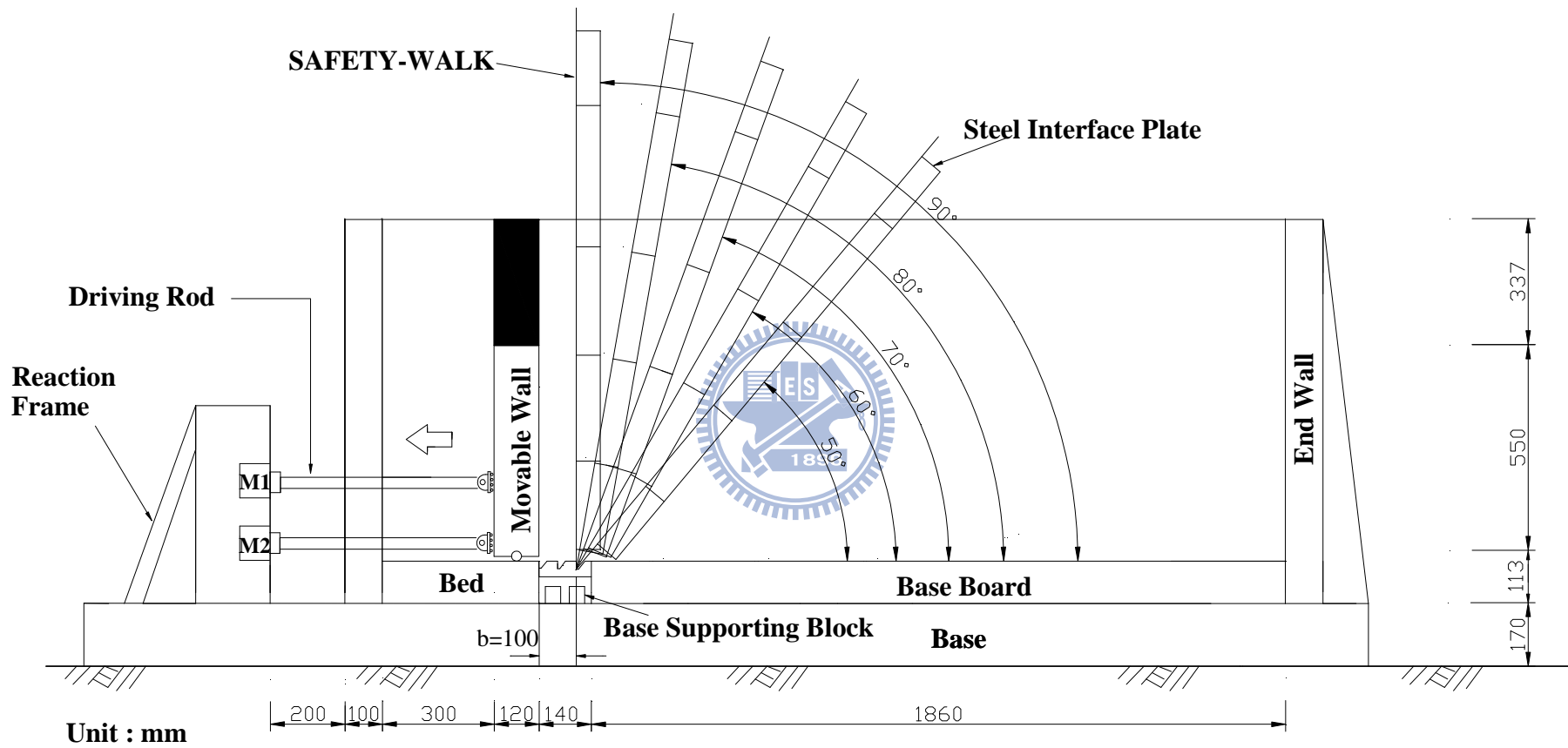


Fig. 2.19. Different interface inclinations for $b = 100$ mm (after Huang, 2009)

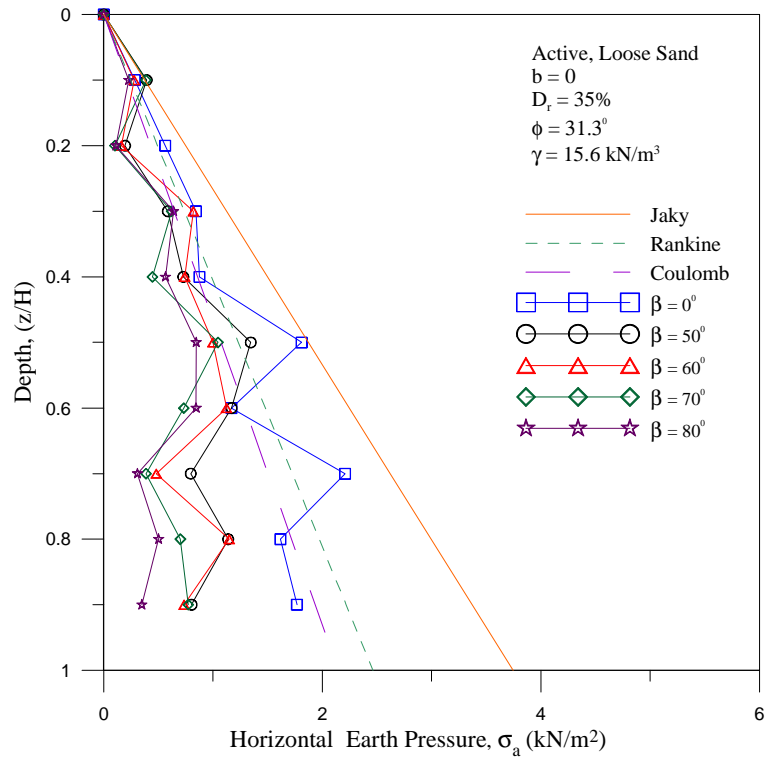


Fig. 2.20. Distribution of active earth pressure at different β angles

for $b = 0$

(after Huang, 2009)

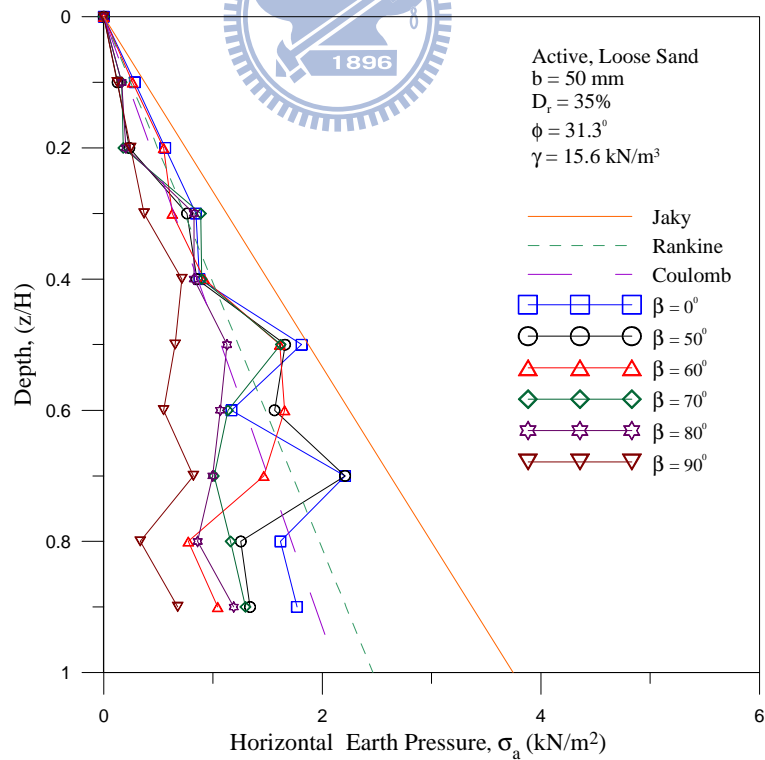


Fig. 2.21. Distribution of active earth pressure at different β angles
 for $b = 50 \text{ mm}$ (after Huang, 2009)

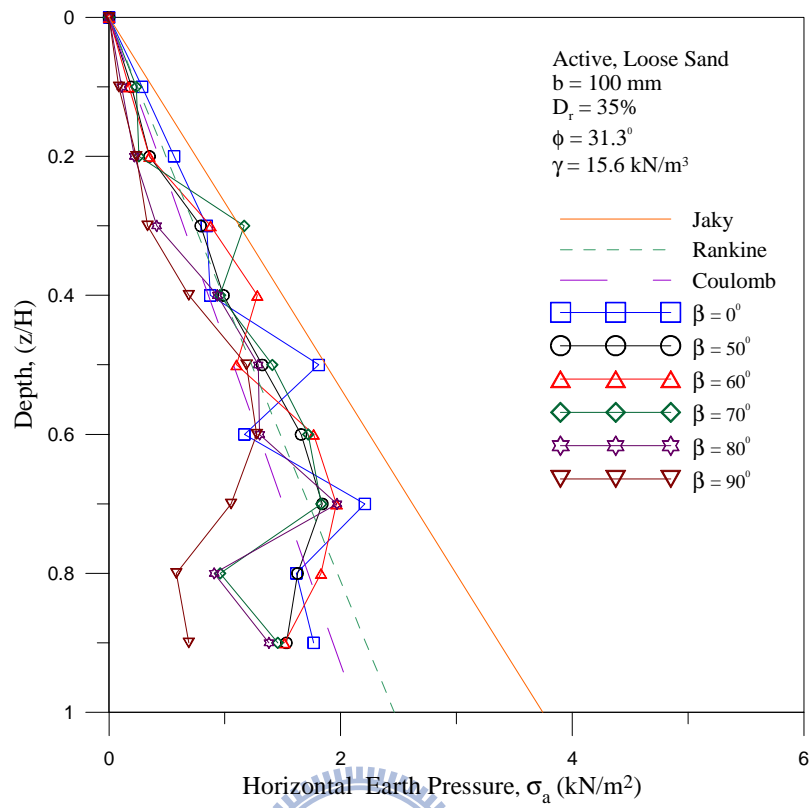


Fig. 2.22. Distribution of active earth pressure at different β angles for $b = 100 \text{ mm}$ (after Huang, 2009)

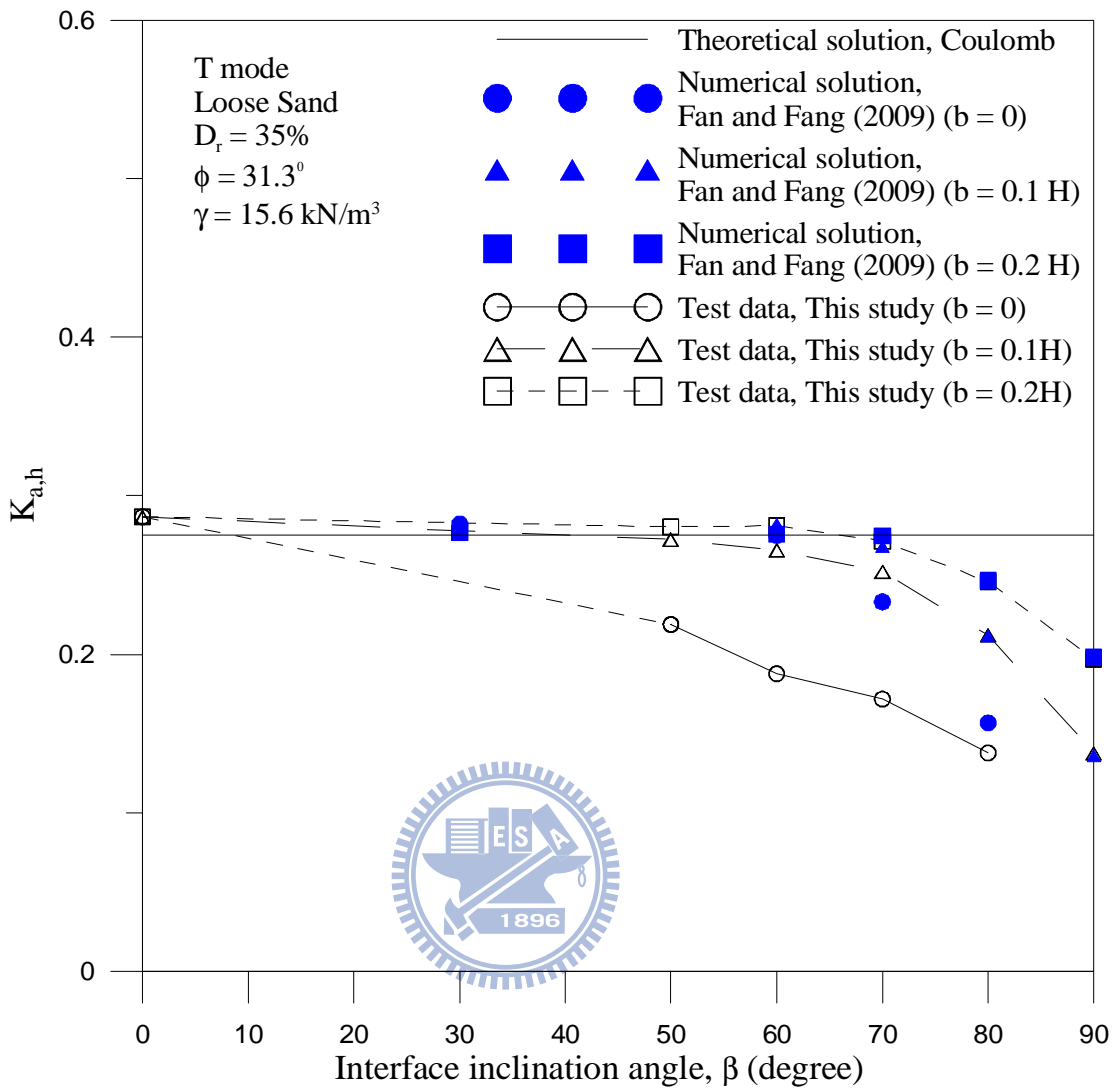


Fig. 2.23. Active earth pressure coefficient $K_{a,h}$ versus interface inclination angle β (after Huang, 2009)

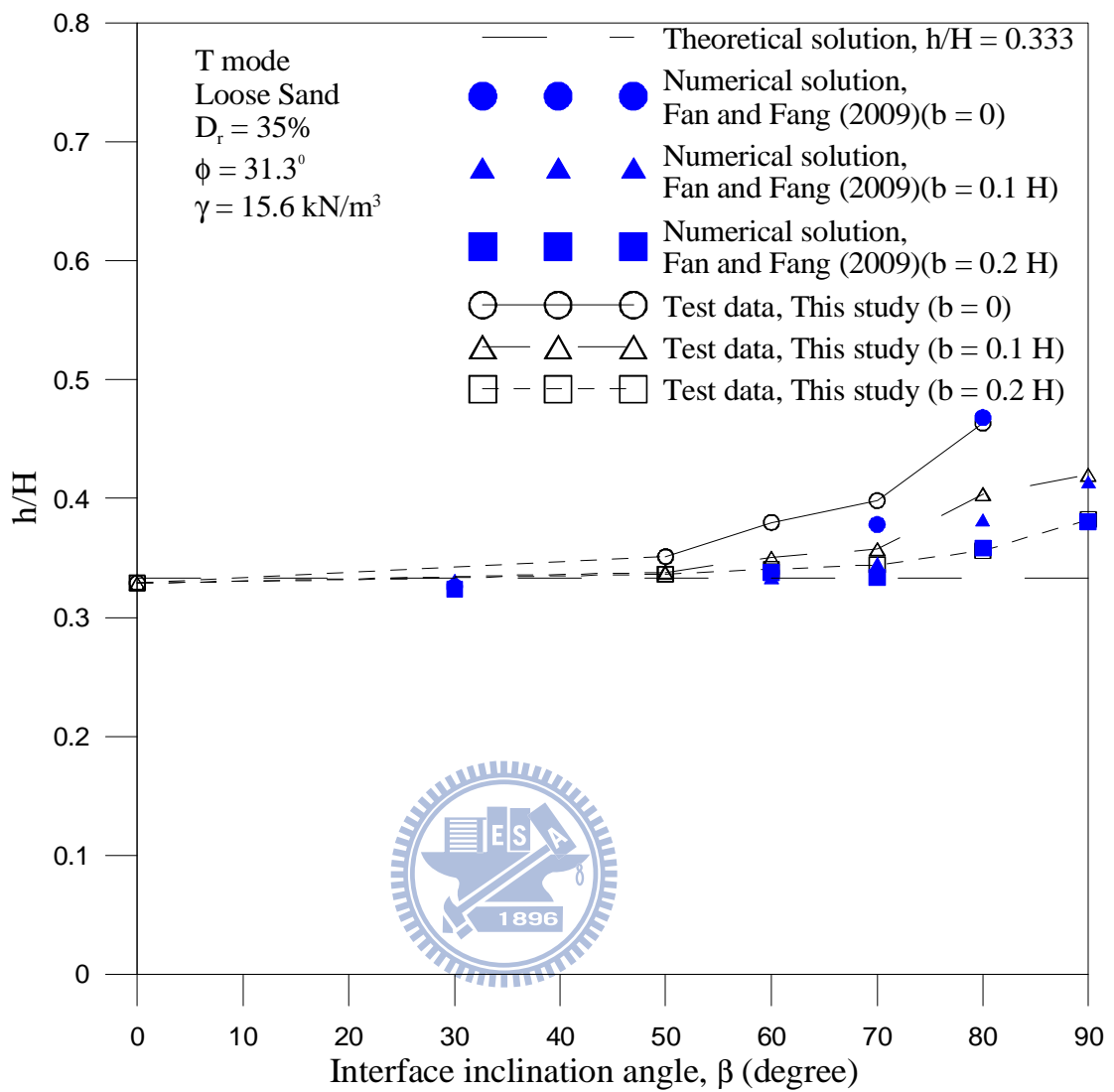


Fig. 2.24. Point of application of active soil thrust versus interface inclination angle β (after Huang, 2009)

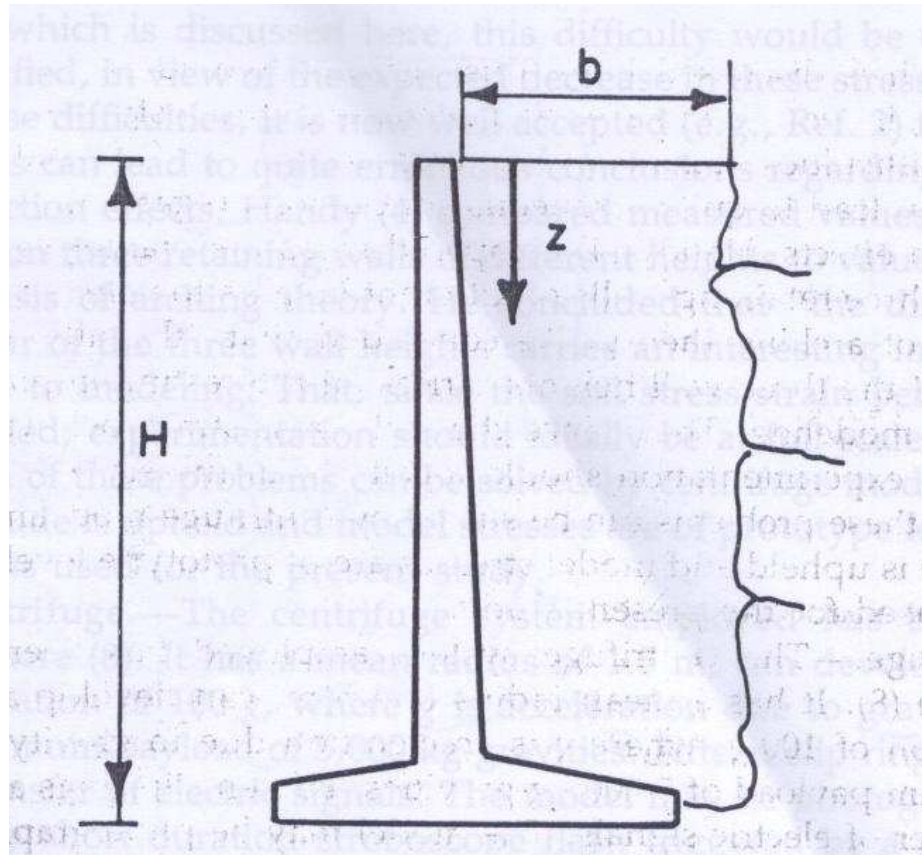


Fig. 2.25 Schematic representation of retaining wall near rock face
(after Frydman and Keissar, 1987)

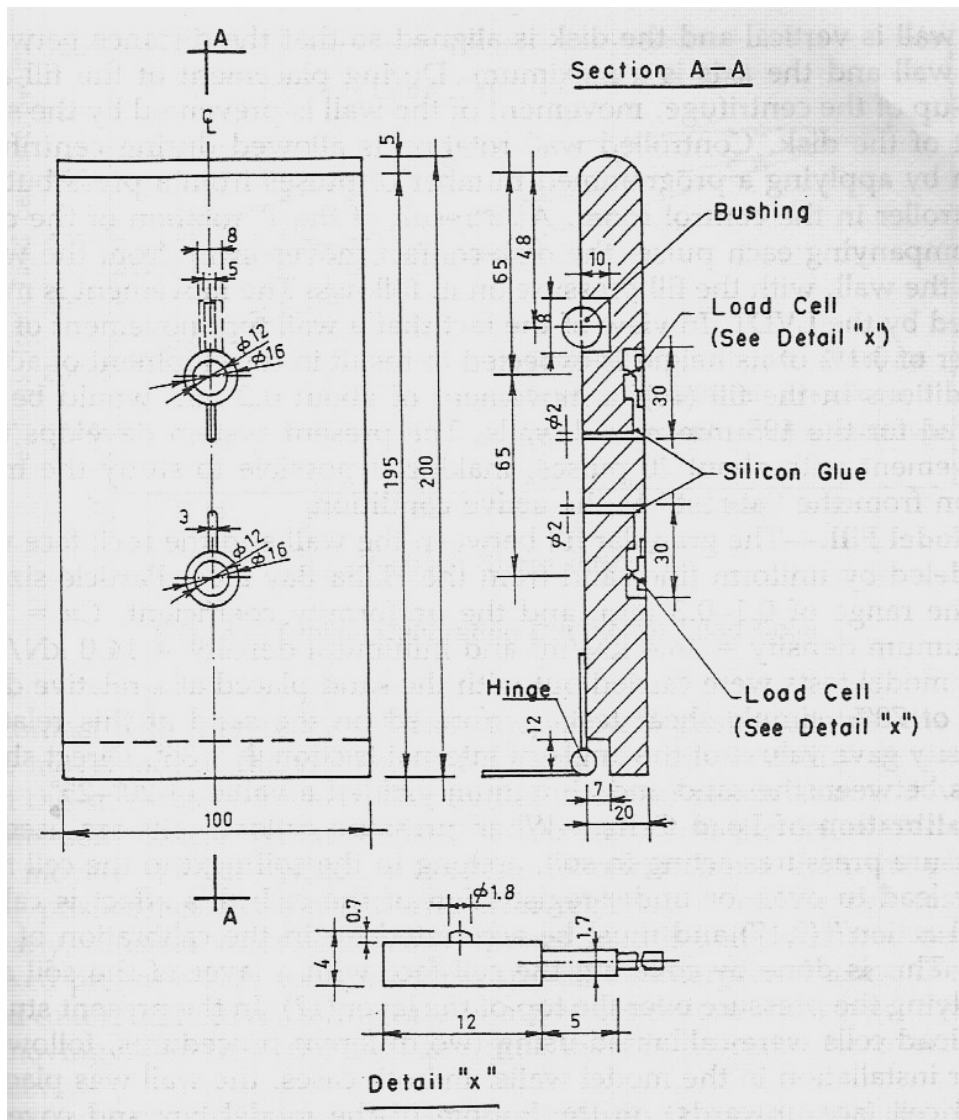


Fig. 2.26. Model retaining wall (after Frydman and Keissar, 1987)

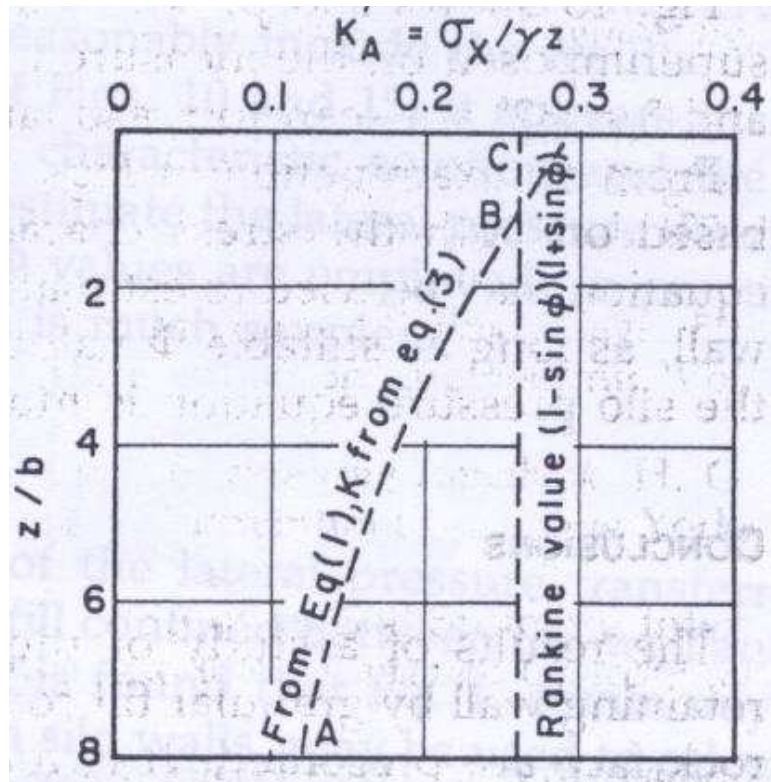
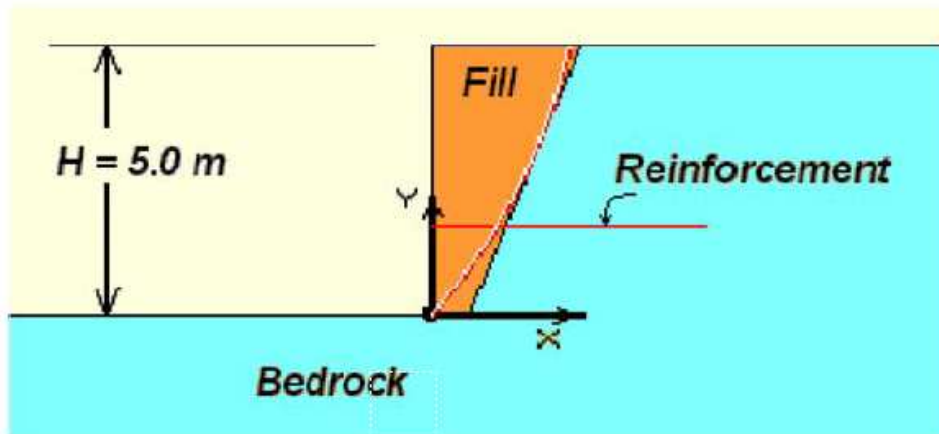
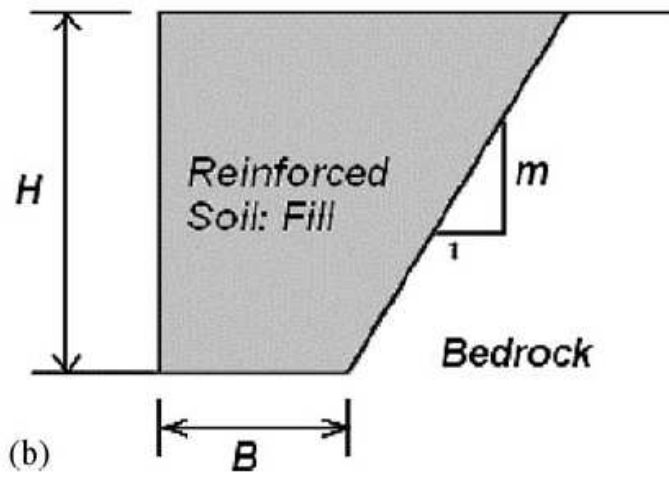


Fig. 2.27. Distribution of K'_a with z/b from silo pressure equation (after Frydman and Keissar, 1987)



(a)



(b)

Fig. 2.28. Typical geometry: (a) analyzed (b) notation
(after Leshchinsky, et al. 2004)

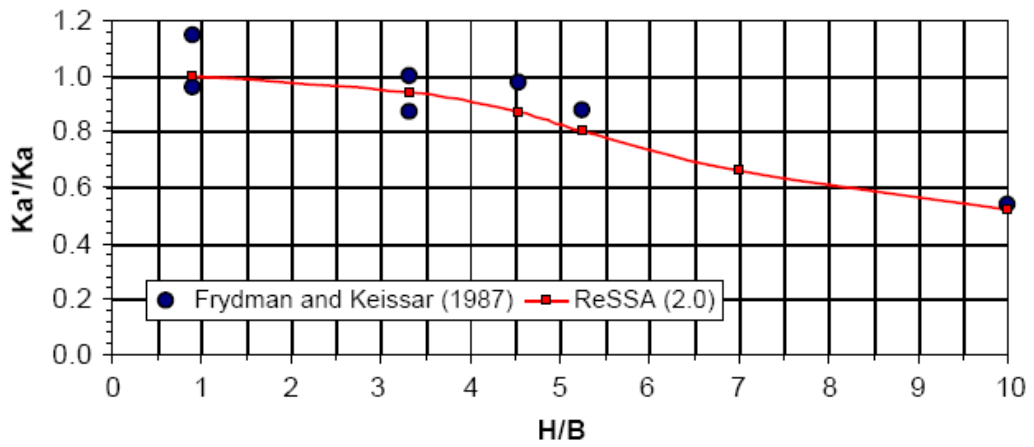


Fig. 2.29. Predictions by ReSSA versus centrifugal test results for $\phi = 36^\circ$ and $m = \infty$ (after Leshchinsky, et al. 2004)

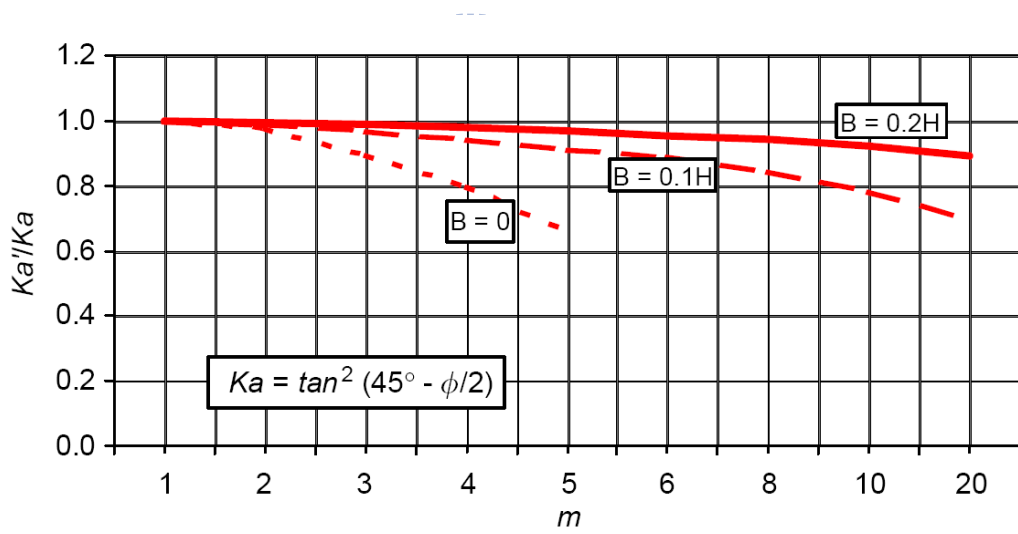
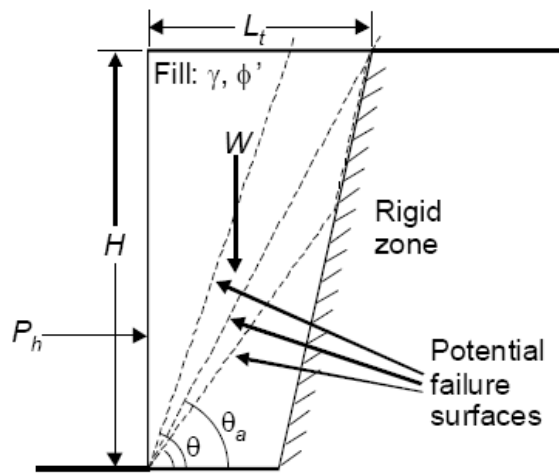
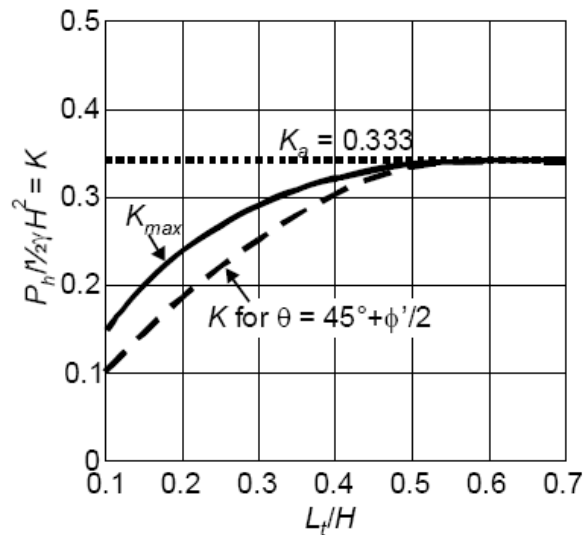


Fig. 2.30. Analysis results (after Leshchinsky, et al. 2004)



a) Forces acting on wall facing, with potential failure surfaces



b) Horizontal force coefficients K for $\phi' = 30^\circ$

Fig. 2.31. Forces acting on wall face, wedge angles, and horizontal force coefficients for fill $\phi' = 30^\circ$ (after Lawson and Yee, 2005)

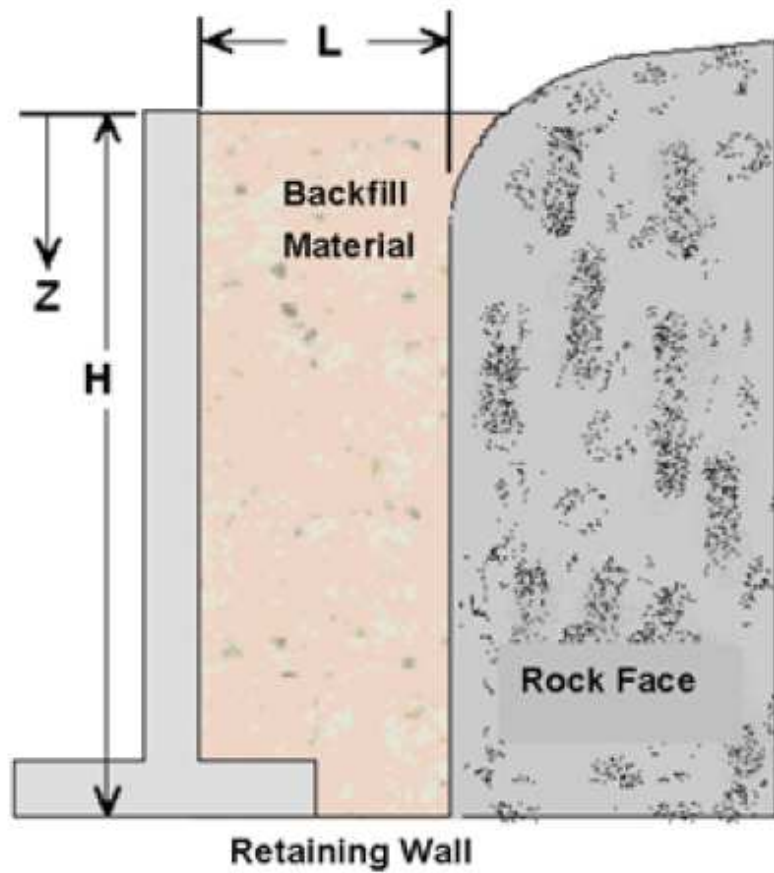
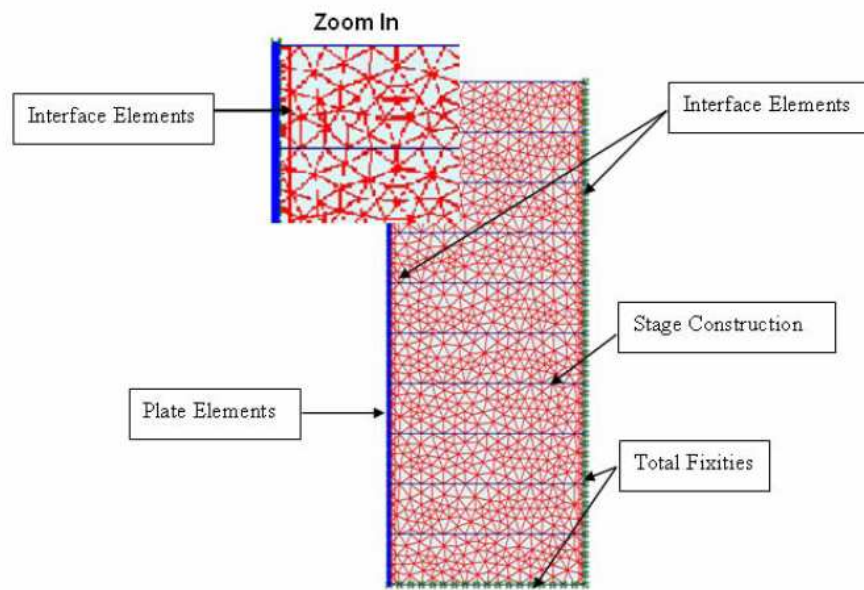
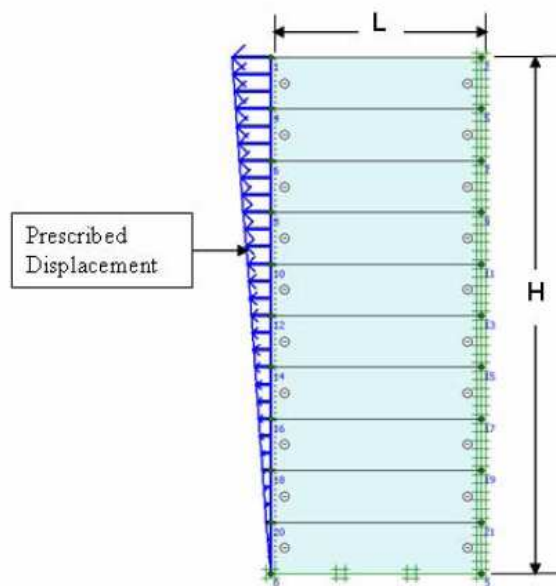


Fig. 2.32. Illustration of the simulated case (after Yang and Liu, 2007)

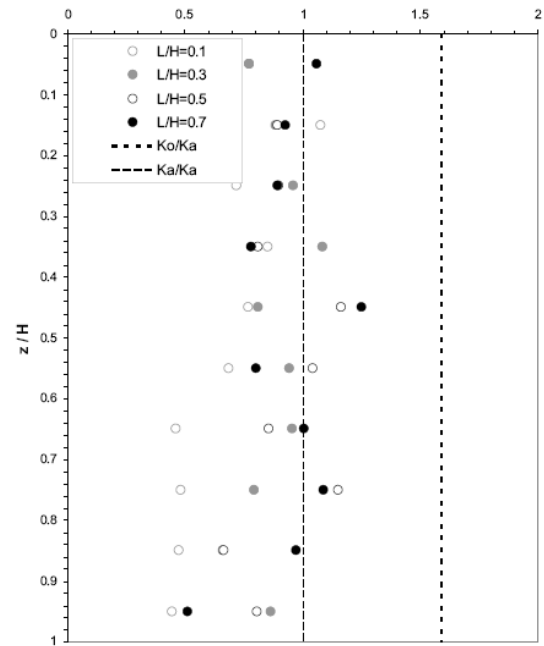
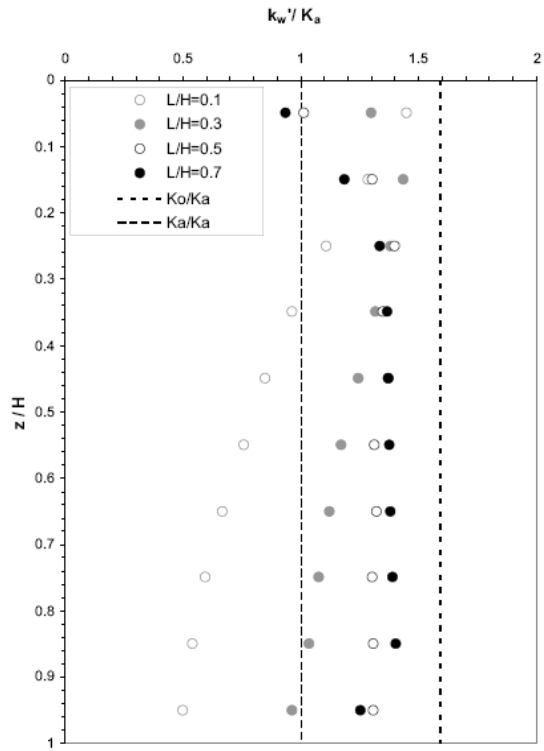


(a)



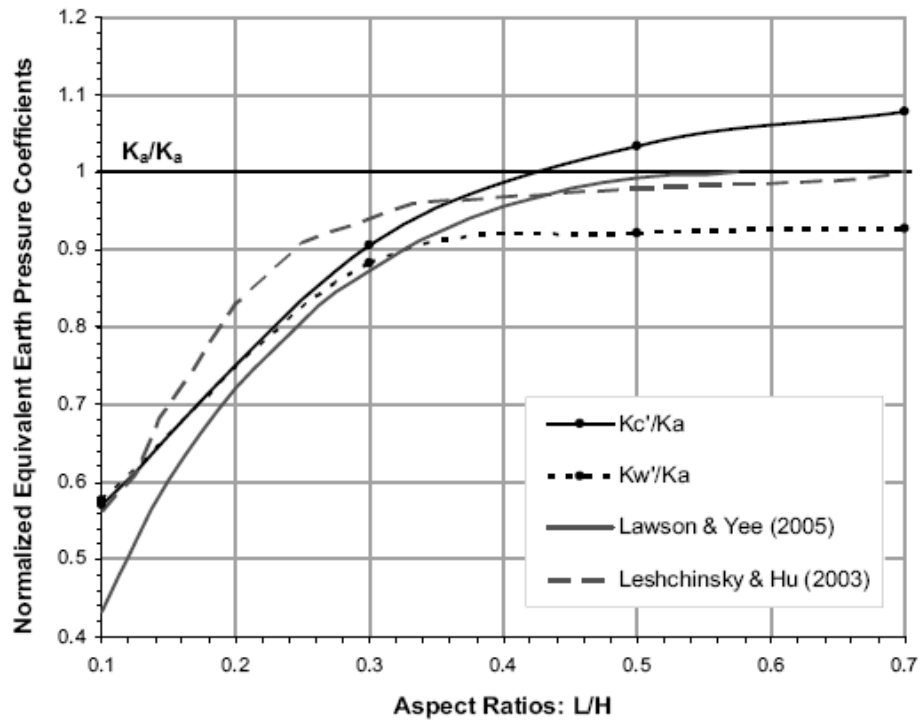
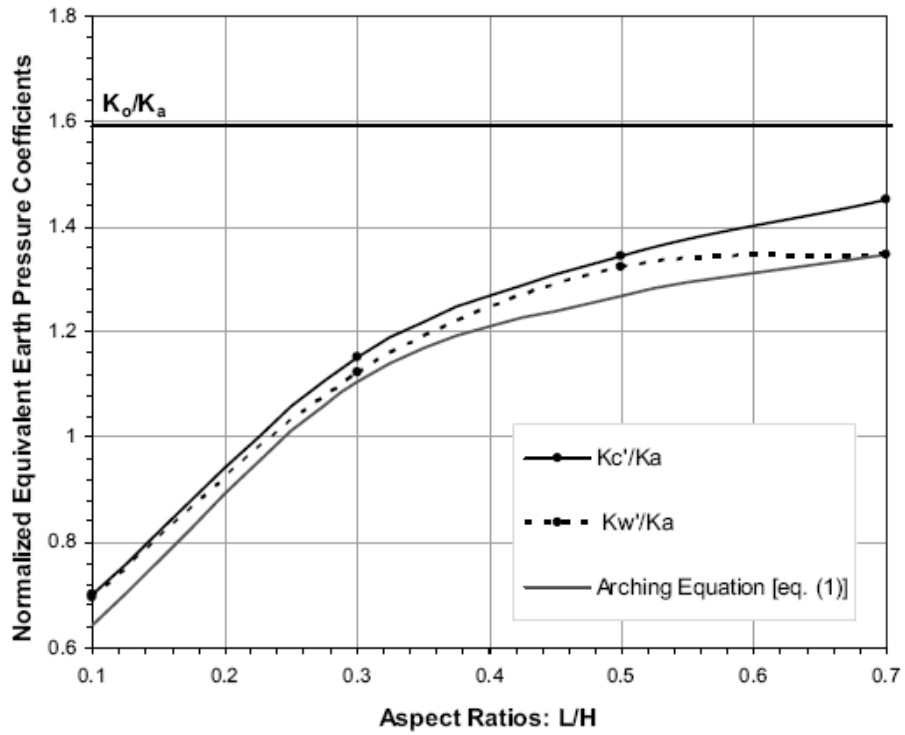
(b)

Fig. 2.33. Finite element (a) meshes for at-rest case and (b) model for active case (after Yang and Liu, 2007)



(b)

Fig. 2.34. Normalized earth pressure coefficient profiles along the wall face for (a) at-rest and (b) active case (after Yang and Liu, 2007)



(b)

Fig. 2.35. Normalized equivalent earth pressure coefficients for (a) at-rest and (b) active case (after Yang and Liu, 2007)

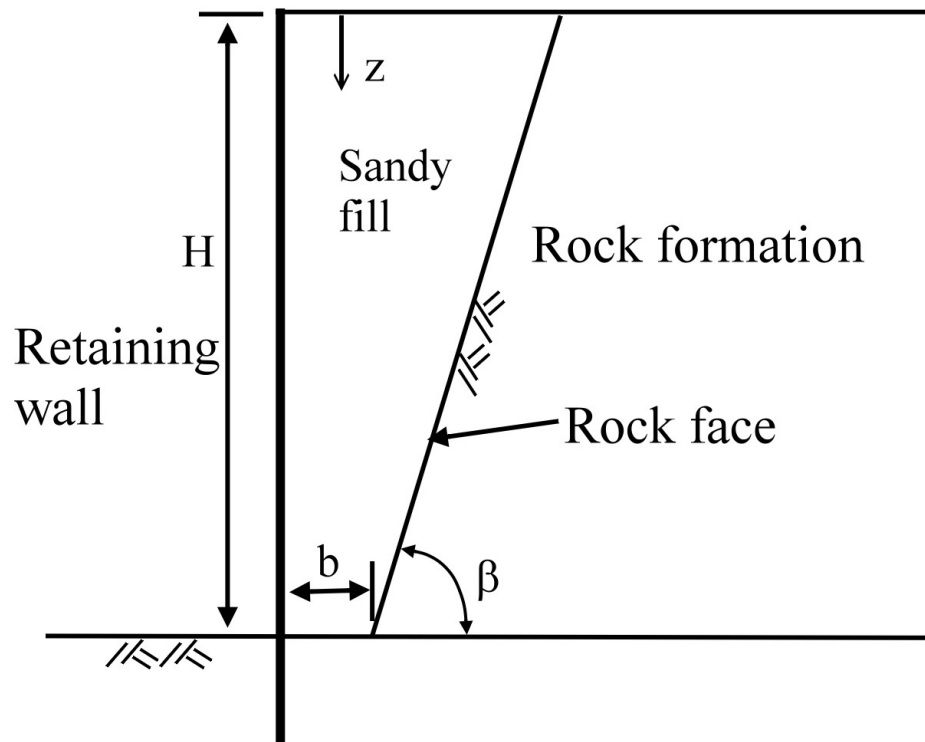


Fig. 2.36. Typical geometry of backfill zone behind a retaining wall used in this study (after Fan and Fang, 2009)

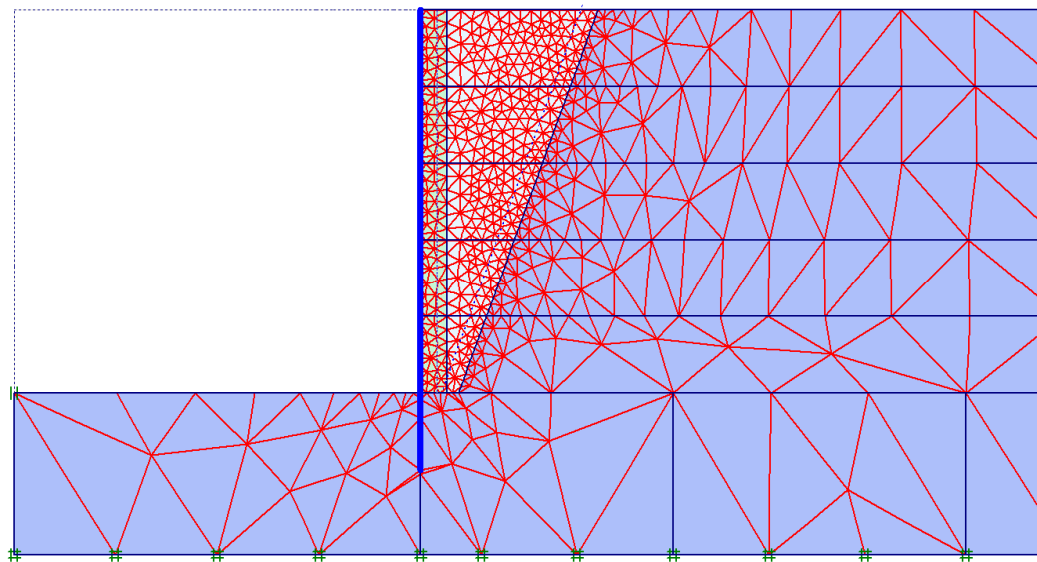


Fig. 2.37. The finite element mesh for a retaining wall with limited backfill space ($\beta=70^\circ$ and $b=0.5\text{m}$) (after Fan and Fang, 2009)

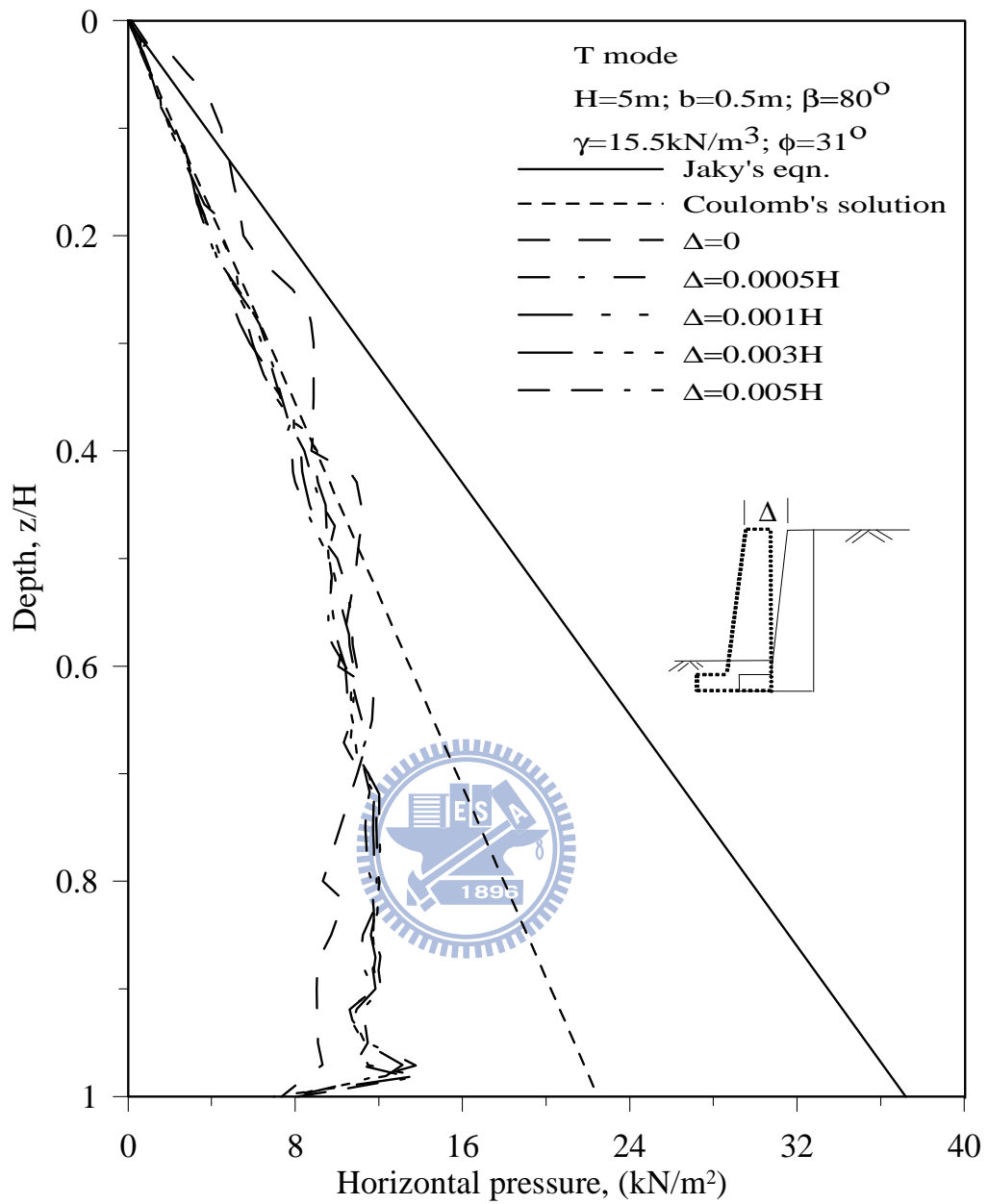


Fig. 2.38. Distribution of earth pressures with the depth at various wall displacements for walls in translation (T mode) (after Fan and Fang, 2009)

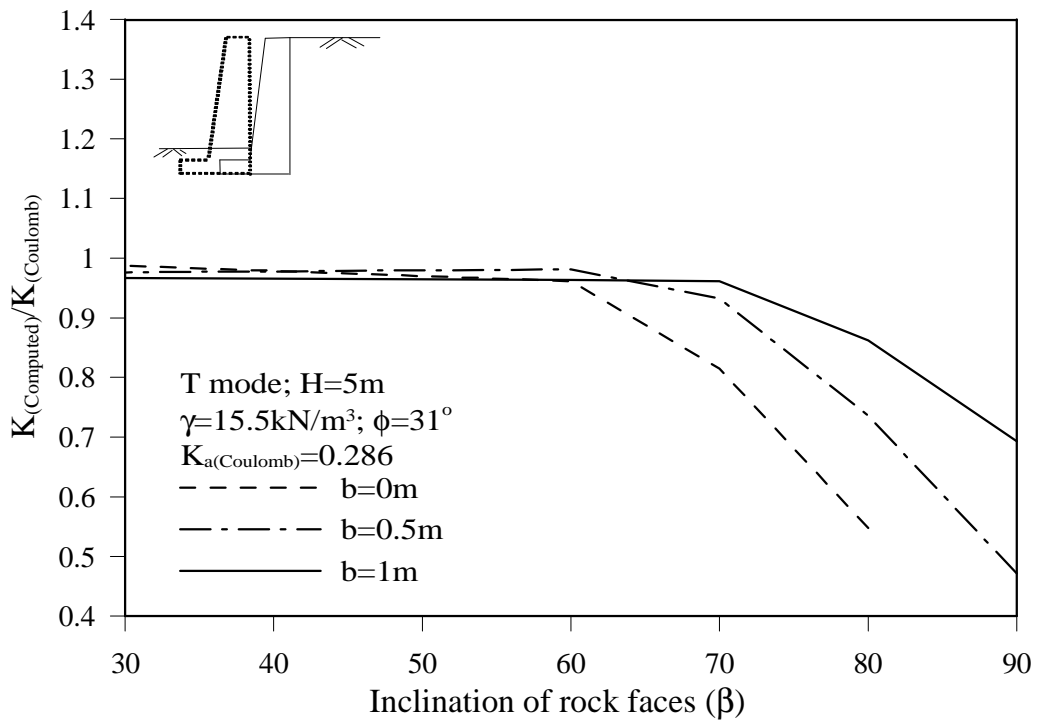


Fig. 2.39. Variation of the coefficient of active earth pressures ($K_{a(\text{Computed})}/K_{a(\text{Coulomb})}$) with the inclination of rock faces at various fill widths (b) for walls undergoing translation (after Fan and Fang, 2009)

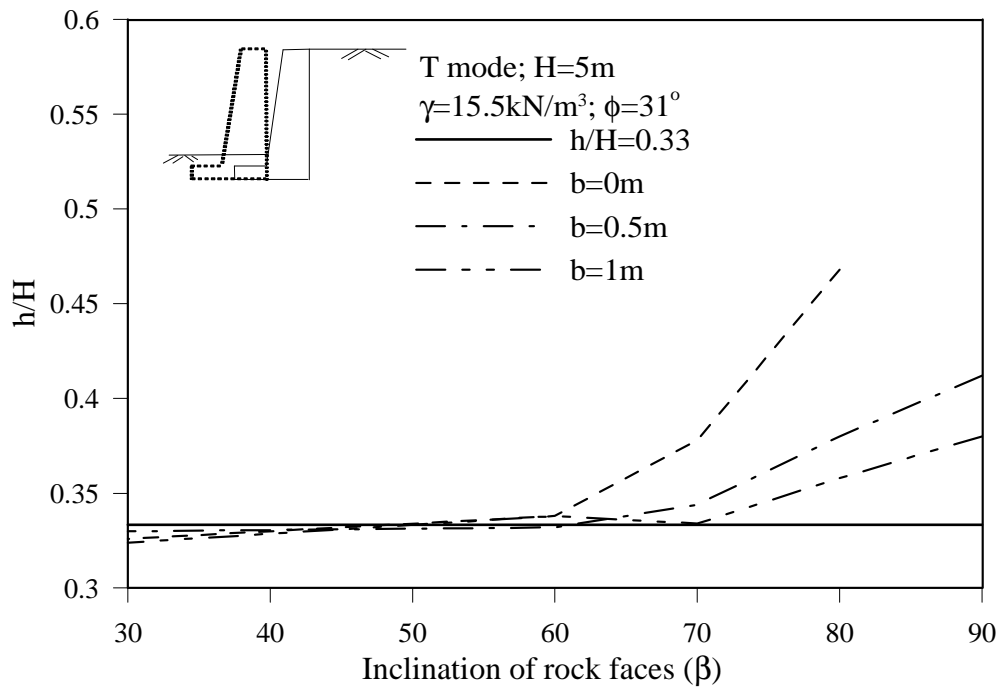


Fig. 2.40. Variation of the location of resultant (h/H) of active earth pressures with the inclination of rock faces at various fill widths (b) for walls undergoing translation (T mode). (after Fan and Fang, 2009)

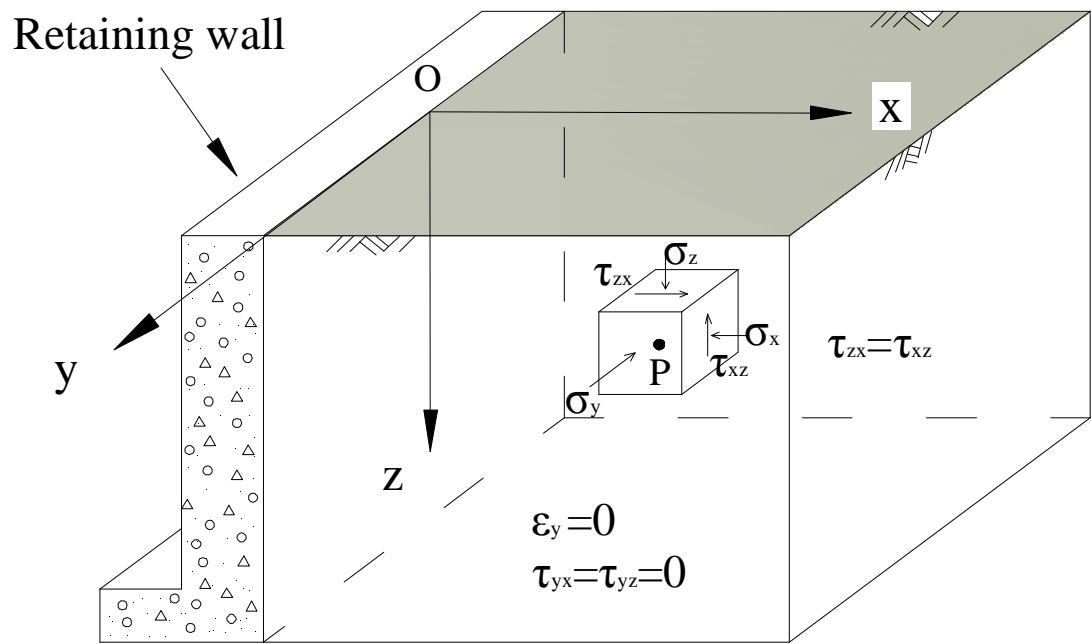
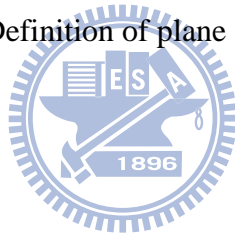
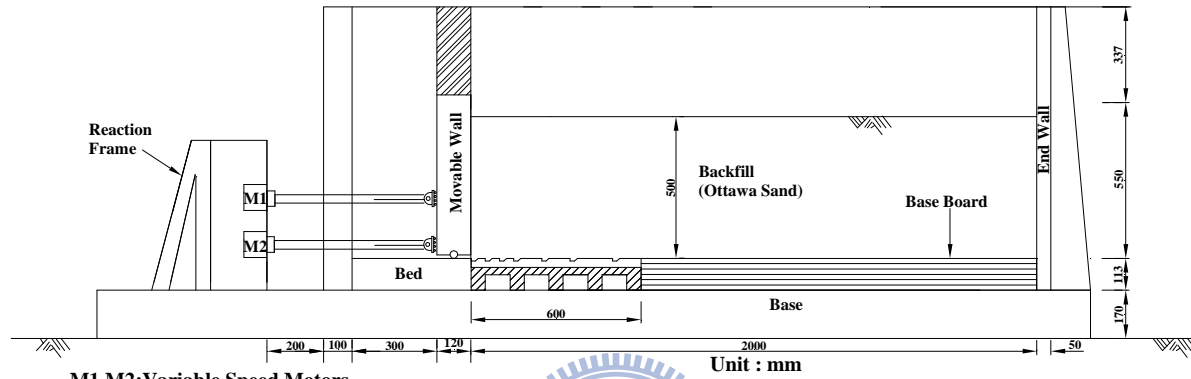
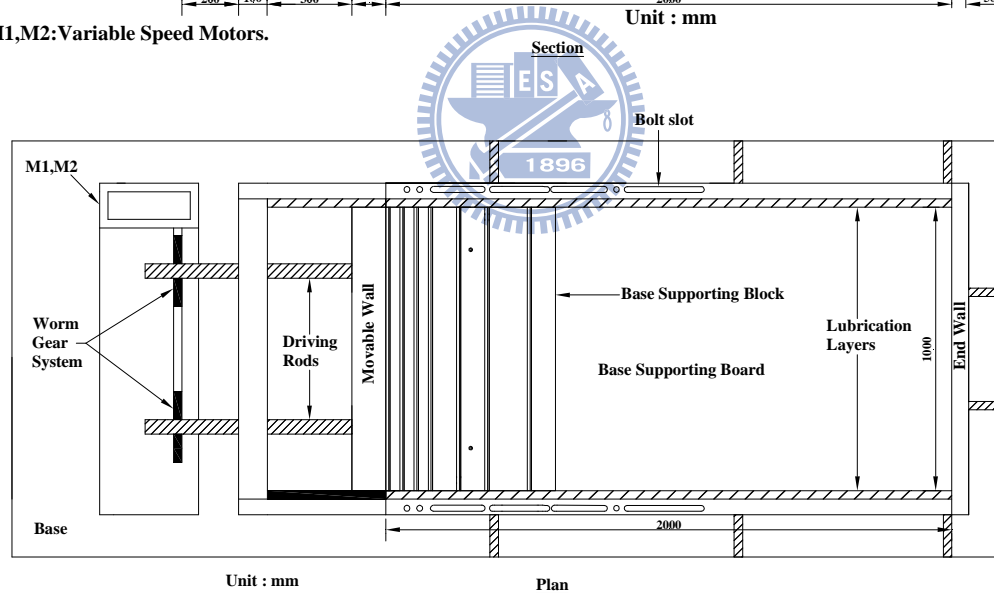


Fig. 2.41. Definition of plane strain state-of-stress





M1,M2: Variable Speed Motors.



Unit: mm

Fig.3.1. NCTU Model Retaining-Wall Facility

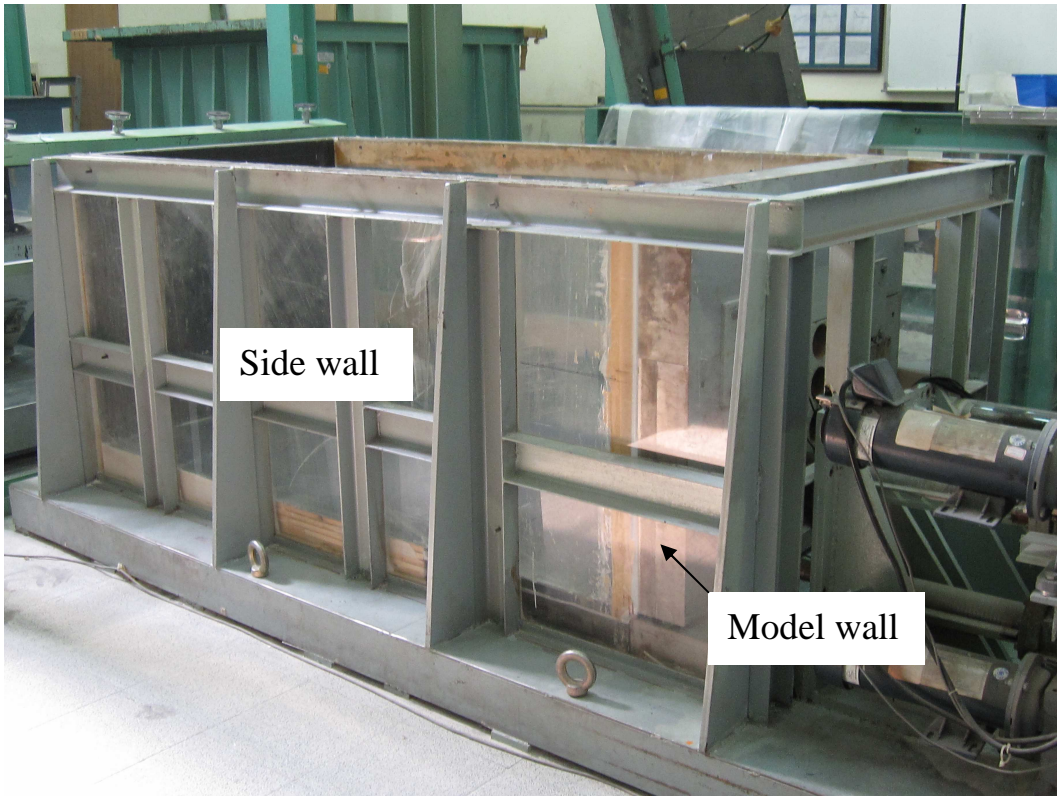


Fig.3.2. NCTU model retaining wall

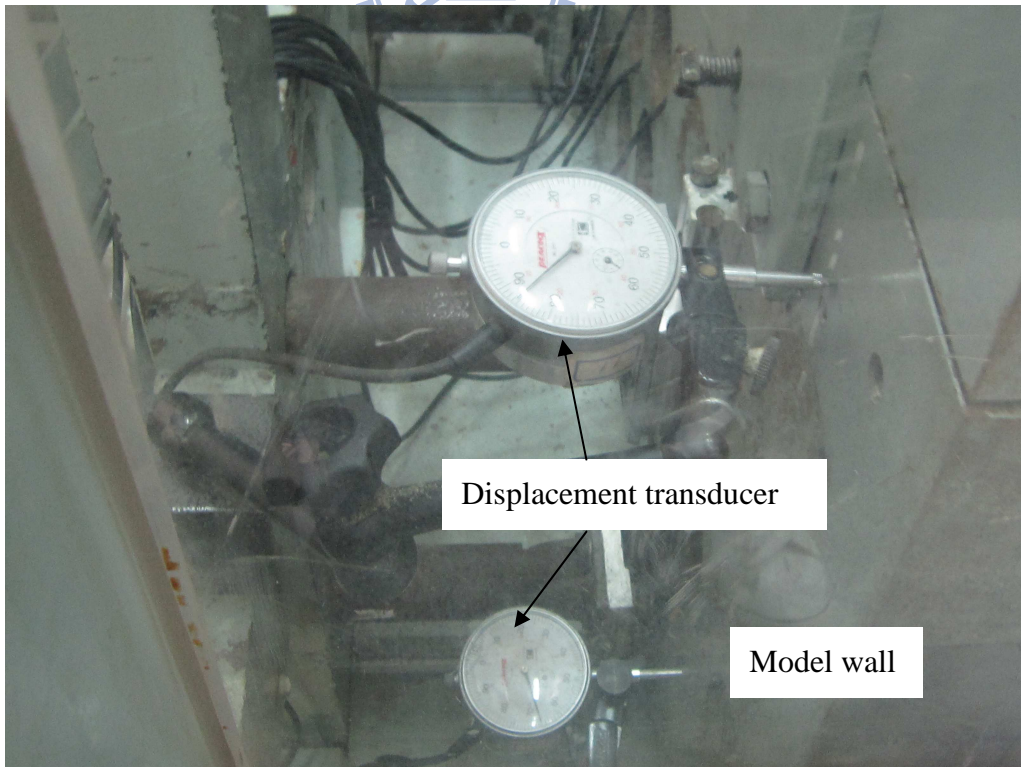
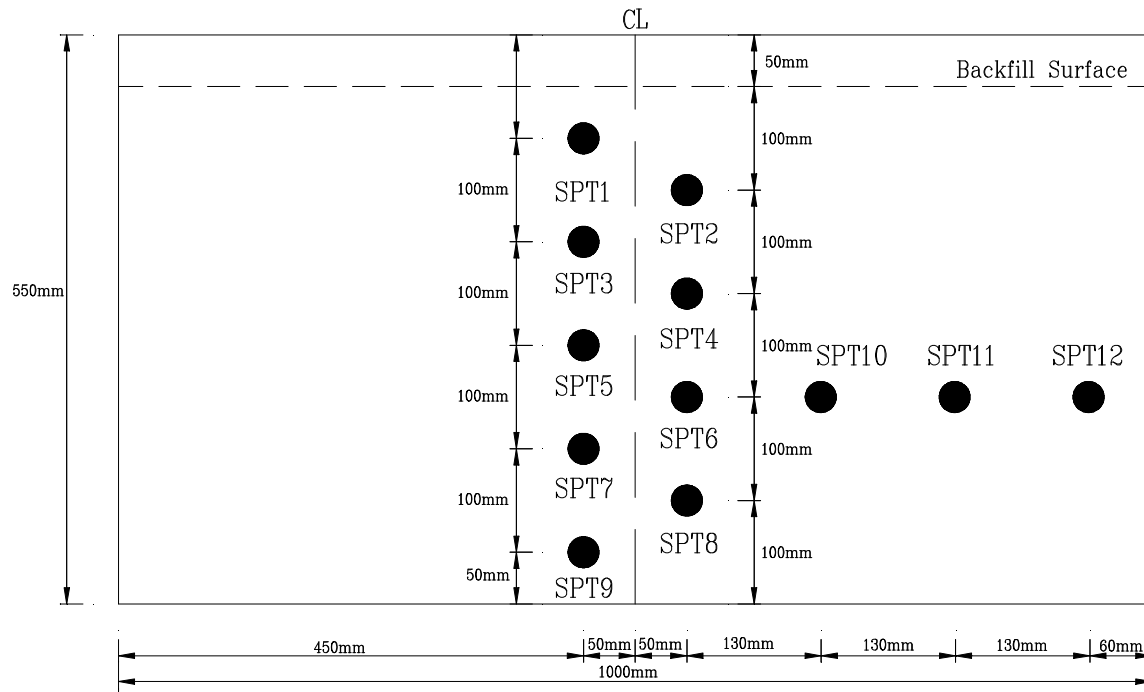


Fig.3.3. Displacement transducer (Kyowa DT-20D)



Front-view

Unit : mm

Fig. 3.4. Locations of pressure transducers on NCTU model wall

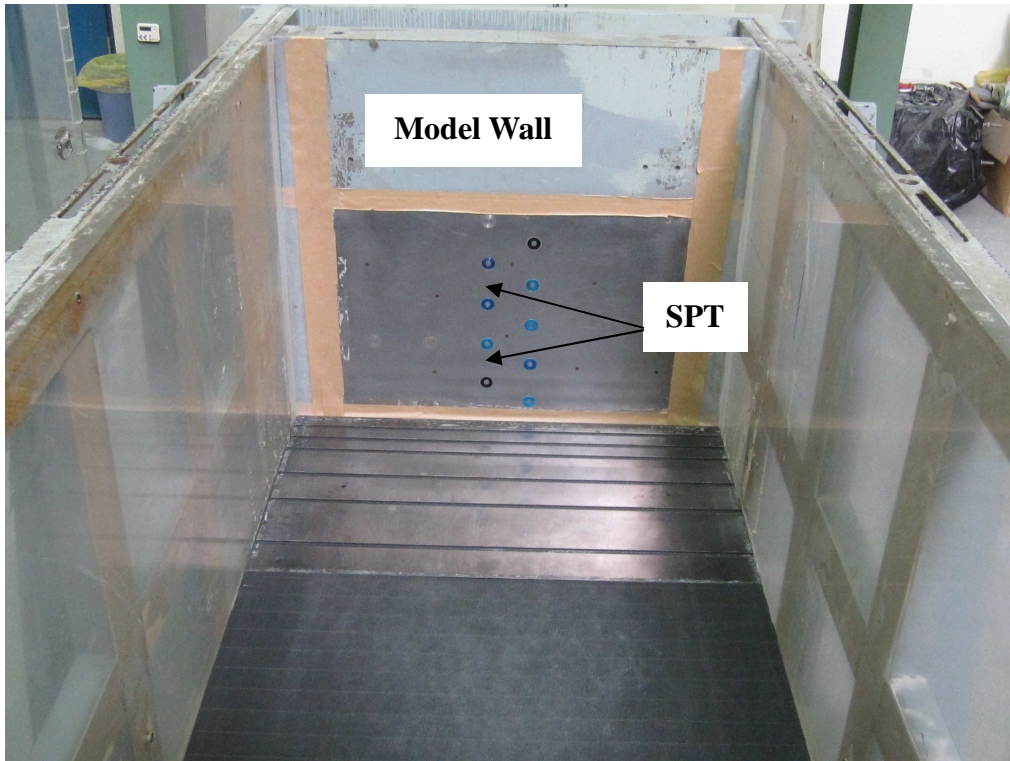


Fig.3.5. Locations of pressure transducers on model wall



Fig. 3.6. Soil pressure transducer (Kyowa PGM-0.2KG)



Fig. 3.7. Plastic-sheet on each sidewall

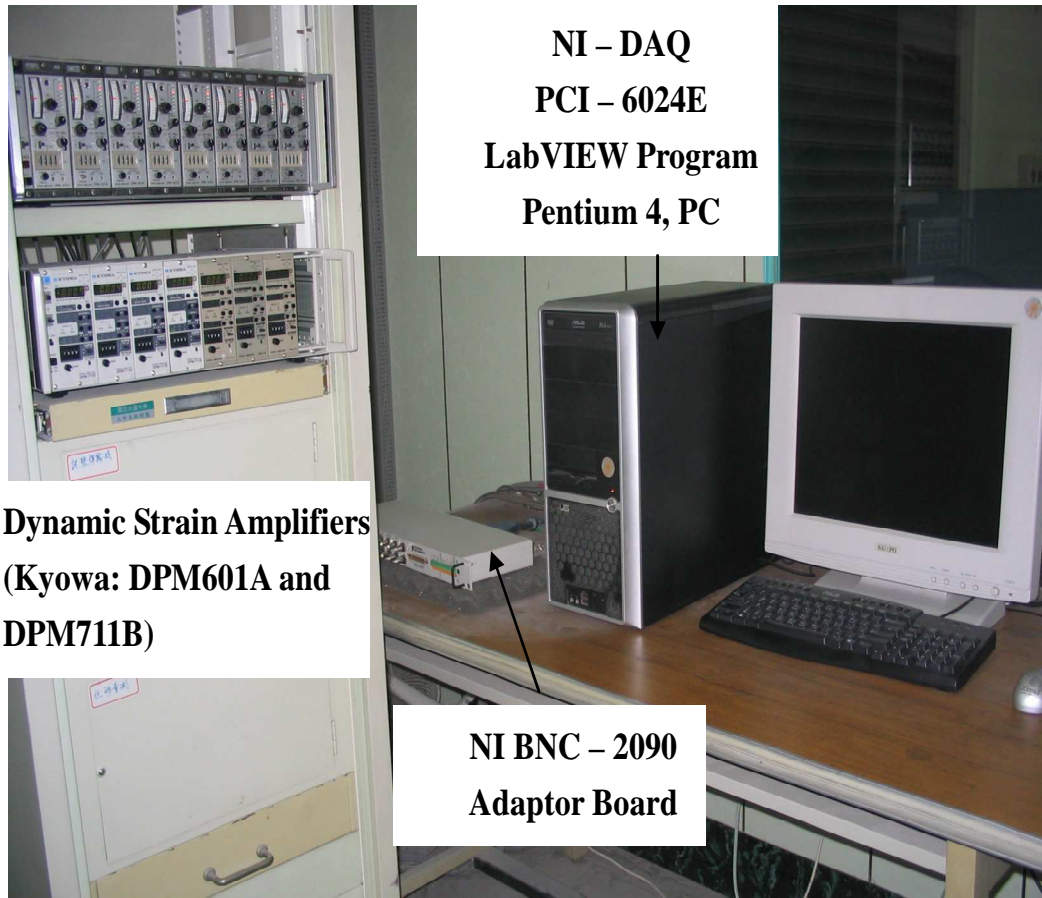


Fig. 3.8. Picture of Data acquisition system

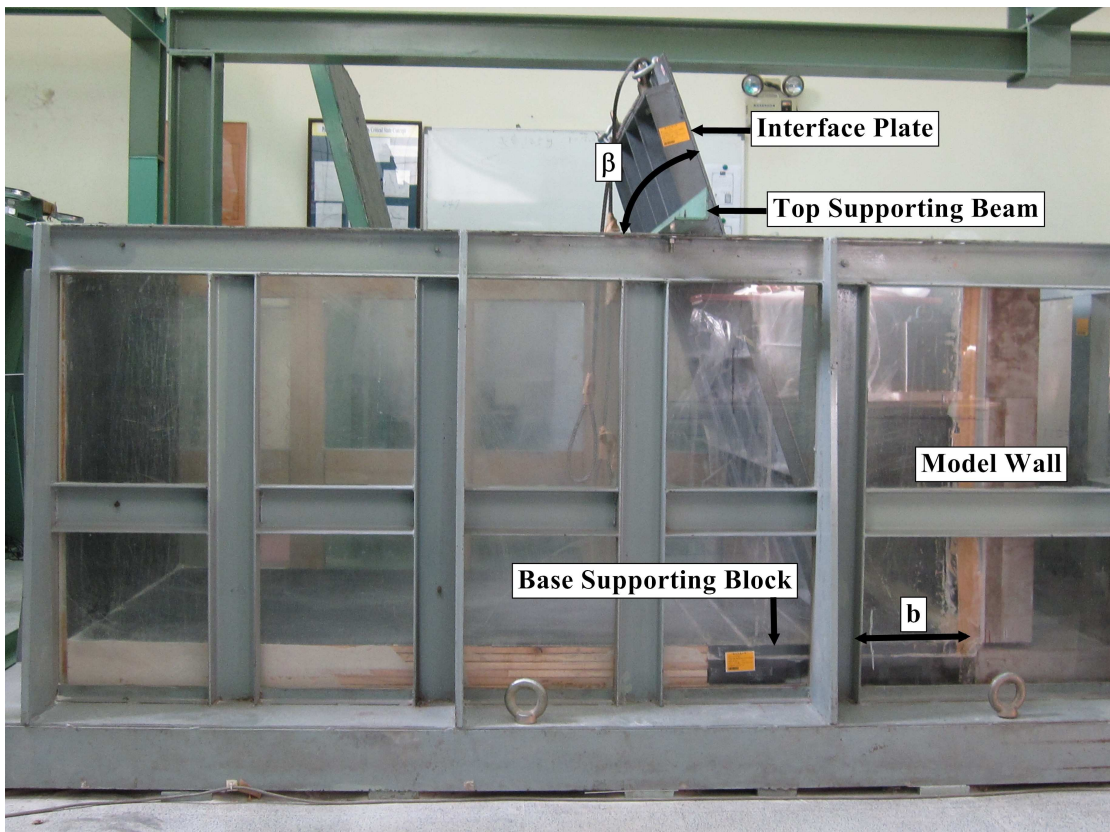


Fig. 4.1. NCTU model retaining wall with inclined interface plate

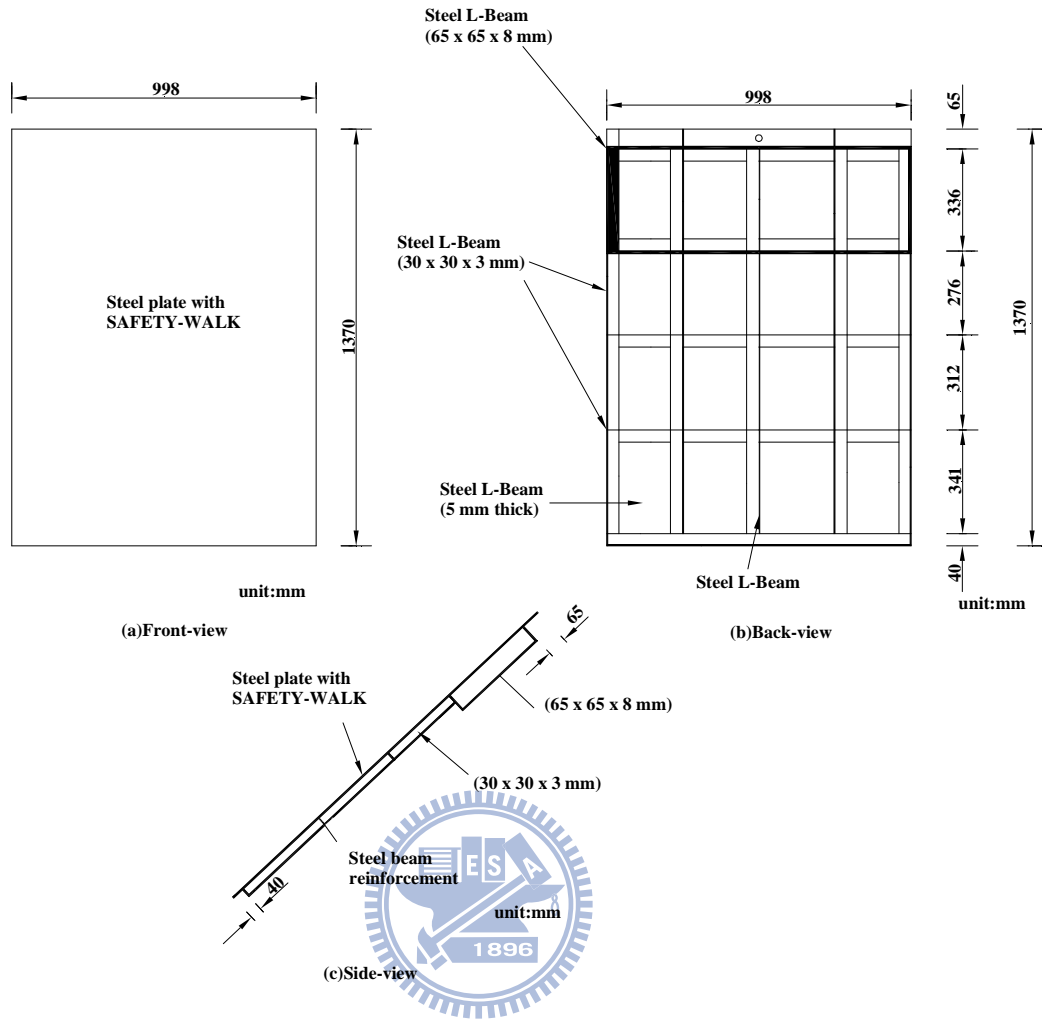
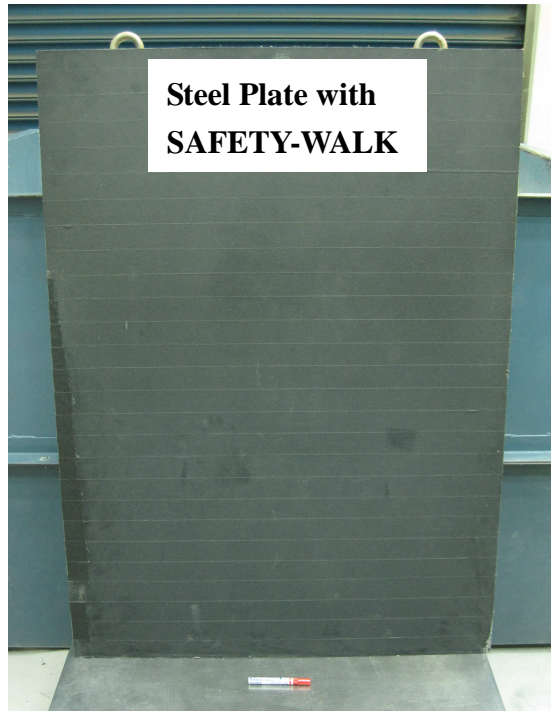
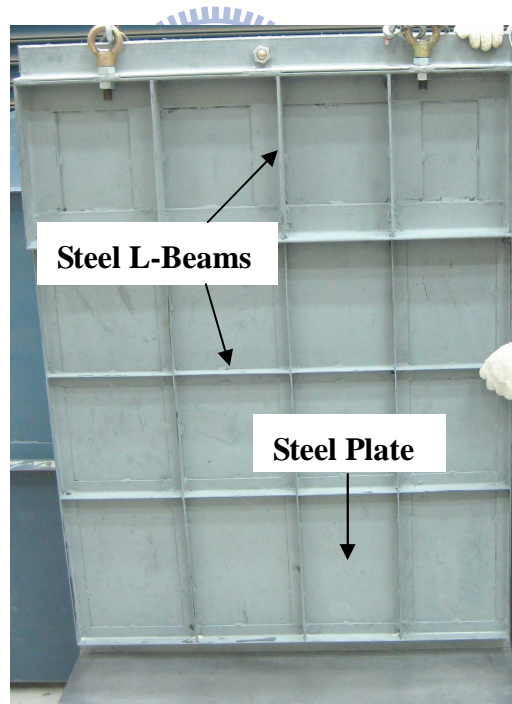


Fig. 4.2. Steel interface plate (after Zheng,2008)



(a) Front-view



(b) Back-view

Fig. 4.3. Steel interface plate (after Zheng,2008)

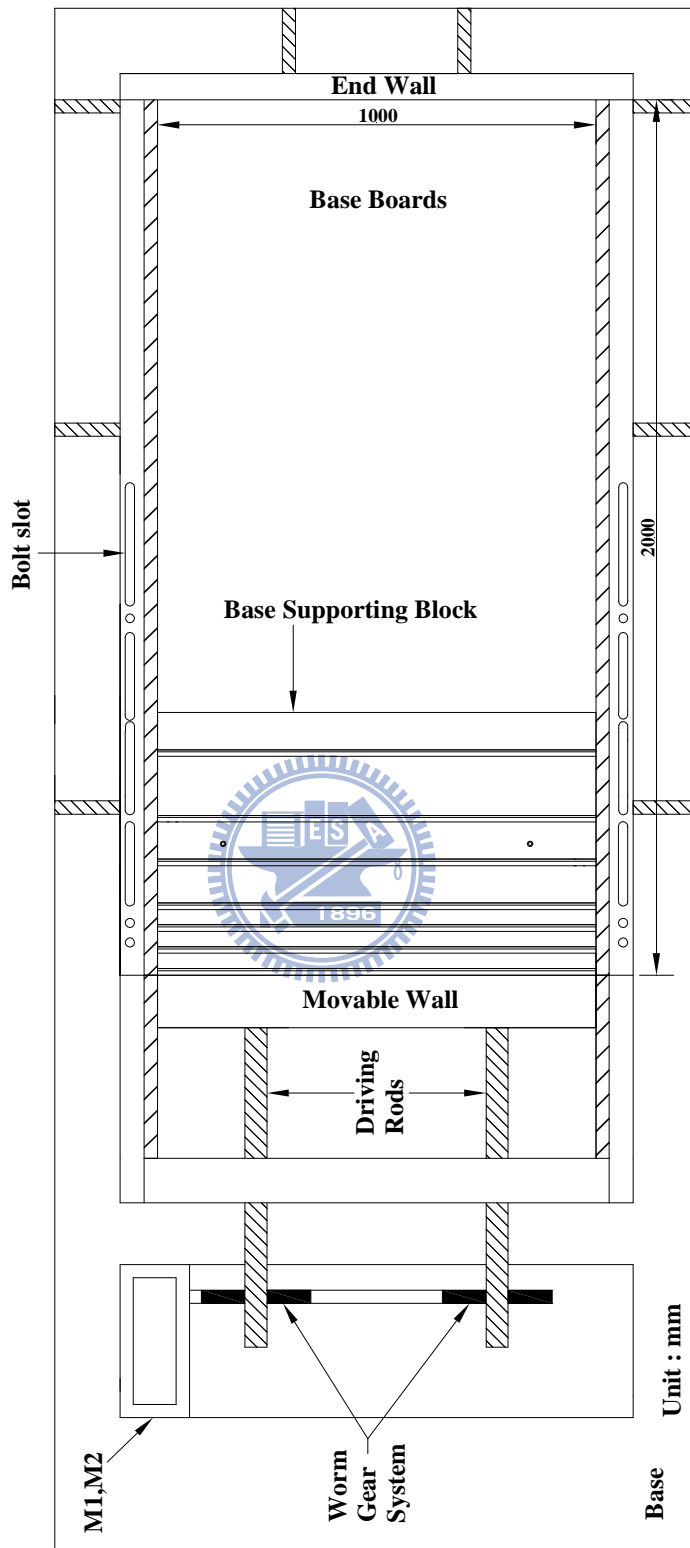


Fig. 4.4 Top-view of model wall

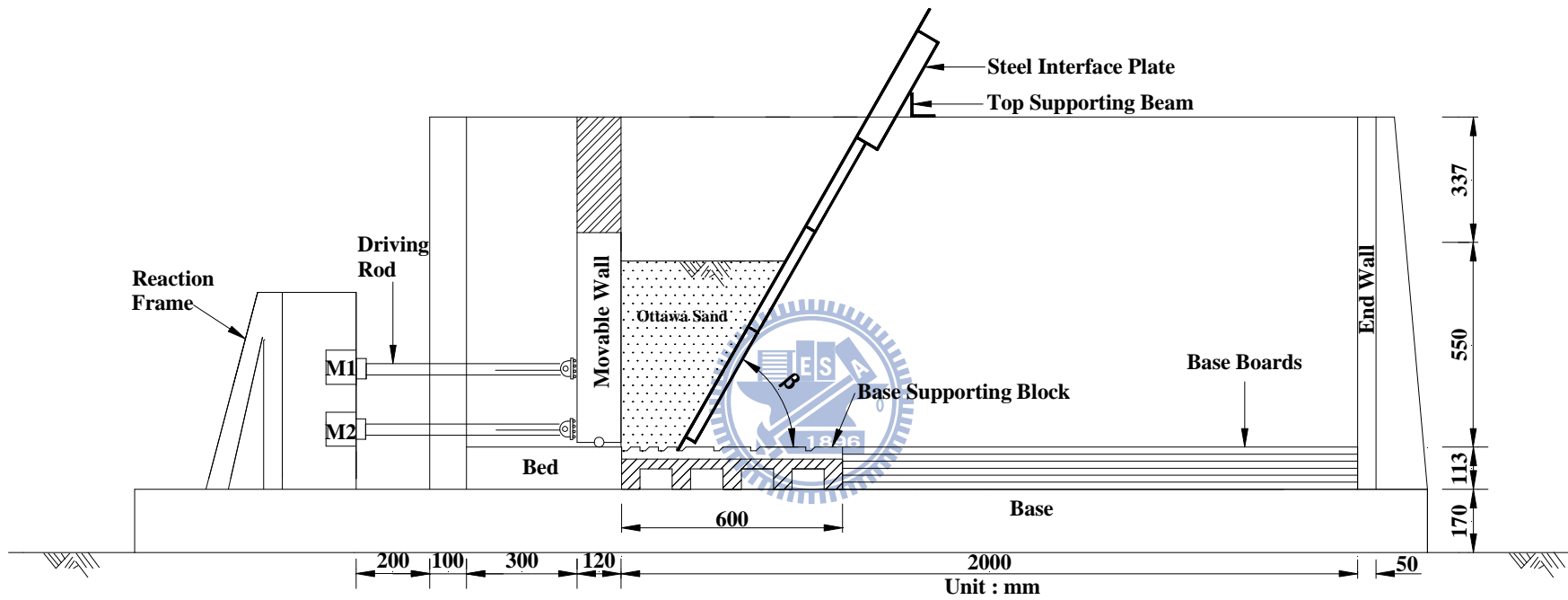
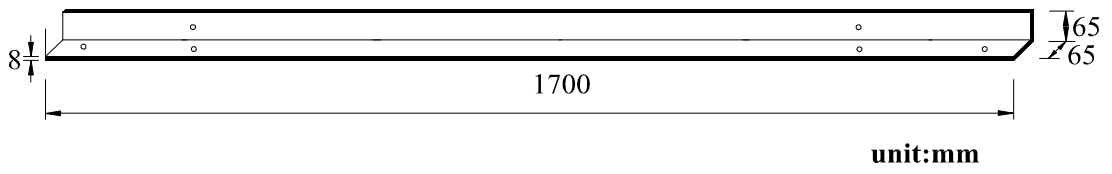
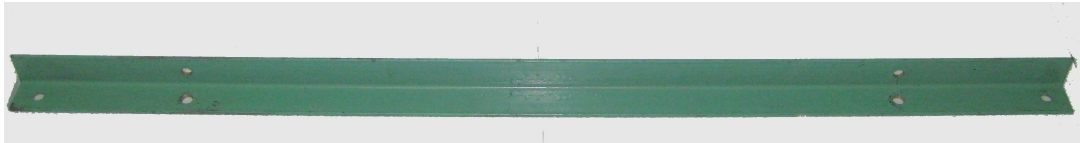


Fig. 4.5. NCTU model retaining wall with interface plate supports

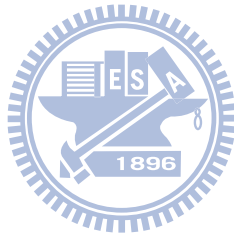


(a)



(b)

Fig. 4.6. Top supporting beam (after Zheng,2008)



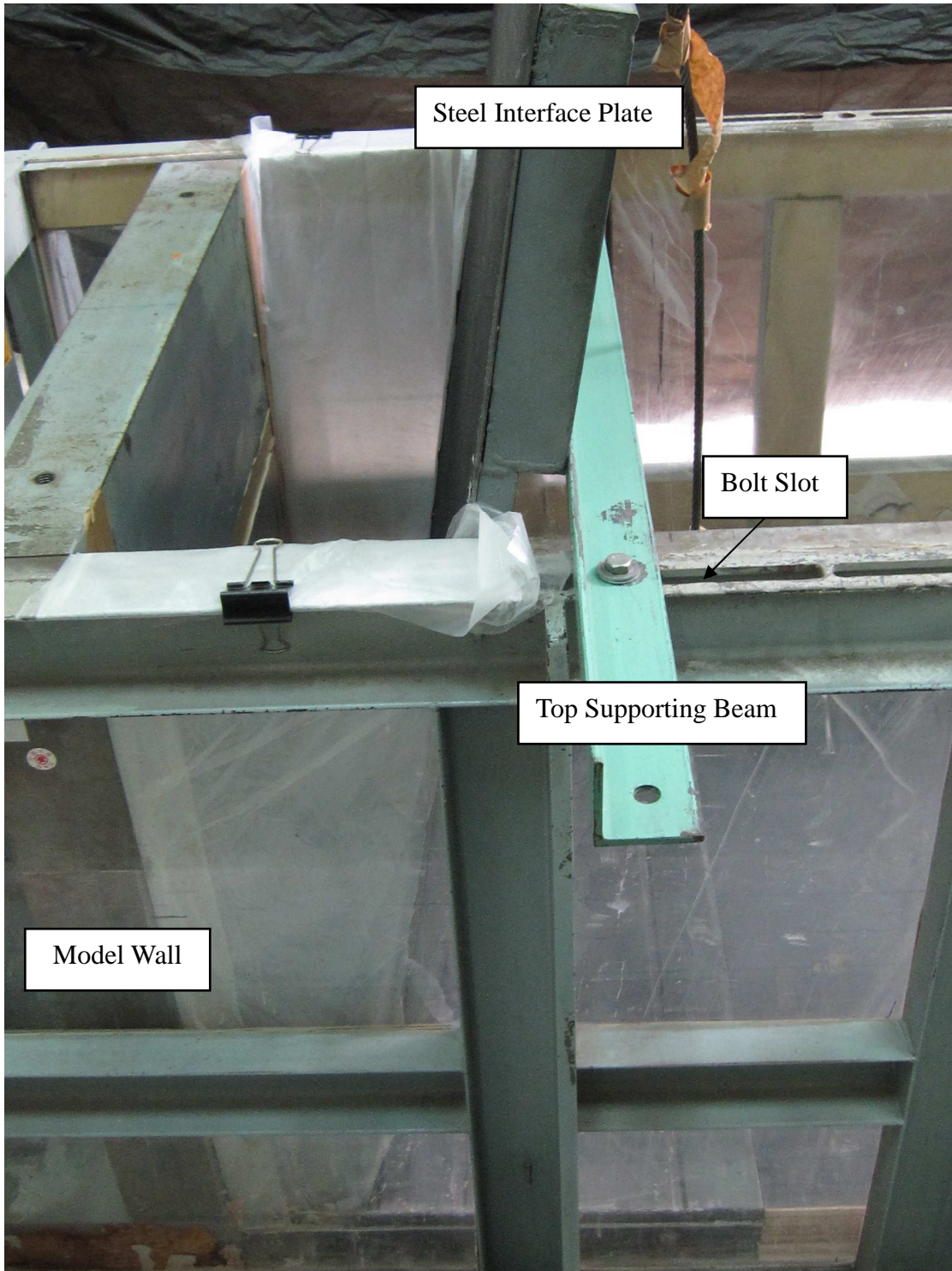
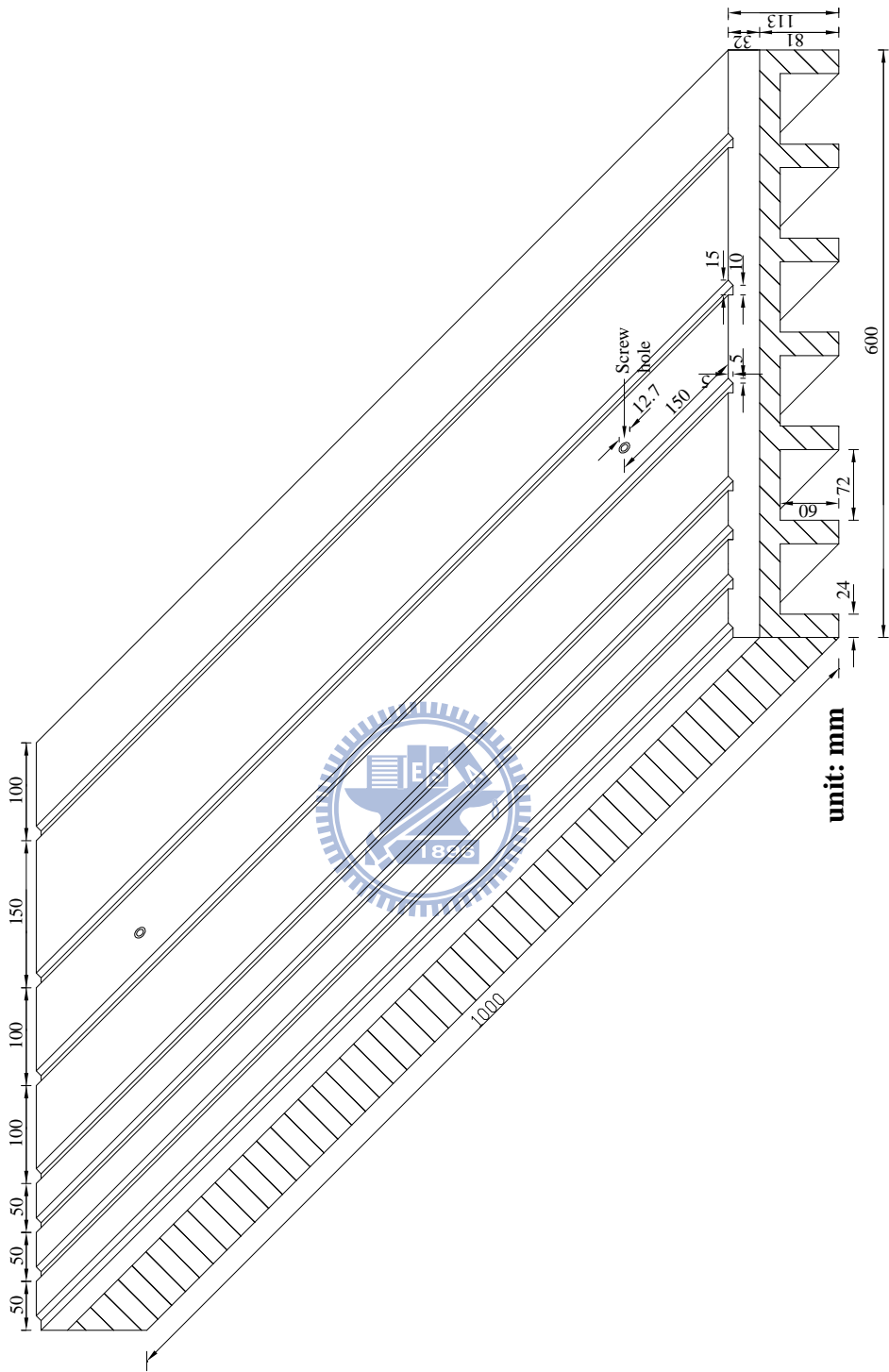
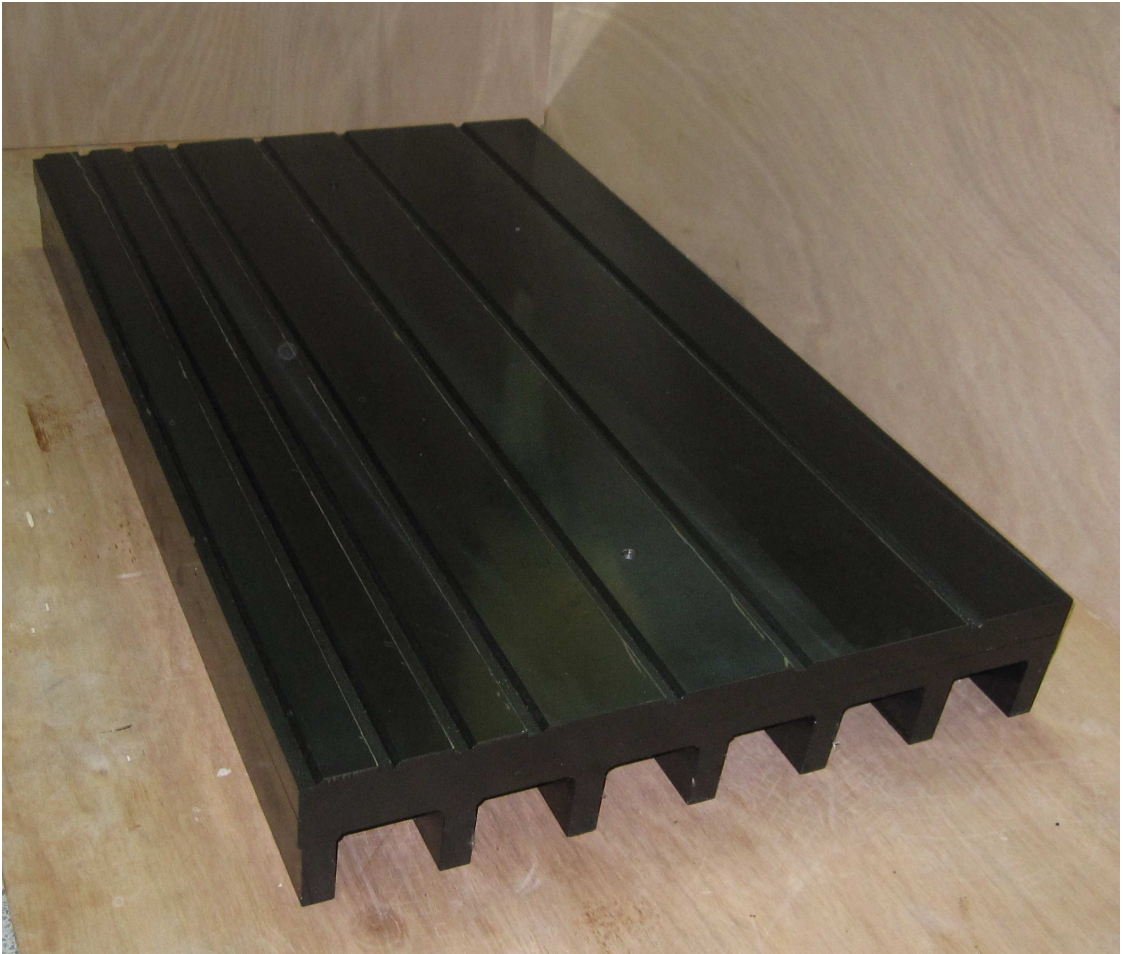


Fig. 4.7. Steel interface plate and top supporting beam



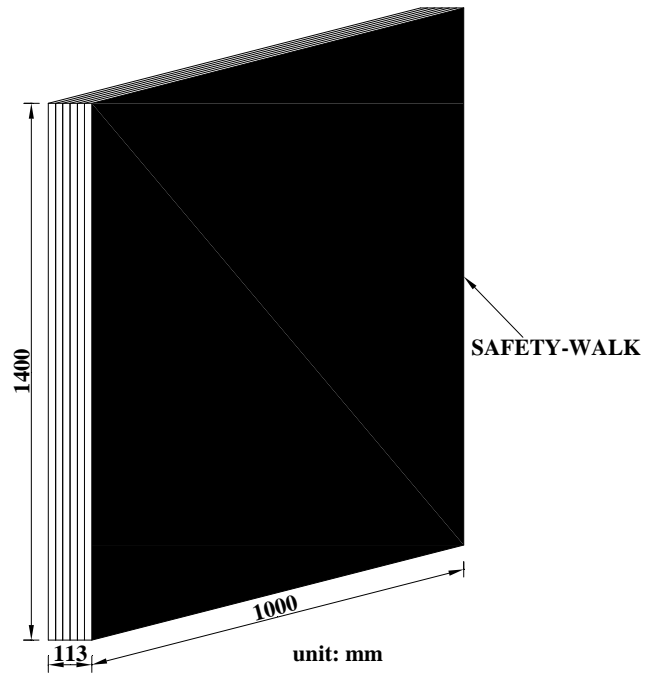
(a)

Fig. 4.8. Base supporting block



(b)

Fig. 4.8. Base supporting block



(b)

Fig. 4.9. Base supporting boards

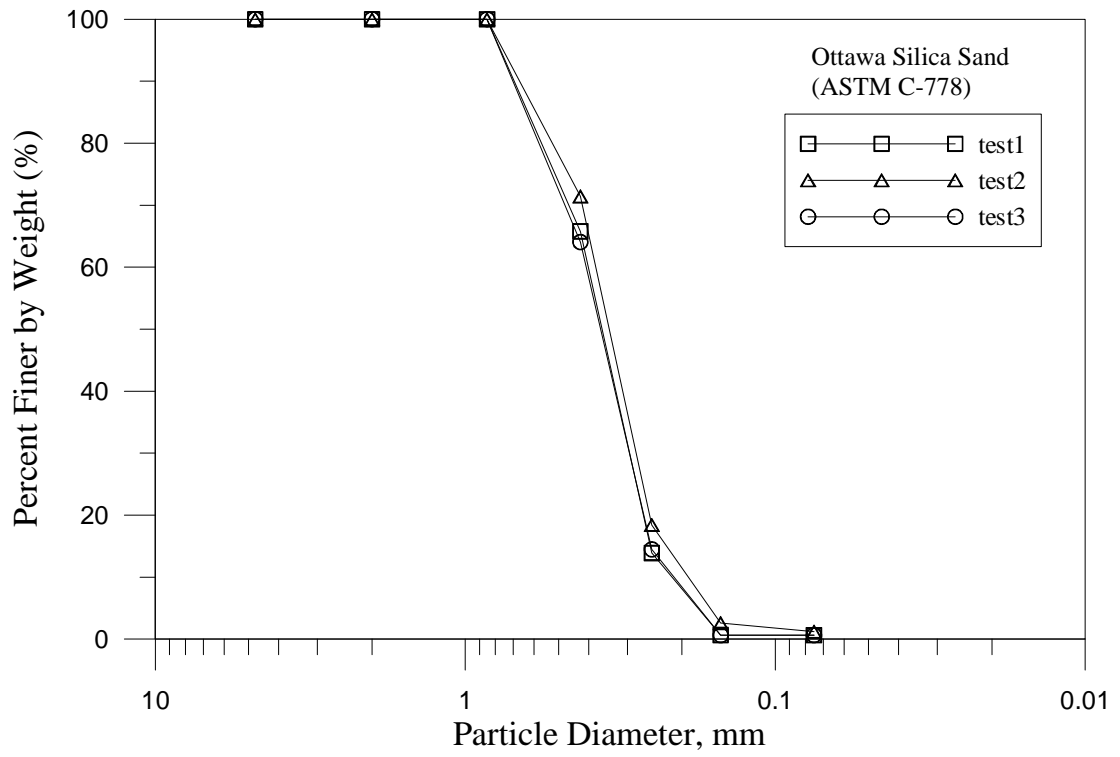
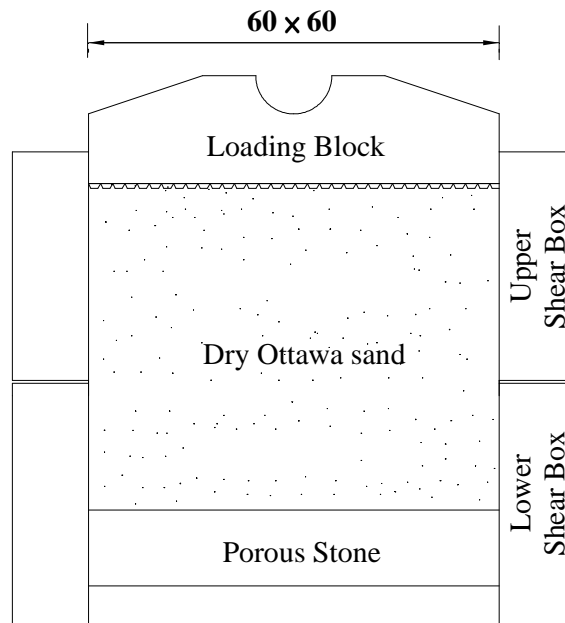


Fig. 5.1. Grain size distribution of Ottawa sand





unit : mm

Fig. 5.2. Shear box of direct shear test device (after Wu, 1992)



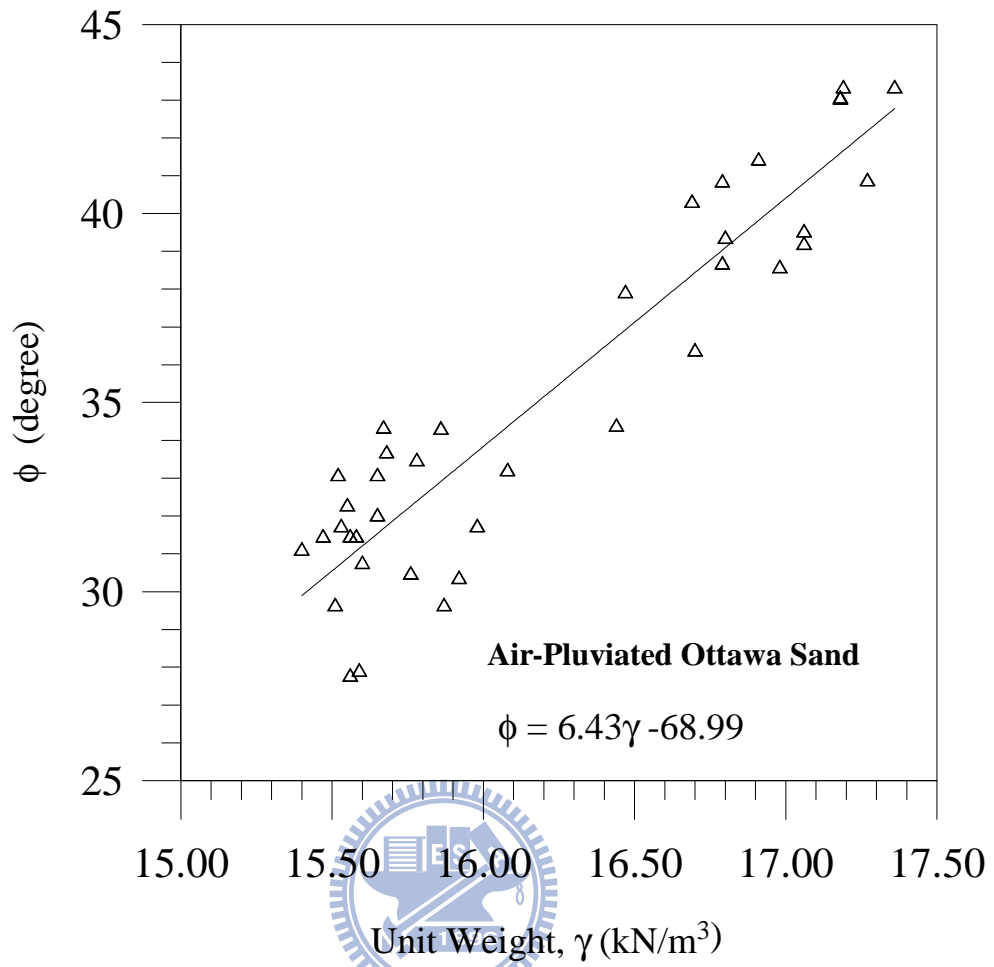
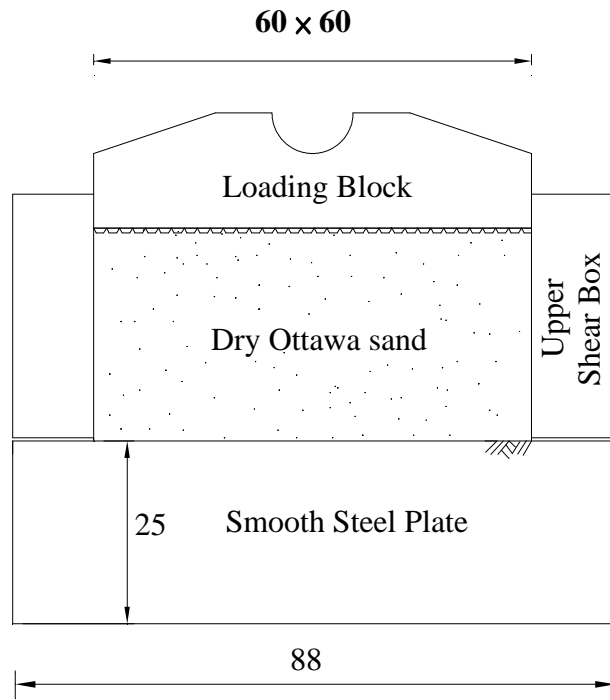


Fig. 5.3. Relationship between unit weight γ and internal friction angle ϕ (after Chang, 2000)



unit : mm

Fig. 5.4. Direct shear test to determinate wall friction (after Chang, 2000)



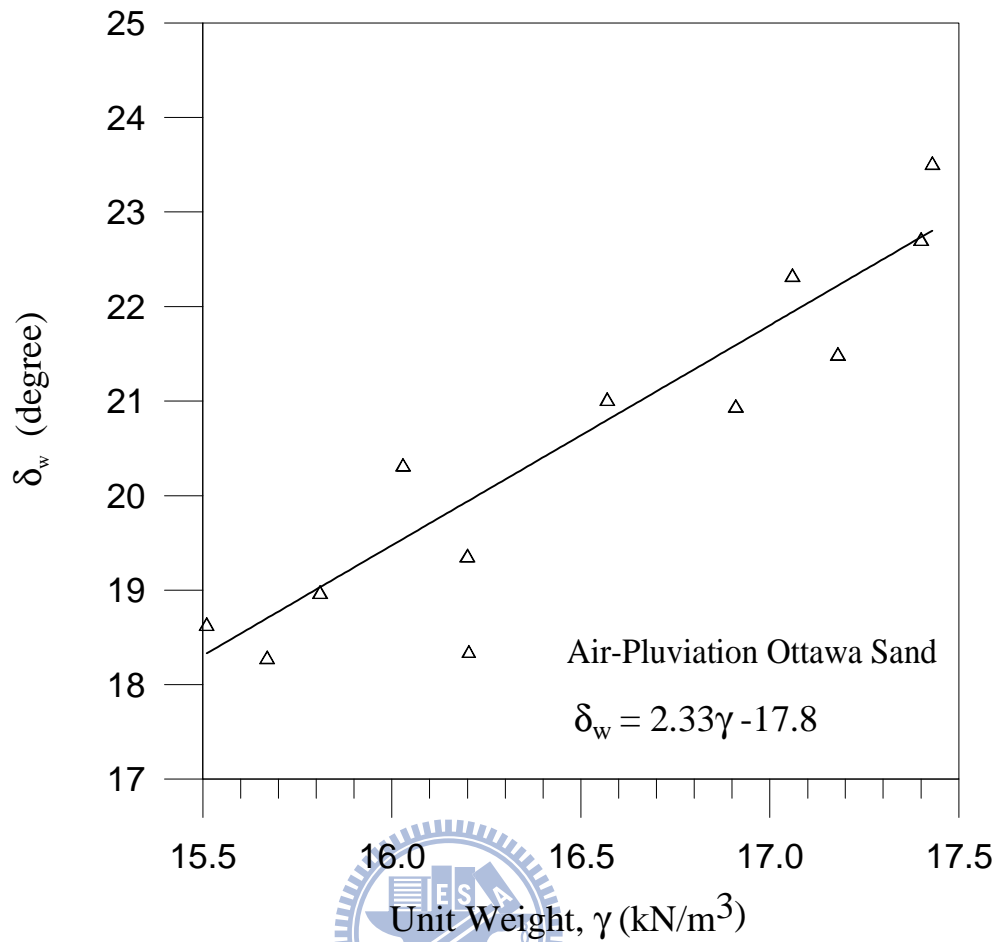


Fig.5.5. Relationship between unit weight γ and wall friction angle δ_w (after Chang, 2000)

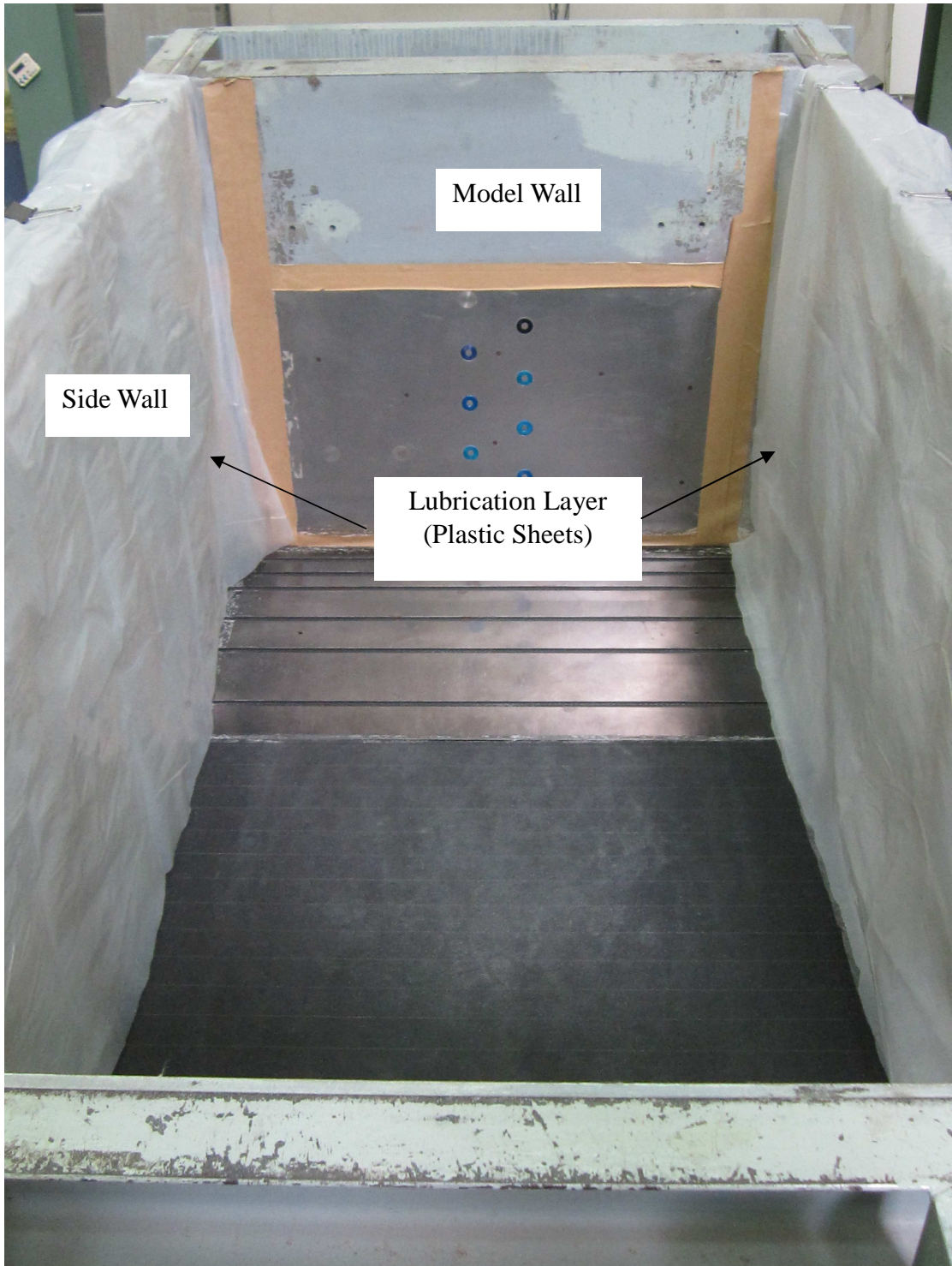


Fig. 5.6. Plastic-sheet lubrication layers on side walls

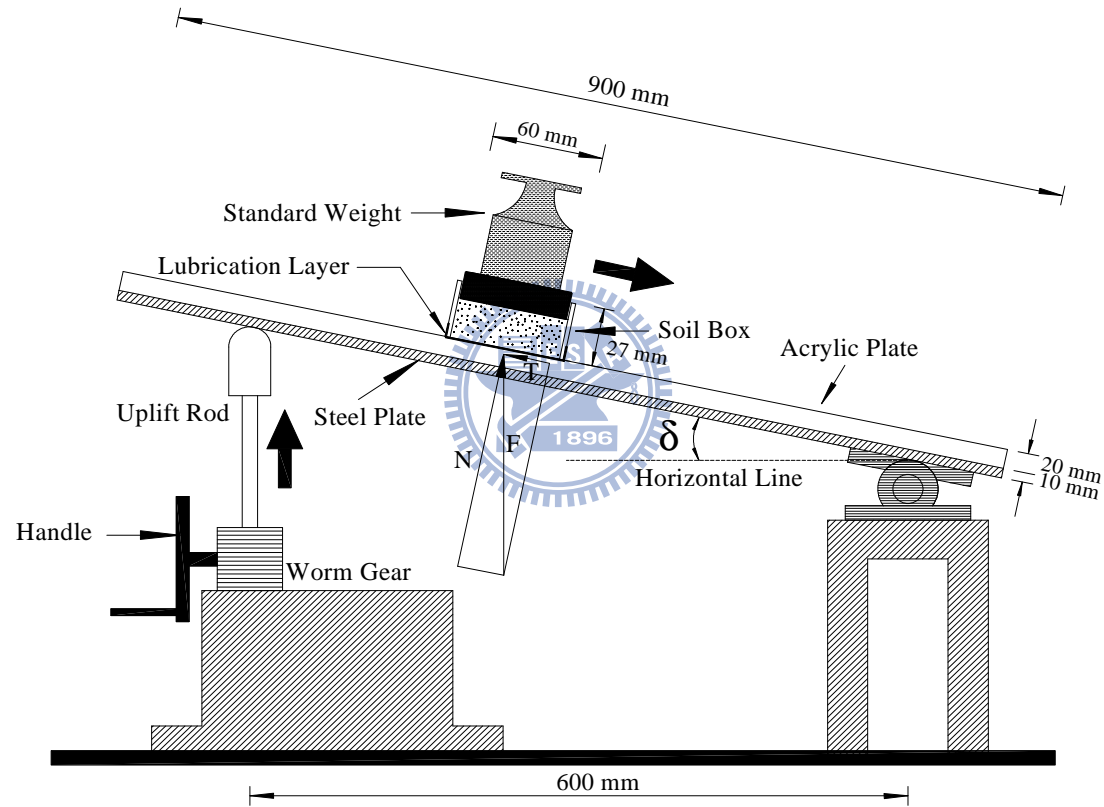


Fig. 5.7. Schematic diagram of sliding block test (after Fang et al., 2004)

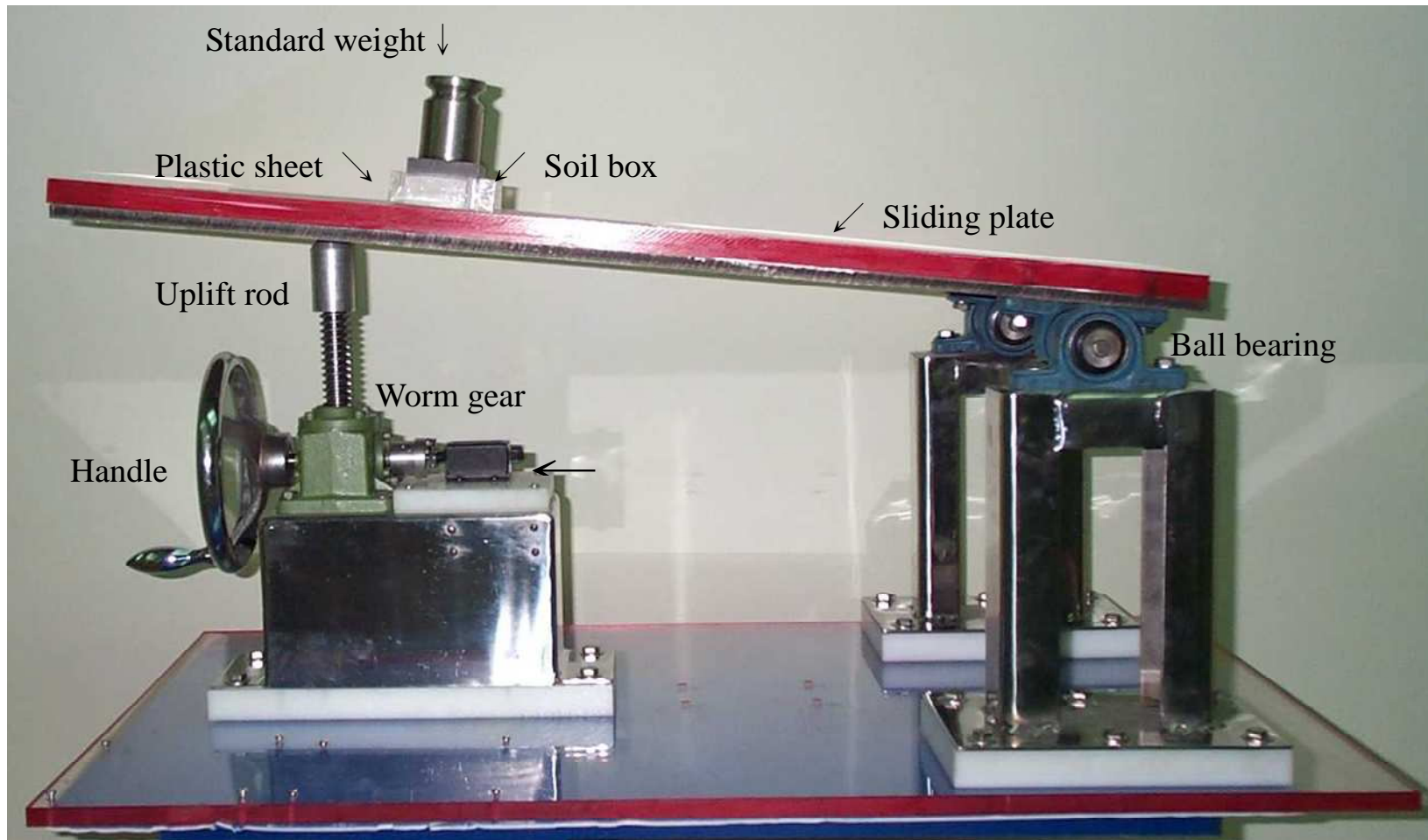


Fig.5.8 Sliding block test apparatus (after Fang et al., 2004)

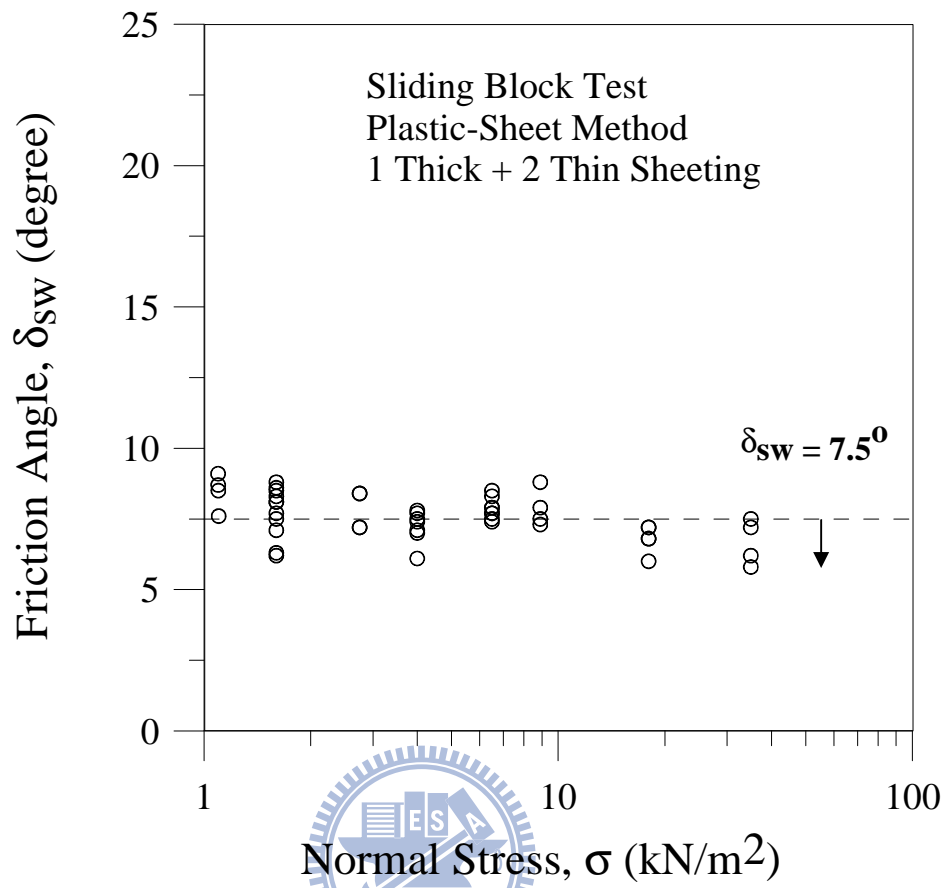
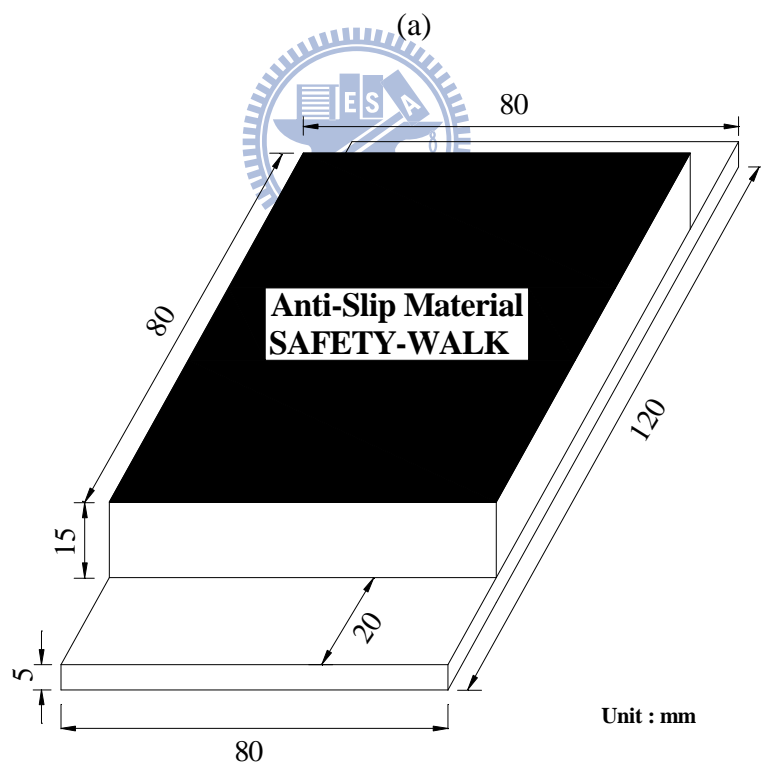
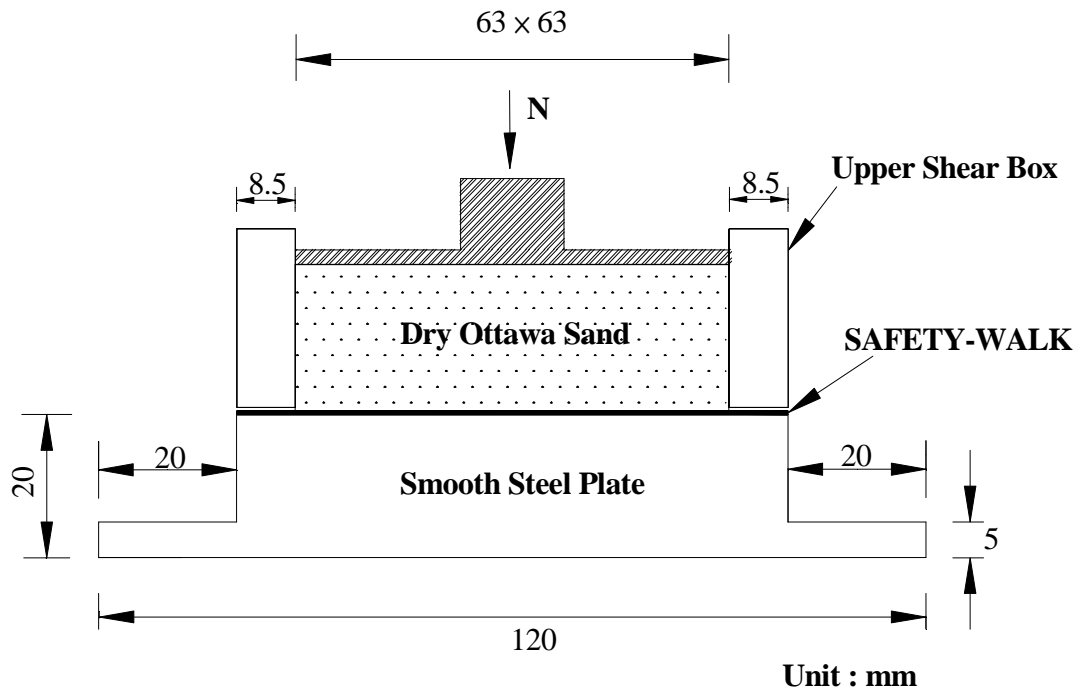


Fig. 5.9 Variation of side-wall friction angle with normal stress
(after Fang et al., 2004)



(b)

Fig. 5.10. Direct shear test to determine interface friction angle
(after Wang, 2005)

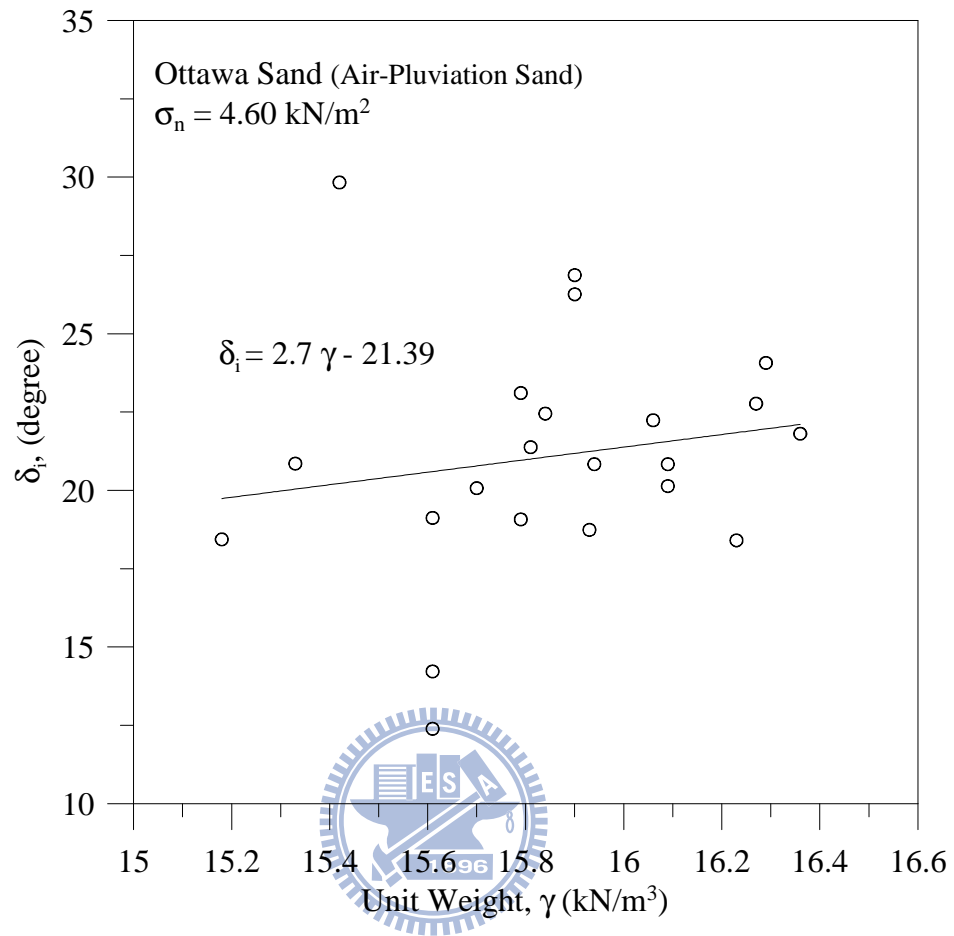


Fig. 5.11. Relationship between unit weight γ and interface plate friction angle δ_i (after Wang, 2005)

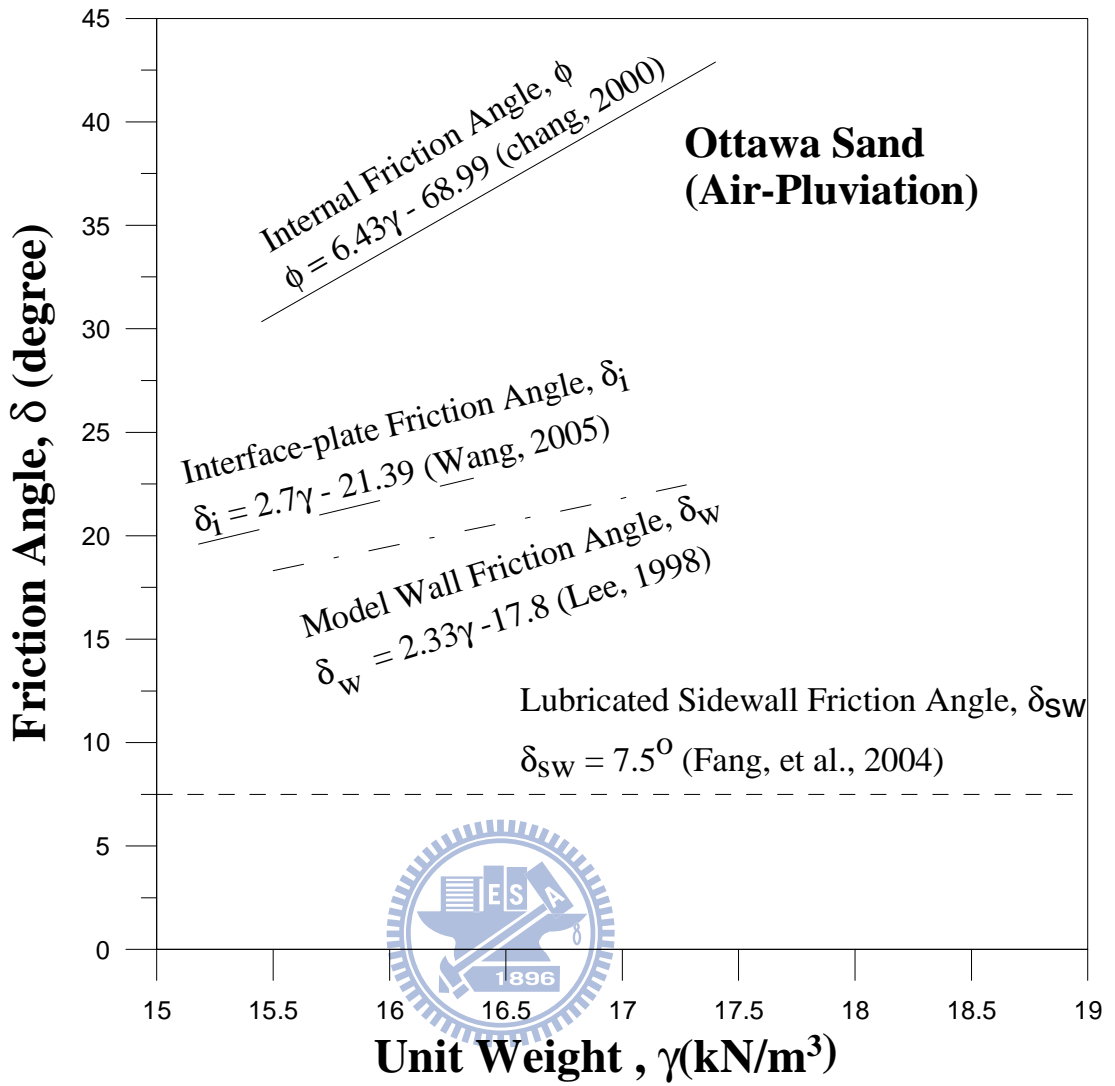
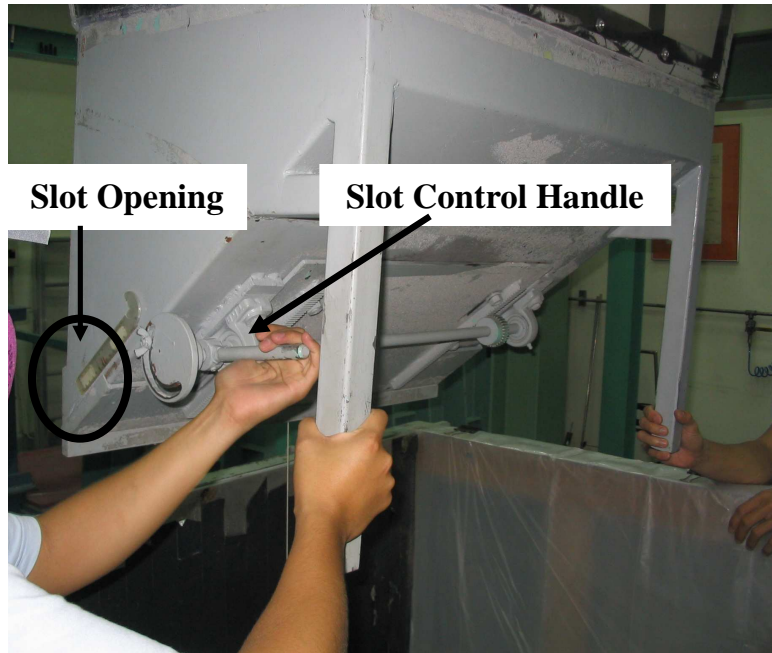
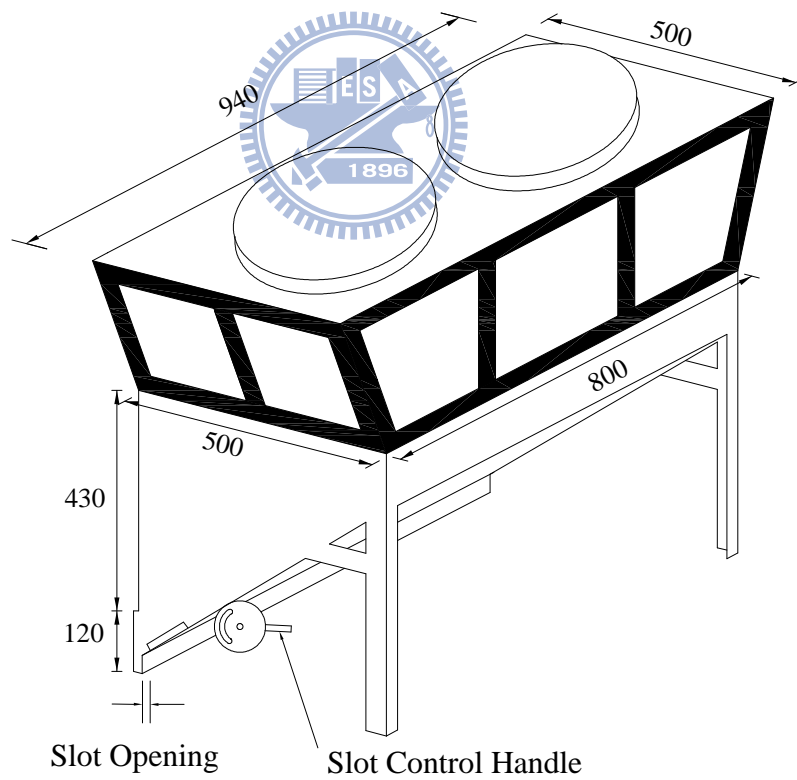


Fig. 5.12. Relationship friction angle δ and soil unit weight γ



(a)



Unit:mm

(b)

Fig. 5.13. Soil hopper (after Chang, 2000)

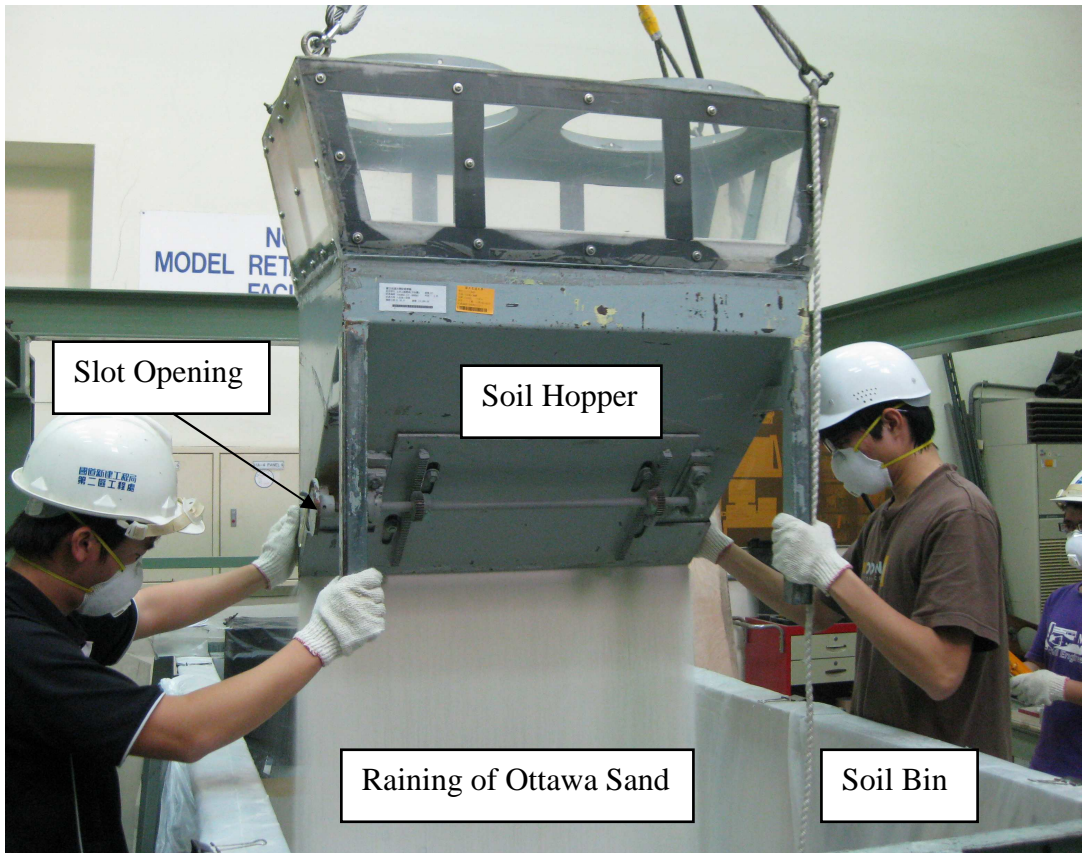


Fig. 5.14. Pluviation of Ottawa sand into soil bin

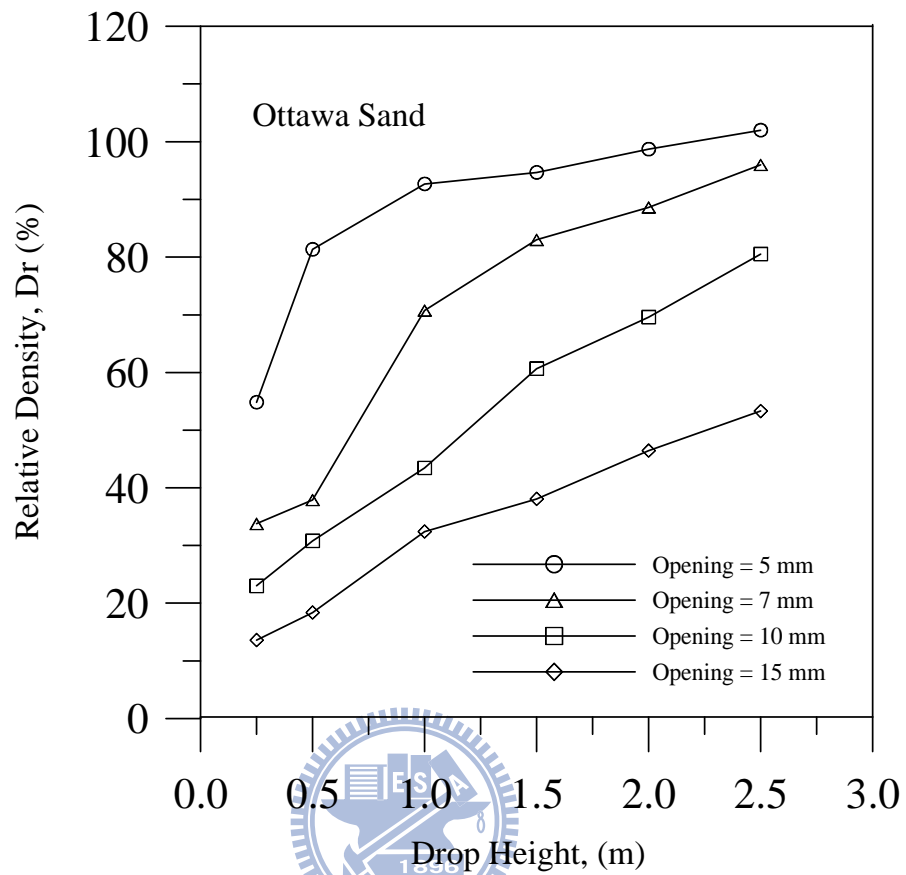
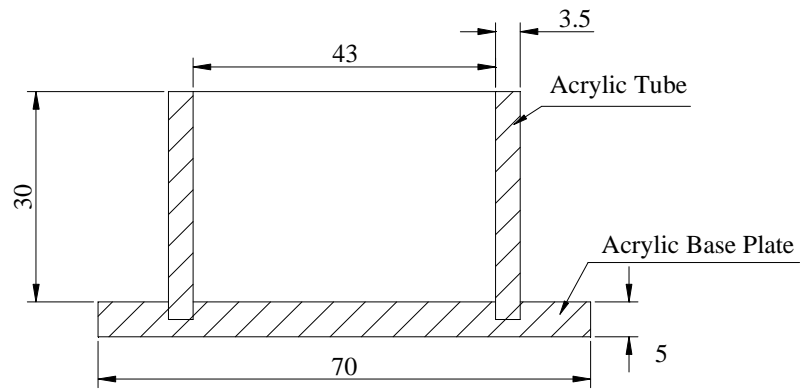
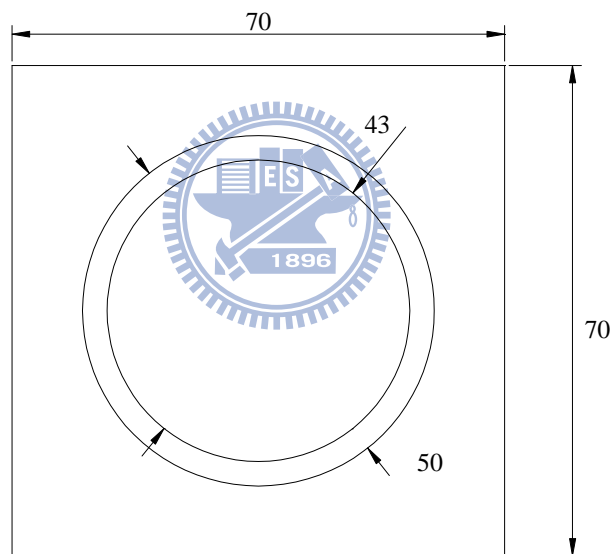


Fig. 5.15. Relationship between relation density and drop height (after Ho, 1999)



Side-view



Top-view

unit : mm

Fig. 5.16. Soil-density control cup
(after Ho, 1999)



Fig. 5.17. Soil-density cup (after Chien, 2007)



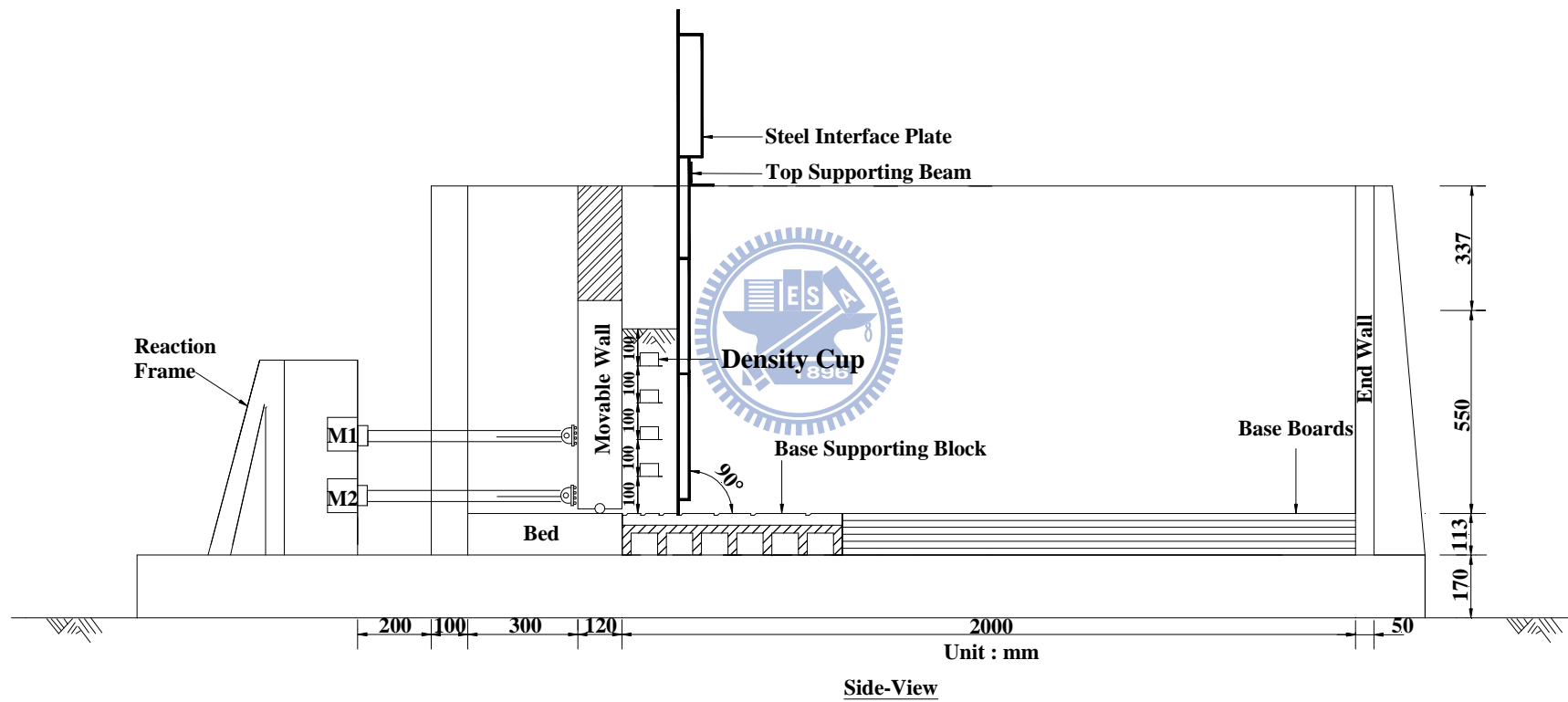


Fig. 5.18. Locations of density cups for $b = 150$ mm and $\beta = 90^\circ$.

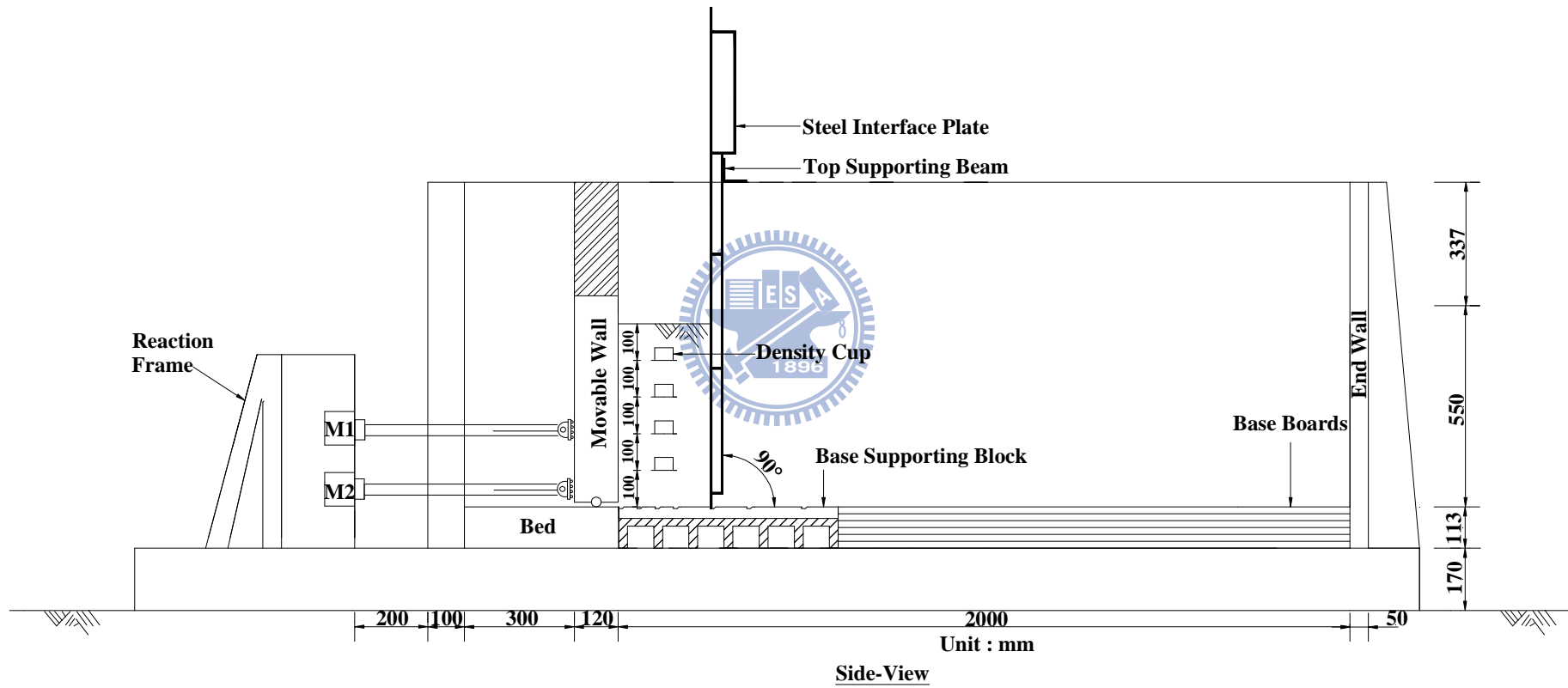


Fig. 5.19. Locations of density cups for $b = 250$ mm and $\beta = 90^\circ$.

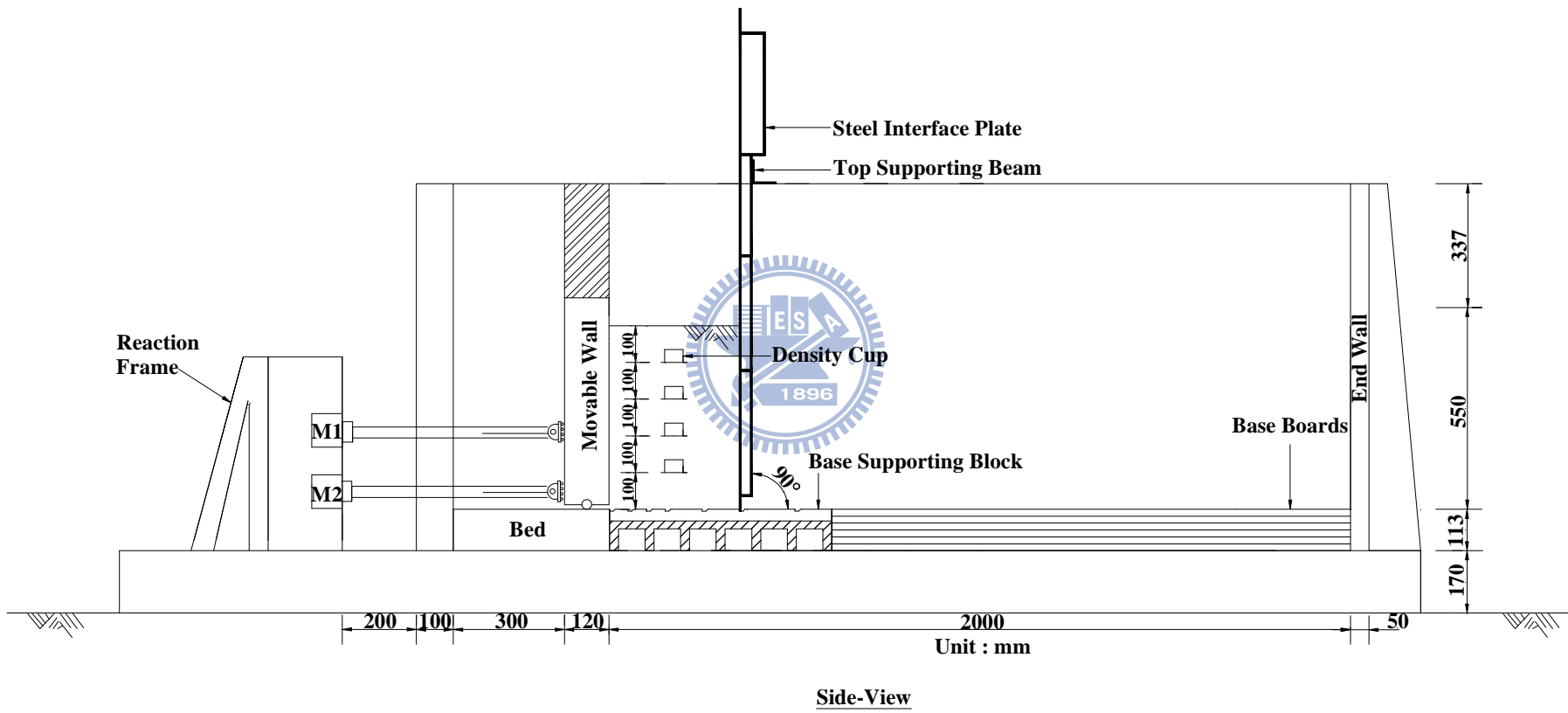


Fig. 5.20. Locations of density cups for $b = 350$ mm and $\beta = 90^\circ$.

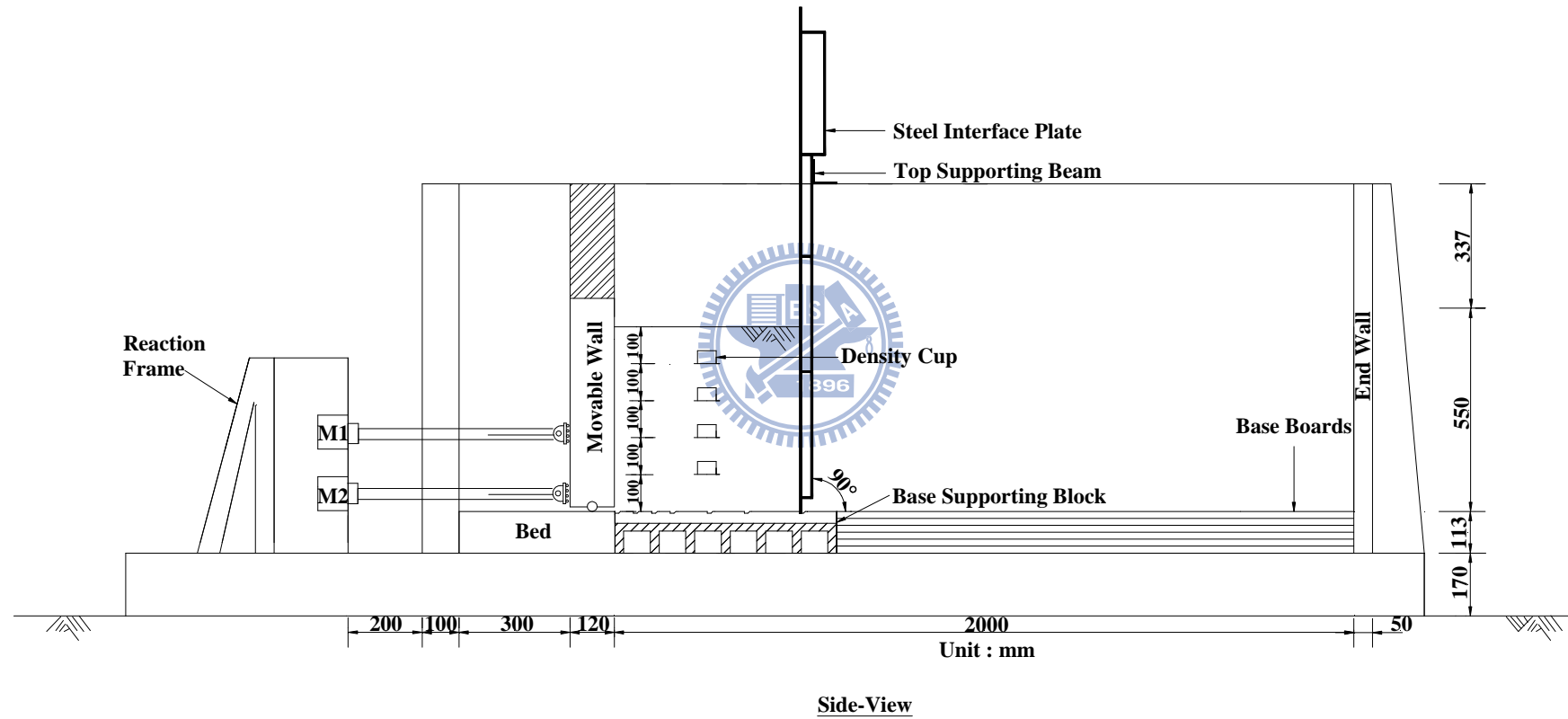


Fig. 5.21. Locations of density cups for $b = 500$ mm and $\beta = 90^\circ$.

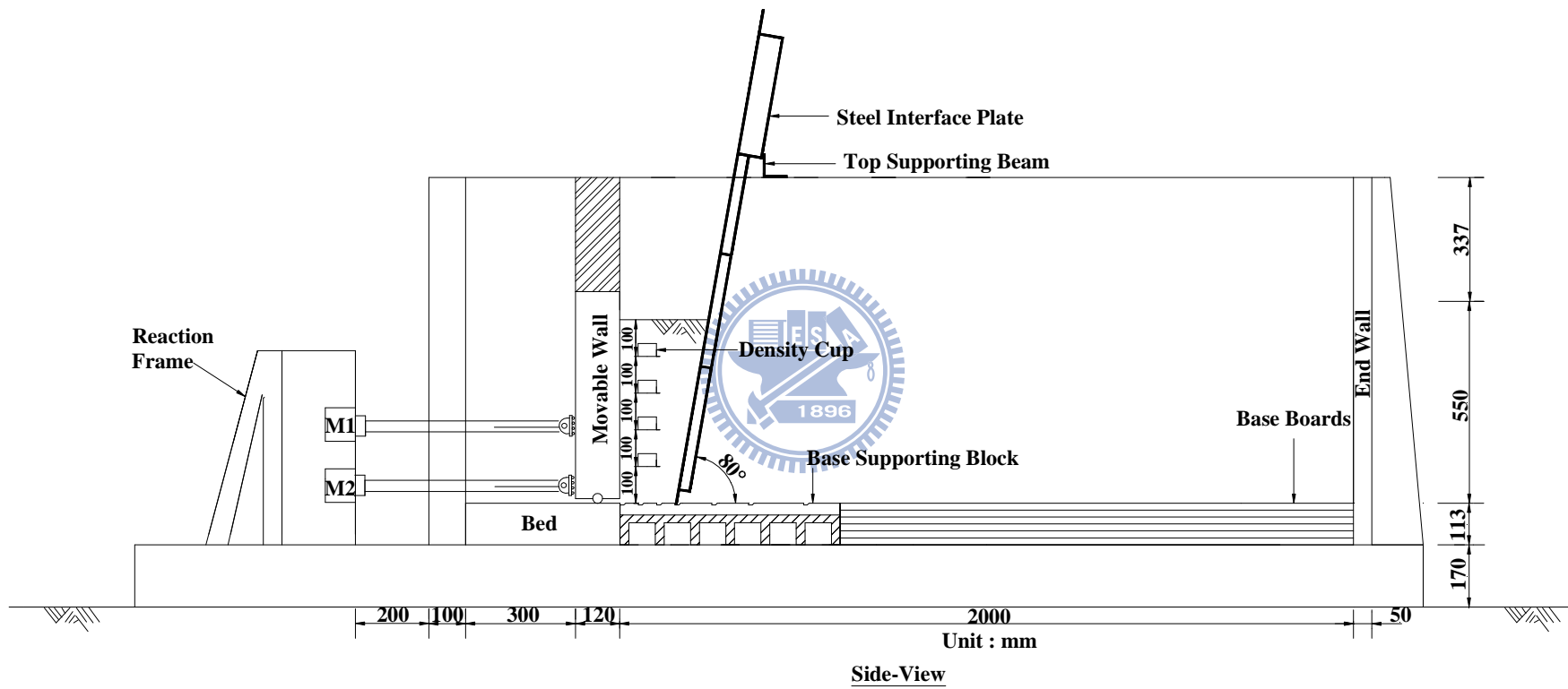


Fig. 5.22. Locations of density cups for $b = 150$ mm and $\beta = 80^\circ$.

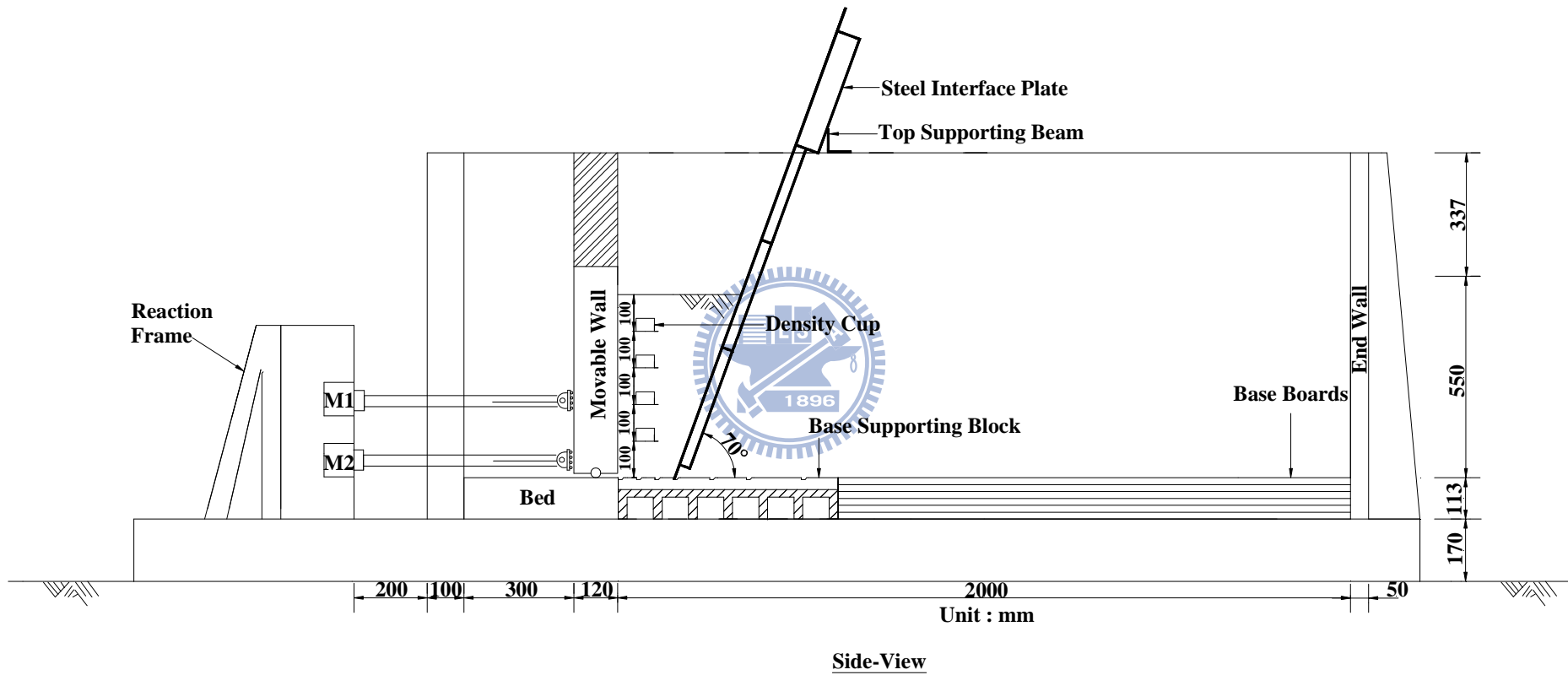


Fig. 5.23. Locations of density cups for $b = 150$ mm and $\beta = 70^\circ$.

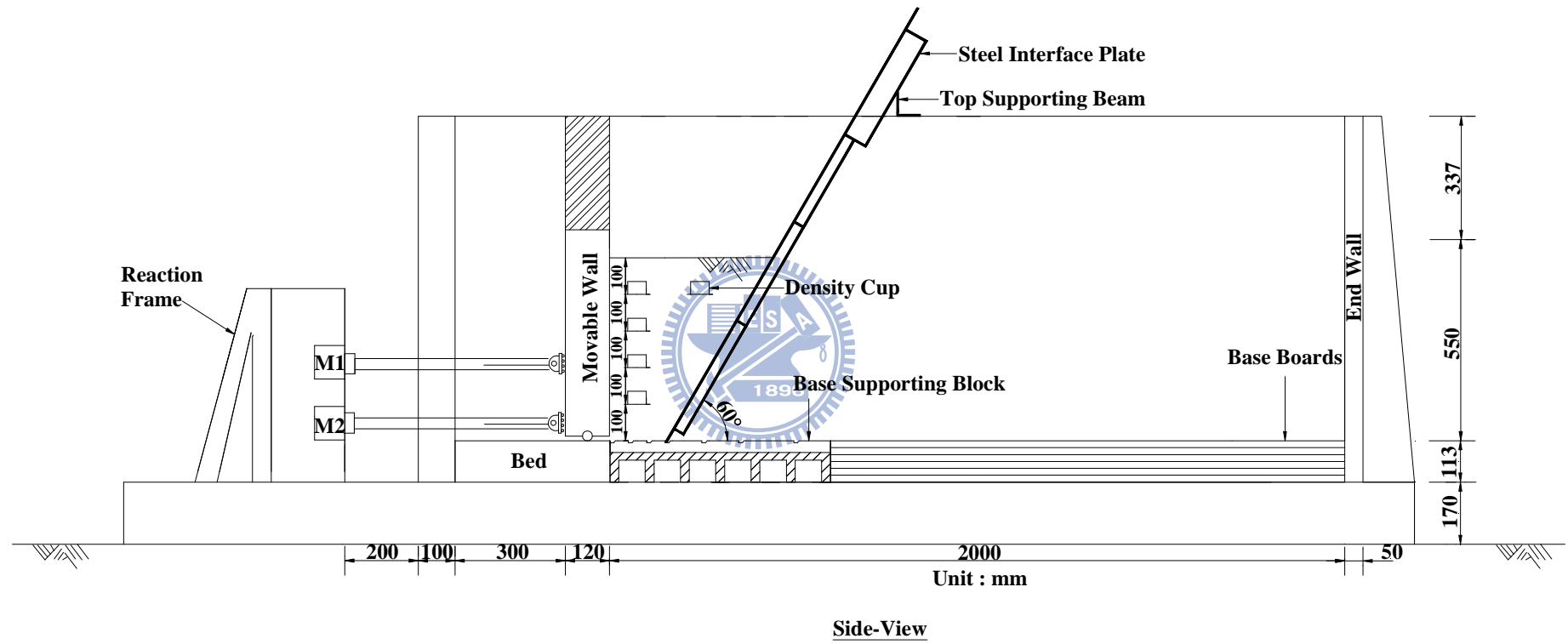


Fig. 5.24. Locations of density cups for $b = 150$ mm and $\beta = 60^\circ$.

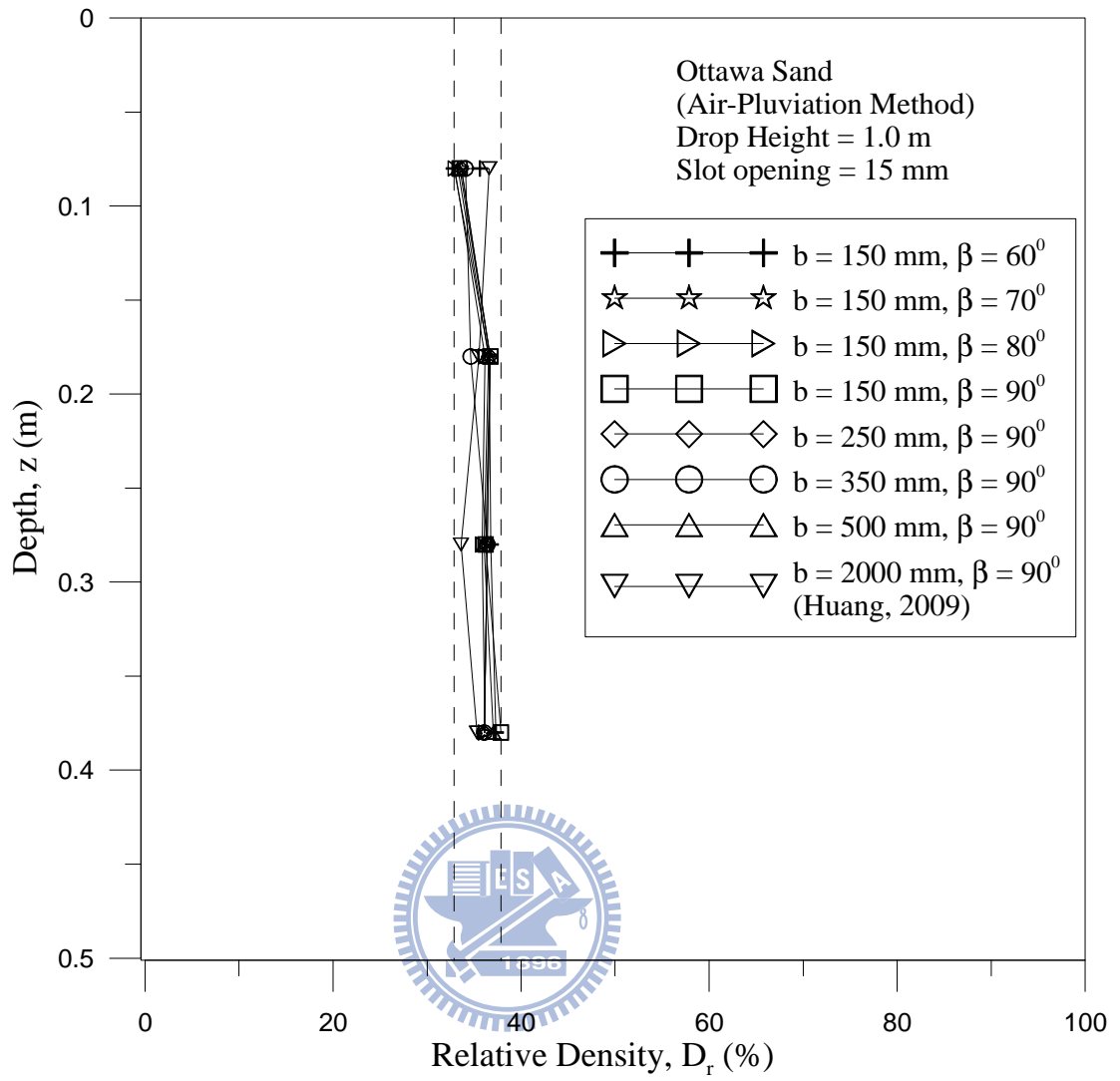
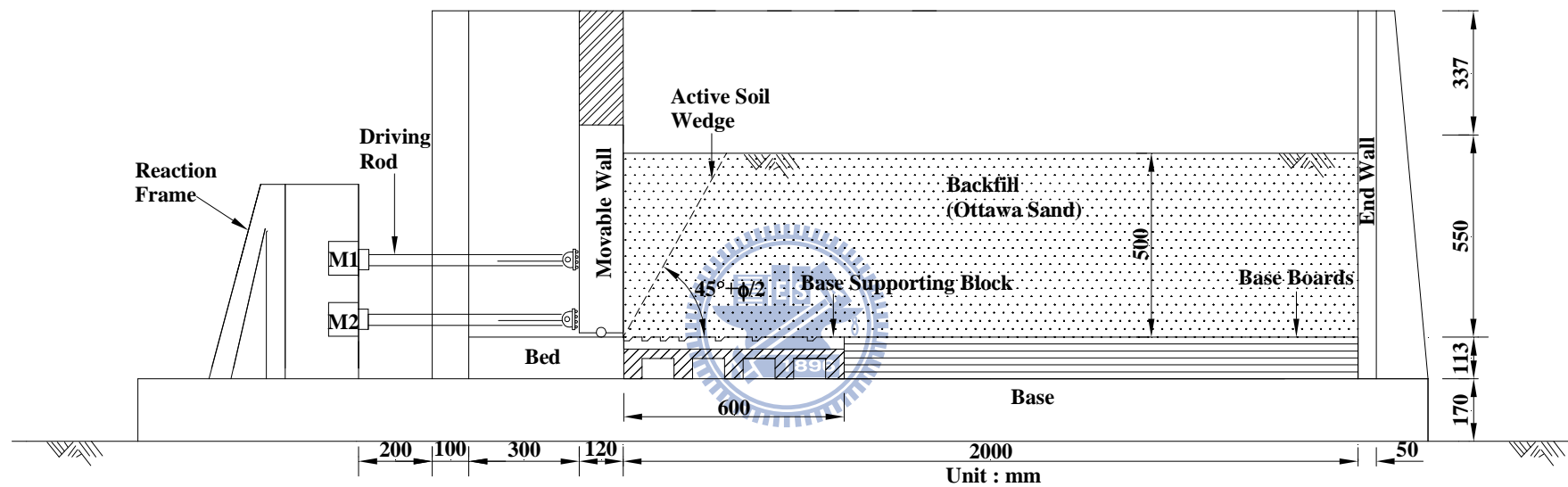
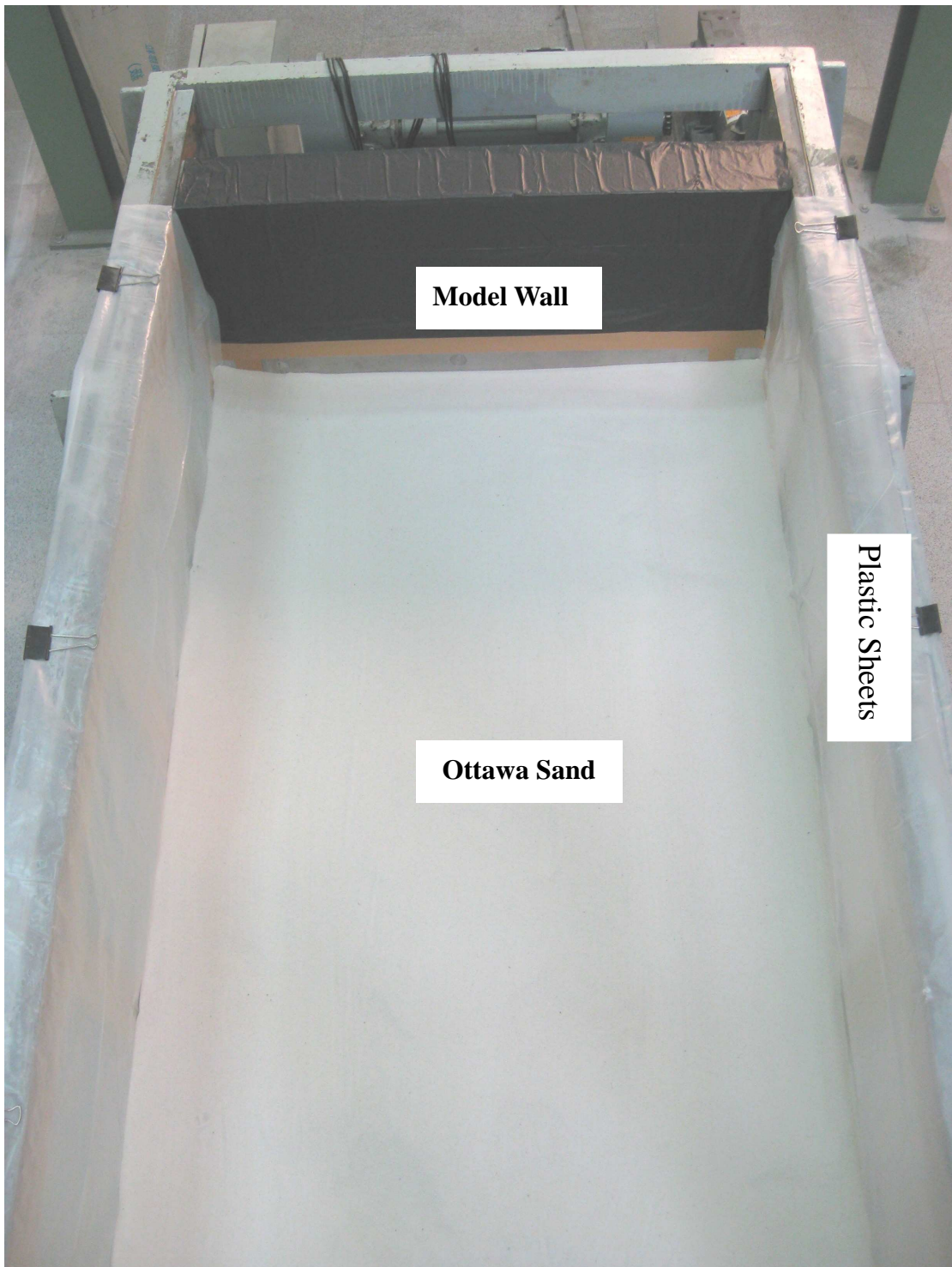


Fig. 5.25 Distribution of relative density



(a)

Fig. 6.1. Model wall test with faraway interface plate ($b = 2,000$ mm and $\beta = 90^\circ$)



(b)

Fig. 6.1. Model wall test with faraway interface plate ($b = 2,000$ mm and $\beta = 90^\circ$)

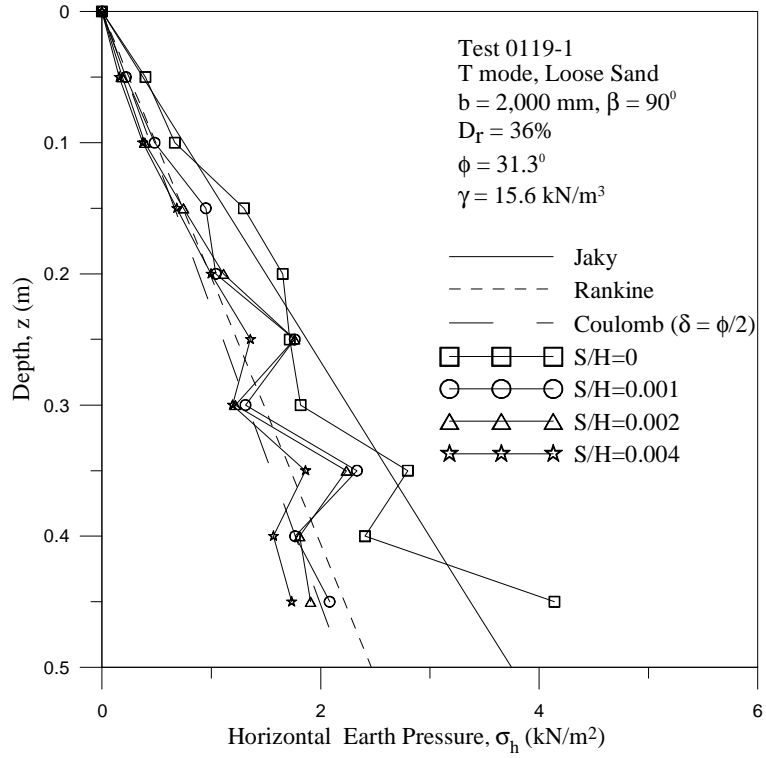


Fig. 6.2. Distribution of horizontal earth pressure for $b = 2,000 \text{ mm}$ and $\beta = 90^\circ$ (Test 0119-1)

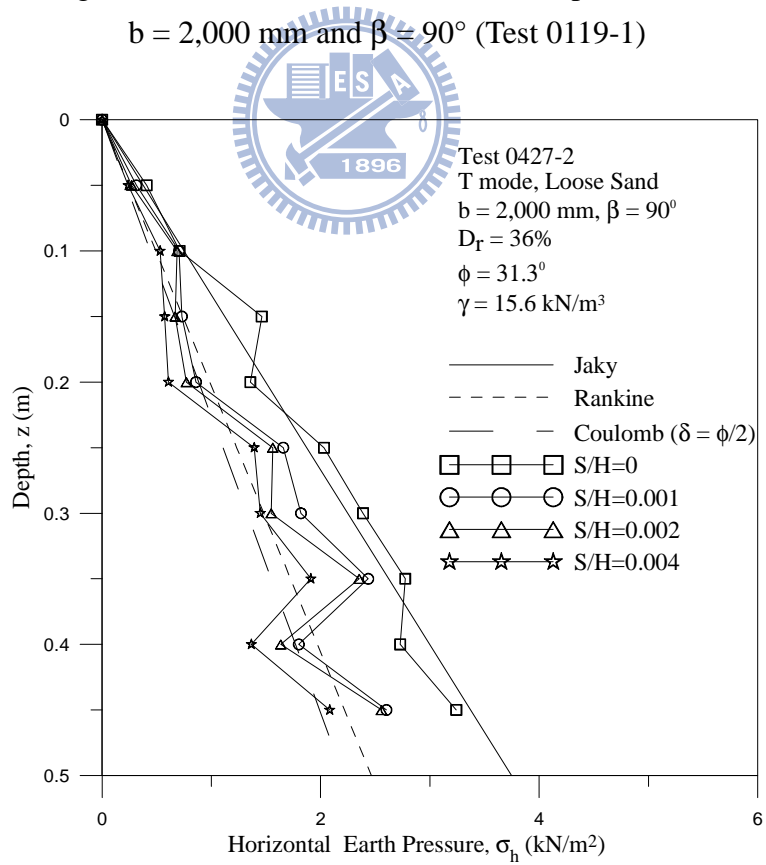


Fig. 6.3. Distribution of horizontal earth pressure for $b = 2,000 \text{ mm}$ and $\beta = 90^\circ$ (Test 0427-2)

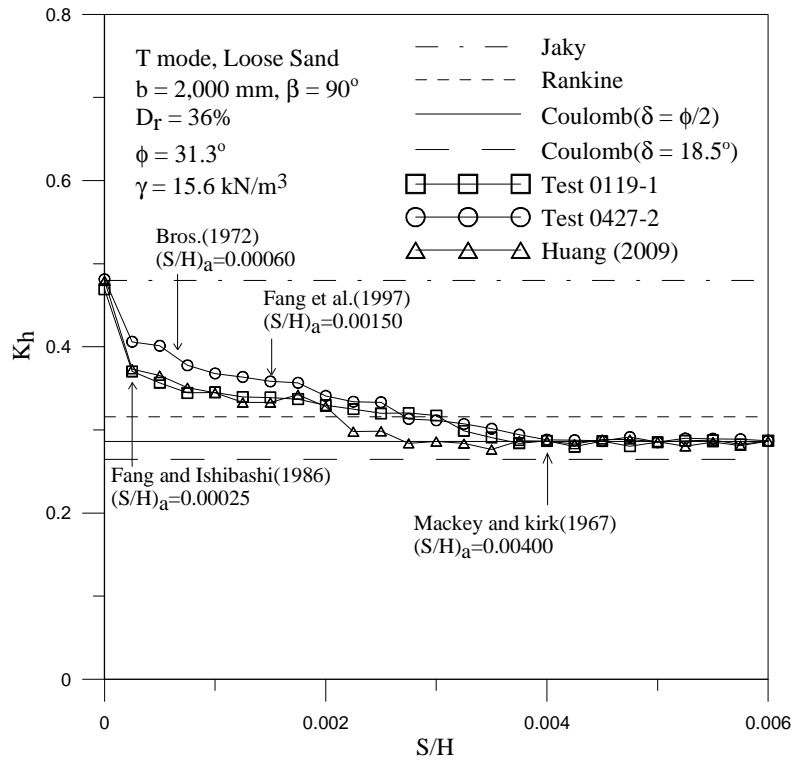


Fig. 6.4. Earth pressure coefficient K_h versus wall movement for $b = 2,000 \text{ mm}$ and $\beta = 90^\circ$

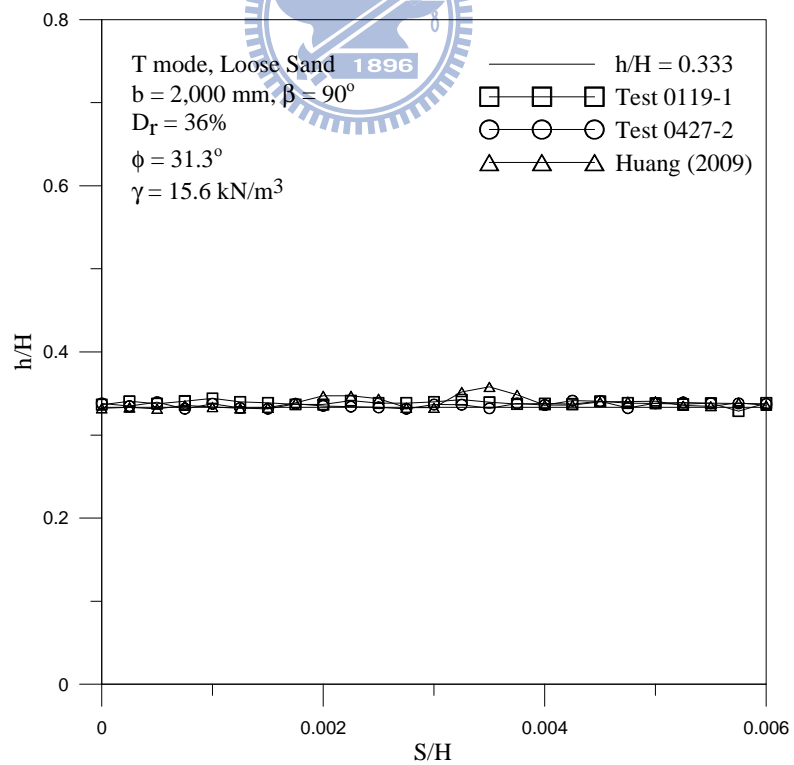
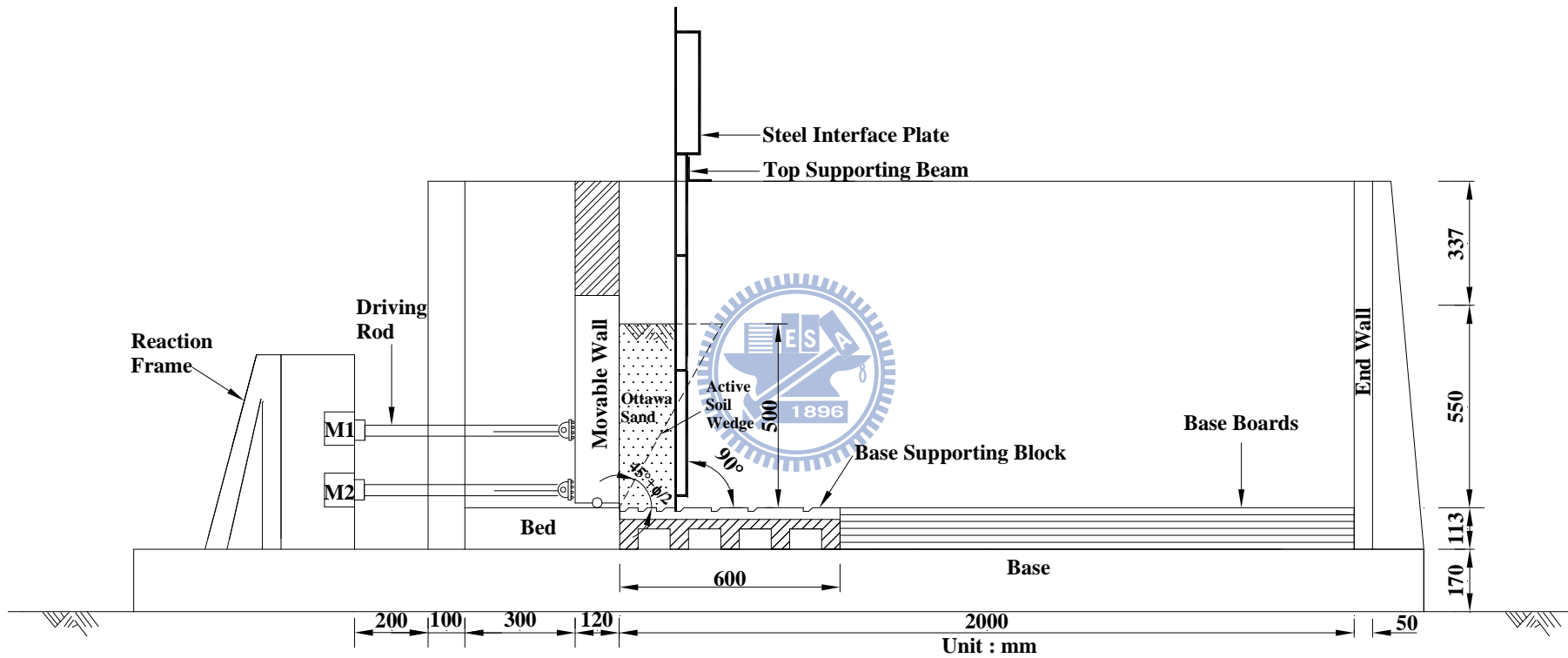


Fig. 6.5. Location of total thrust application for $b = 2,000 \text{ mm}$ and $\beta = 90^\circ$



(a)

Fig. 6.6. Model wall test with interface spacing $b = 150$ mm and $\beta = 90^\circ$



(b)

Fig. 6.6. Model wall test with interface spacing $b = 150$ mm and $\beta = 90^\circ$

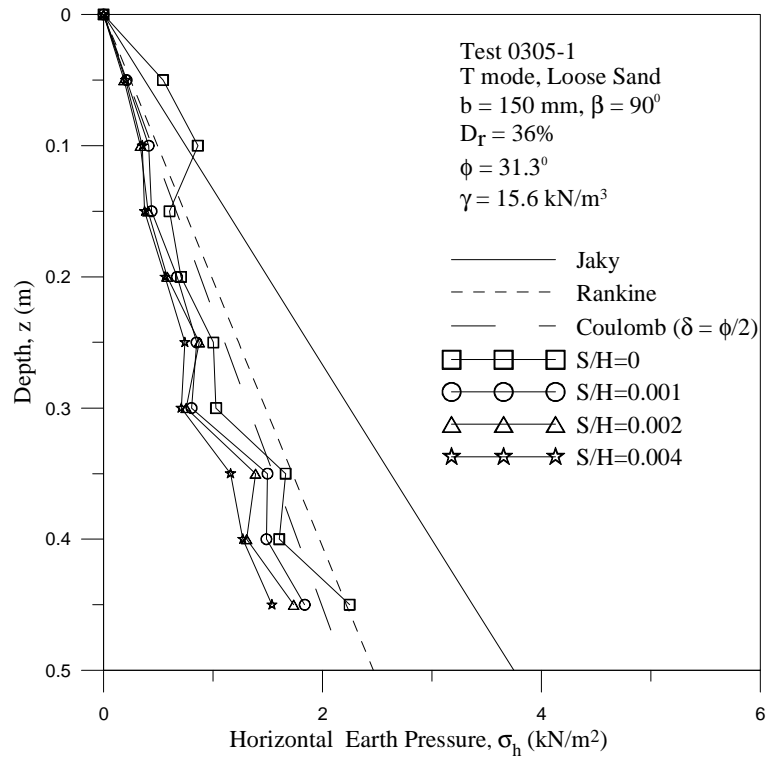


Fig. 6.7. Distribution of horizontal earth pressure for $b = 150 \text{ mm}$ and $\beta = 90^\circ$
 (Test 0305-1)

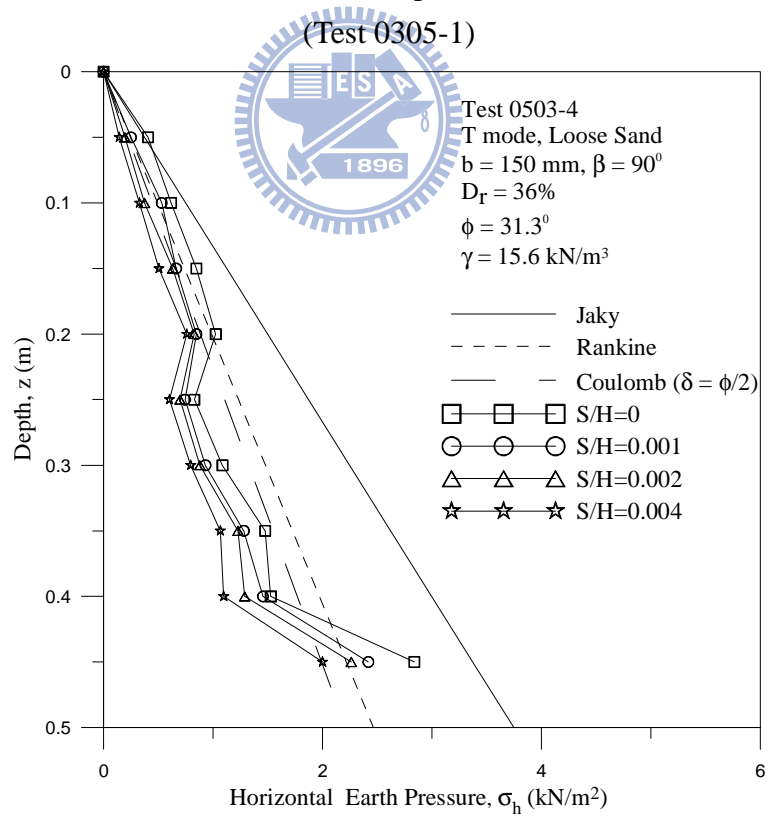
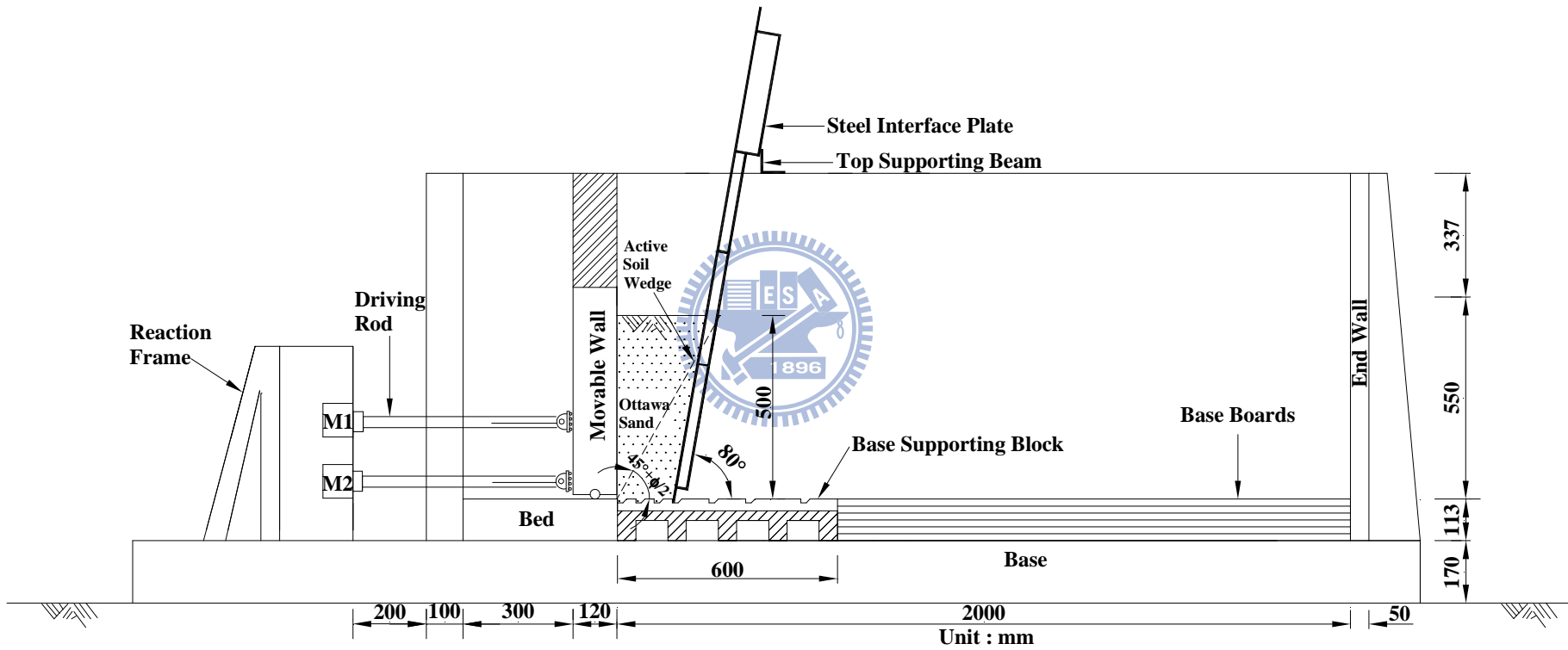


Fig. 6.8. Distribution of horizontal earth pressure for $b = 150 \text{ mm}$ and $\beta = 90^\circ$
 (Test 0503-4)



(a)

Fig. 6.9. Model wall test with interface spacing $b = 150$ mm and $\beta = 80^\circ$



(b)

Fig. 6.9. Model wall test with interface spacing $b = 150$ mm and $\beta = 80^\circ$

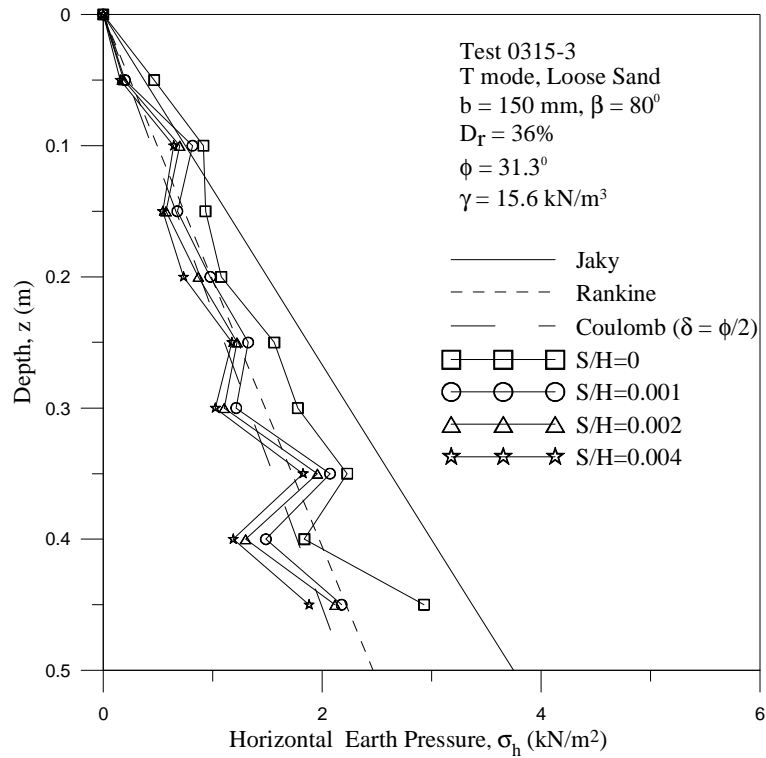


Fig. 6.10. Distribution of horizontal earth pressure for $b = 150 \text{ mm}$ and $\beta = 80^\circ$

(Test 0315-3)

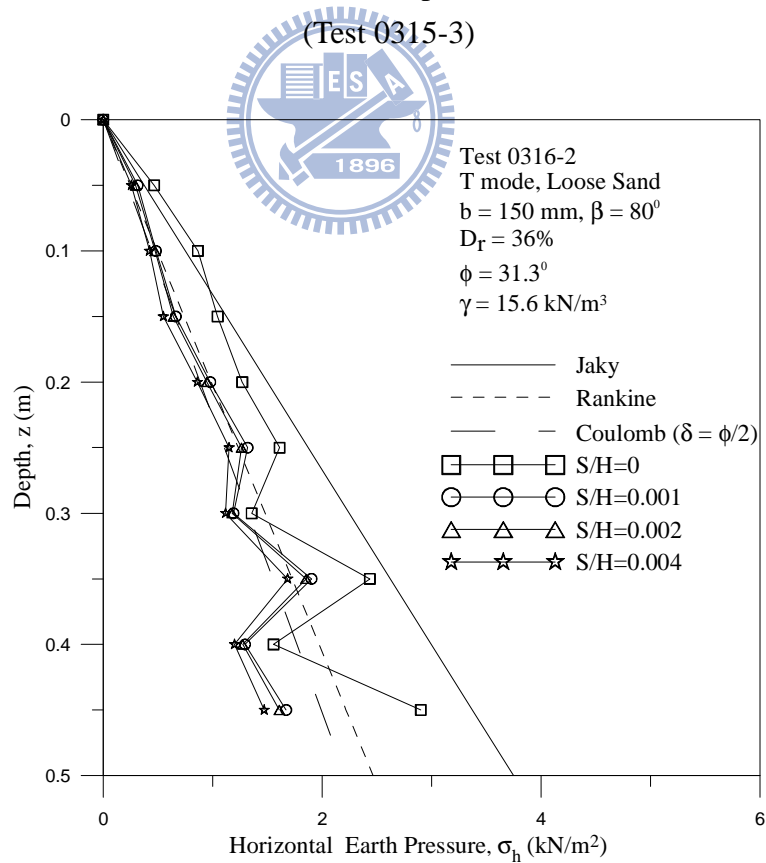
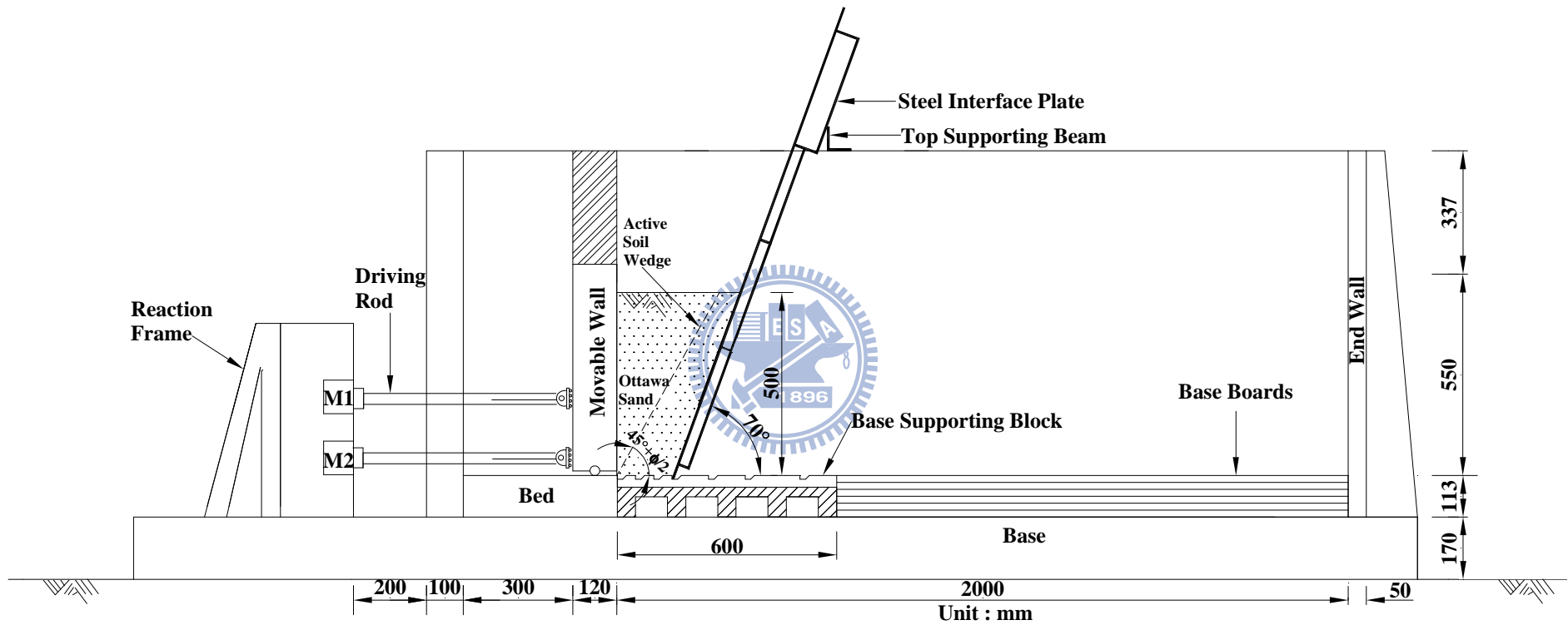


Fig. 6.11. Distribution of horizontal earth pressure for $b = 150 \text{ mm}$ and $\beta = 80^\circ$

(Test 0316-2)



(a)

Fig. 6.12. Model wall test with interface spacing $b = 150$ mm and $\beta = 70^\circ$



(b)

Fig. 6.12. Model wall test with interface spacing $b = 150$ mm and $\beta = 70^\circ$

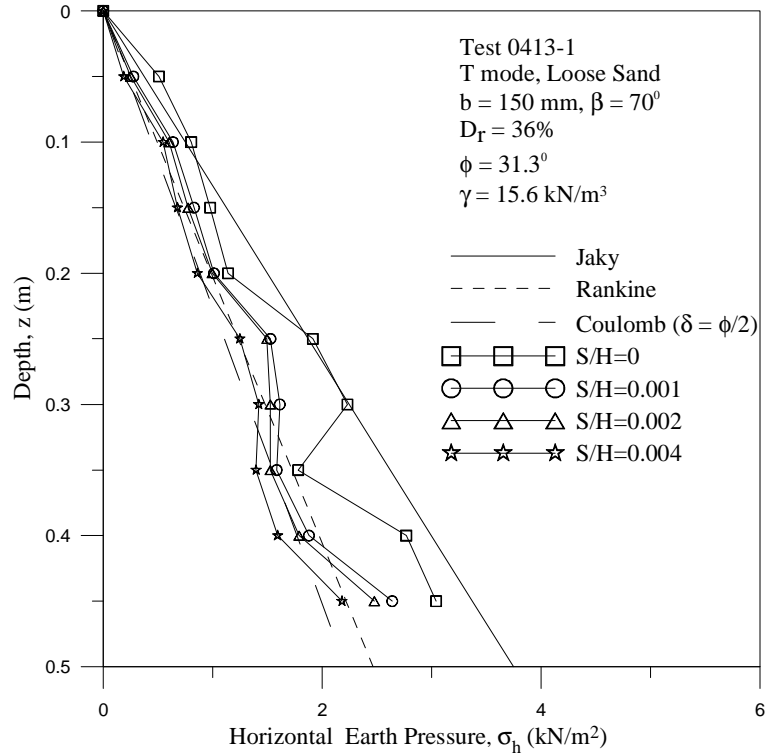


Fig. 6.13. Distribution of horizontal earth pressure for $b = 150 \text{ mm}$ and $\beta = 70^\circ$ (Test 0413-1)

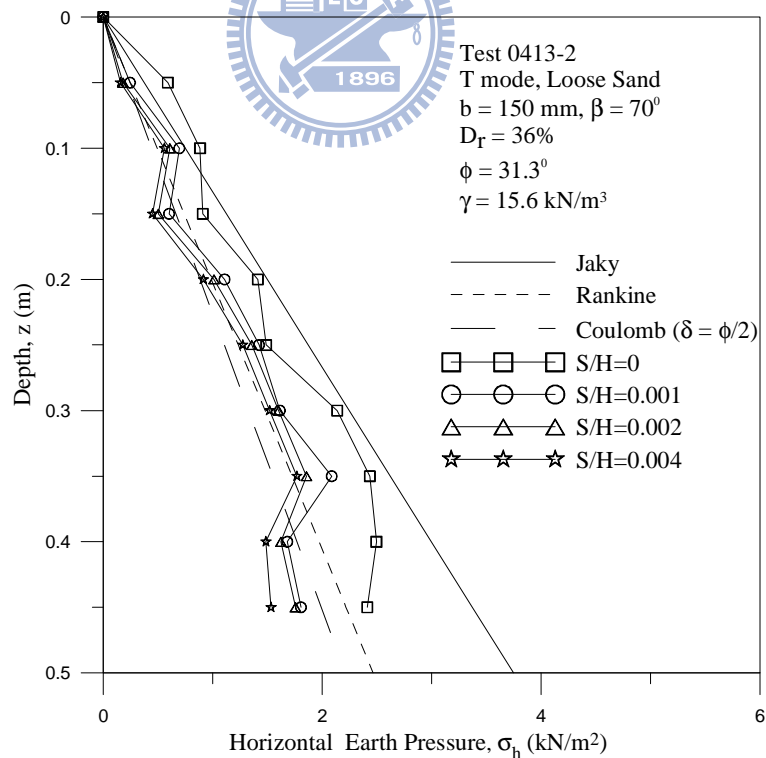
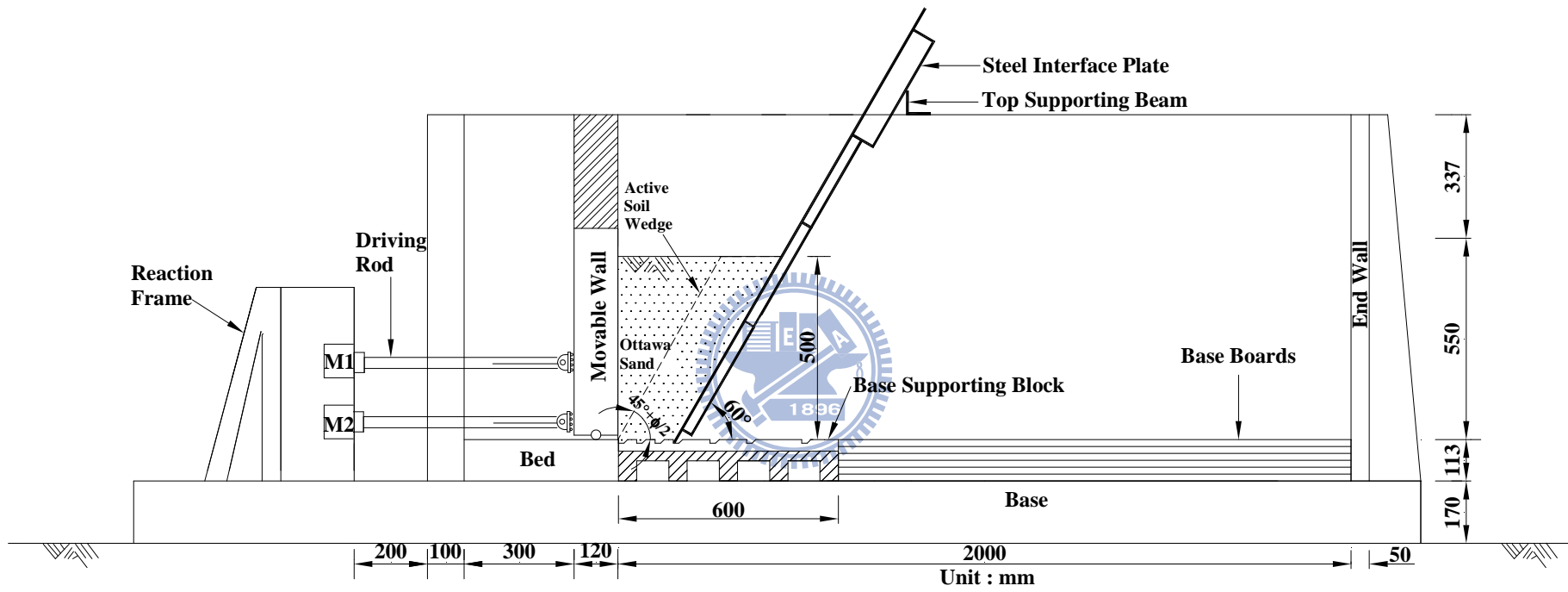


Fig. 6.14. Distribution of horizontal earth pressure for $b = 150 \text{ mm}$ and $\beta = 70^\circ$ (Test 0413-2)



(a)

Fig. 6.15. Model wall test with interface spacing $b = 150$ mm and $\beta = 60^\circ$



(b)

Fig. 6.15. Model wall test with interface spacing $b = 150$ mm and $\beta = 60^\circ$

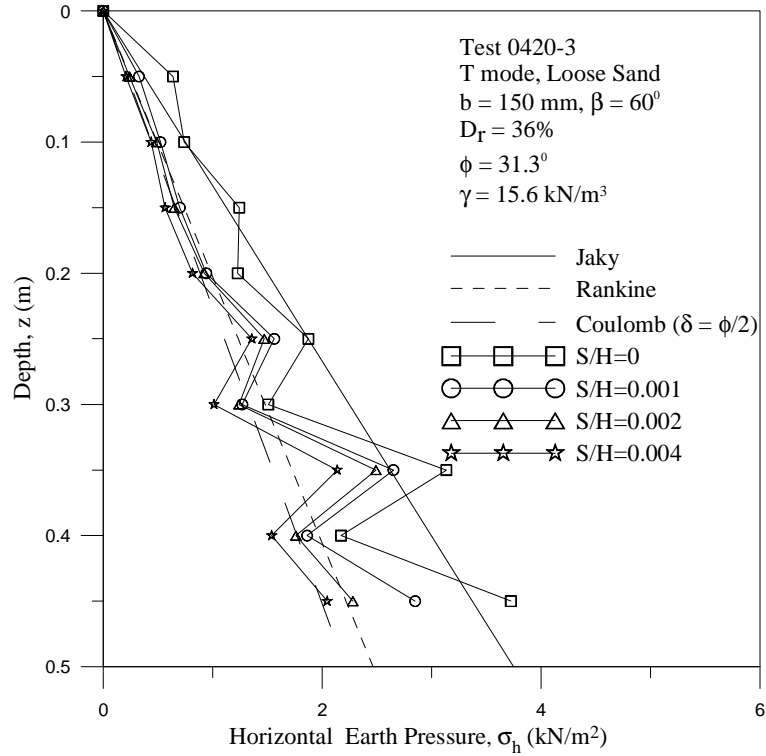


Fig. 6.16. Distribution of horizontal earth pressure for $b = 150 \text{ mm}$ and $\beta = 60^\circ$ (Test 0420-3)

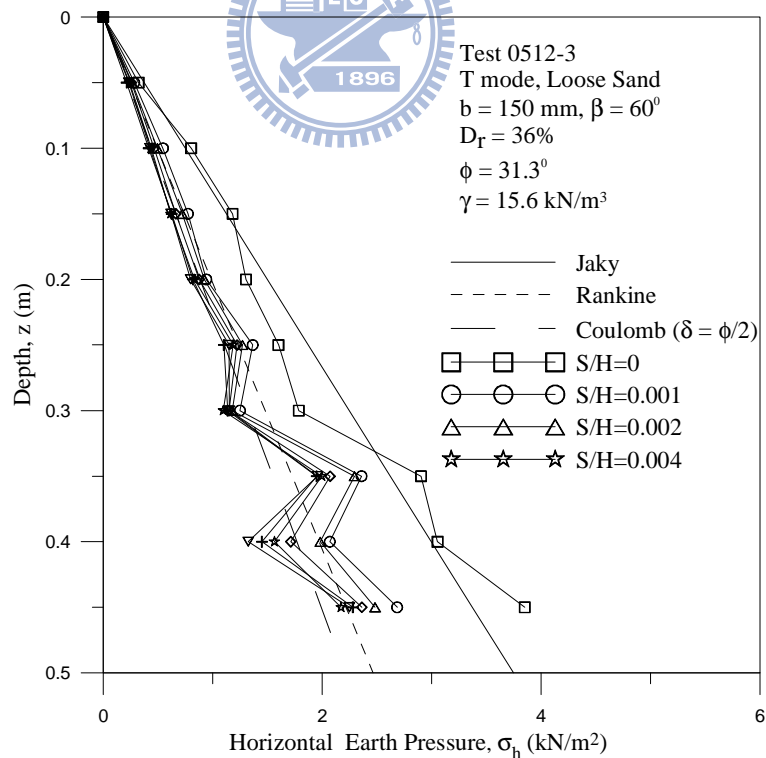


Fig. 6.17. Distribution of horizontal earth pressure for $b = 150 \text{ mm}$ and $\beta = 60^\circ$ (Test 0512-3)

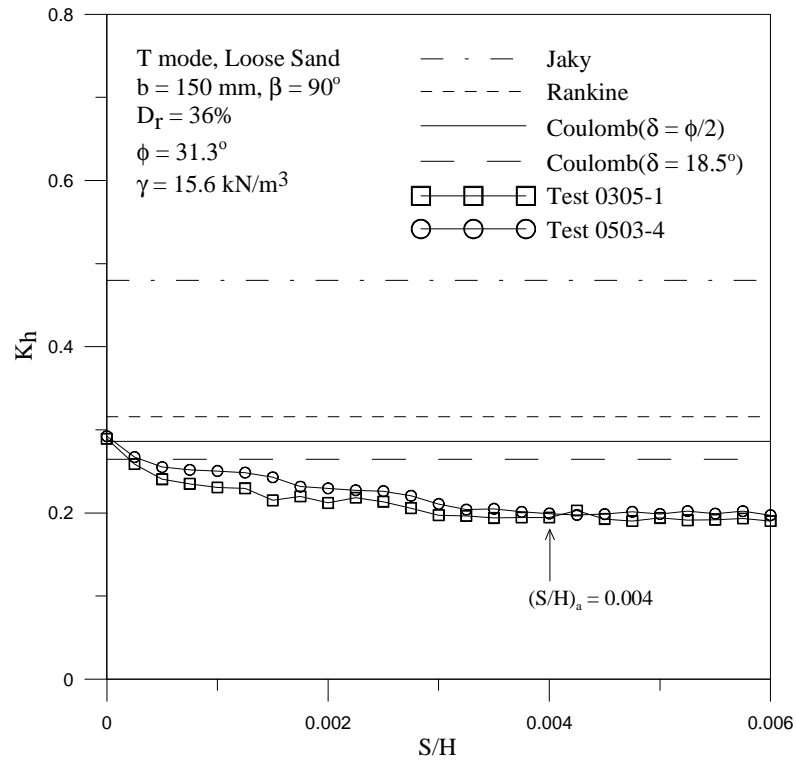


Fig. 6.18. Earth pressure coefficient K_h versus wall movement for $b = 150 \text{ mm}$ and $\beta = 90^\circ$

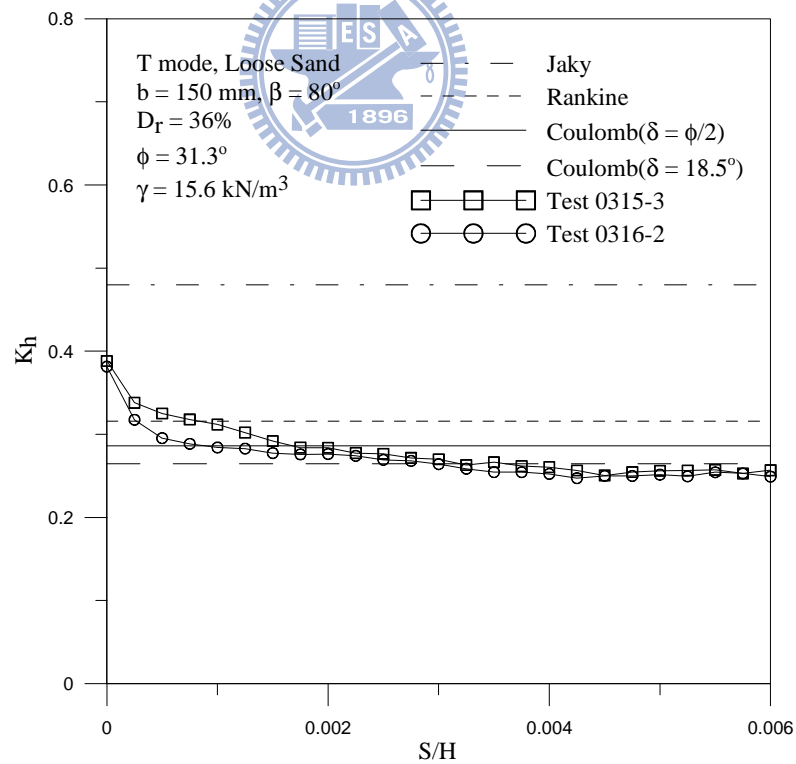


Fig. 6.19. Earth pressure coefficient K_h versus wall movement for $b = 150 \text{ mm}$ and $\beta = 80^\circ$

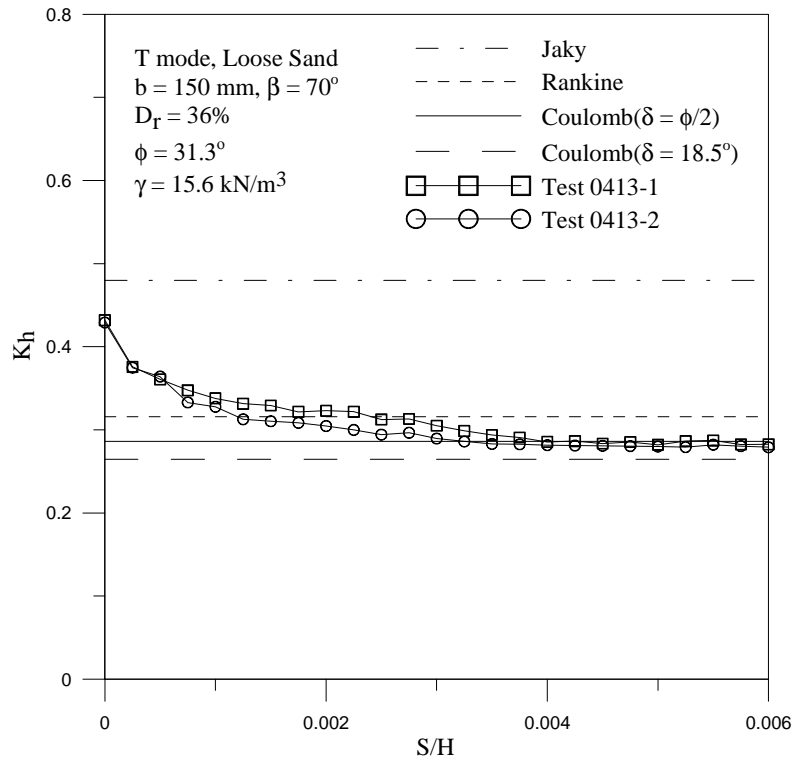


Fig. 6.20. Earth pressure coefficient K_h versus wall movement for $b = 150 \text{ mm}$ and $\beta = 70^\circ$

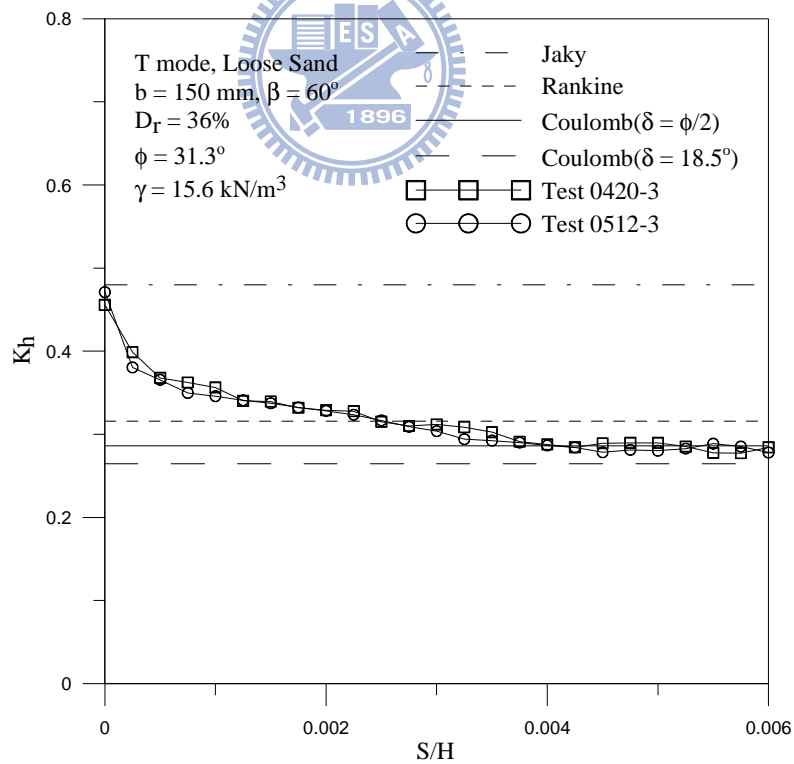


Fig. 6.21. Earth pressure coefficient K_h versus wall movement for $b = 150 \text{ mm}$ and $\beta = 60^\circ$

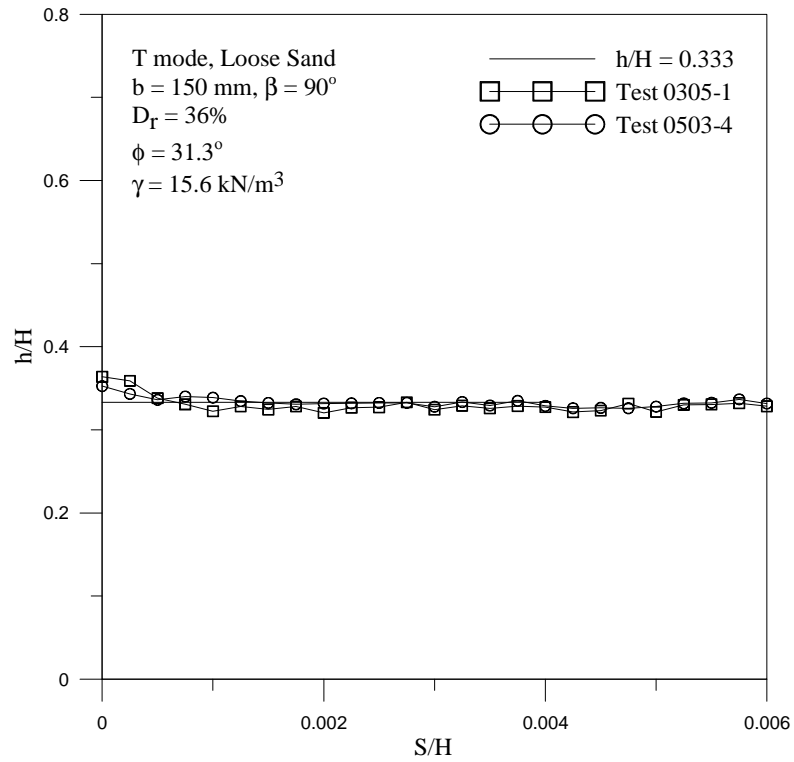


Fig. 6.22. Location of total soil thrust for $b = 150 \text{ mm}$ and $\beta = 90^\circ$

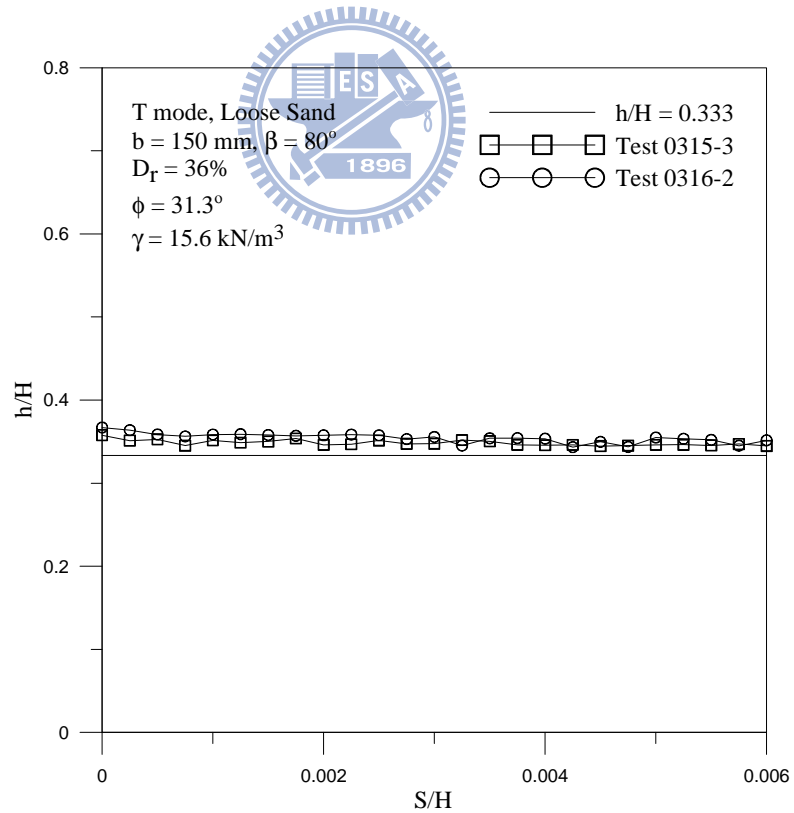


Fig. 6.23. Location of total soil thrust for $b = 150 \text{ mm}$ and $\beta = 80^\circ$

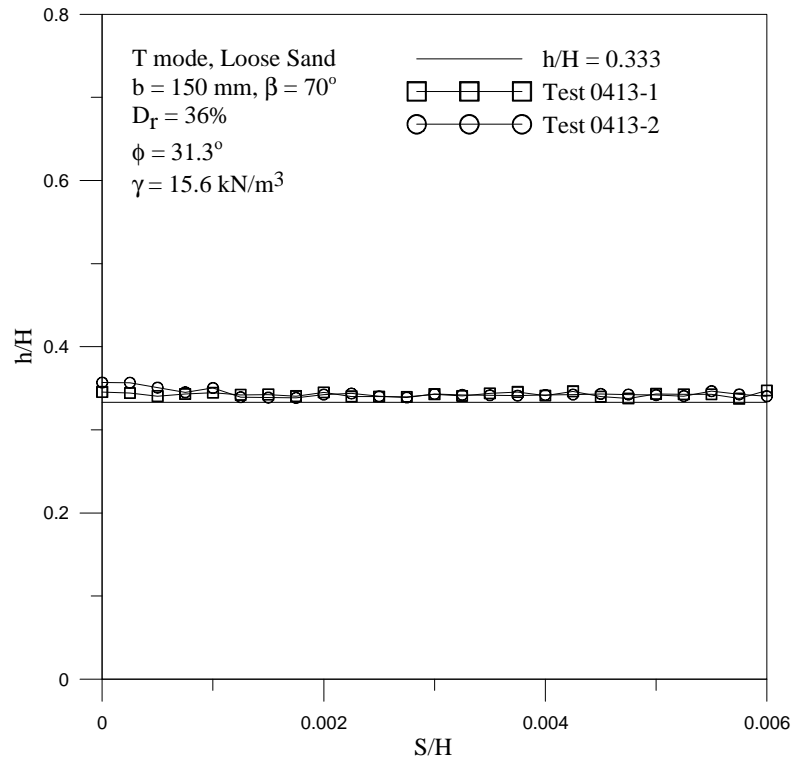


Fig. 6.24. Location of total soil thrust for $b = 150 \text{ mm}$ and $\beta = 70^\circ$

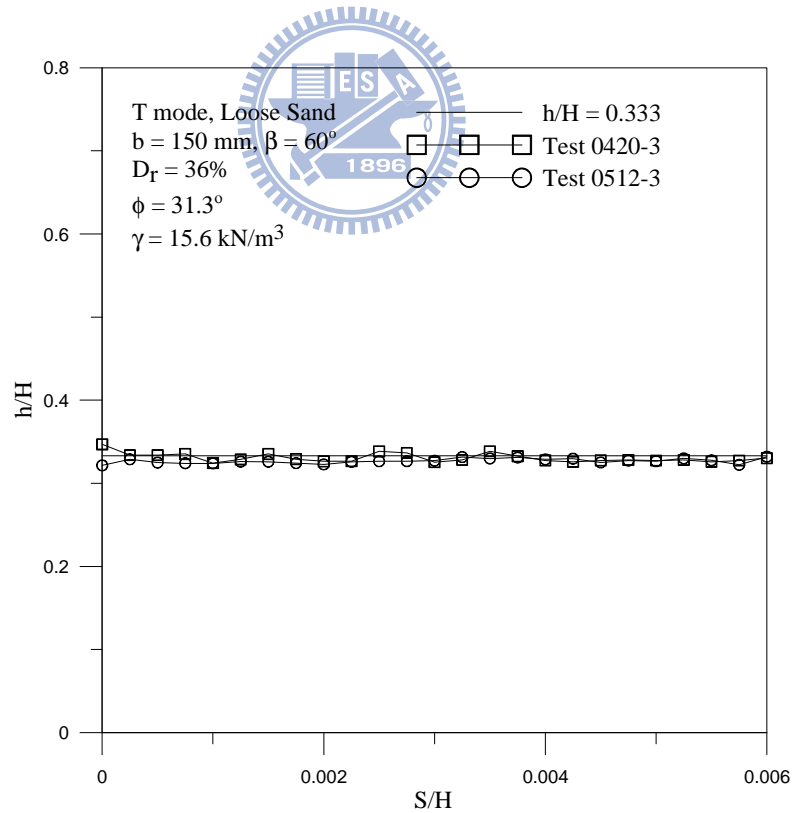
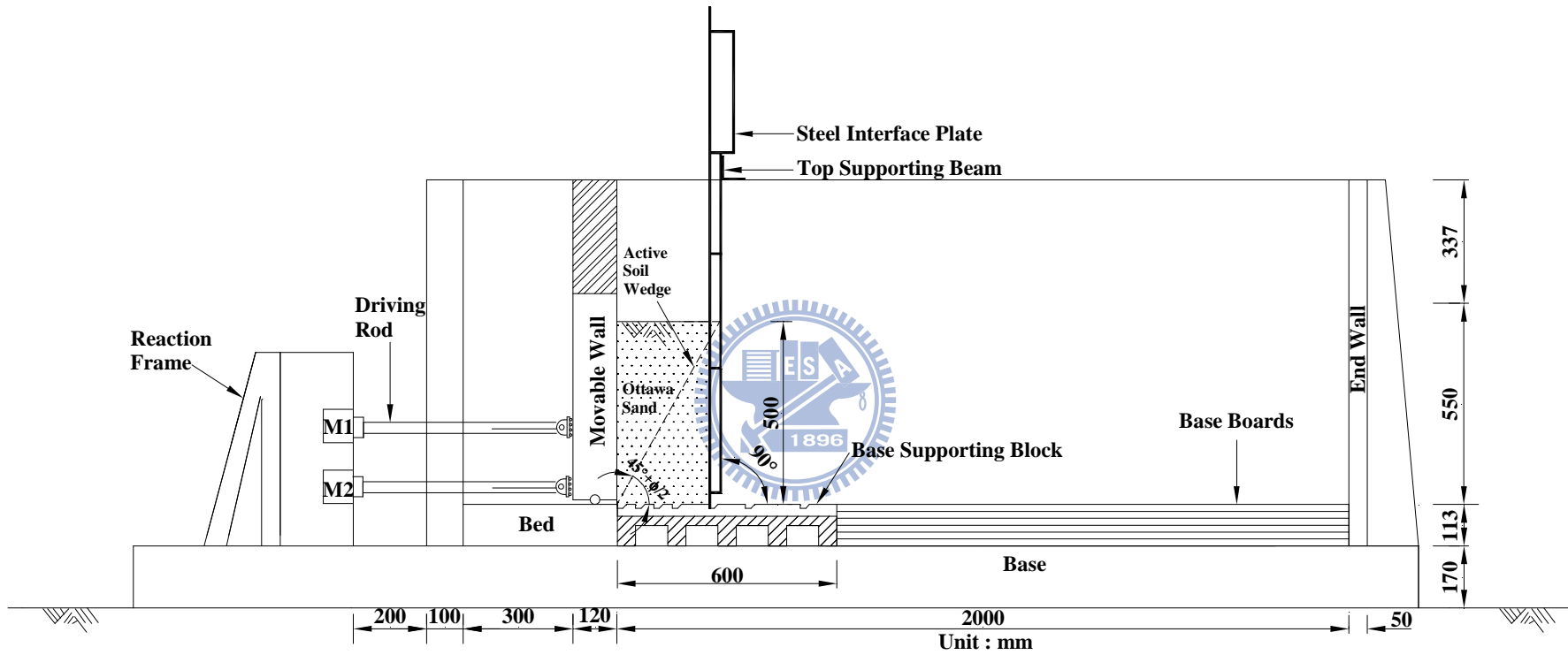
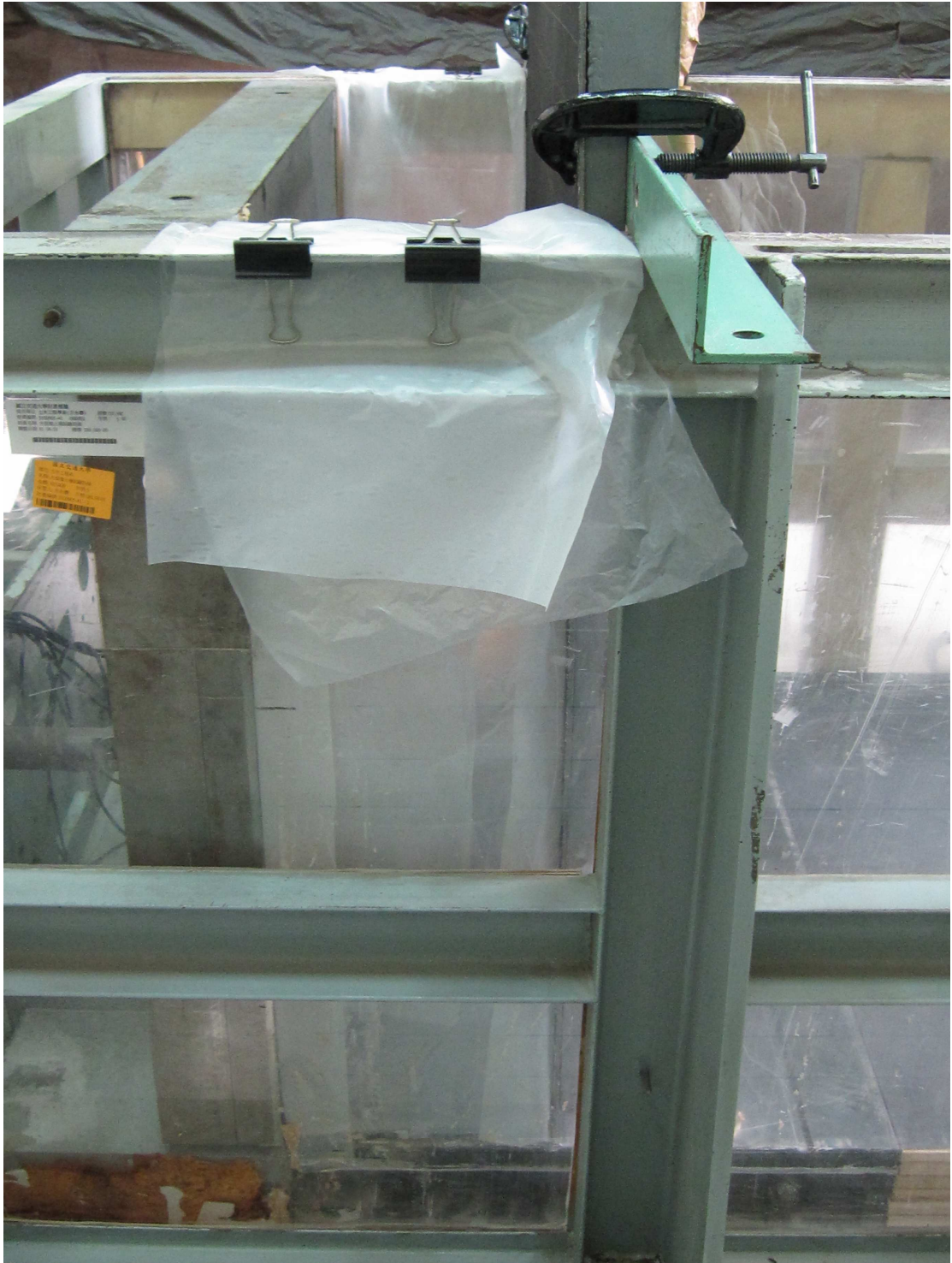


Fig. 6.25. Location of total soil thrust for $b = 150 \text{ mm}$ and $\beta = 60^\circ$



(a)

Fig. 6.26. Model wall test with interface spacing $b = 250$ mm and $\beta = 90^\circ$



(b)

Fig. 6.26. Model wall test with interface spacing $b = 250$ mm and $\beta = 90^\circ$

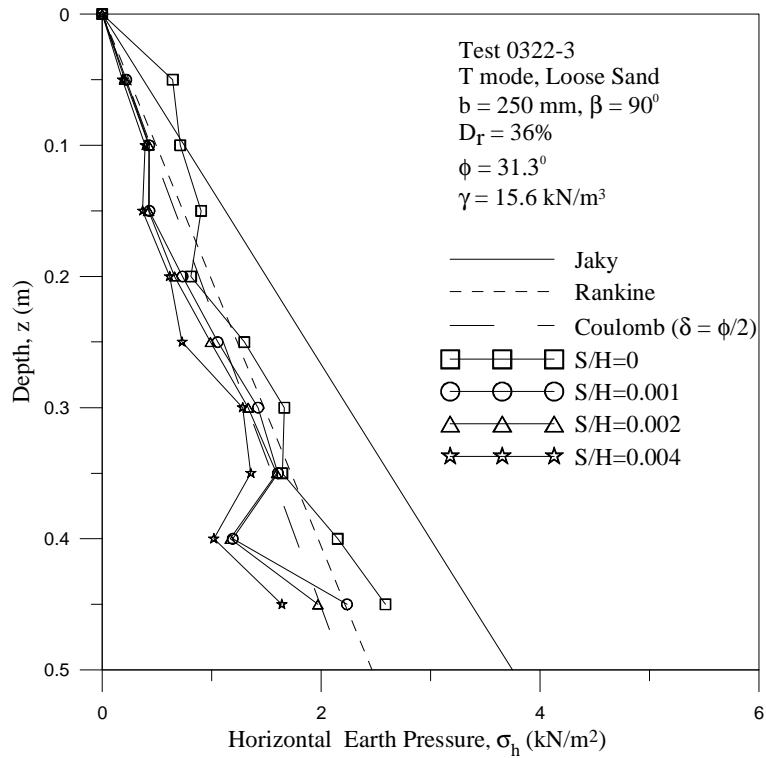


Fig. 6.27. Distribution of horizontal earth pressure for $b = 250 \text{ mm}$ and $\beta = 90^\circ$ (Test 0322-3)

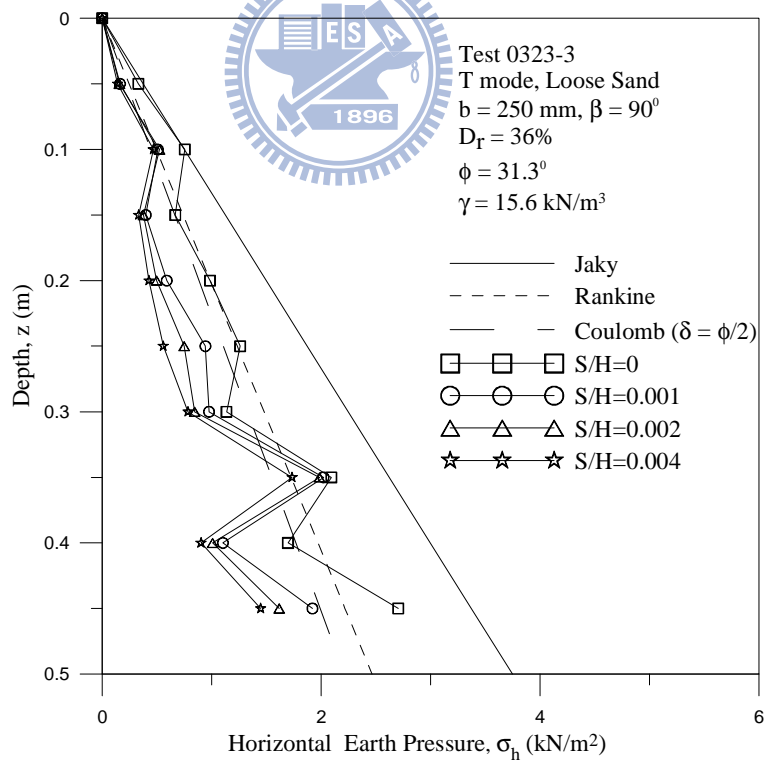
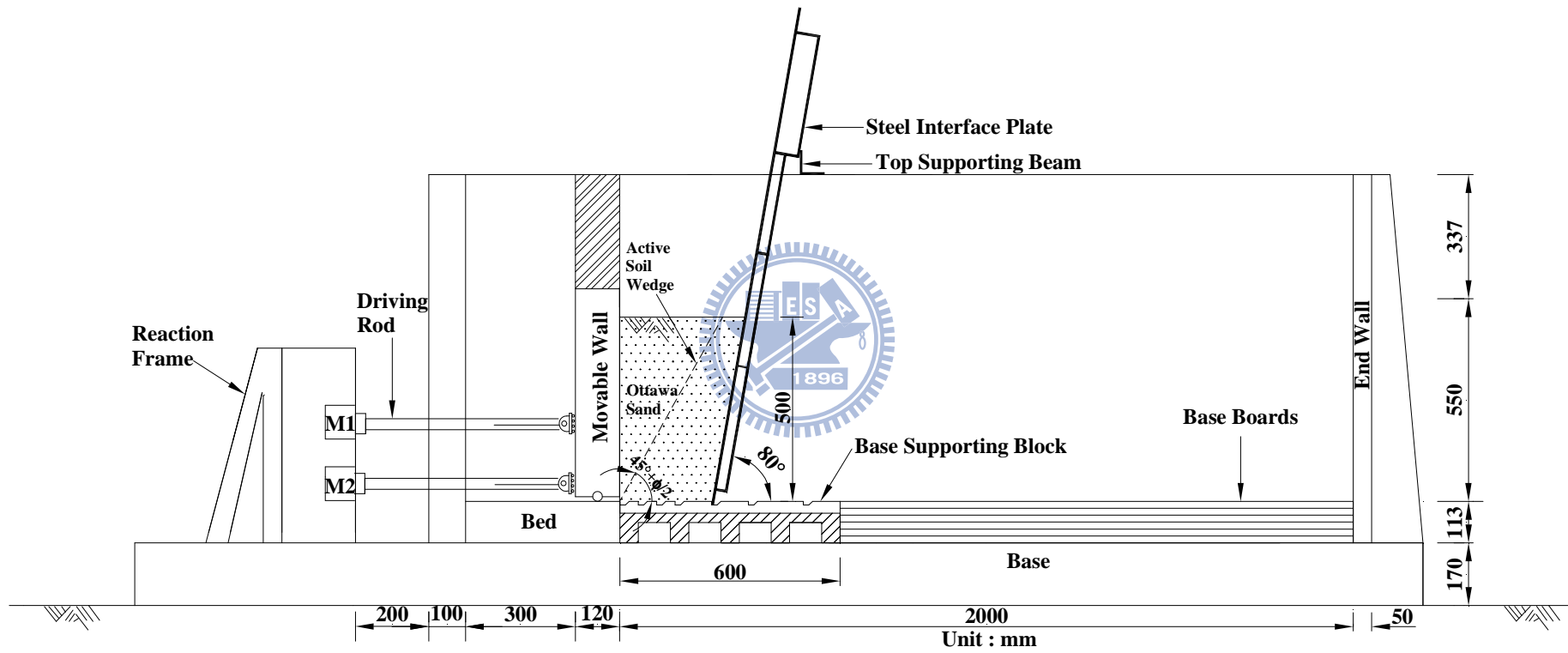


Fig. 6.28. Distribution of horizontal earth pressure for $b = 250 \text{ mm}$ and $\beta = 90^\circ$ (Test 0323-3)



(a)

Fig. 6.29. Model wall test with interface spacing $b = 250$ mm and $\beta = 80^\circ$



(b)

Fig. 6.29. Model wall test with interface spacing $b = 250$ mm and $\beta = 80^\circ$

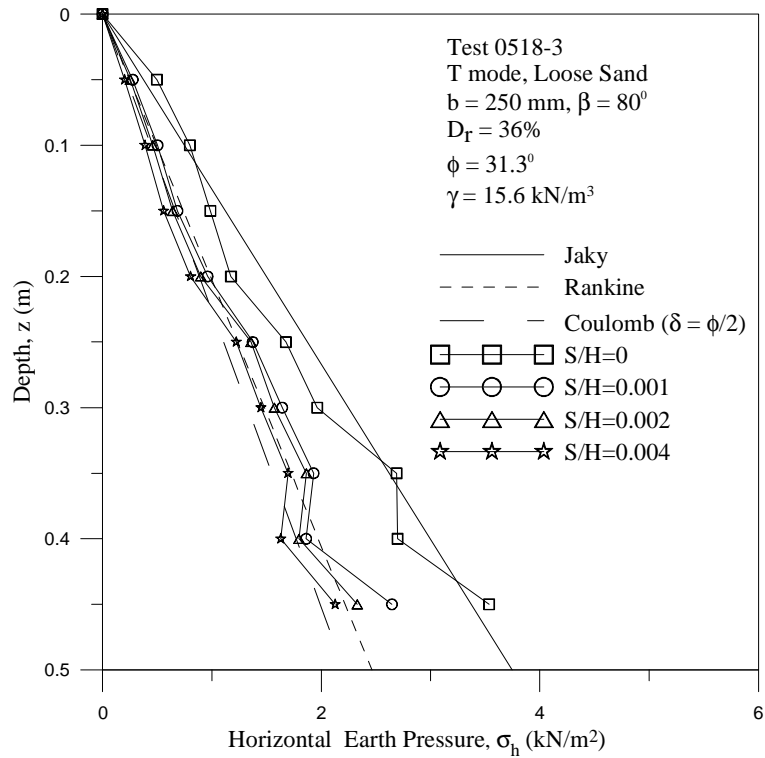


Fig. 6.30. Distribution of horizontal earth pressure for $b = 250 \text{ mm}$ and $\beta = 80^\circ$ (Test 0518-3)

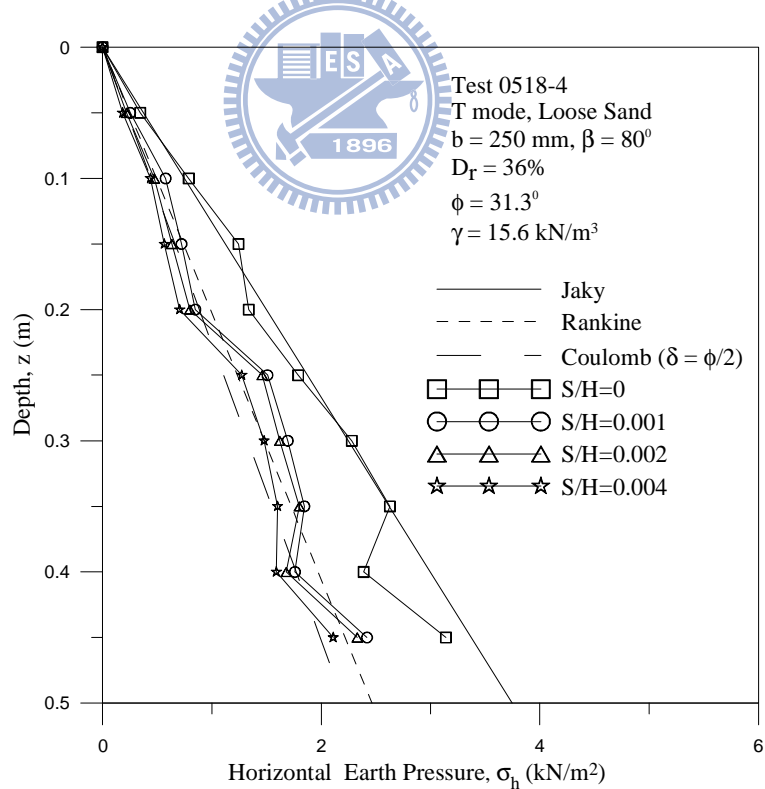
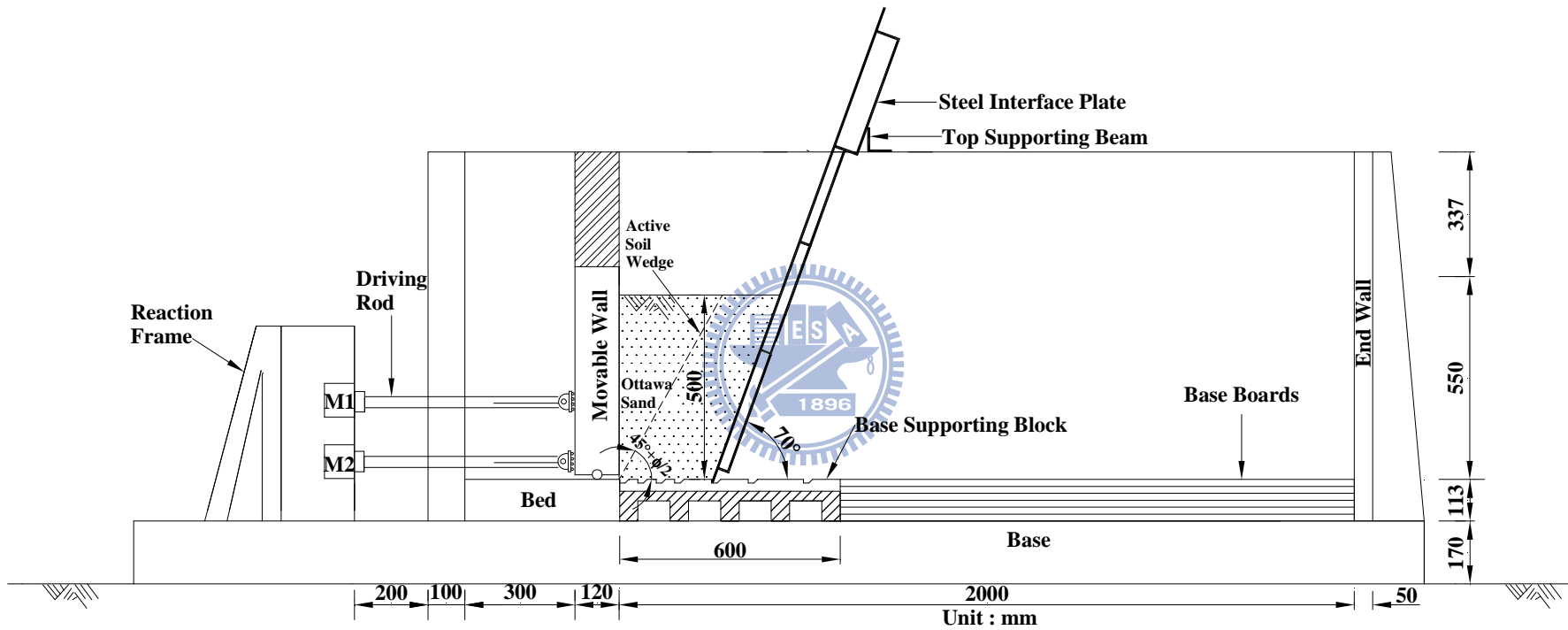


Fig. 6.31. Distribution of horizontal earth pressure for $b = 250 \text{ mm}$ and $\beta = 80^\circ$ (Test 0518-4)



(a)

Fig. 6.32. Model wall test with interface spacing $b = 250$ mm and $\beta = 70^\circ$



(b)

Fig. 6.32. Model wall test with interface spacing $b = 250$ mm and $\beta = 70^\circ$

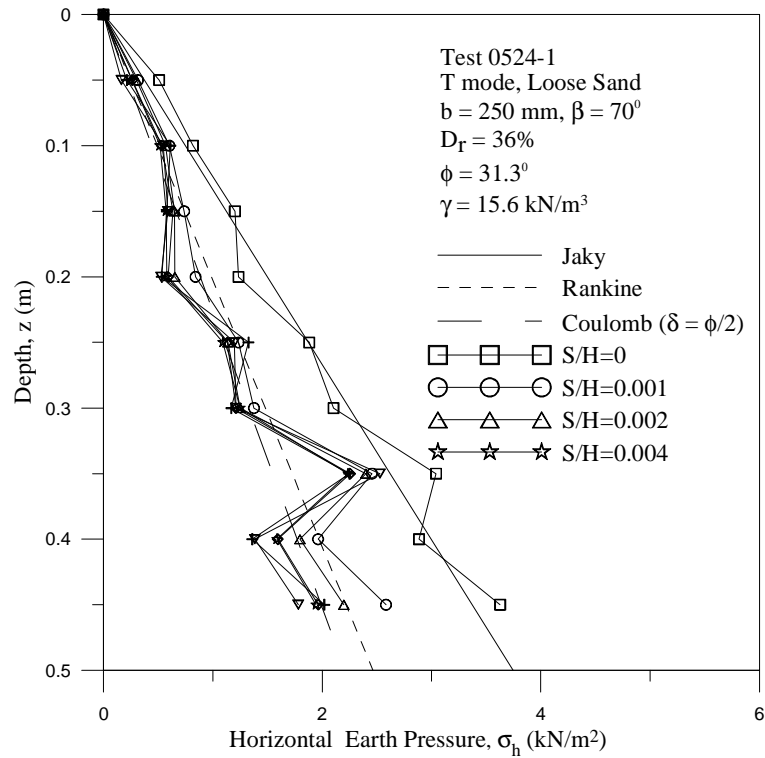


Fig. 6.33. Distribution of horizontal earth pressure for $b = 250 \text{ mm}$ and $\beta = 70^\circ$

(Test 0524-1)

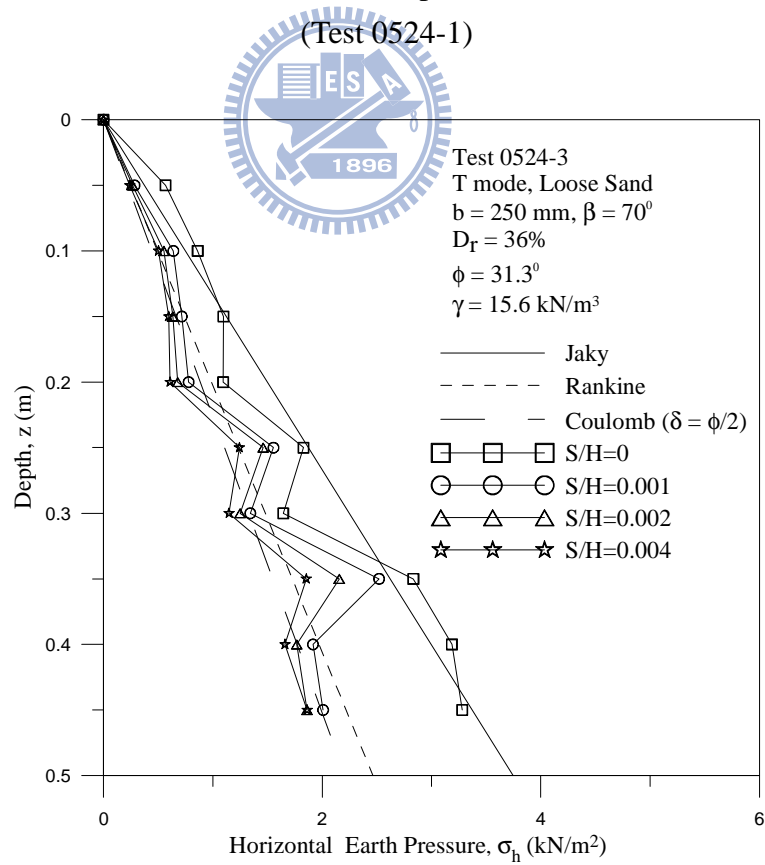


Fig. 6.34. Distribution of horizontal earth pressure for $b = 250 \text{ mm}$ and $\beta = 70^\circ$

(Test 0524-3)

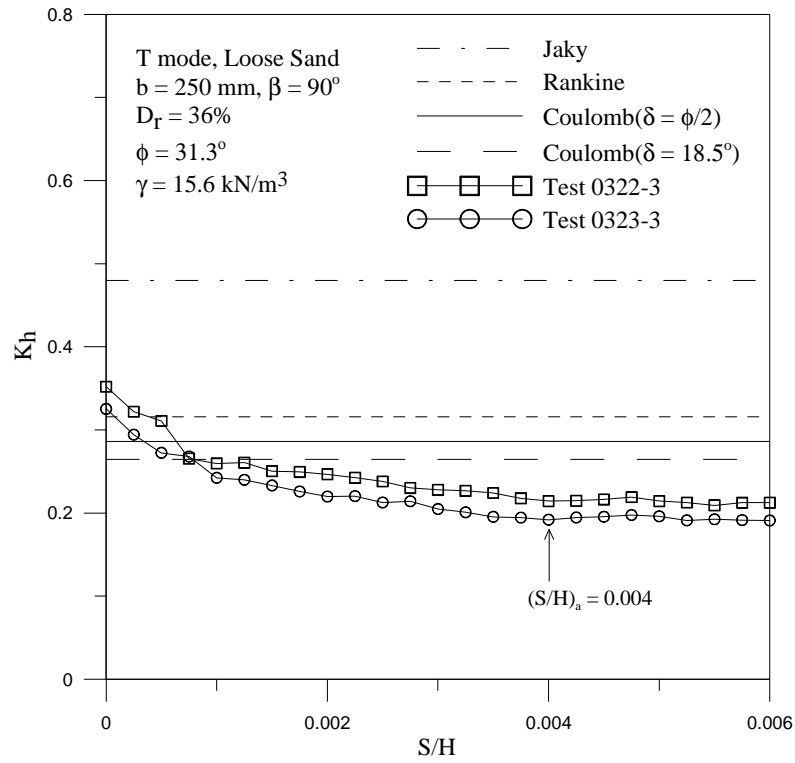


Fig. 6.35. Earth pressure coefficient K_h versus wall movement for $b = 250 \text{ mm}$ and $\beta = 90^\circ$

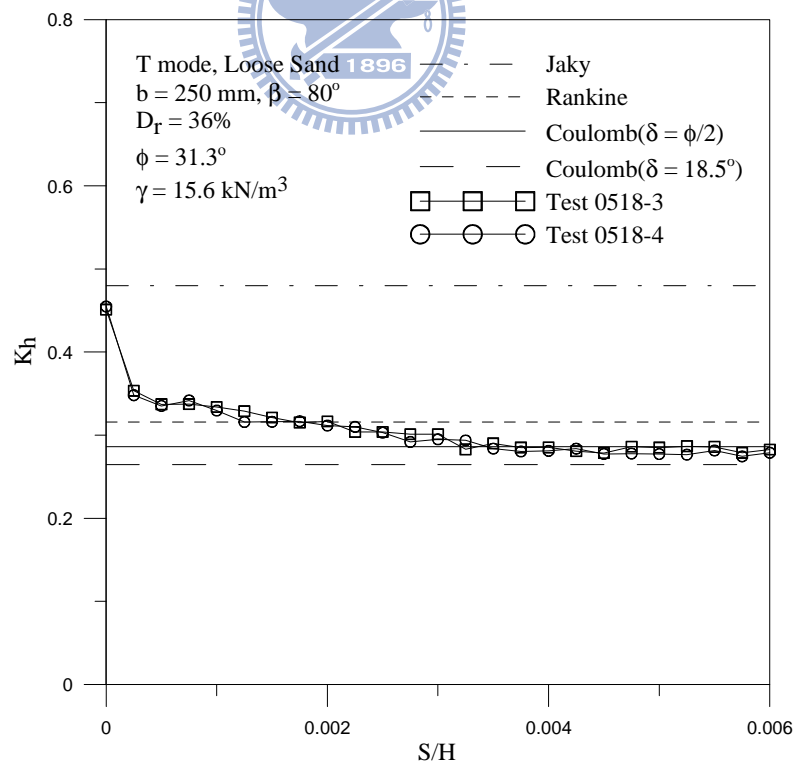


Fig. 6.36. Earth pressure coefficient K_h versus wall movement for $b = 250 \text{ mm}$ and $\beta = 80^\circ$

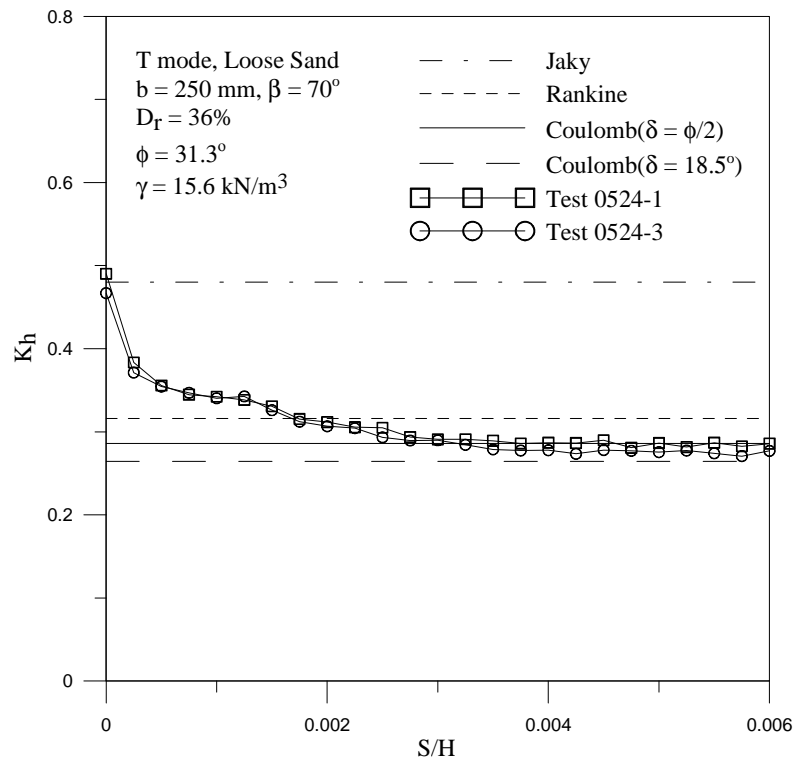
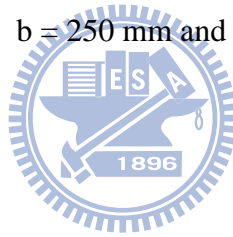


Fig. 6.37. Earth pressure coefficient K_h versus wall movement for $b = 250 \text{ mm}$ and $\beta = 70^\circ$



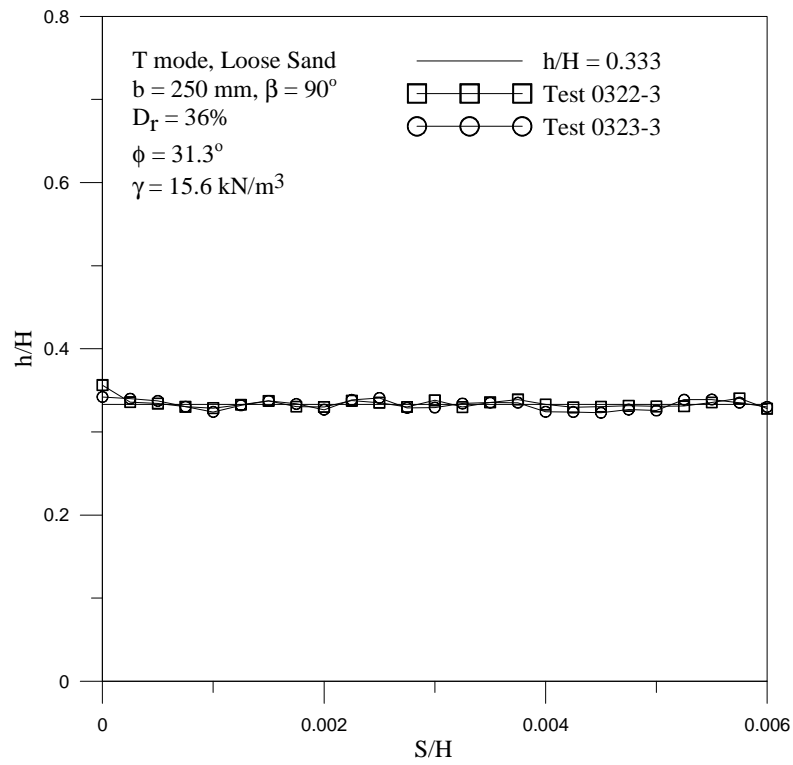


Fig. 6.38. Location of total soil thrust for $b = 250 \text{ mm}$ and $\beta = 90^\circ$

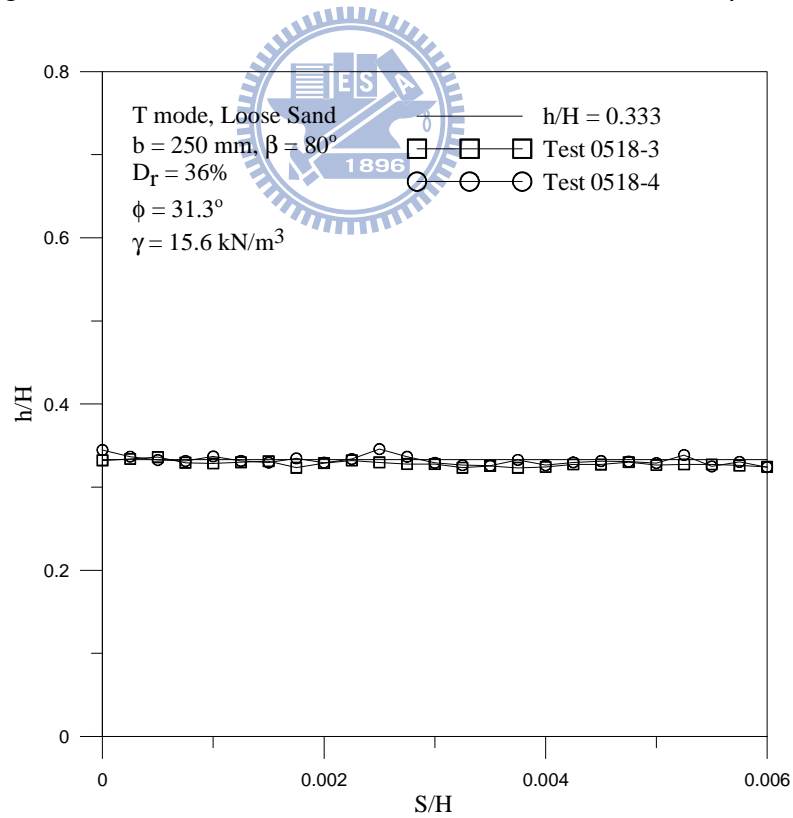


Fig. 6.39. Location of total soil thrust for $b = 250 \text{ mm}$ and $\beta = 80^\circ$

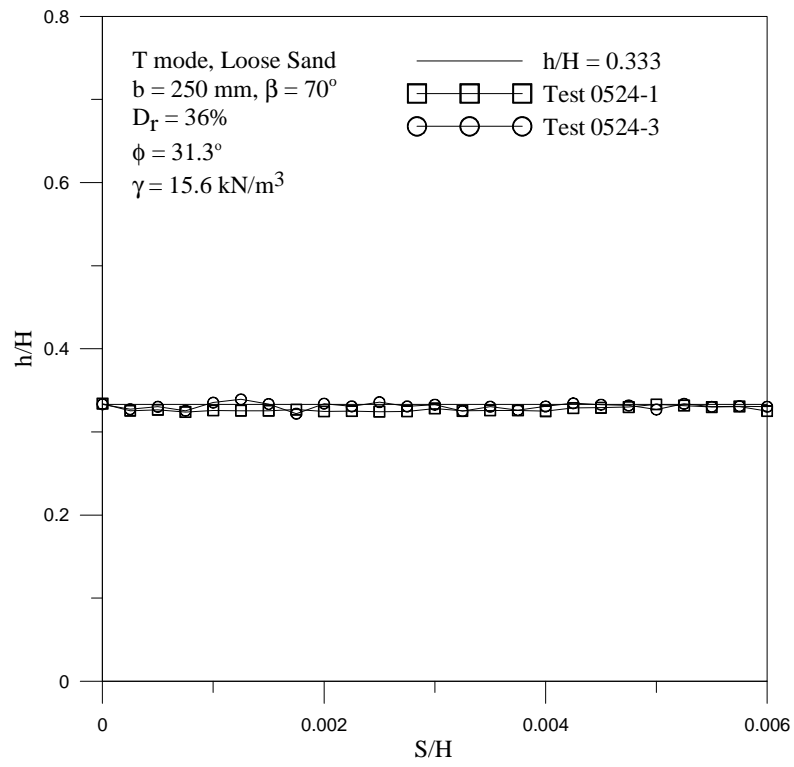
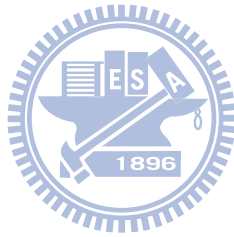
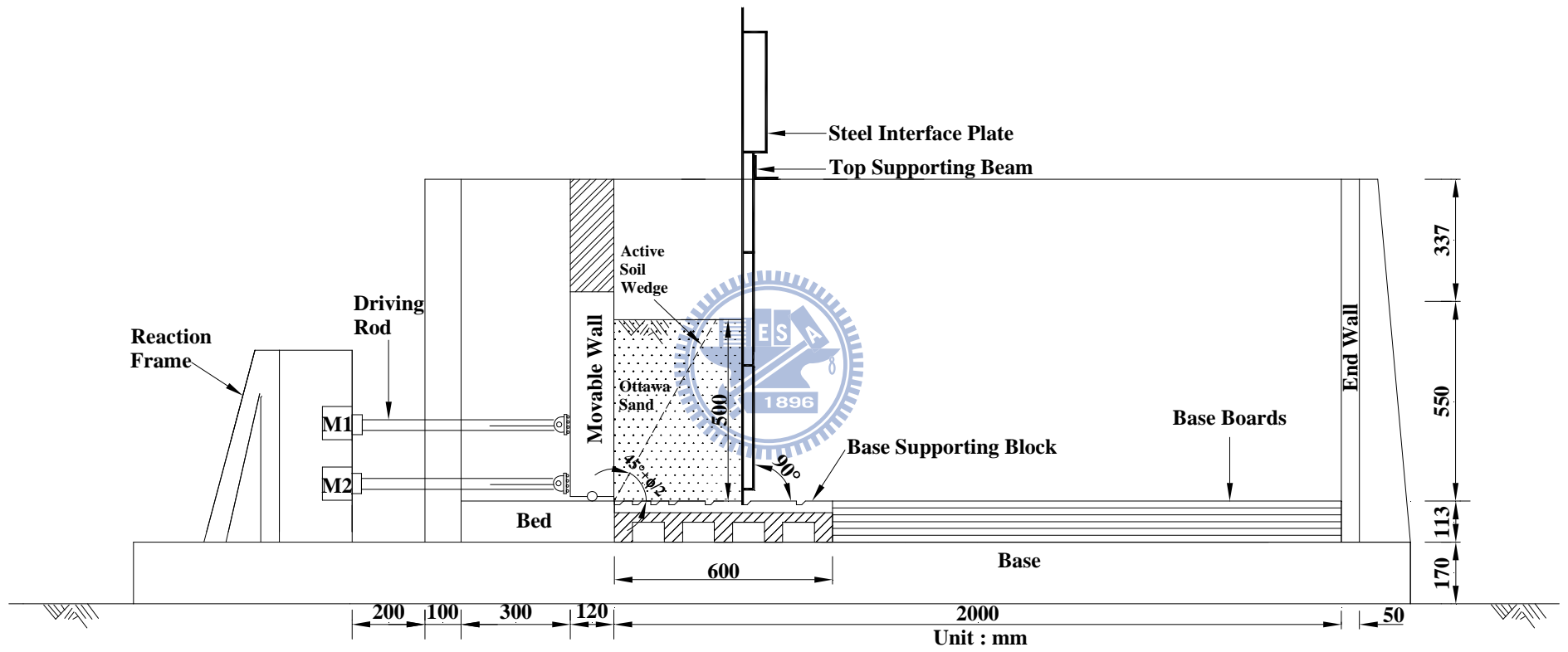


Fig. 6.40. Location of total soil thrust for $b = 250 \text{ mm}$ and $\beta = 70^\circ$





(a)

Fig. 6.41. Model wall test with interface spacing $b = 350$ mm and $\beta = 90^\circ$



(b)

Fig. 6.41. Model wall test with interface spacing $b = 350$ mm and $\beta = 90^\circ$

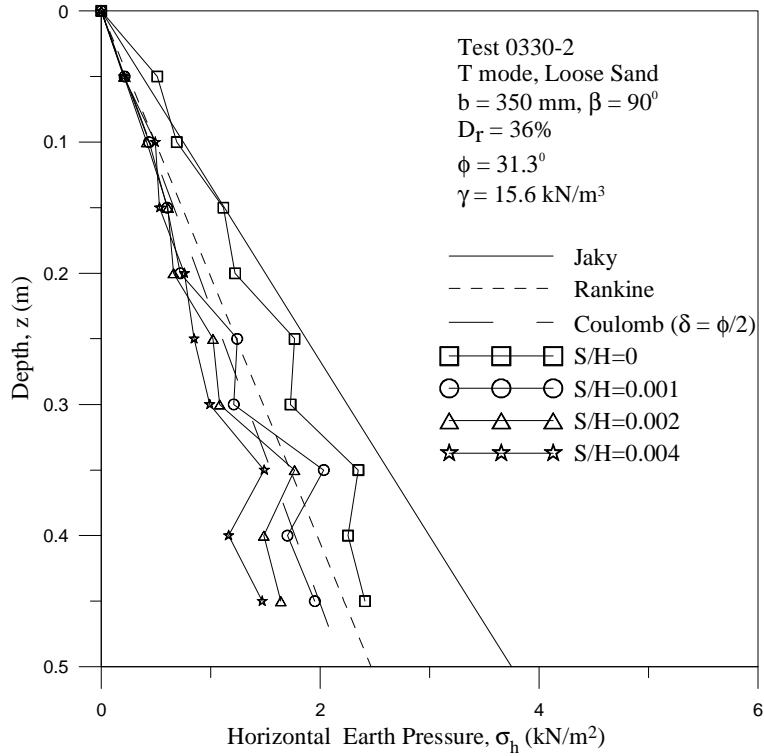


Fig. 6.42. Distribution of horizontal earth pressure for $b = 350 \text{ mm}$ and $\beta = 90^\circ$ (Test 0330-2)

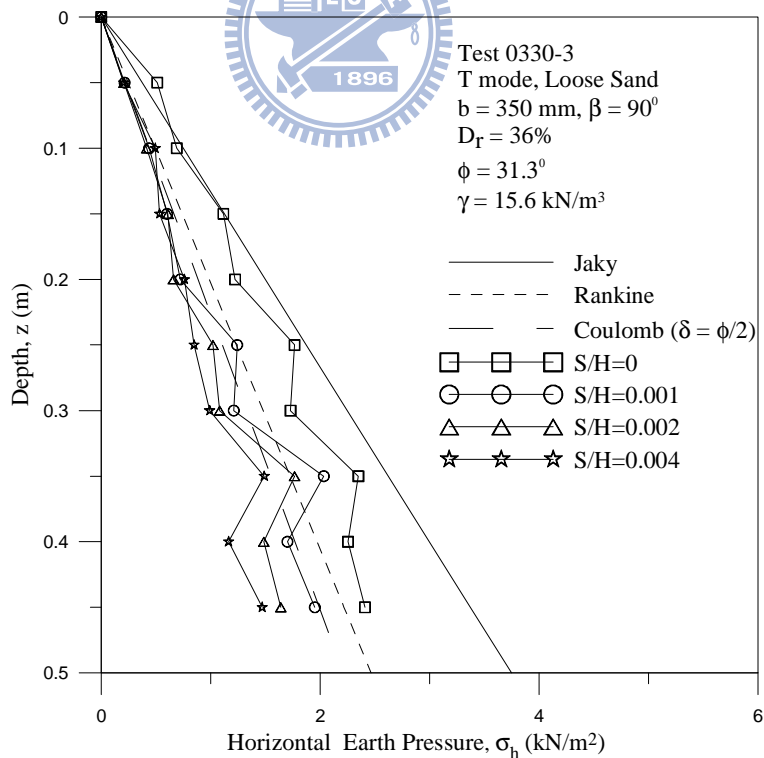
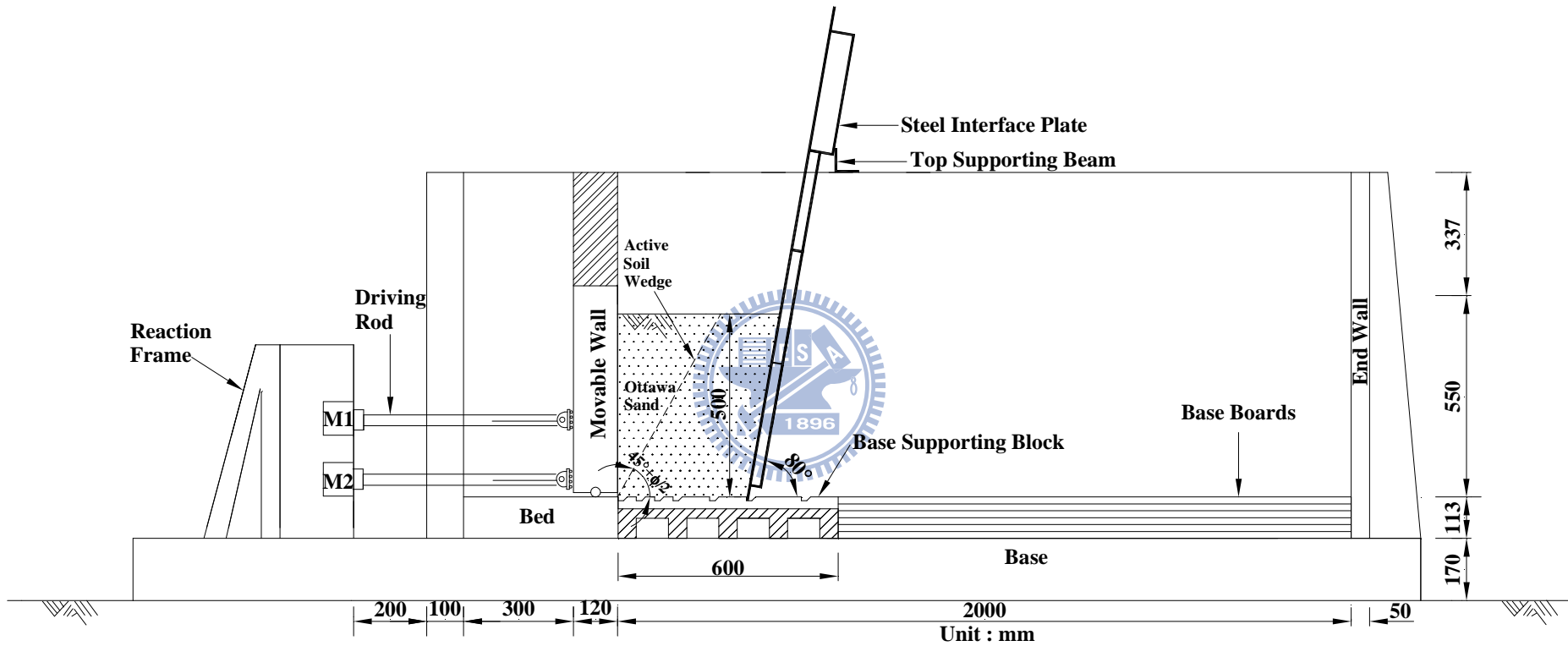
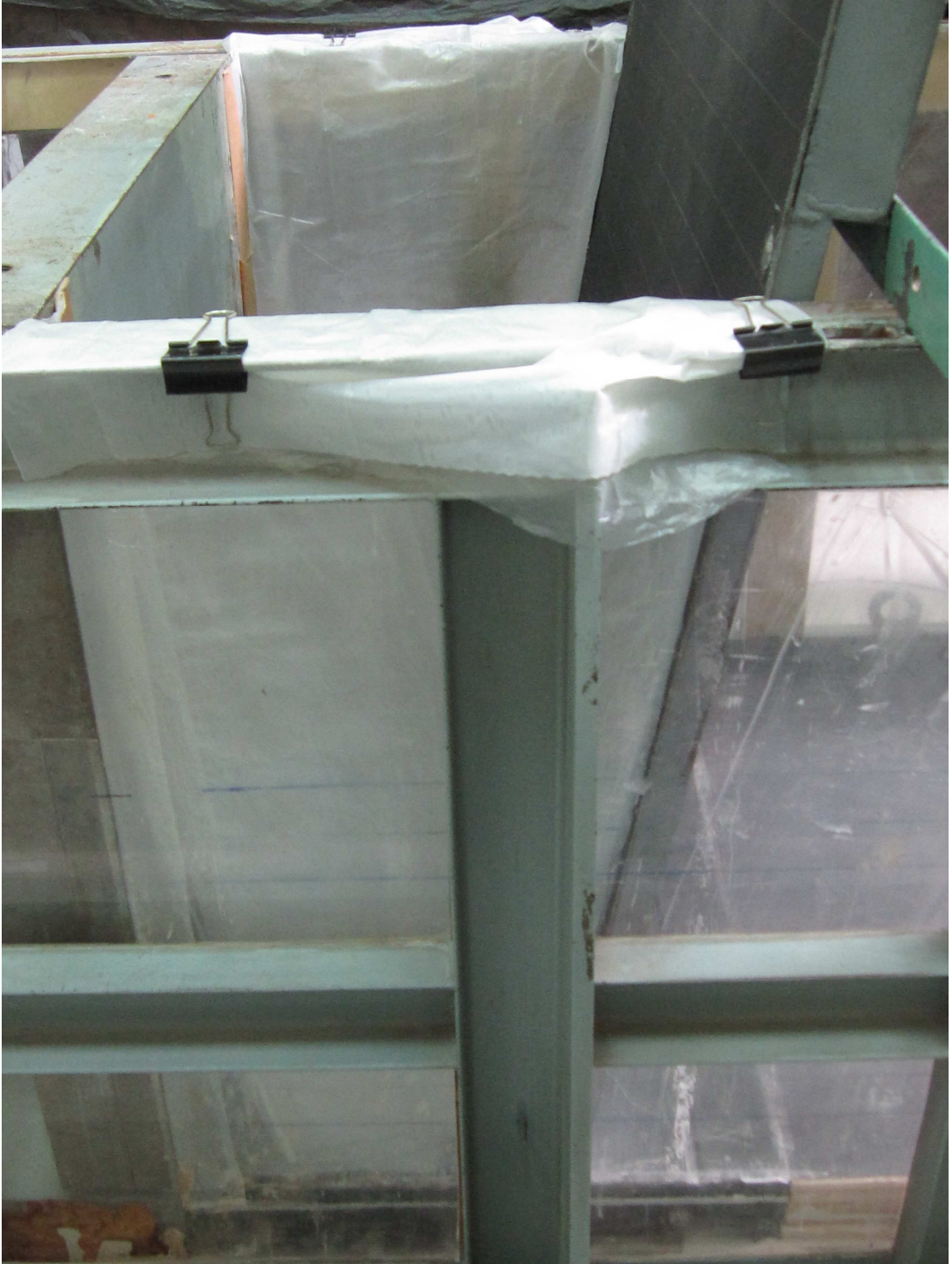


Fig. 6.43. Distribution of horizontal earth pressure for $b = 350 \text{ mm}$ and $\beta = 90^\circ$ (Test 0330-3)



(a)

Fig. 6.44. Model wall test with interface spacing $b = 350$ mm and $\beta = 80^\circ$



(b)

Fig. 6.44. Model wall test with interface spacing $b = 350$ mm and $\beta = 80^\circ$

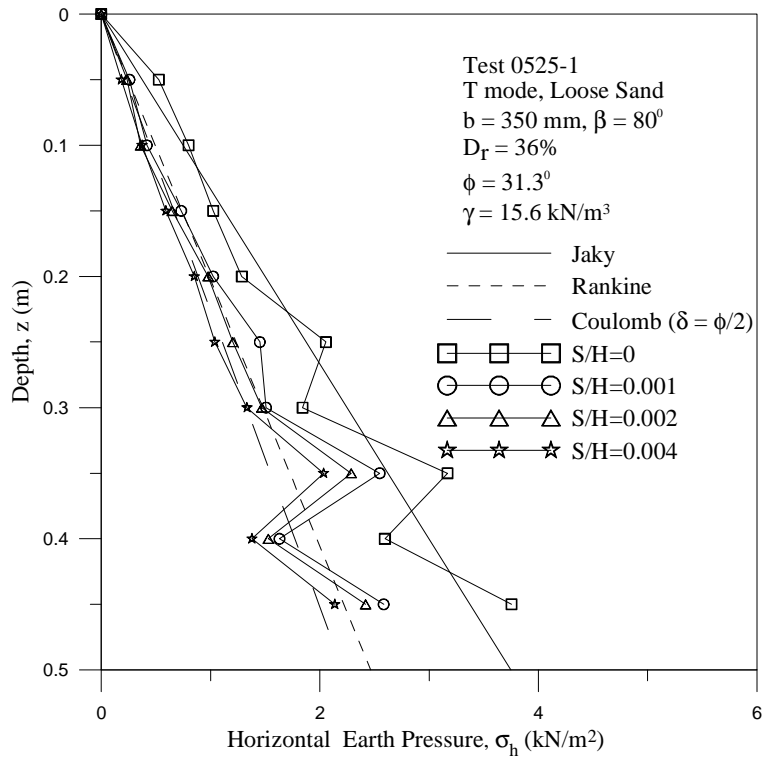


Fig. 6.45. Distribution of horizontal earth pressure for $b = 350 \text{ mm}$ and $\beta = 80^\circ$ (Test 0525-1)

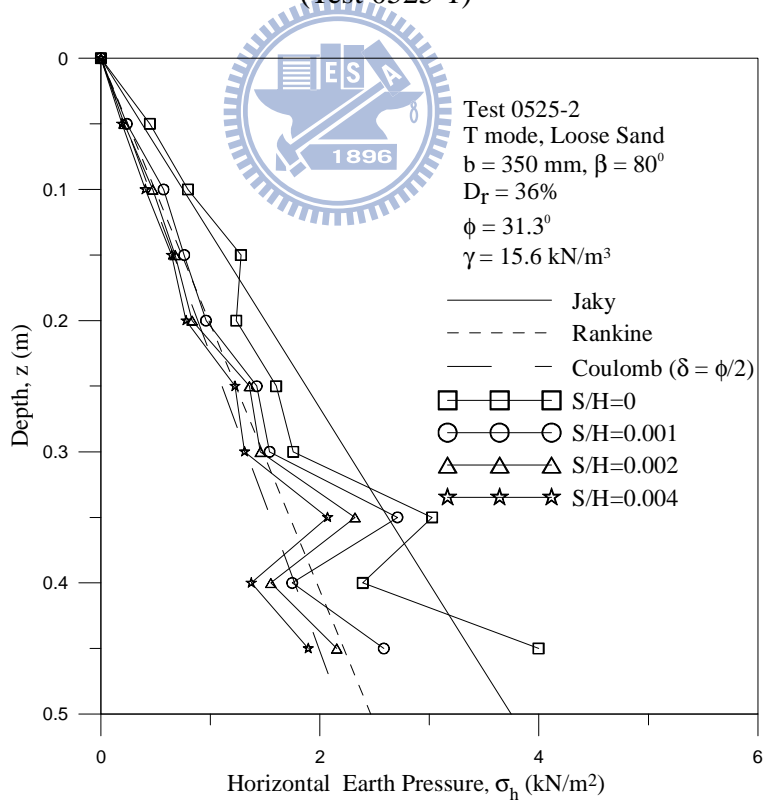


Fig. 6.46. Distribution of horizontal earth pressure for $b = 350 \text{ mm}$ and $\beta = 80^\circ$ (Test 0525-2)

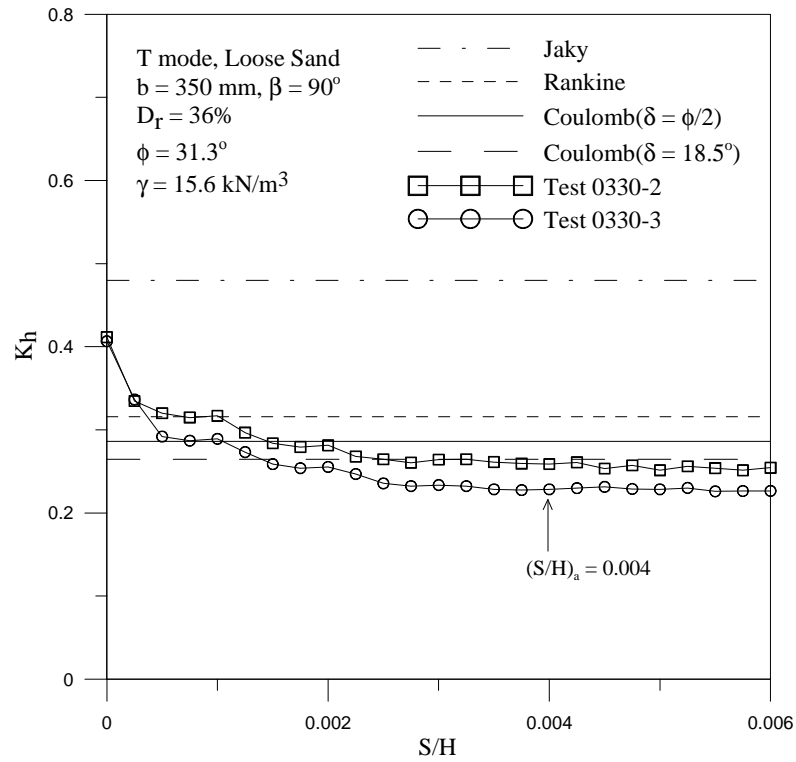


Fig. 6.47. Earth pressure coefficient K_h versus wall movement for $b = 350 \text{ mm}$ and $\beta = 90^\circ$

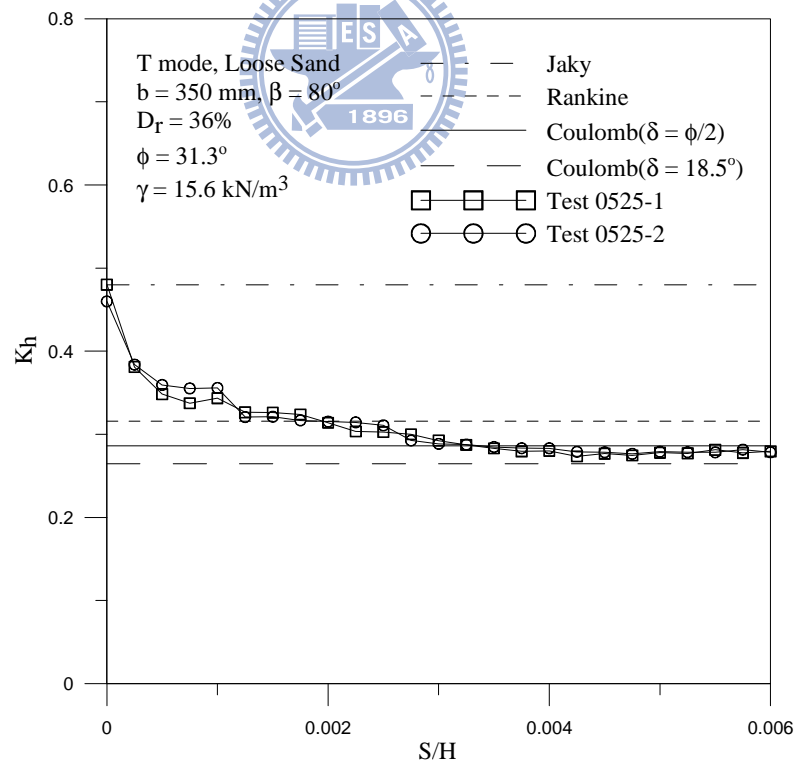


Fig. 6.48. Earth pressure coefficient K_h versus wall movement for $b = 350 \text{ mm}$ and $\beta = 80^\circ$

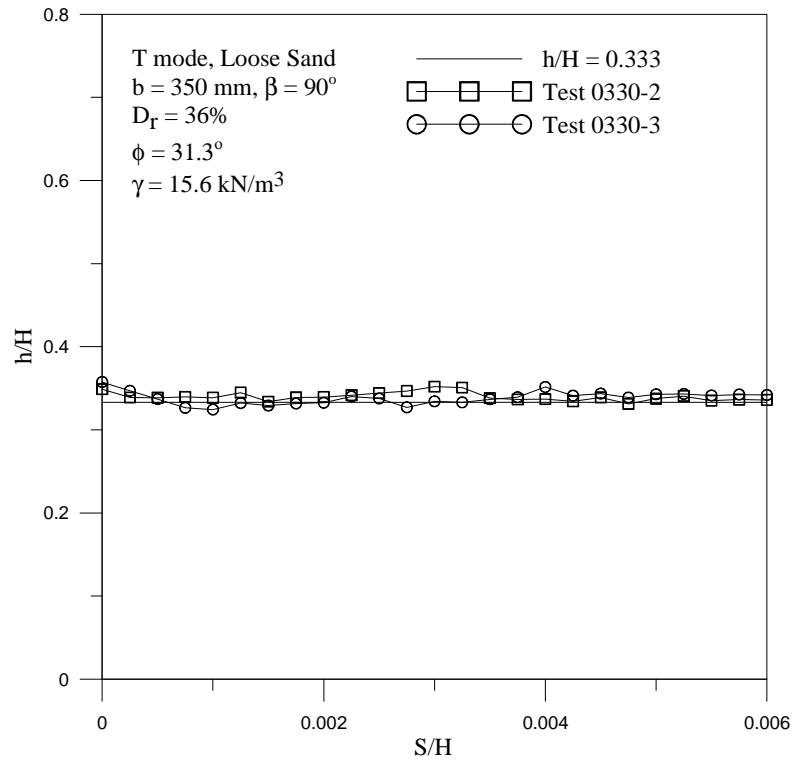


Fig. 6.49. Location of total thrust application for $b = 350 \text{ mm}$ and $\beta = 90^\circ$

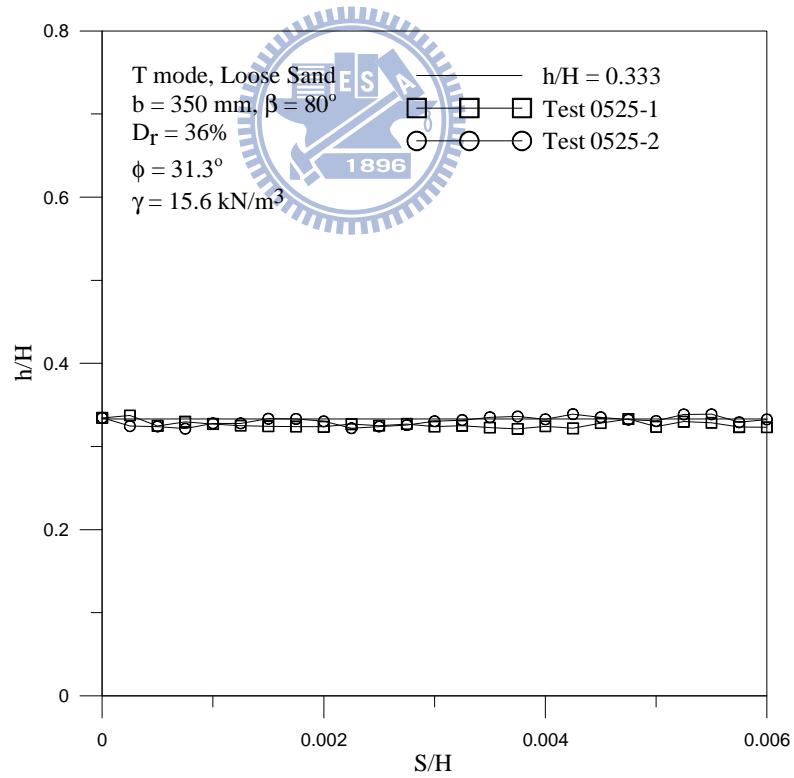
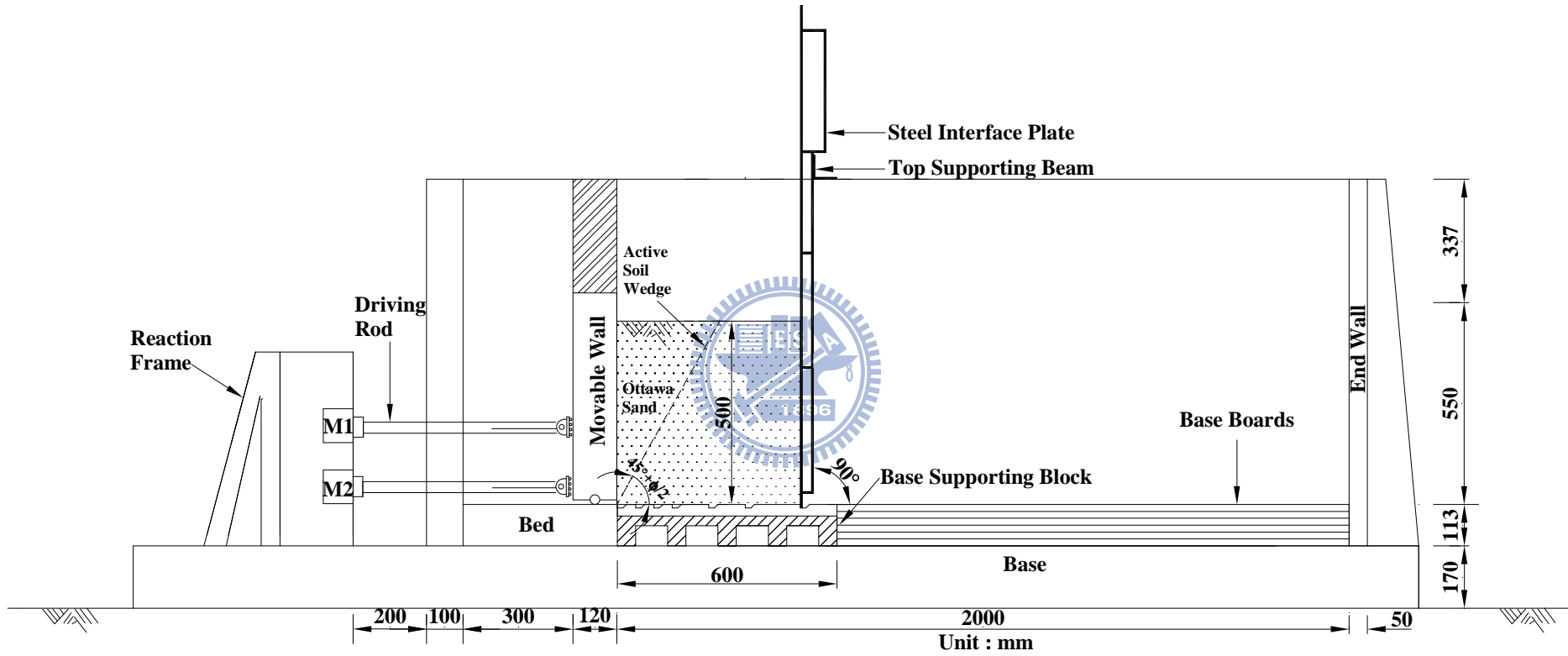


Fig. 6.50. Location of total thrust application for $b = 350 \text{ mm}$ and $\beta = 80^\circ$



(a)

Fig. 6.51. Model wall test with interface spacing $b = 500$ mm and $\beta = 90^\circ$



(b)

Fig. 6.51. Model wall test with interface spacing $b = 500$ mm and $\beta = 90^\circ$

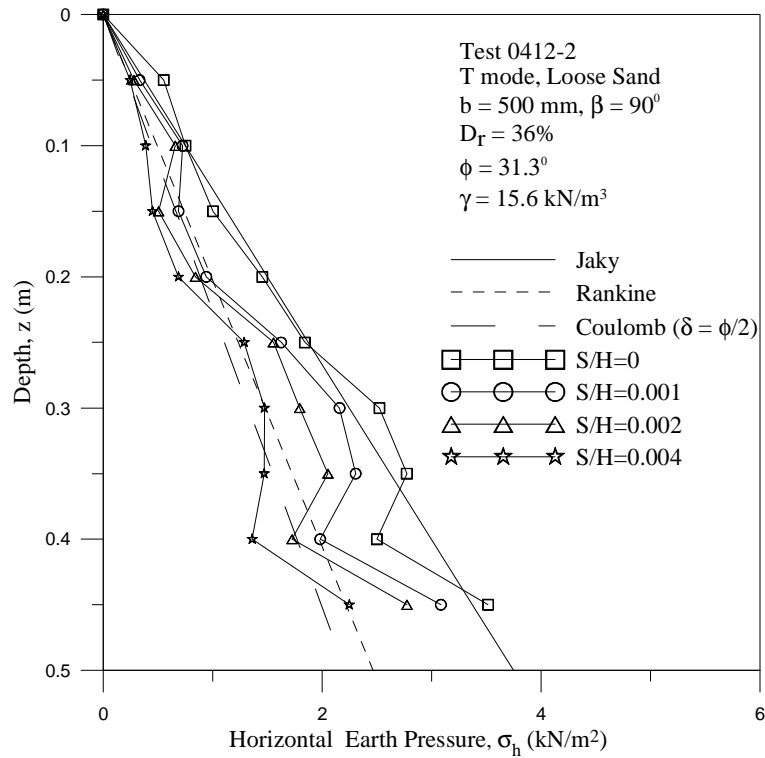


Fig. 6.52. Distribution of horizontal earth pressure for $b = 500 \text{ mm}$ and $\beta = 90^\circ$ (Test 0412-2)

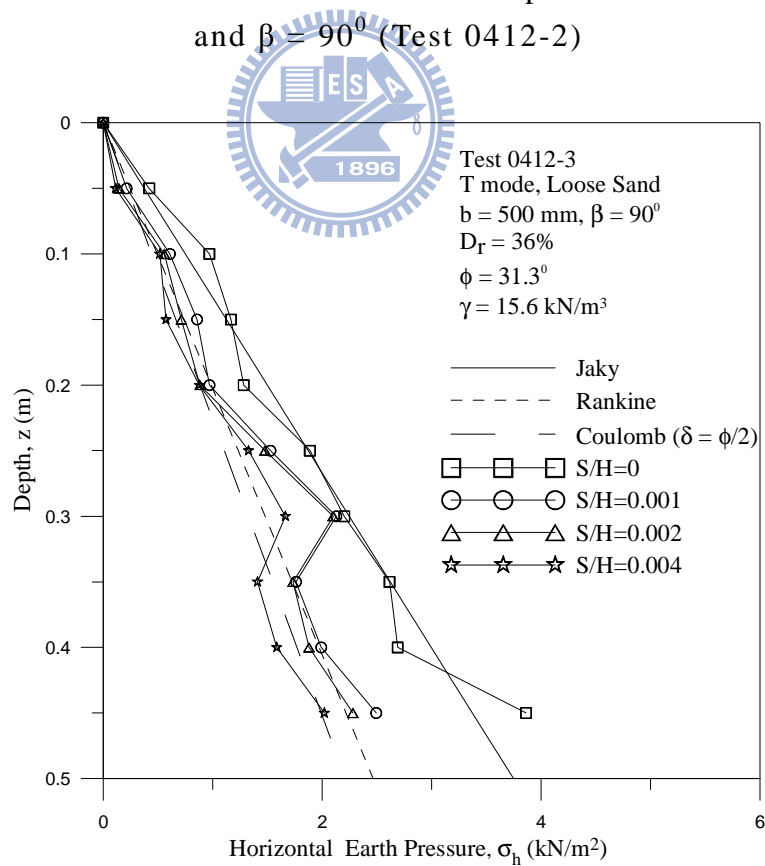


Fig. 6.53. Distribution of horizontal earth pressure for $b = 500 \text{ mm}$ and $\beta = 90^\circ$ (Test 0412-3)

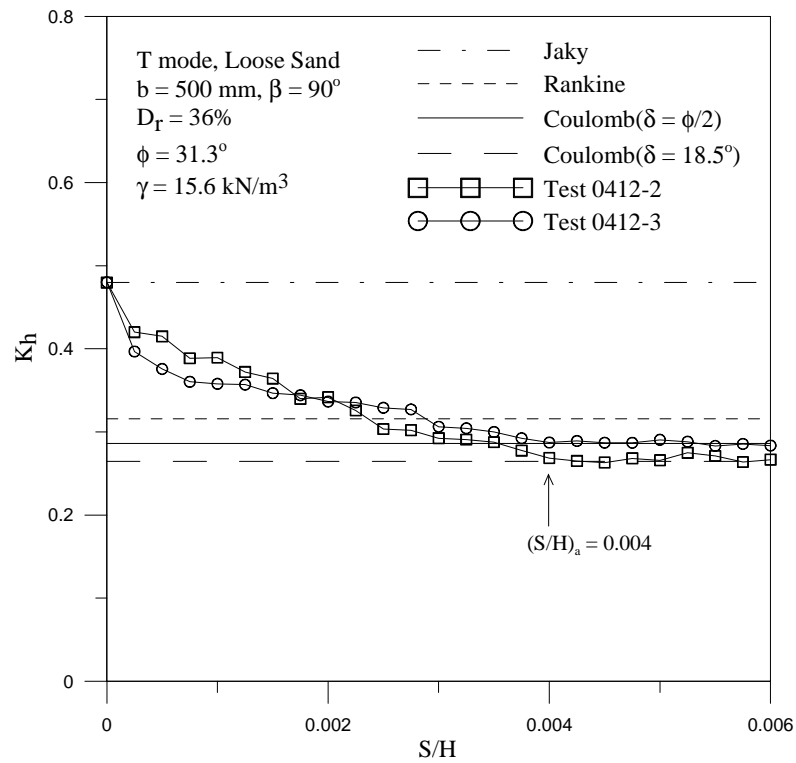


Fig. 6.54. Earth pressure coefficient K_h versus wall movement for $b = 500 \text{ mm}$ and $\beta = 90^\circ$

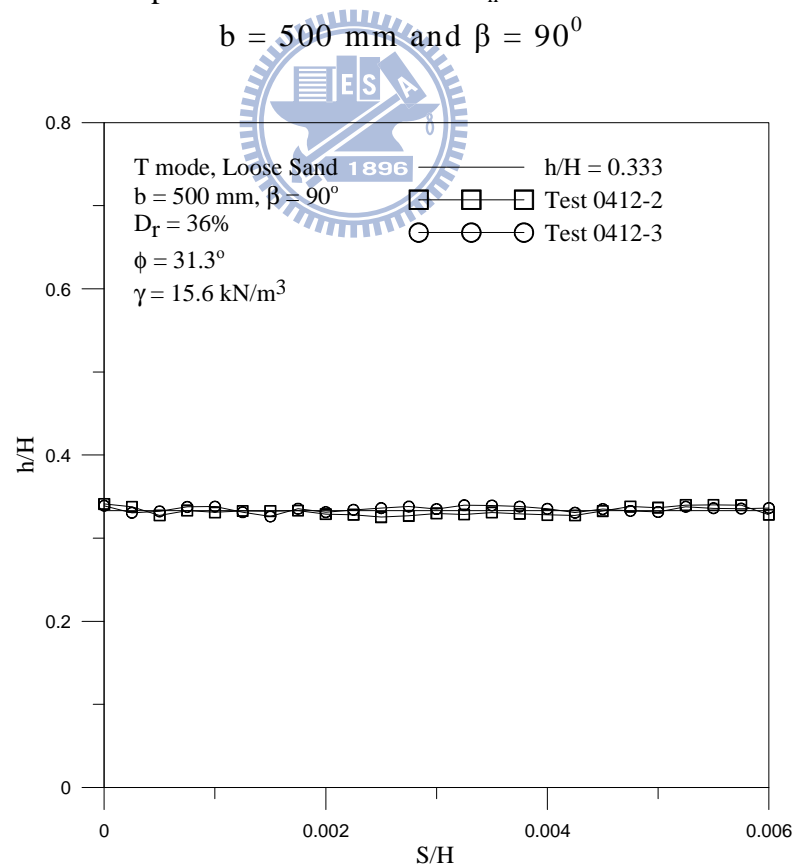


Fig. 6.55. Location of total thrust application for $b = 500 \text{ mm}$ and $\beta = 90^\circ$

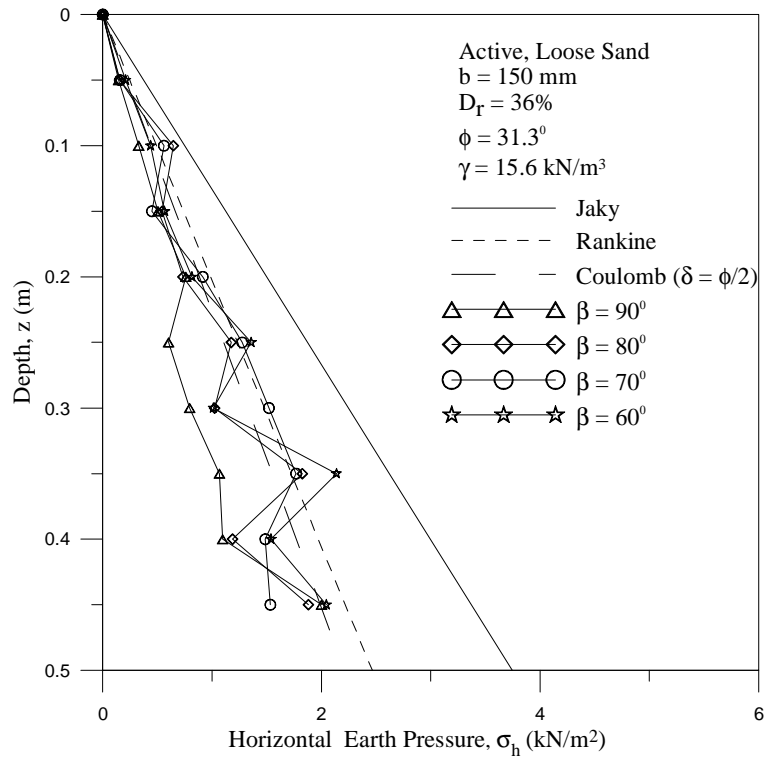


Fig. 6.56. Distribution of active earth pressure at different interface inclination angle β for $b = 150 \text{ mm}$

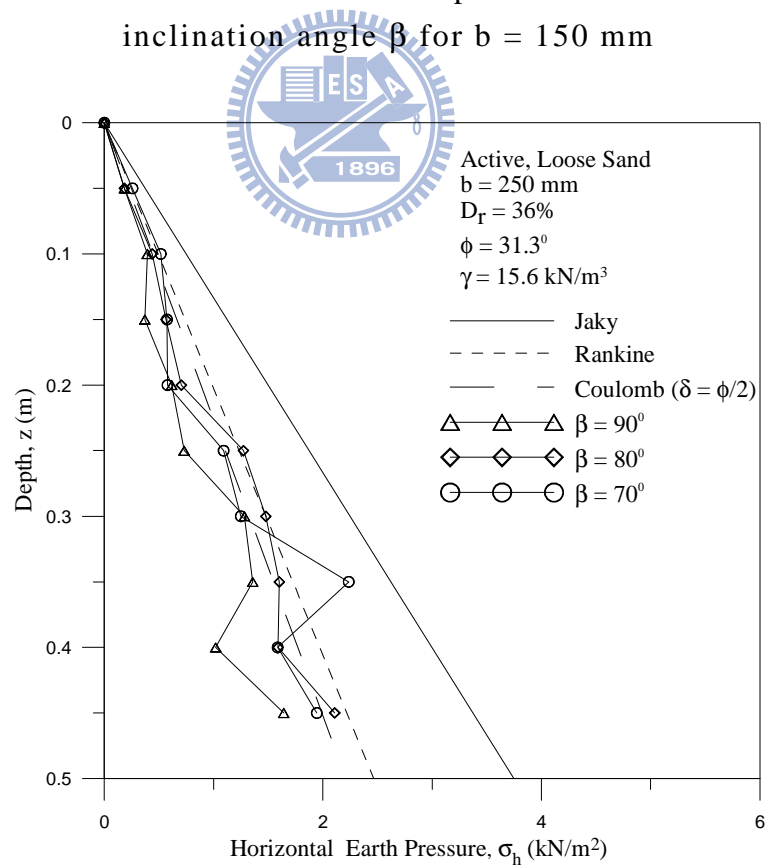


Fig. 6.57. Distribution of active earth pressure at different interface inclination angle β for $b = 250 \text{ mm}$

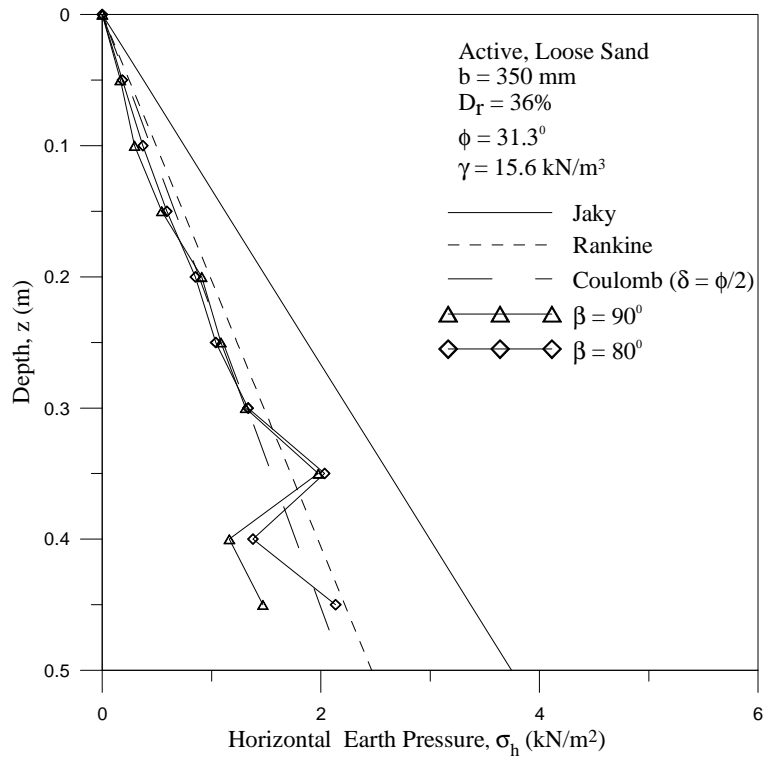


Fig. 6.58. Distribution of active earth pressure at different interface inclination angle β for $b = 350 \text{ mm}$

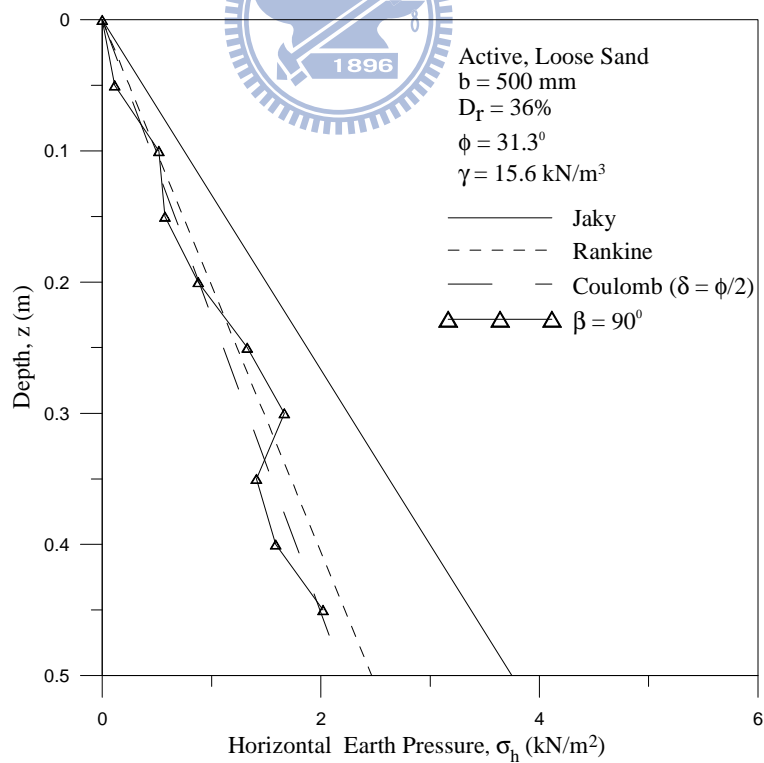


Fig. 6.59. Distribution of active earth pressure for $b = 500 \text{ mm}$

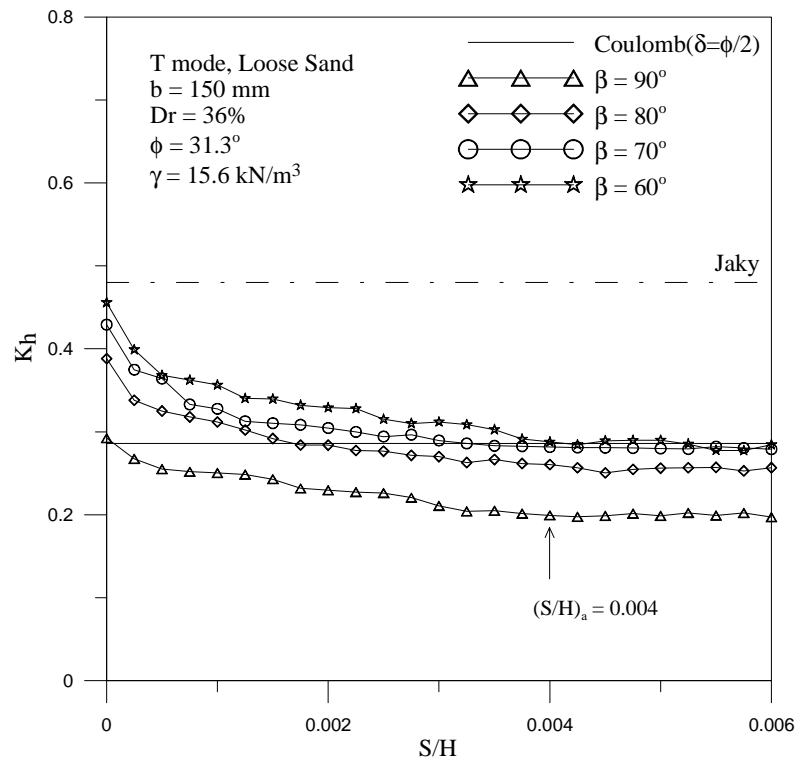


Fig. 6.60. Variation of earth pressure coefficient K_h with wall movement for $b = 150 \text{ mm}$

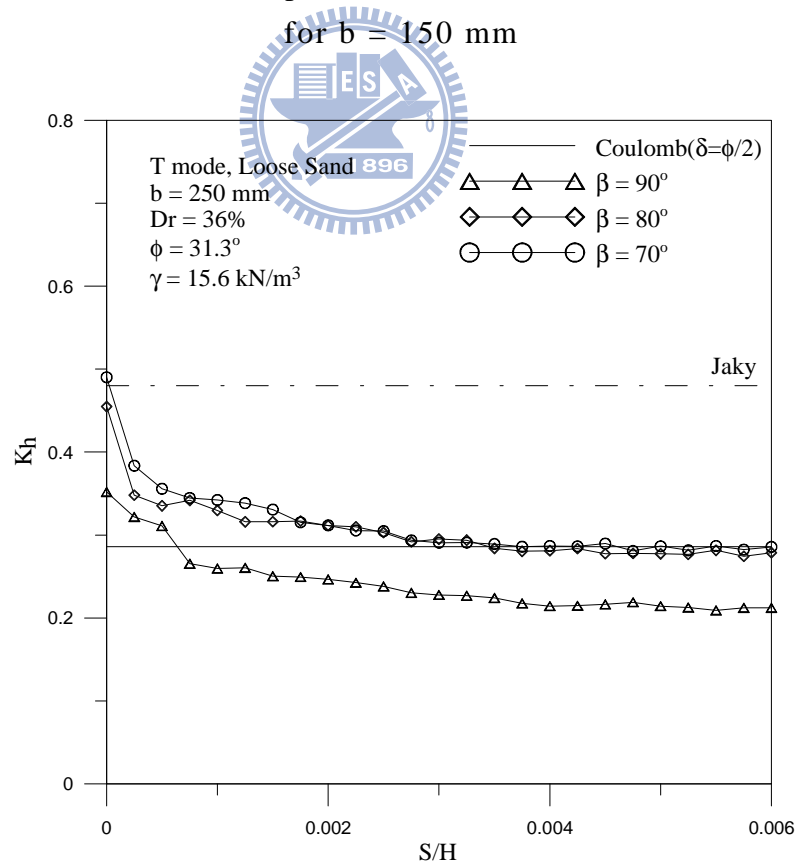


Fig. 6.61. Variation of earth pressure coefficient K_h with wall movement for $b = 250 \text{ mm}$

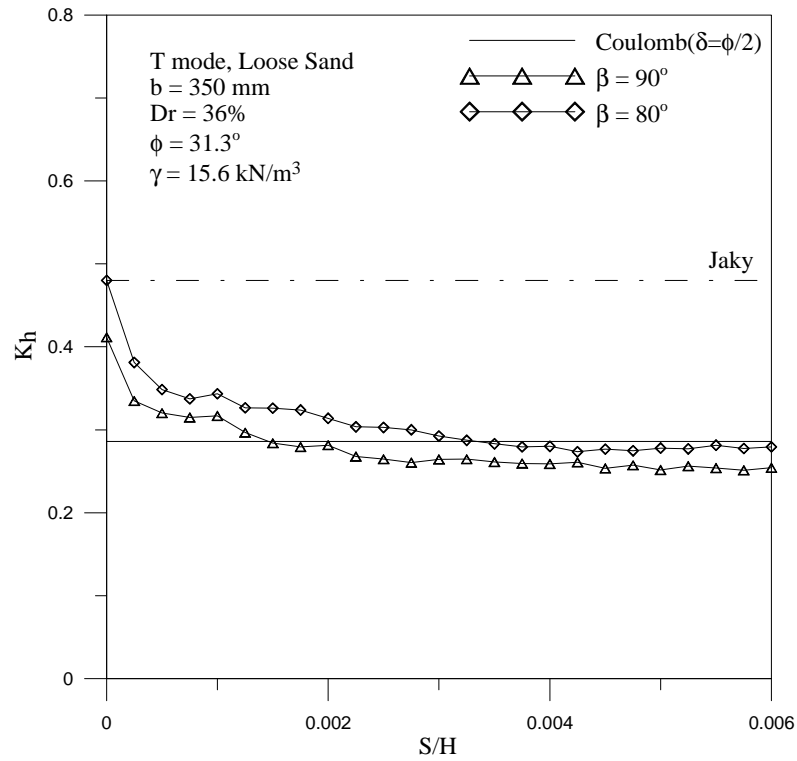


Fig. 6.62. Variation of earth pressure coefficient K_h with wall movement for b = 350 mm

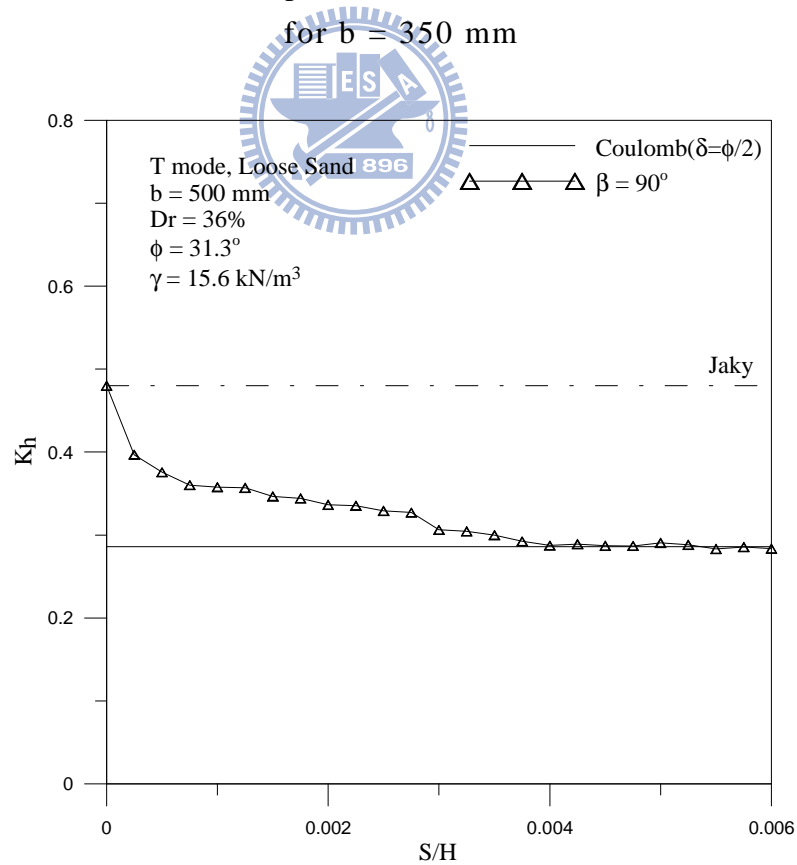


Fig. 6.63. Variation of earth pressure coefficient K_h with wall movement for b = 500 mm

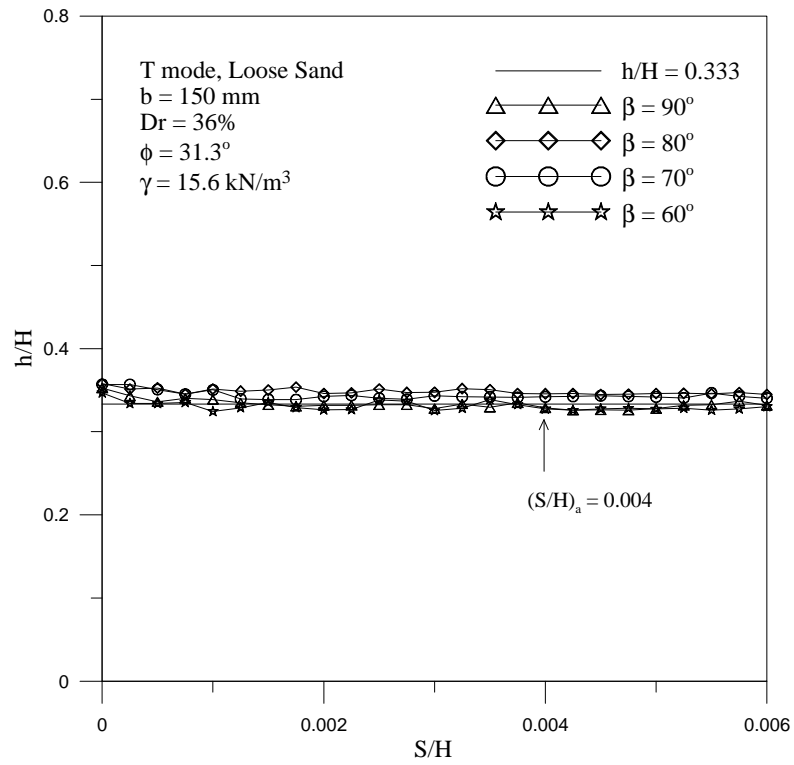


Fig. 6.64. Variation of total thrust location with wall movement for

$b = 150 \text{ mm}$

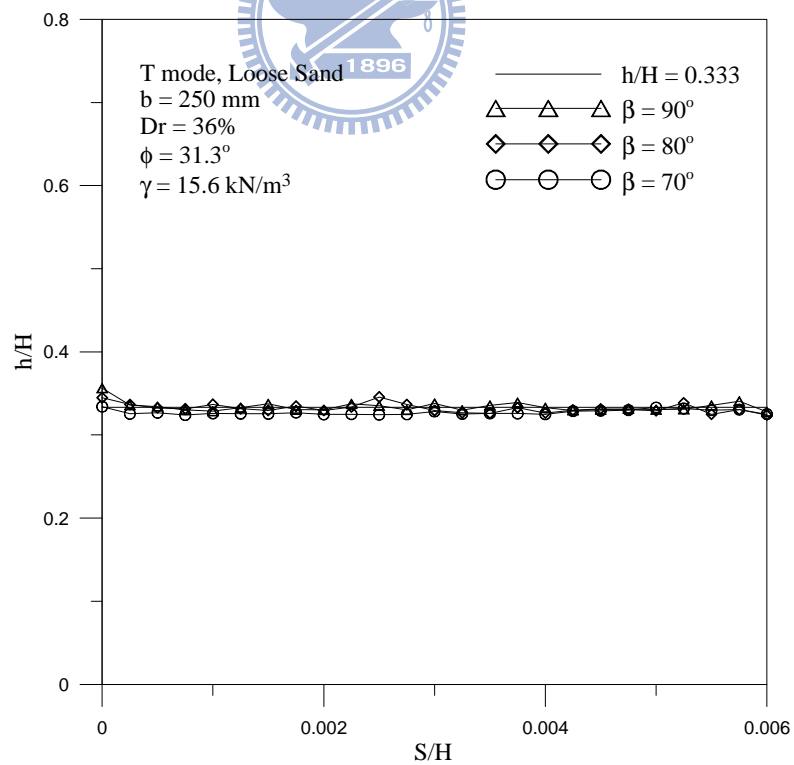


Fig. 6.65. Variation of total thrust location with wall movement for

$b = 250 \text{ mm}$

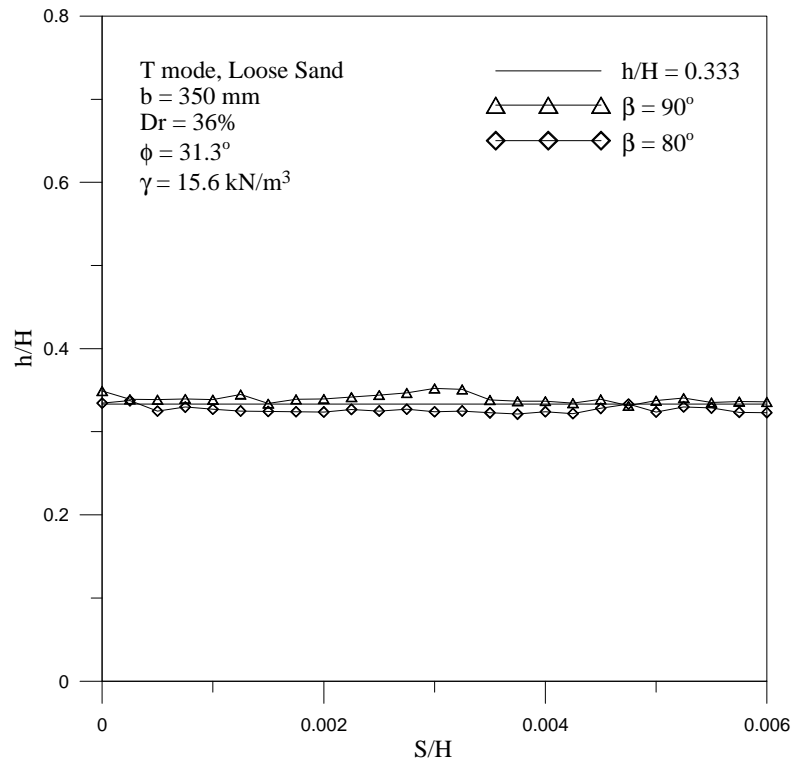


Fig. 6.66. Variation of total thrust location with wall movement for

$b = 350 \text{ mm}$

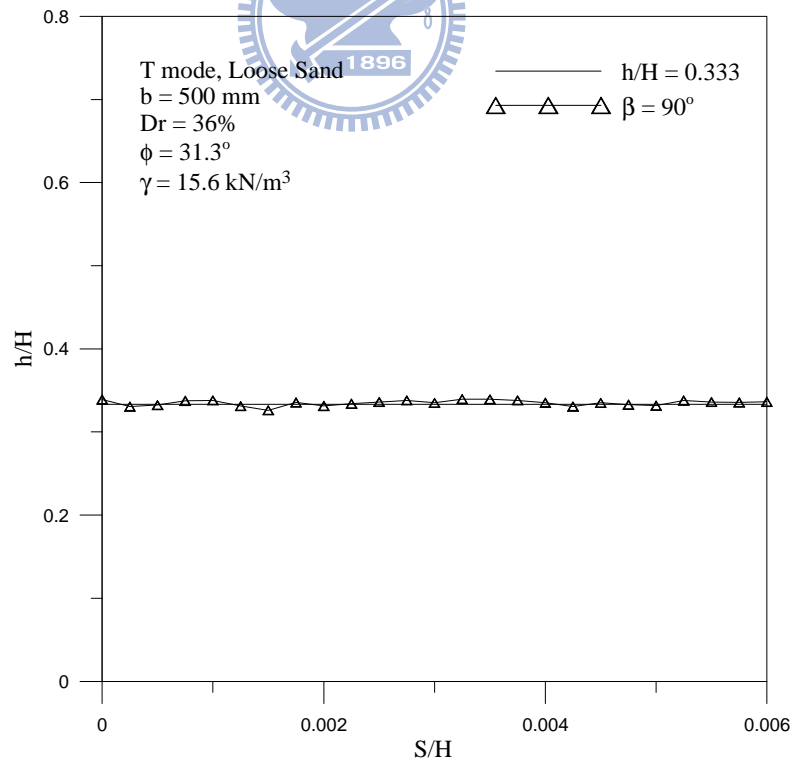


Fig. 6.67. Variation of total thrust location with wall movement for

$b = 500 \text{ mm}$

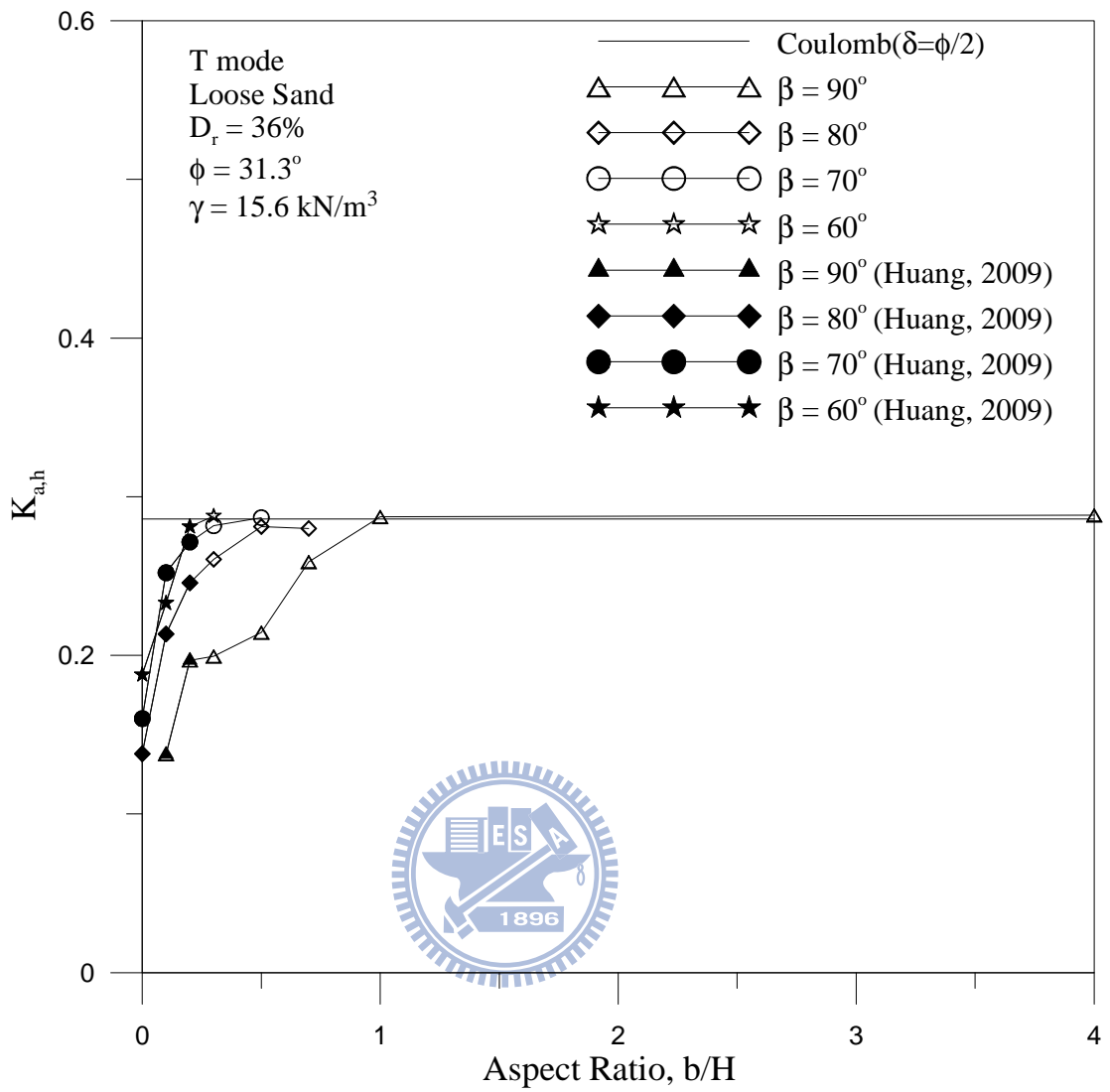


Fig. 6.68. Active earth pressure coefficient $K_{a,h}$ versus constrained backfill aspect ratio b/H

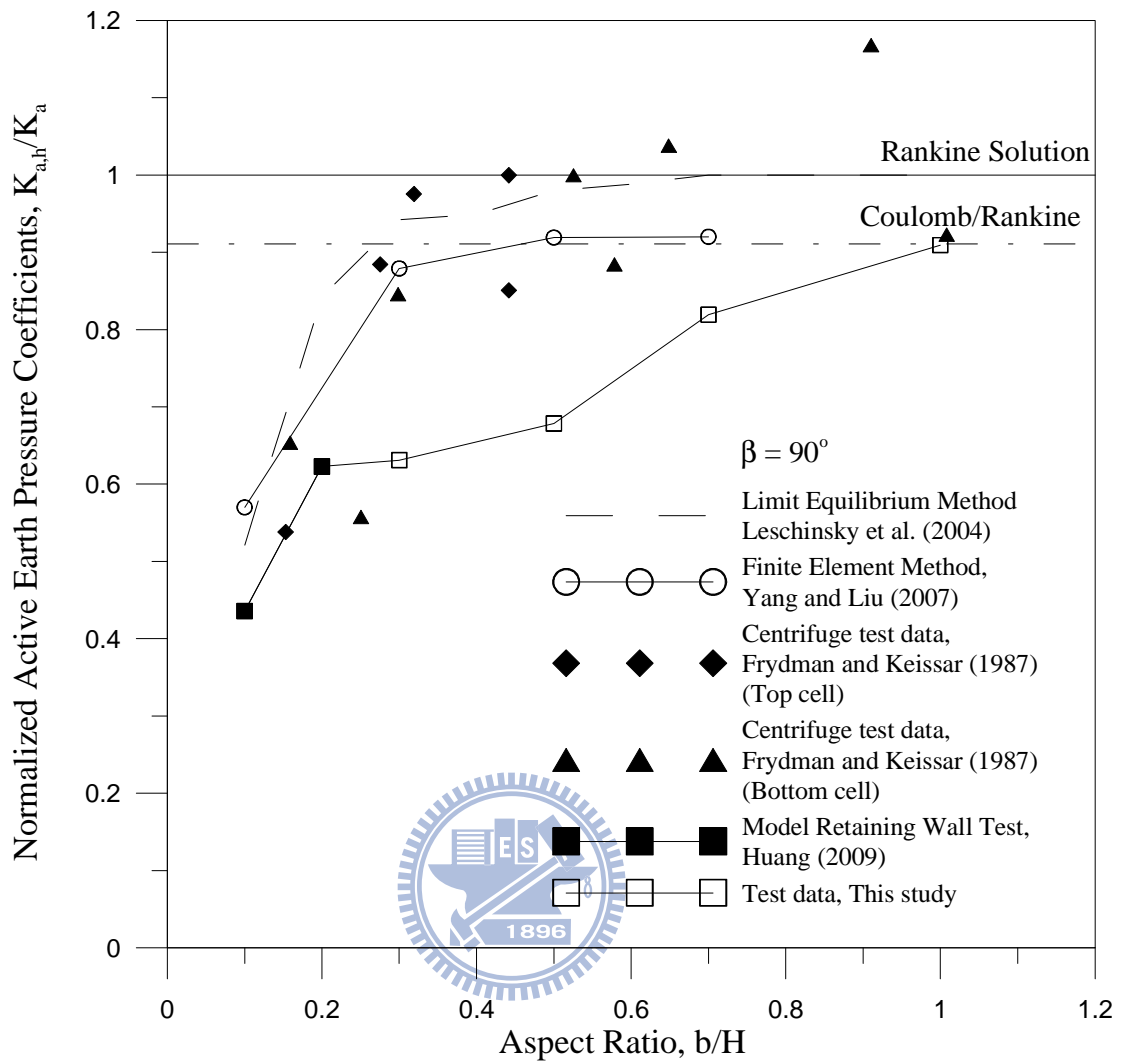


Fig. 6.69. Normalized active earth pressure coefficient with aspect ratio b/H

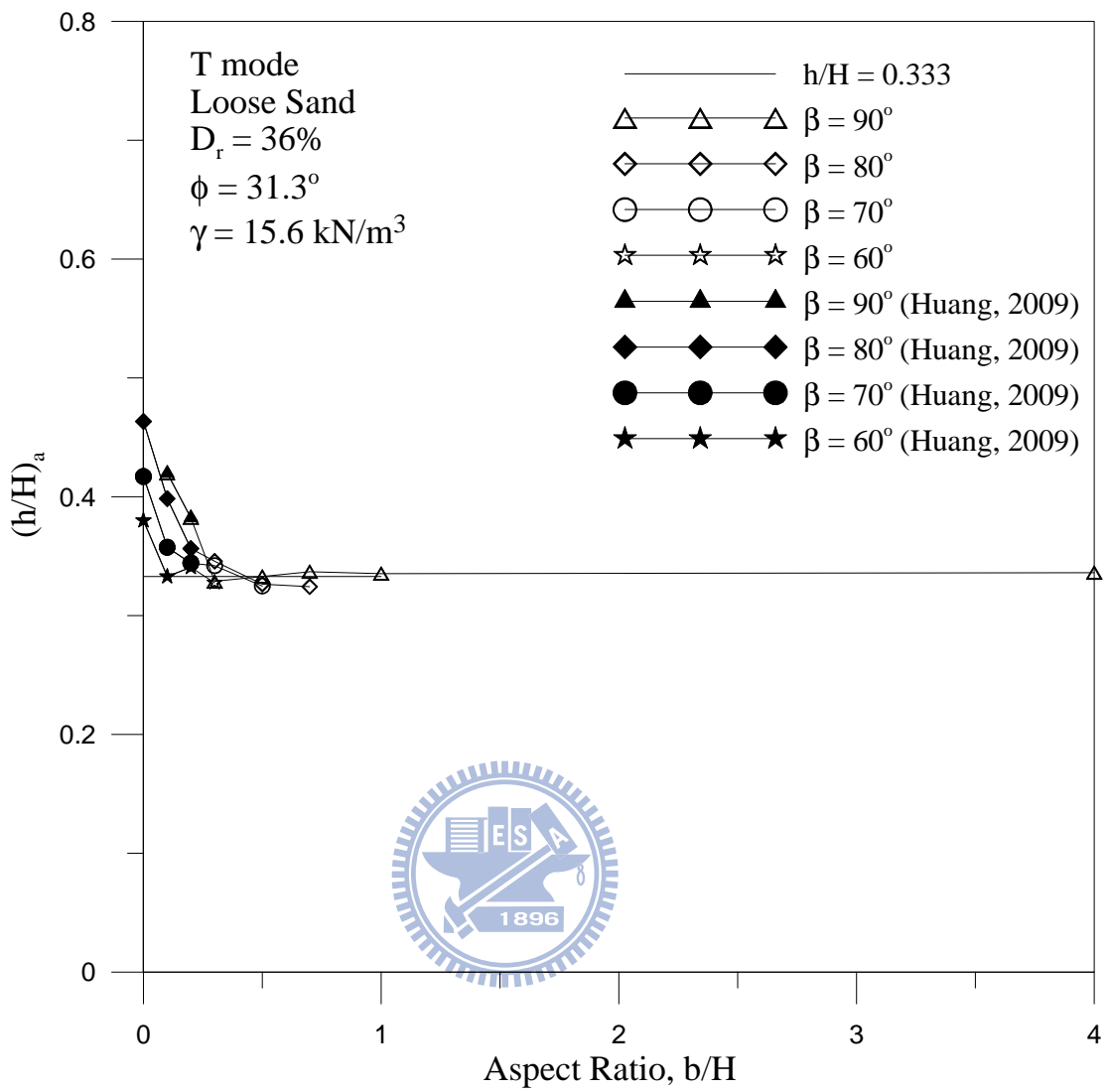


Fig. 6.70. Point of application of active soil thrust versus aspect ratio b/H

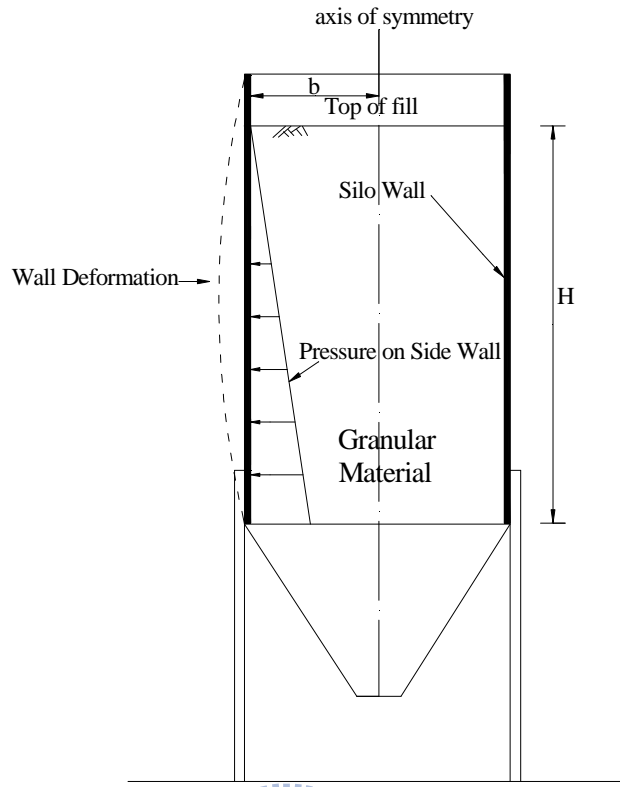


Fig. 6.71. Cylindrical silo filled with granular material

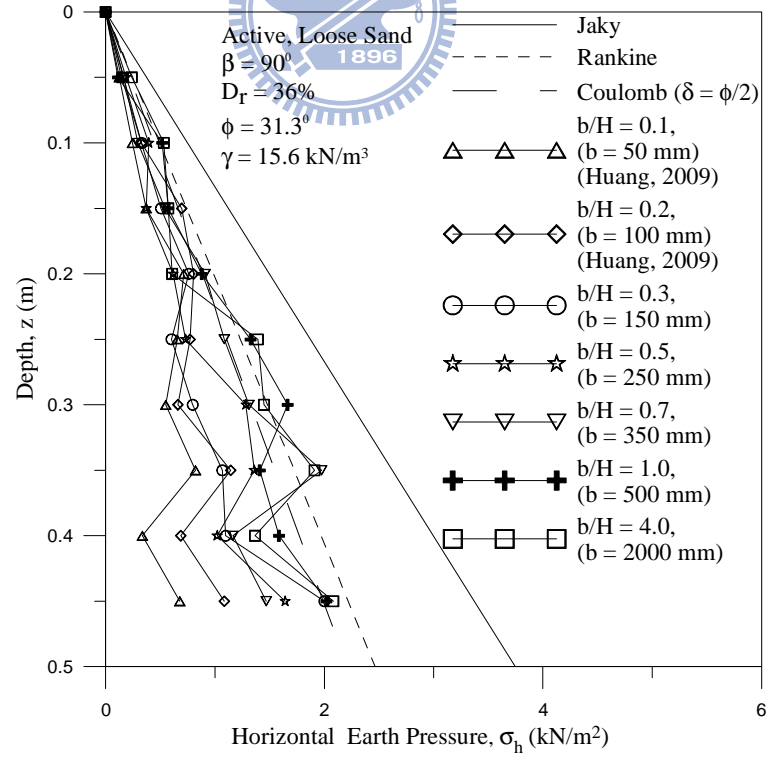


Fig. 6.72. Distribution of active earth pressure at different backfill aspect ratio b/H for $\beta = 90^\circ$

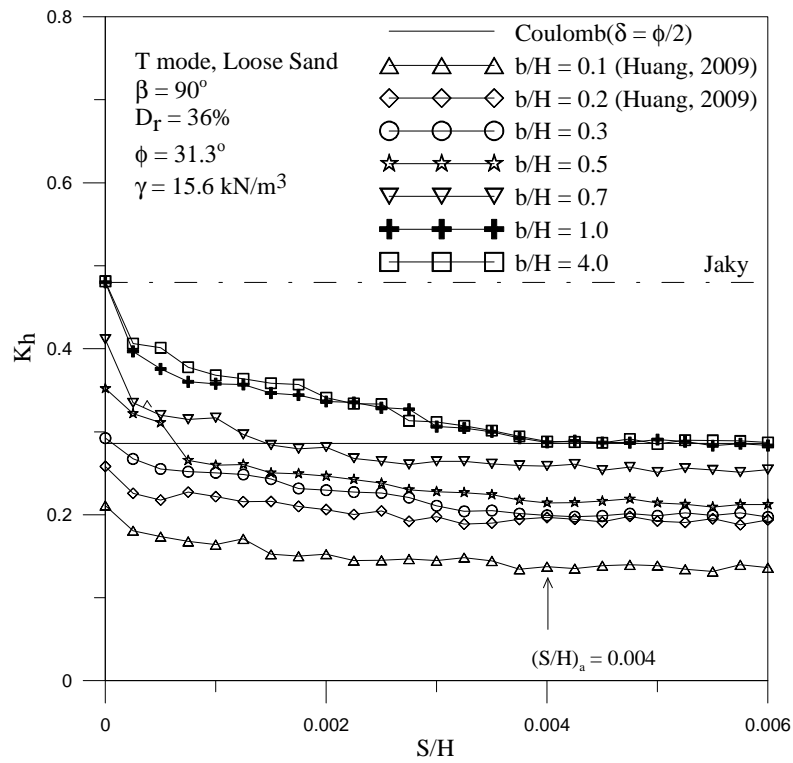


Fig. 6.73. Variation of earth pressure coefficient K_h with wall movement for $\beta = 90^\circ$

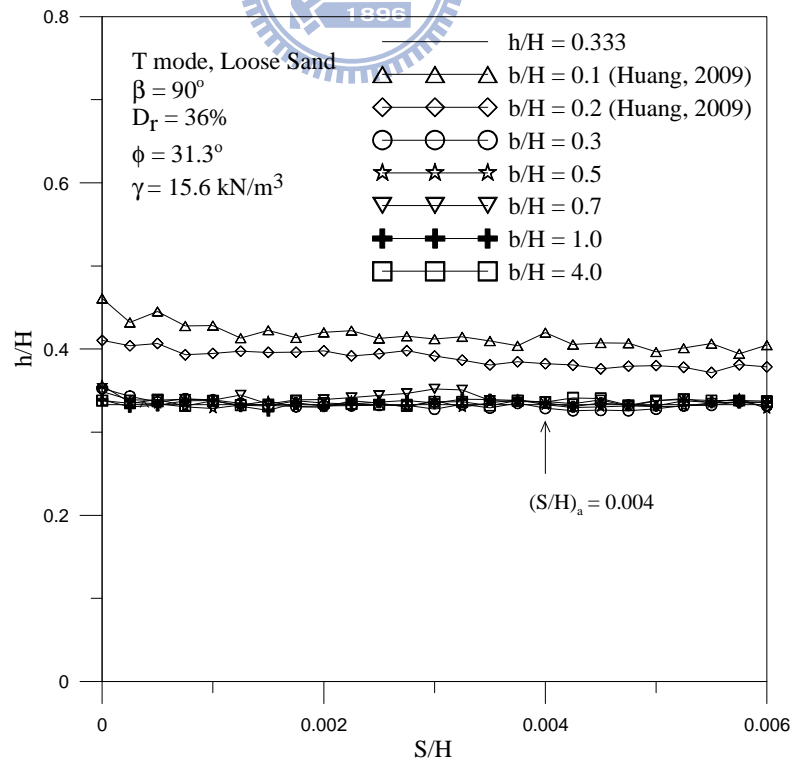


Fig. 6.74. Variation of soil thrust location with wall movement for $\beta = 90^\circ$

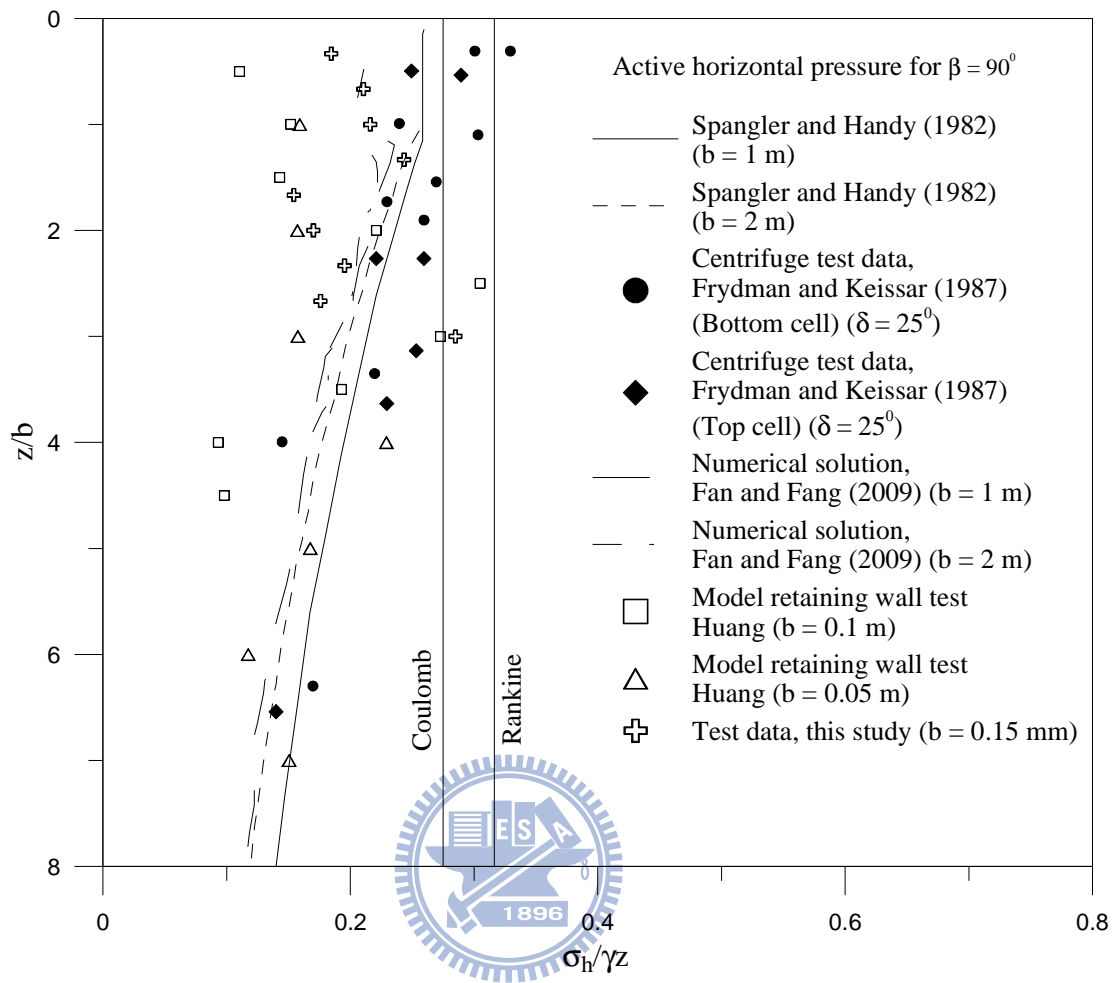
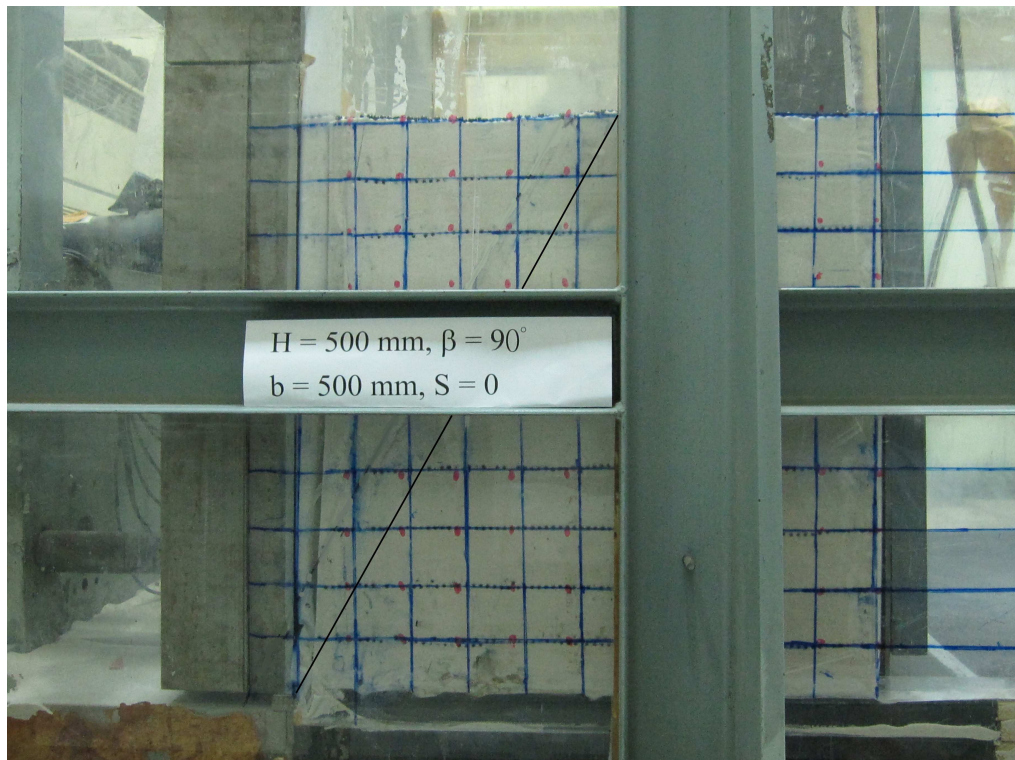
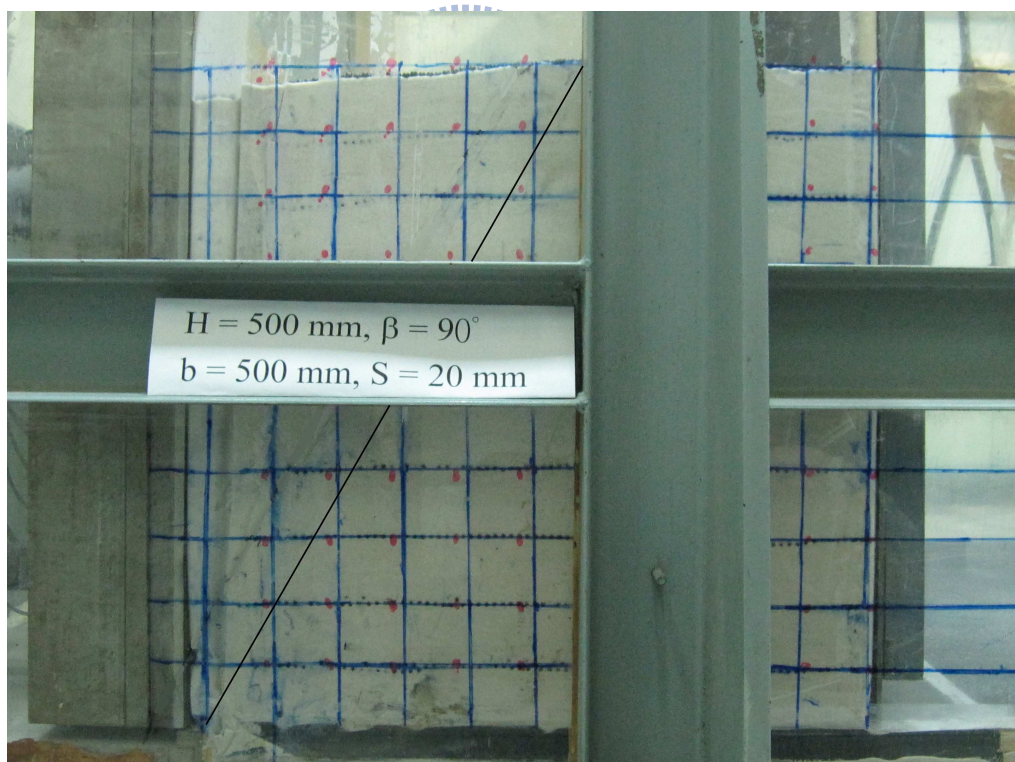


Fig. 6.75. Comparison of the distribution of active earth pressures



(a)



(b)

Fig. 6.76 Observed backfill displacement for $b = 500 \text{ mm}$ and $\beta = 90^\circ$ for
 (a) $S = 0$ (b) $S/H = 0.04$

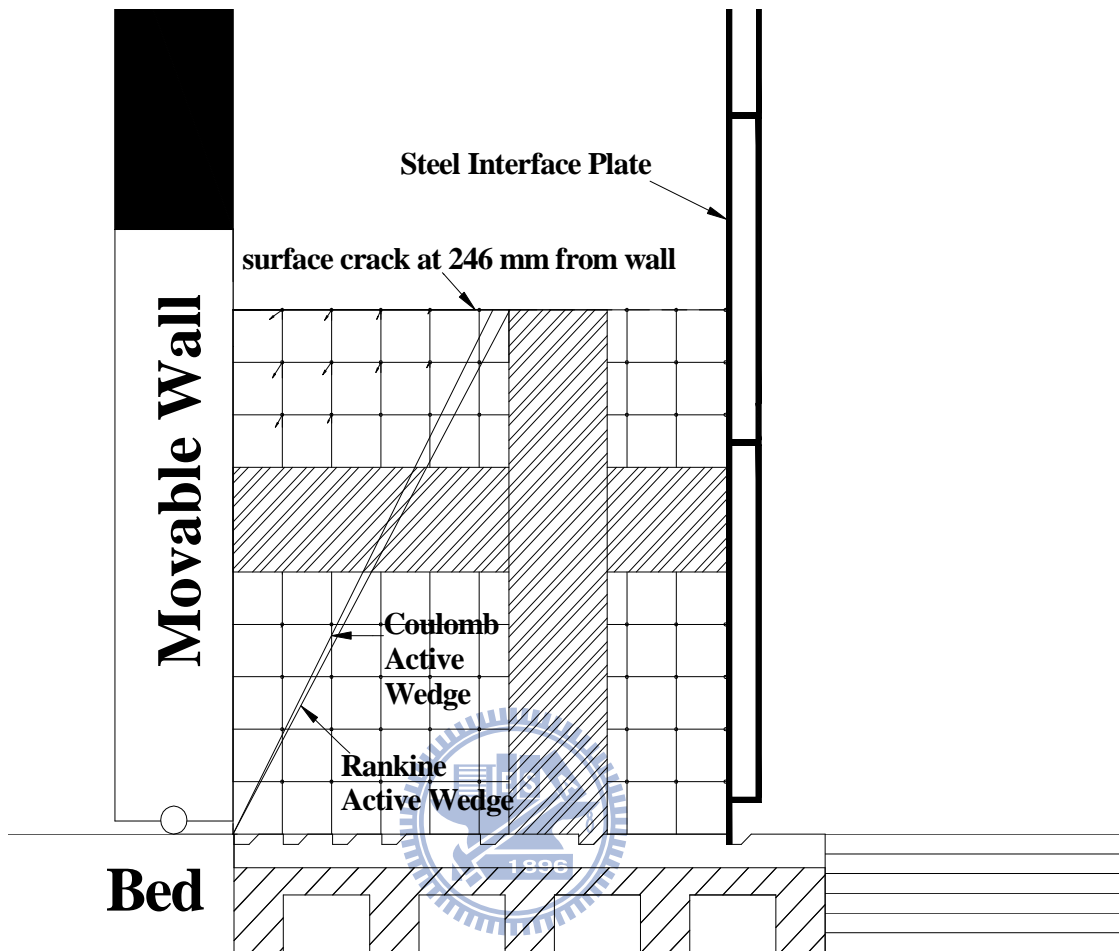
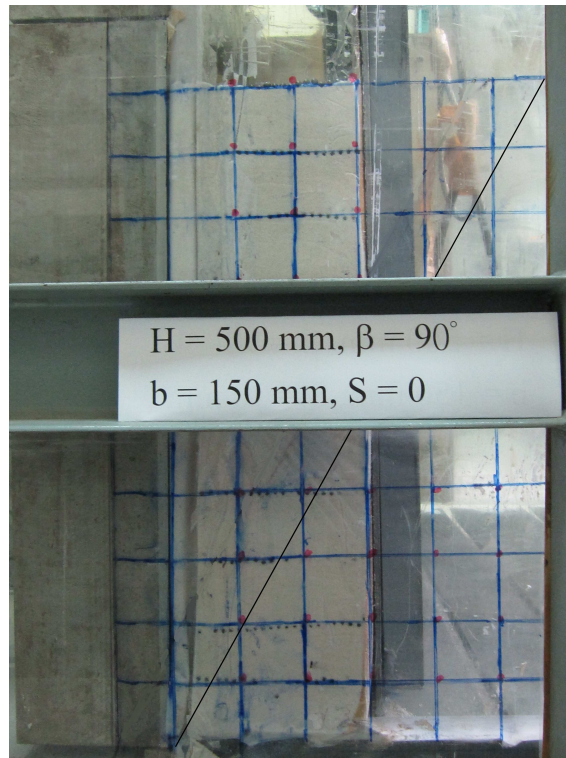
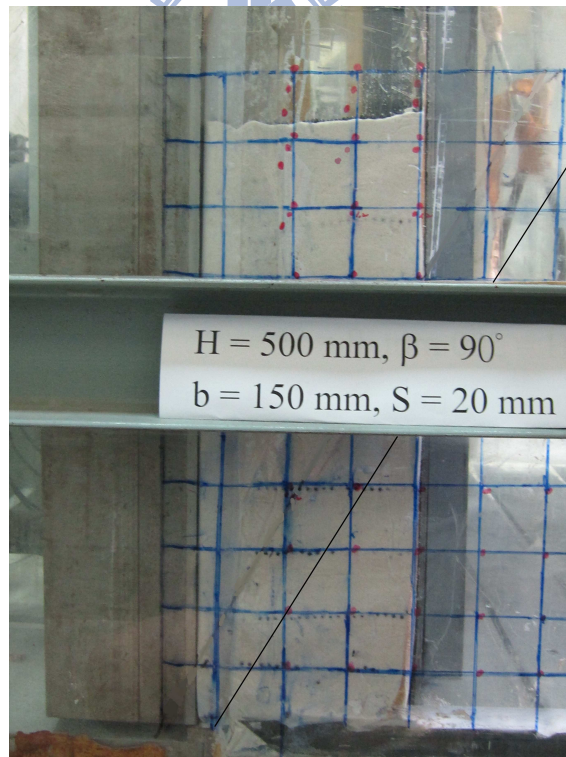


Fig. 6.77 Accumulated displacement for $b = 500$ mm and $\beta = 90^\circ$
for $S = 20$ mm ($S/H = 0.04$)



(a)



(b)

Fig. 6.78 Observed backfill displacement for $b = 150 \text{ mm}$ and $\beta = 90^\circ$ for (a) $S = 0$ and (b) $S = 20 \text{ mm}$ ($S/H = 0.04$)

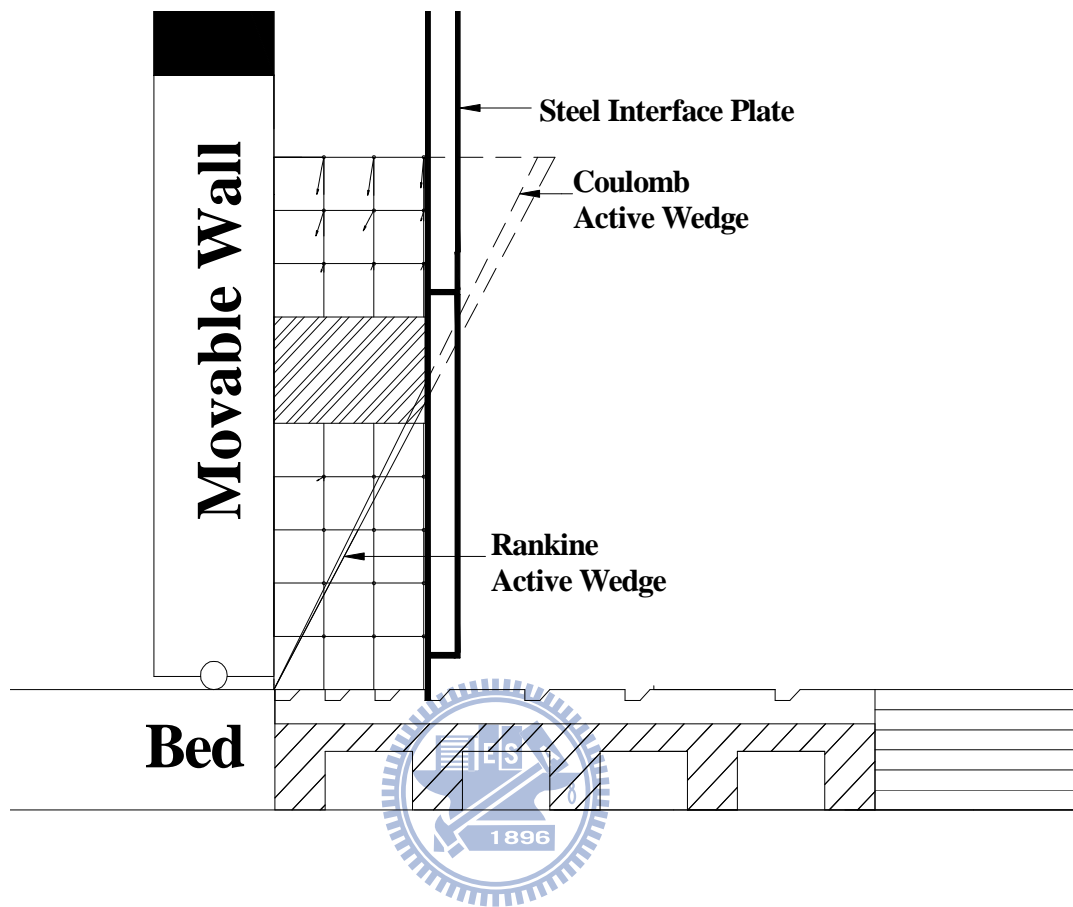


Fig. 6.79 Accumulated displacement for $b = 150 \text{ mm}$ and $\beta = 90^\circ$
for $S = 20 \text{ mm}$ ($S/H = 0.04$)

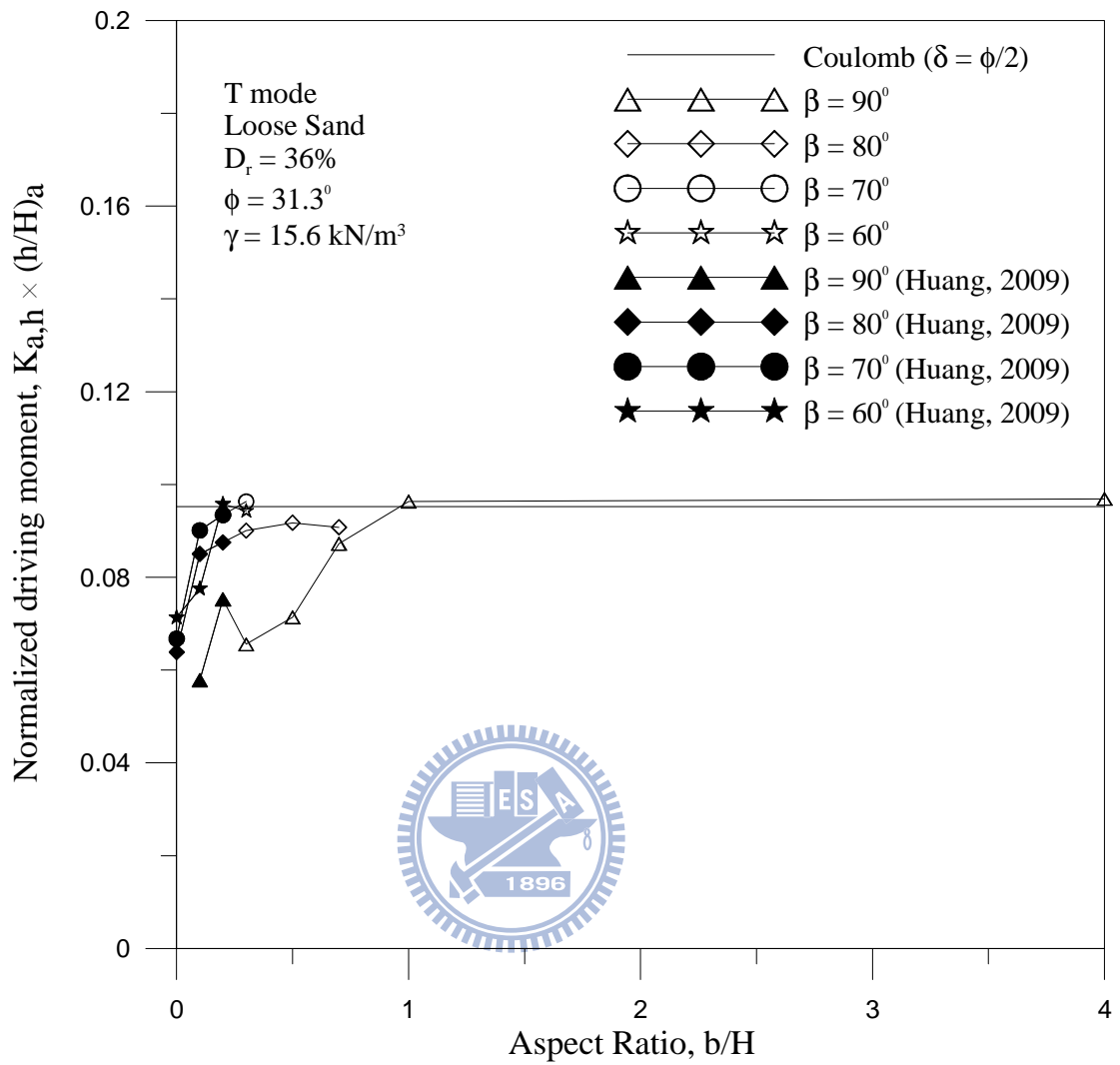


Fig. 6.80. Normalized driving moment versus backfill aspect ratio b/H

Appendix A:

Calibration of Soil Pressure Transducers

To investigate the lateral earth pressure acting on the model retaining wall, nine strain-gage type soil pressure transducers (SPT) were used. The transducers PGM-02KG manufactured by KYOWA are installed on the surface of model retaining wall to measure the lateral earth pressure against the retaining wall. The pressure acts between soil particles and the transducer is quite different from the pressure that acts between liquid and transducer. It is necessary to calibrate the soil pressure transducer in an environment similar to that of the actual testing condition. A special system was designed for the calibration of the strain-gage type soil-pressure transducers. The system consists of the calibration device, the controlled air-pressure system, signal conditioner, and the sensor data acquisition system, as indicated in Fig. A1 and Fig. A2.

The calibration device is a shallow cylindrical chamber with an inner diameter of 400 mm and a height of 30 mm. The chamber is made of a solid steel plate, which is the same material as the model retaining wall. The soil-pressure transducer was inserted through the bottom of the chamber. It is important that the surface of the sensor was installed flush with the upper face of the chamber. To simulate the interface between the sand particle and soil pressure transducer, 10 mm-thick sand layer was poured into the calibration device over the transducer. Then a 0.2 mm-thick rubber membrane was placed over the sandy layer, as shown in Fig. A.1.

A uniformly distributed air-pressure was applied on the membrane, over the soil particles, and transmitted to the transducer. The output voltage of the transducer was found to increase linearly with the increase of applied pressure, as shown in Fig. A.3 to Fig. A.7.

A rubber O-ring was arranged to prevent air leakage between the chamber and the cap. It should be noted that the air pressure applied for the calibration of transducer should be consistent with the operating pressure range for model wall experiments. To reduce the effect of sidewall friction, the thickness of sand layer in the chamber should be limited, so that the side-friction between the sand the sidewall of the chamber could be minimized. Fig. A.3 to Fig. A.7 shows the test results of the soil pressure transducers calibrated without the compressible layer. Table A.1 is a summary of the calibration factors of each soil pressure transducer.

Table A1. Soil Pressure Transducer Calibration Factors

| Transducer No. | Dynamic Strain Amplifier | | | Capacity(kN/m ²) | Calibration Factor[(kN/m ²)/volt] |
|----------------|--------------------------|---------------------------------|--------------------------------|------------------------------|---|
| | No. | Range Selector (*100 $\mu\xi$) | Calibration Setter($\mu\xi$) | | |
| EZ0660029 | 9 | 5 | 2090 | 19.62 | 2.9323 |
| EX3270002 | 10 | 5 | 2014 | 19.62 | 3.9138 |
| FL8550012 | 11 | 5 | 1794 | 19.62 | 3.7048 |
| FG6900006 | 12 | 5 | 1815 | 19.62 | 3.8560 |
| FL8550010 | 13 | 5 | 1880 | 19.62 | 3.7389 |
| FL8550011 | 14 | 5 | 2047 | 19.62 | 3.8362 |
| EG6210026 | 15 | 5 | 1906 | 19.62 | 2.4392 |
| EZ0660017 | 16 | 5 | 2014 | 19.62 | 3.5872 |
| EG6210005 | 17 | 5 | 2005 | 19.62 | 2.5706 |

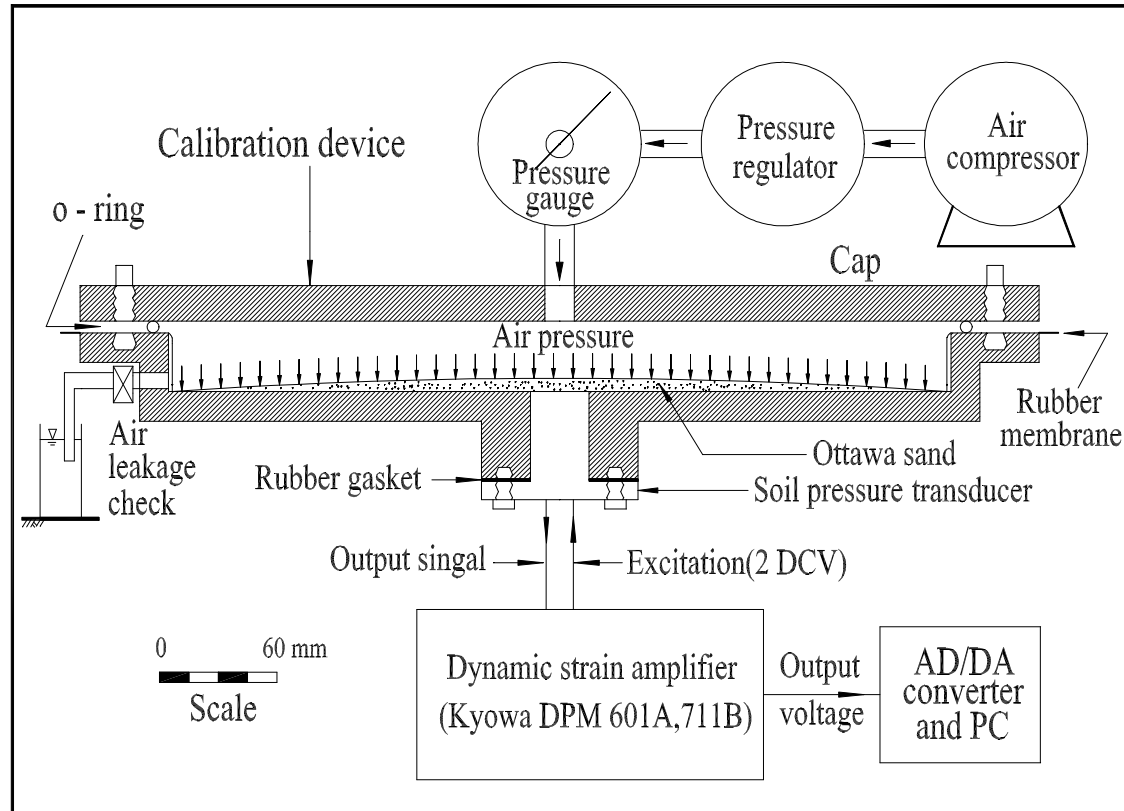


Fig. A.1 Schematic diagram of the soil pressure transducer calibration system

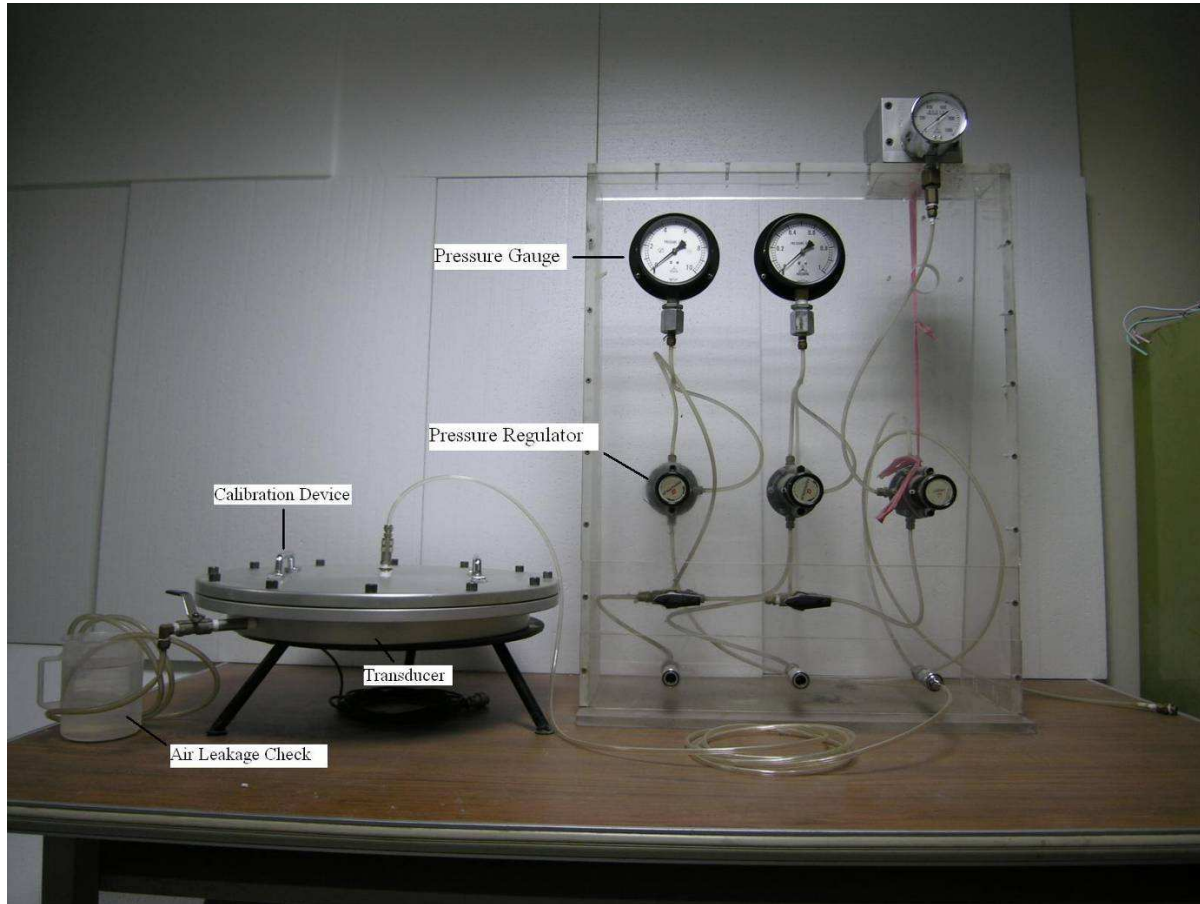


Fig. A2. Soil pressure transducer calibration system

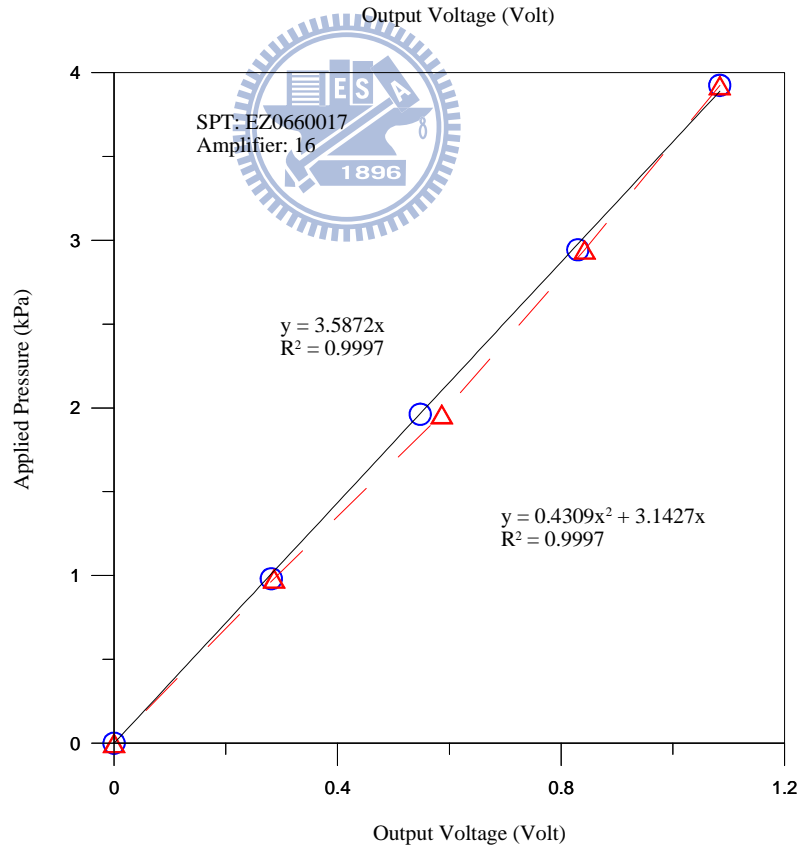
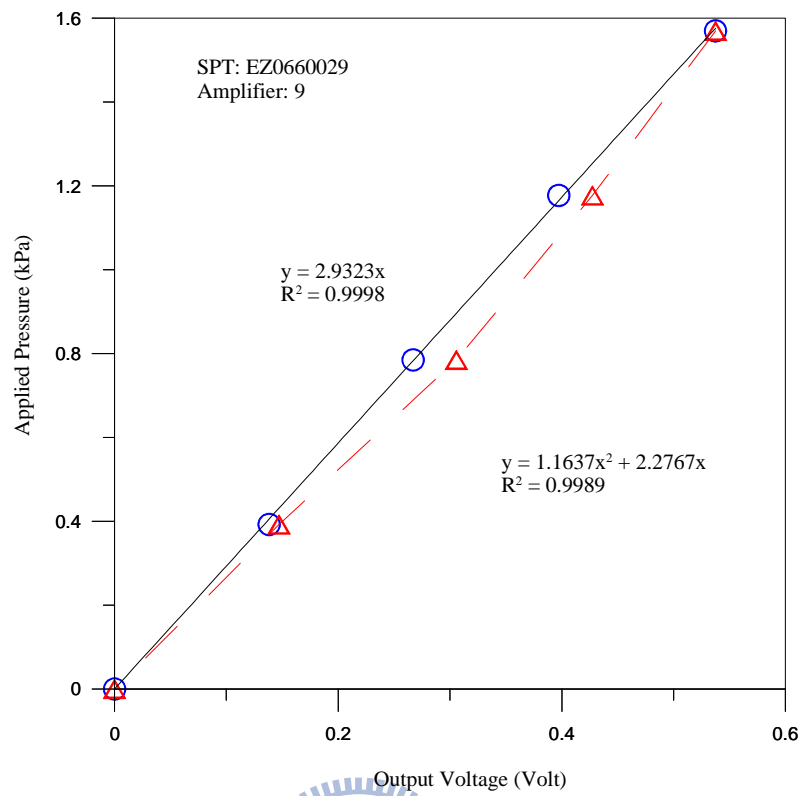


Fig. A3. Applied pressure versus voltage output for soil pressure transducer SPT01 and SPT02

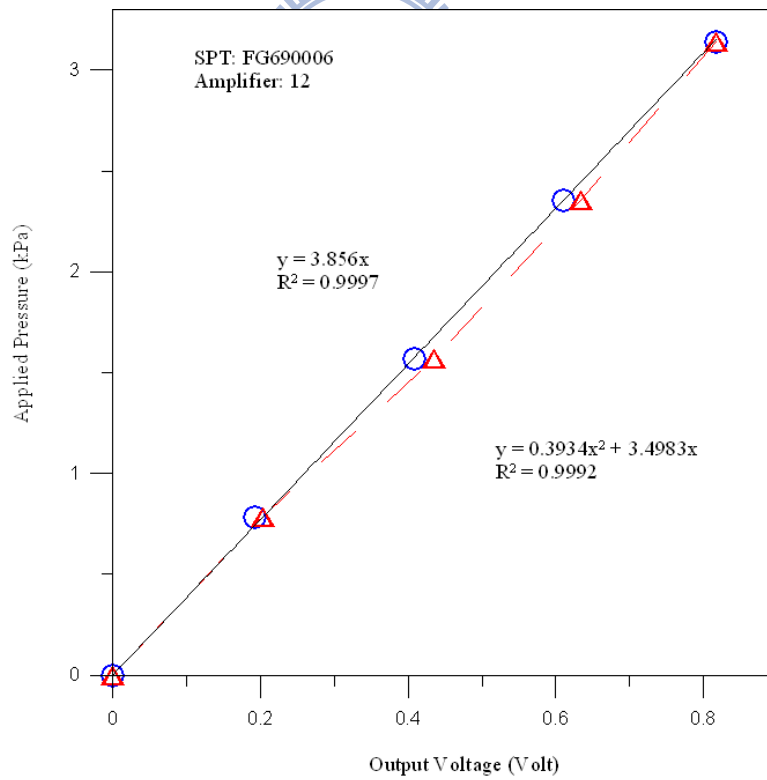
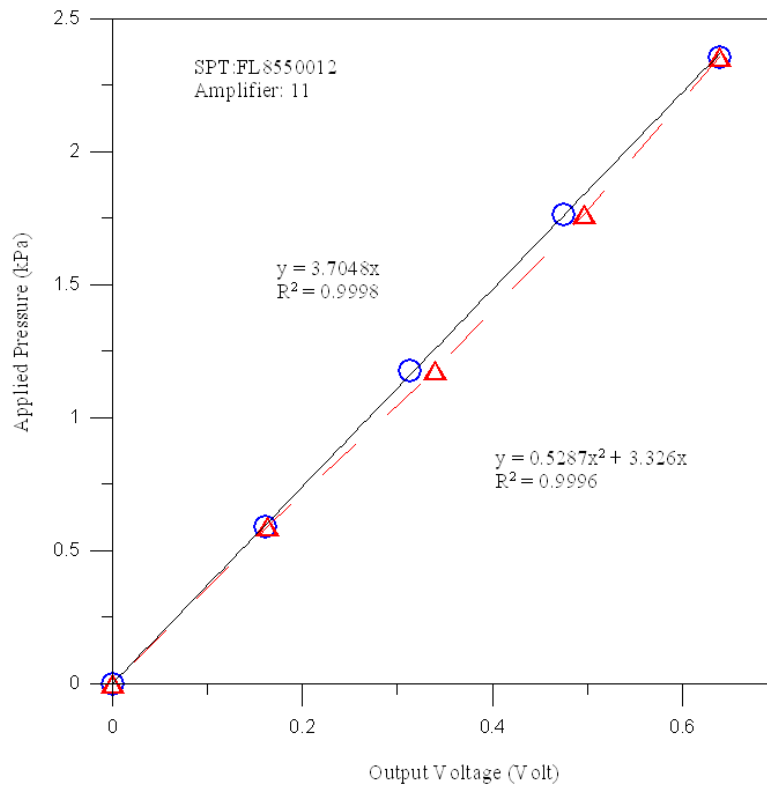


Fig. A4. Applied pressure versus voltage output for soil pressure transducer SPT03 and SPT04

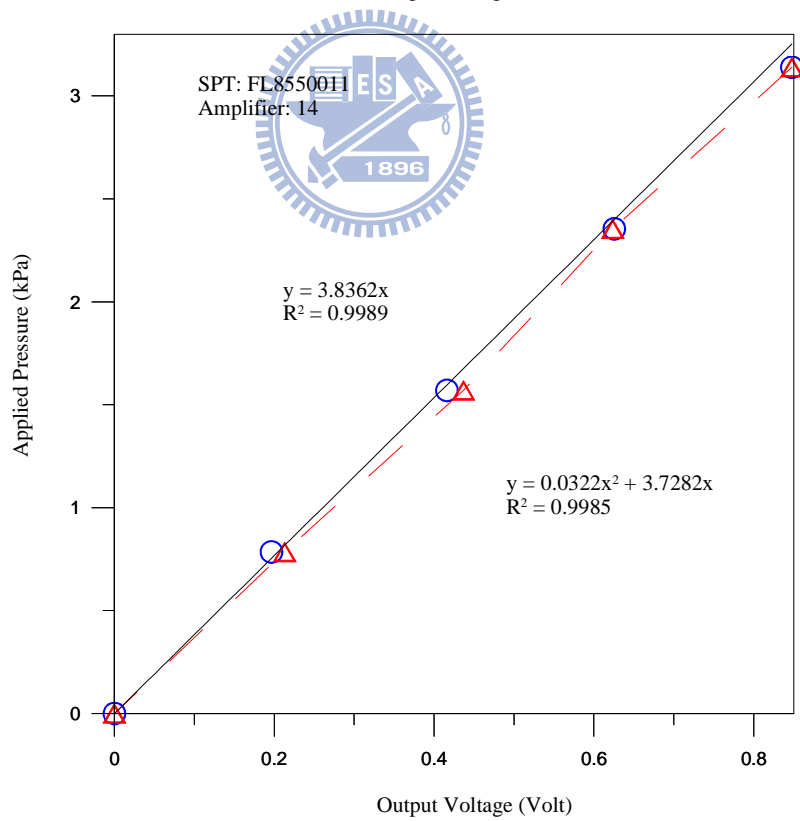
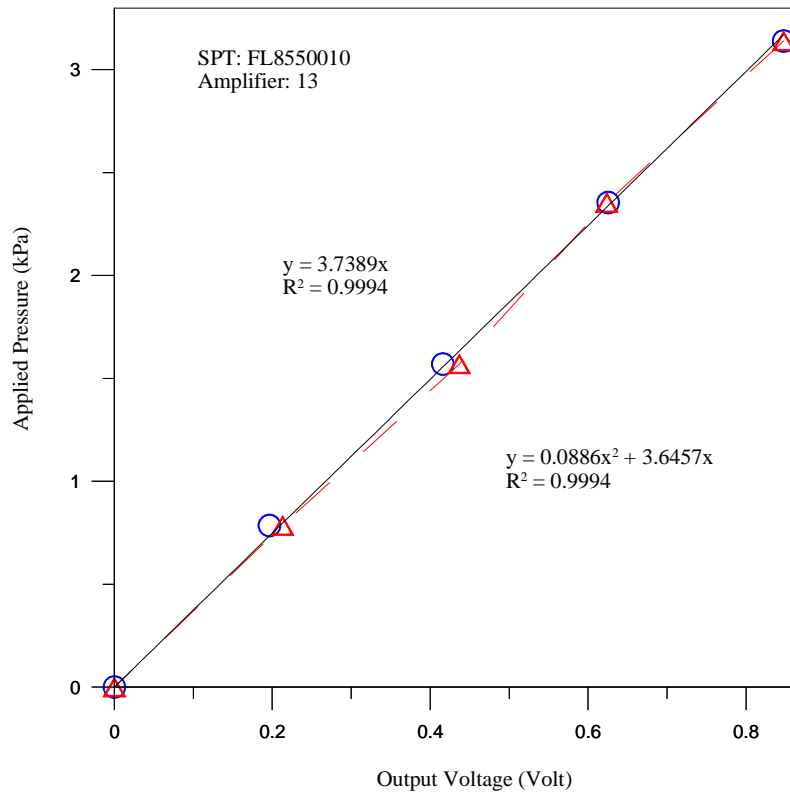


Fig. A5. Applied pressure versus voltage output for soil pressure transducer SPT05 and SPT06

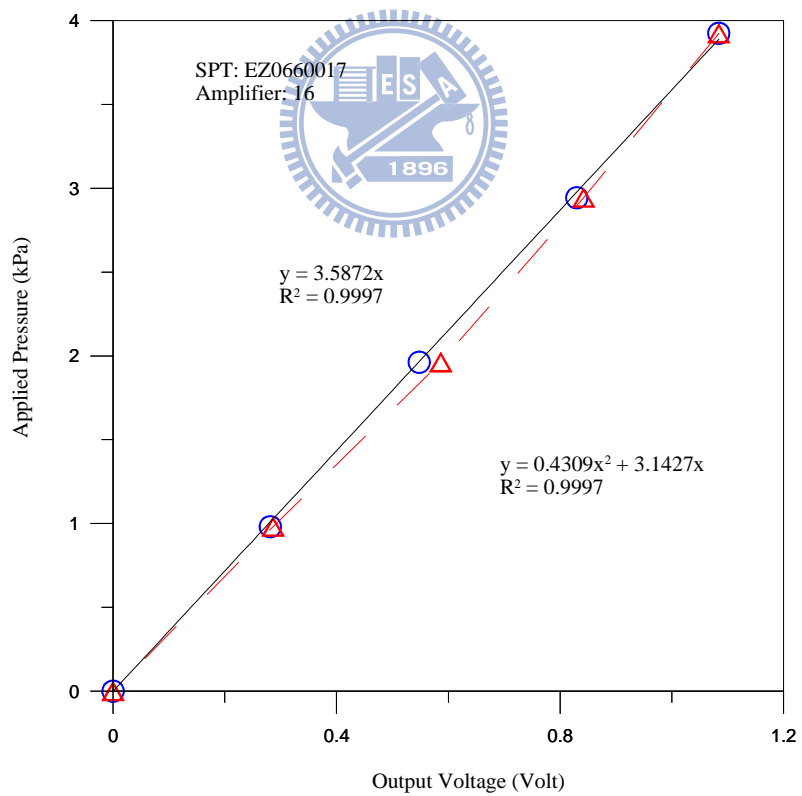
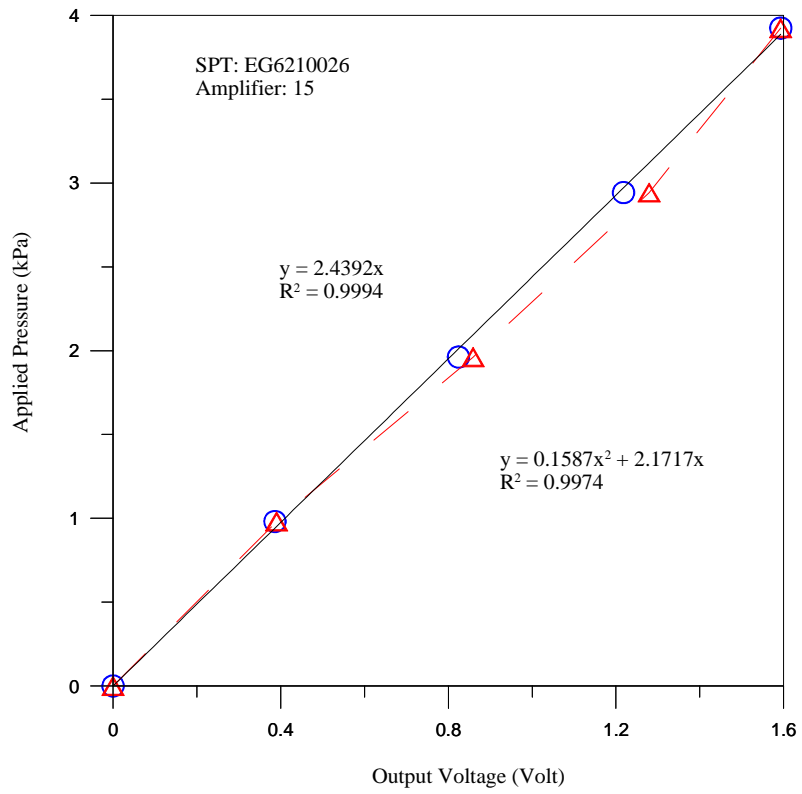


Fig. A6. Applied pressure versus voltage output for soil pressure transducer SPT07 and SPT08

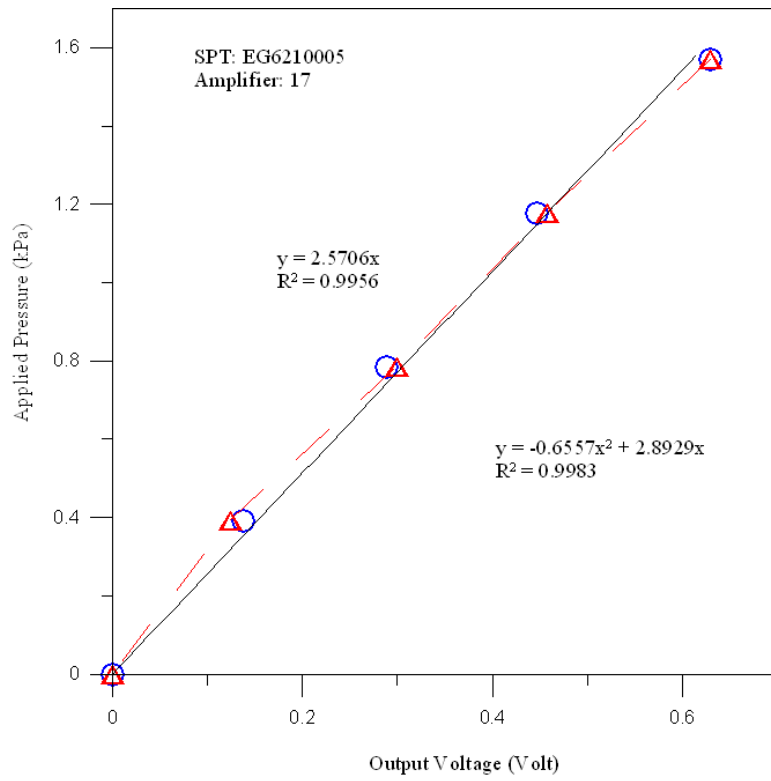


Fig. A7. Applied pressure versus voltage output for soil pressure transducer SPT09

